

**Numerical Approaches for Solving
the Combined Reconstruction and Registration
of Digital Breast Tomosynthesis**

Guang Yang



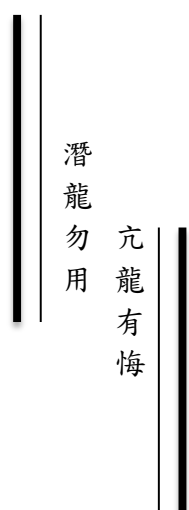
Centre for Medical Image Computing
Department of Computer Science and Medical Physics
University College London

A dissertation submitted in partial fulfillment
of the requirements for the degree of
Doctor of Philosophy
of
University College London.

2012

[This page intentionally left blank]

I, Guang Yang, confirm that the work presented in this thesis is my own. Where information has been derived from other sources, I confirm that this has been indicated in the thesis. Permissions to reproduce Figures 1.1, 1.2, 2.8 have been granted by the corresponding copyright holders listed in the bibliography.



Abstract

Heavy demands on the development of medical imaging modalities for breast cancer detection have been witnessed in the last three decades in an attempt to reduce the mortality associated with the disease. Recently, Digital Breast Tomosynthesis (DBT) shows its promising in the early diagnosis when lesions are small. In particular, it offers potential benefits over X-ray mammography — the current modality of choice for breast screening — of increased sensitivity and specificity for comparable X-ray dose, speed, and cost.

An important feature of DBT is that it provides a pseudo-3D image of the breast. This is of particular relevance for heterogeneous dense breasts of young women, which can inhibit detection of cancer using conventional mammography. In the same way that it is difficult to see a bird from the edge of the forest, detecting cancer in a conventional 2D mammogram is a challenging task. Three-dimensional DBT, however, enables us to step through the forest, *i.e.*, the breast, reducing the confounding effect of superimposed tissue and so (potentially) increasing the sensitivity and specificity of cancer detection.

The workflow in which DBT would be used clinically, involves two key tasks: reconstruction, to generate a 3D image of the breast, and registration, to enable images from different visits to be compared as is routinely performed by radiologists working with conventional mammograms. Conventional approaches proposed in the literature separate these steps, solving each task independently. This can be effective if reconstructing using a complete set of data. However, for ill-posed limited-angle problems such as DBT, estimating the deformation is difficult because of the significant artefacts associated with DBT reconstructions, leading to severe inaccuracies in the registration.

The aim of my work is to find and evaluate methods capable of allying these two tasks, which will enhance the performance of each process as a result. Consequently, I prove that the processes of reconstruction and registration of DBT are not independent but reciprocal.

This thesis proposes innovative numerical approaches combining reconstruction of a pair of temporal DBT acquisitions with their registration iteratively and simultaneously. To evaluate the performance of my methods I use synthetic images, breast MRI, and DBT simulations with in-vivo breast compressions. I show that, compared to the conventional sequential method, jointly estimating image intensities and transformation parameters gives superior results with respect to both reconstruction fidelity and registration accuracy.

[This page intentionally left blank]

Acknowledgements

First and foremost, I would like to thank Prof. Simon Arridge for being such an excellent primary supervisor. Without his acumen and motivation I would never have completed my beloved Ph.D and this thesis. He always treats me like his own child, and I could not thank him enough for his pertinent advice, vigorous debate, and robust support throughout the last few years. Dr. John Hipwell has been an extremely patient and supportive supervisor and mentor. I could not have made my Ph.D this far without his guidance and reassurance, firstly through helping me immeasurably with my daily research, but also by inspiring me with the quality of his own research. I am indebted grateful to Prof. David Hawkes for being my tertiary supervisor and the project assessor through my whole Ph.D study. His wisdom on leadership and morale makes our Centre for Medical Image Computing (CMIC) a great success in academia.

Support was given by the Department of Trade and Industry, who fully funded this project in all its stages. I also gratefully acknowledge the Department of Computer Science, University College London (UCL) for funding my Ph.D tuition. Thanks are also due to Prof. Sir Michael Brady and Dr Julia Schnabel, who gave me much valuable advice in the early stages of this work through our project meetings. I would like to thank Dr. Ed Bullard and Mr. Spencer Gunn from Dexela Ltd. for their kindly collaboration alongside our team during this research project.

To my Ph.D external examiners, Prof. Jamshid Dehmeshki and Dr. Graeme Penney, I would like to express my sincerely thanks in advance for reading through the thesis.

UCL administrative team is great, and thanks go to Ms. Dominique Drai and Ms. Dawn Bailey. I am particularly grateful to Mr. Ron Gaston, who gave me lots of support through my Ph.D, not only helping me to purchase my desktop machine but also accommodating me at CMIC at the last few months of my writing-up.

Also, I would like to thank my friends and colleagues for their technical help and emotional support. In particular, I would like to thank Yu Bai, Marta Betcke, Matthew Clarkson, Teresa Correia, Lianghao Han, Mingxing Hu, James Martin, Andrew Melbourne, Thomy Mertzanidou, Rob Miller, Greg Slabaugh, Christine Tanner, Xujióng Ye, Gary Zhang, and Xiahai Zhuang. Special thanks to Degang Guo and Qian Yu, who extricated me from a predicament of life.

Finally, to my parents, Mr. Xiaoming Yang and Ms. Shuhua Fan, and my wife, Rui, my thankfulness and indebtedness are more than words that I can say. Please accept this thesis in appreciation of all you have done for me.

[This page intentionally left blank]

To my parents, giving me a life.

To my wife, giving me a different one.

[This page intentionally left blank]

Nomenclature

A	Forward projection matrix. (First used in Equation 3.39 on page 90).
A^T	Backward projection matrix. (First used in Equation 3.40 on page 91).
c	Speed of light in vacuum. (First used in Equation 2.1 on page 50).
F	Fourier Transform. (First used in Equation 3.19 on page 79).
f	Objective functional. (First used in Equation 3.41 on page 91).
g	Gradient information. (First used in Equation 3.42 on page 91).
H	Hessian matrix. (First used in Equation 3.65 on page 96).
h	Planck's constant. (First used in Equation 2.1 on page 50).
I	Identity matrix. (First used in Equation 3.66 on page 96).
I_0	Incident intensity. (First used in Equation 3.3 on page 71).
I_A, I_B	Transmitted intensities. (First used in Equation 3.3 on page 71).
n_0	Intensity of the incoming beam. (First used in Equation 2.5 on page 50).
n_A	Intensity of the output beam A. (First used in Equation 2.5 on page 50).
n_B	Intensity of the output beam B. (First used in Equation 2.5 on page 50).
P	Projection. (First used in Equation 3.6 on page 73).
\mathbb{R}	Real number space. (First used in Equation 3.57 on page 93).
\mathcal{D}	Data discrepancy functional. (First used in Equation 3.58 on page 93).
\mathcal{I}	Interpolation operation. (First used in Equation 4.1 on page 100).

\mathcal{L}	Lagrangian functional. (First used in Equation E.5 on page 220).
\mathcal{M}	Probability density function (PDF). (First used in Equation 5.29 on page 145).
\mathcal{N}	Adding noise operation. (First used in Equation 5.30 on page 145).
\mathcal{P}	Extra penalty functional. (First used in Equation 4.22 on page 111).
\mathcal{R}	Regularisation functional. (First used in Equation 3.58 on page 93).
\mathcal{S}	Similarity measurement. (First used in Equation 4.21 on page 110).
\mathcal{T}	Transformation operation. (First used in Equation 4.9 on page 104).
β	B-spline interpolation basis function. (First used in Equation 4.8 on page 102).
$\delta(\cdot)$	Dirac delta function. (First used in Equation 3.11 on page 74).
ι, ς	Lamé constants. (First used in Equation 4.26 on page 112).
λ	Regularisation parameter. (First used in Equation 4.22 on page 111).
ξ	Extra penalty parameter. (First used in Equation 4.22 on page 111).
ν_f	ESE to AGD dose conversion factor. (First used in Equation 2.7 on page 62).
φ	Interpolation basis function. (First used in Equation 4.1 on page 100).
ζ	Transformations. (First used in Equation 4.21 on page 110).
a	Weight of lines of the ART method. (First used in Equation 3.26 on page 85).
C	Relevant radiation contrast. (First used in Equation 2.5 on page 50).
D	Quantity absorbed dose. (First used in Equation 2.6 on page 61).
M	Unit mass of material. (First used in Equation 2.6 on page 61).
D_g	Average Glandular Dose (AGD). (First used in Equation 2.7 on page 62).
E	Energy, <i>e.g.</i> , photon energy. (First used in Equation 2.1 on page 50).
e	Charge of electrons. (First used in Equation 3.1 on page 71).
f	Unknown intensities. (First used in Equation 3.26 on page 85).

m_e	Mass of electrons. (First used in Equation 3.1 on page 71).
p	Projection data. (First used in Equation 3.26 on page 85).
R	Fixed image. (First used in Equation 4.21 on page 110).
T	Moving image. (First used in Equation 4.21 on page 110).
U	Voltage. (First used in Equation 3.1 on page 71).
v	Electron velocity. (First used in Equation 3.1 on page 71).
X	Entrance Skin Exposure (ESE). (First used in Equation 2.7 on page 62).
u	Displacement vector. (First used in Equation 6.23 on page 165).
$*$	Adjoint operator. (First used in Equation 6.3 on page 160).
\square	End of proof. (First appears on page 205).
\otimes	Convolution. (First used in Equation 4.8 on page 102).
\mapsto	Maps to. (First appears on page 130).
\dagger	Moore-Penrose pseudo-inverse. (First appears on page 91).
\star	Minimised solution. (First used in Equation 3.40 on page 91).
\times	Multiplication. (First appears on page 50).

[This page intentionally left blank]

Contents

Abstract	5
Acknowledgements	7
Nomenclature	11
Contents	15
List of Figures	21
List of Tables	33
1 Introduction	35
1.1 Problem Statement	40
1.2 Research Objective	40
1.3 Contributions.....	40
1.4 Thesis Structure	41
2 An Introduction to Breast Imaging and DBT	42
2.1 Breast Imaging: An Overview	42
2.1.1 Breast MRI	43
2.1.2 Breast Ultrasonography	46
2.1.3 X-ray Mammography.....	49
2.1.4 Other Breast Imaging Modalities	57
2.2 Digital Breast Tomosynthesis	58

2.3 Conclusions and Discussion	64
3 Tomographic Reconstruction and Its Applications in DBT	70
3.1 Forward Problem: Imaging	70
3.1.1 Forward Radon Transform.....	70
3.1.2 DBT Geometry and Hardware Parameters.....	75
3.2 Inverse Problem: Reconstruction	76
3.2.1 Analytical Methods	76
3.2.1.1 Shift-And-Add (SAA) and Back-projection (BP) Methods	76
3.2.1.2 Filtered Back-projection Method (FBP)	78
3.2.2 ART Based Iterative Methods	85
3.2.2.1 Algebraic Reconstruction Technique (ART)	85
3.2.2.2 Simultaneous Iterative Reconstruction Technique (SIRT)	87
3.2.2.3 Simultaneous Algebraic Reconstruction Technique (SART)	89
3.2.3 Least Squares Estimation	90
3.2.3.1 Least Squares Approximation	90
3.2.3.2 Numerical Optimisation	94
3.3 Conclusions and Discussion	97
4 Image Registration and Its Applications in DBT	99
4.1 Forward Problem: Warping	100
4.1.1 Image Interpolation	100
4.1.2 Transformation Models.....	103
4.2 Inverse Problem: Registration	106
4.2.1 Category of the Image Registration	107
4.2.1.1 Landmark-Based Image Registration	107
4.2.1.2 Segmentation-Based Registration.....	107
4.2.1.3 Intensity-Based Registration	107
4.2.1.4 Parametric Image Registration	108
4.2.1.5 Non-Parametric Image Registration.....	108

4.2.2	Solving the Image Registration Problem	109
4.2.2.1	Distance Measures	109
4.2.2.2	Numerical Optimisation	110
4.2.2.3	Ill-Posed and Regularisation	111
4.2.2.4	Validation Methods.....	112
4.3	Registration Algorithms in Breast Imaging and DBT	113
4.4	Conclusions and Discussion	118
5	Iterative Reconstruction and Registration	120
5.1	Motivation	120
5.2	Problem Outline	122
5.2.1	Forward and Inverse Problems	122
5.2.1.1	Reconstruction Part	122
5.2.1.2	Registration Part	123
5.2.2	Forward and Backward Projectors	123
5.3	Materials	127
5.3.1	DBT Simulation Using Synthetic Toroid Phantom	127
5.3.2	DBT Simulation Using Uncompressed MRI.....	128
5.3.3	DBT Simulation Using In-Vivo Compressed Breast MRI	129
5.4	Sequential Method versus Iterative Method	130
5.4.1	Sequential Method	130
5.4.2	Iterative Method	131
5.4.3	Validation	134
5.4.4	Implementation.....	134
5.5	Experiments and Results using Affine Model.....	135
5.5.1	Hypothetical Experiment HA1: Test on the Identity Registration Transformations with the Same Projections	135
5.5.2	Hypothetical Experiment HA2: Test on the Different Forward Projections with Known Registration Parameters	136
5.5.3	Experiment IA1: Test on the DBT Simulation Using Synthetic Toroid.....	138

5.5.4	Experiment IA2: Test on the DBT Simulation Using Uncompressed MRI	140
5.5.5	Experiment IA3: Test on the DBT Simulation with In-Vivo Compression	142
5.5.6	Experiment IA4: Test on the Noisy Data	145
5.5.7	Experiment IA4: Test on Different Displacements	148
5.6	Conclusions and Discussion	151
6	Simultaneous Reconstruction and Registration	154
6.1	Motivation	154
6.2	Problem Outline	155
6.2.1	Forward and Inverse Problems	155
6.2.2	Decoupled Approach.....	156
6.3	Materials	157
6.4	Simultaneous Method	159
6.4.1	Simultaneous Method	159
6.4.2	Transformation Operator	162
6.4.2.1	Adjoint Operator	162
6.4.2.2	Derivative Operator	164
6.4.2.3	Implementation and Experimental Settings.....	164
6.5	Experiments and Results using the Affine Model	167
6.5.1	Experiment SA1: Test on the DBT Simulation Using Synthetic Toroid	167
6.5.2	Experiment SA2: Test on the DBT Simulation Using Uncompressed MRI	172
6.5.3	Experiment SA3: Test on Different Displacements.....	178
6.5.4	Experiment SA4: Test on the DBT Simulation with In-Vivo Compression	180
6.6	Experiments and Results using the B-spline Model	183
6.6.1	Experiment SB1: Test on the DBT Simulation using 3D Shepp-Logan.....	183
6.6.2	Experiment SB2: Test on the DBT Simulation using 3D Breast Phantom.....	190
6.6.3	Experiment SB3: Test on Different Initial TRE	196
6.7	Conclusions and Discussion	198
7	Conclusion	202

A Forward and Inverse Radon Transform	204
B Optimality Conditions	209
B.1 Taylor's Theorem	209
B.2 Local Minimum	210
B.3 First-Order Necessary Conditions	210
B.4 Second-Order Necessary Conditions	211
B.5 Second-Order Sufficient Conditions	211
C Conditioning of Least Squares Problem	212
D Nonlinear Optimisation Algorithms	213
E Constrained Reconstruction and Registration	219
Bibliography	222

[This page intentionally left blank]

List of Figures

1.1 <i>Left: The anatomy of adult premenopause women breast. The breast itself consists mostly of fat, glandular structures and has no muscular tissue. Around 15 to 25 lactiferous ducts converge at the nipple. The ribs are numbered from 1 to 6; Middle: The Terminal Duct Lobular Unit (TDLU) and normal duct cell; Right: The anatomy of adult postmenopausal female breast. The vascularity of the intervening connective tissue is reduced due to the regression of lobular and alveolar structures. The illustration is reproduced from Jatoi et al. [129].</i>	36
1.2 <i>Four sub-figures above from left to right: Illustration of the normal cells inside the breast, common microscopic abnormal variations, and breast cancer <i>in situ</i> leading to an invasive cancer; The sub-figure below: Metastasis of breast cancer. The illustration is reproduced from Breast Cancer Booklet by Cancer Council Victoria, Australia [3].</i>	37
1.3 <i>The summarised structure of this Ph.D. thesis.</i>	41
2.1 <i>The image acquisition process is performed by rotating the transducer 360°, and the full 3D volume of the breast is covered. Two images, which are acquired 180° apart, are registered to represent the same 2D image plane in the 3D volume.</i>	47
2.2 <i>Scheme of a basic X-ray tube consists of a source and target of electrons, a vacuum envelope, and connection of the electrodes to a high-voltage source.</i>	49
2.3 <i>A simple model of breast, which contains normal breast tissue and a structure of interest, shows various X-ray transmissions in two different paths A and B. The mean number of X-rays transmitted along the two paths are n_A and n_B. The thickness of the breast and the structure of interest are denoted by z and a. Light travels in straight lines in a material of constant refractive index.</i>	50

- 2.4 An illustration of a typical mammography system with gantry. From top to bottom, it consists of an X-ray tube anode, the focal spot, a filter, a compression paddle, an anti-scatter grid, and a receptor. Firstly, the X-ray tube anode of the mammography apparatus is made of molybdenum material, or a dual material anode with an additional rhodium track. Most X-ray tubes have a tungsten material anode; however, materials such as molybdenum and rhodium are used because they yield a nearly optimal characteristic radiation spectrum for breast imaging. Secondly, a typical x-ray tube for mammography has two selectable focal spots for contact imaging and magnification imaging. The nominal size 0.1mm is small in order to reduce the geometric blurring caused by the magnification. Thirdly, most of the X-ray machines use aluminium to filter the x-ray beam to reduce unnecessary exposure to the patient. However, mammography uses molybdenum or rhodium filter to optimize the spectrum for specific breast conditions. Next, the compression is essential to reduce the radiation dose and overlapping breast tissues. Furthermore, an anti-scatter grid is applied to absorb the scattered radiation, and improves the contrast sensitivity. Lastly, phosphor screen and film receptor, or digital receptor is employed for the mammography system..... 52
- 2.5 Left: Schematic of a flat panel detector with CsI(Tl) scintillator, and the amorphous silicon detector array (a-Si sensor matrix). The individual detector element is optimised for high photon detection efficiency, and the structure with a Thin-Film Transistor (TFT) readout element is enlarged as illustrated in the details. Top right: An electron microscope view of the CsI(Tl) needles that constitute the scintillator layer [83]. The X-ray photons are produced by the X-ray tube, and they go through the patient and the scintillation layer converts them to visible light photons. Then these visible photons reach the array of photodiodes or Charge-Coupled Devices (CCDs), and output the electrons. Amorphous silicon or a selenium layer receives these electrons, and generates the electronic image data. An Analog-to-Digital Converter (ADC), which converts the voltage to a digital number, is used to produce the digital image. Bottom right: Photo of a flat panel detector [83]..... 53
- 2.6 Left: DBT system geometries use isocentric motion and the coordinates; Middle: Both the x-ray source and detector move in an arc shape oppositely (Grossman geometry); Right: the x-ray source and detector move parallel to the in-focus tomographic plane oppositely (Twinning geometry)..... 60

2.7 The most left: Photograph of the latest development of MAMMOMAT® Inspiration (Siemens) with a 3D tomosynthesis option. Left: One of the earlier developed digital mammography machines (Siemens) with a tomosynthesis facility. Right: Top view and bottom view of an amorphous selenium detector used for tomosynthesis imaging. The most right: A FFDM machine (Siemens) with no tomosynthesis function.	61
2.8 Left: Contrast and dose as a function of kVp (the plot is based on the data published in [34]). Right: Optimum photon energy (spectrum) of mammography depends on the size and density of the breast (this plot is reproduced from [272]).	62
2.9 Statistics of scientific publications on tomosynthesis research field indexed by ISI Web of Knowledge and PubMed. Actually, there are some papers on tomosynthesis before 1972 when Grant defined the term 'tomosynthesis'.	63
2.10 Comparison between mammography and breast MRI for the same 33-year-old patient with documented BRCA1 mutation. Left: Screening mammogram (MLO view of the right breast); Upper right: Pre-contrast T1-weighted breast MRI; Lower right: First post contrast of the dynamic series. The images are taken from Morris et al. [205].	67
2.11 Comparison between breast MRI and breast ultrasound for the same 47-year-old patient. Left: T1-weighted breast MRI in sagittal view showing two lesions (red and green arrows); Middle: Breast ultrasound shows a hypoechoic mass that is taller than wide (red arrow), corresponding to the superior MRI lesion; Right: Breast ultrasound shows a hypoechoic mass that is taller than wide (green arrow), corresponding to the inferior MRI lesion. The images are taken from Morris et al. [205].	67
2.12 Comparison between mammography and DBT for the two different patients. Two sub-figures on the left hand side: Original mammography with in-plane artefacts caused by breast tissues overlapping (yellow circle) vs. a selected DBT slice (reconstructed) and the lesion is clearly shown in the DBT reconstruction (red circle); Two sub-figures on the right hand side: Original mammography showing overlapped breast tissues (yellow circle) vs. a selected DBT slice (reconstructed) showing the lesion clearly (red circle) and the in-plane streak artefacts are shown (green square). The images are taken from Bick and Diekmann [22].	69
2.13 Comparison between mammography and DBT slices. The sub-figure on the left hand side: Original 2D mammography showing a potential lesion (yellow square); Other sub-figures: The individual structures that make up the potential lesion can be clearly seen on the separated slices (No. 14, 18, 22, 26 and 30) of 3D DBT, and no lesion is presented in fact. The images are taken from Dallessio [54].	69

3.1	<i>Detailed classification of the reconstruction algorithms.</i>	71
3.2	<i>Left: A single X-ray beam is passing through a segment of breast tissue with multiple inhomogeneous attenuation coefficients; Right: A 3D matrix of discrete attenuation coefficients can be created.</i>	72
3.3	<i>Schematic illustration of the relationship between x, y, ρ, σ and θ.</i>	74
3.4	<i>Left, line type X-ray source; Middle, circle type X-ray source; Right, schematic of DBT synthesis (A) and conventional summing up (B). For example, we focus on the red circular object on the tomographic focal plane. By shifting and adding synthesis method, DBT imaging increases the visibility of objects by blurring out objects (e.g., the green triangle) from other planes.</i>	77
3.5	<i>Left: Three sets of line project the target to three projection views. While only three views are shown above, a typical CT scan uses hundreds of views at slightly different angles. Right: Backprojection reconstructs an image by taking each view and smearing it along the path it was originally acquired; however, the resulting image is a blurry version of the original image. These images are copied from Steven W. Smith [268].</i>	78
3.6	<i>Illustration of the Fourier Slice Transform.</i>	79
3.7	<i>Samples in the μ, v domain and the interpolation to the Cartesian coordinates.</i>	80
3.8	<i>Flow chart of the DFT reconstruction procedure in 2D.</i>	81
3.9	<i>Filtered backprojection reconstructs an image by filtering each view before backprojection. This removes the blurring effects in the simple backprojection, and the results in a mathematically exact reconstruction of the image. Filtered backprojection is the most commonly used algorithm for CT scanner. [268]</i>	83
3.10	<i>A human breast demonstrating a solitary calcification. Left: Traditional SAA. Middle: BP. Right: FBP (Hamming and Gaussian filters). The in-plane slices shown here are 7.5mm above the surface plate. There are some inter-plane artefacts shown in both SAA and BP reconstructions. These artefacts, which due to the interferences of features in other planes, form the suspicious masses (red circles) and they are eliminated using the FBP method. Results are collected from Chen's thesis [41]</i>	84
3.11	<i>Square grid on the image.</i>	86

3.12 <i>Diagram of the trade-off between the data fidelity and the regularisation terms represented by data error and image regularity metric respectively. The plot shows the fidelity and regularity plane for an undersampled (blue area) versus a completely sampled tomographic system (red area). For completely sampled systems, a unique image minimises the data error because only one value of the regularity is possible, whereas many possible candidate volumes correspond to the situation of minimum data error for undersampled systems. The two curves represent a generic behaviour of standard iterative algorithms for the case of no regularisation (solid curve) and with regularisation (dashed curve).</i>	98
4.1 <i>Interpolation examples using a 1D signal. First row: Various interpolation kernels; Second row: Coarse interpolation using samples (green square) on the original signal; Third row: Fine interpolation using more samples (zoomed in area of the red box).</i>	102
4.2 <i>Illustration of the taxonomy of spatial transforms.</i>	103
4.3 <i>Examples of 2D transformations.</i>	104
4.4 <i>Summary of image registration key components and categories.</i>	118
5.1 <i>Flow chart of breast tomosynthesis iterative reconstruction-registration method. Blocks from right to left: 1. Initial setup to simulate X-ray acquisitions; 2. Perform two incomplete reconstruction loops; 3. Register for the reconstructed volumes and return the transformation parameters to update the fixed volume.</i>	121
5.2 <i>Forward projection geometry in 3D.</i>	122
5.3 <i>A 2D schematic illustration of the DBT geometry. Firstly, we define the X-ray source to detector distance L_{SID} to 66cm, and the length of the rotation arm R is 44.3cm and the distance L between the rotation centre of the X-ray source and the detector is 21.7cm. L_z is the depth of the object, which is around 3cm to 8cm in real applications. In addition, L_{Dx} is the width of the forward projection images, which depends on the width L_x of the object, and L_{SRD} defines the X-ray source to its rotation centre distance.</i>	124
5.4 <i>Schematic illustration of the ray-casting method.</i>	125

5.5	<i>Different line-integration schemes of the ray-casting method. Vertical dash lines are slices of the x-y plane. Siddon's method is only defined by the length of intersection between two adjacent slices; In Josephs method, only bilinear interpolation is required on the x-y plane; Equal sampling approach employs trilinear Interpolation with equidistance along the line and there might be more than one interpolations between two adjacent slices; Köhler's method finds the bilinear interpolations on both x-y and x-z planes, and then applies the trilinear interpolation according to the position of the bilinear interpolations.....</i>	126
5.6	<i>Red circle: Define the major radius of the toroid (24mm). Blue circle: Define the minor radius of the toroid (10mm).....</i>	127
5.7	<i>Left: Fixed (target) image; Right: Moving image. The transformations R_ζ between the target and the moving images contain a translation of $\mathcal{T}_{\text{translation}} = [10, 0, -20]\text{mm}$ and a rotation about the y axis of -30 degrees. Intensities have been normalised into the range of 0 to 1.</i>	128
5.8	<i>Left: Projection of the fixed image. Right: Projection of the moving image.....</i>	128
5.9	<i>Left: Fixed (Target) Image; Right: Moving Image. The transformations R_ζ between the target and the moving images contain a translation of $\mathcal{T}_{\text{translation}} = [10, 0, -20]\text{mm}$ and a rotation about the y axis of -30 degrees.</i>	129
5.10	<i>Left: Projection of the fixed image. Right: Projection of the moving image.....</i>	129
5.11	<i>Left: Projection of the fixed image. Right: Projection of the moving image.....</i>	130
5.12	<i>Results of the sequential method and the iterative method when the correct registration transformations have been provided. (a)-(c): Results of the sequential method; (d)-(f): Results of the iterative method. (Left: Coronal view; Middle: Transverse view; Right: Sagittal view. Original ground truth of the fixed and moving images are shown below in Figure 5.13 (a) and (e)).....</i>	137
5.13	<i>(a) Original test volume f_1^g; (e) Transformed test volume f_2^g; Sequential results (b)-(d): (b) reconstruction f_1^*, (c) reconstruction f_2^*, and (d) transformed reconstruction $\mathcal{T}_\zeta^* f_2^*$; Iterative results (f)-(h): (f) reconstruction f_1^*, (g) reconstruction f_2^*, and (h) transformed reconstruction $\hat{\mathcal{T}}_\zeta f_2$.....</i>	138

5.14 Plot of the cost function $f(f_1) = \frac{1}{2} \ Af_1 - p_1\ ^2$ for the 3D toroid experiment. In this graph, we plot the cost function value with respect to the iteration number for both sequential and iterative methods. There are 100 iterations in total and the cost function values are the same for both methods at the first iteration. For the sequential method, we have got a cost function which is decreasing smoothly. In contrast, the iterative method updates f_1 with the transformation of \hat{f}_2 , i.e., $\hat{T}_\zeta \hat{f}_2$, after 10 iterations of the reconstruction and a single registration. This results in the increasing and peaks in the cost function plot of the iterative method (including the initial first iteration).	139
5.15 As Figure 5.13 but for a 3D uncompressed breast MR image.	140
5.16 As Figure 5.14 but for the 3D uncompressed breast MR image.	141
5.17 As Figure 5.13 but applied to in-vivo MRI acquisition of a breast before and after plate compression (Images have been segmented and mapped to effective X-ray attenuation).	142
5.18 As Figure 5.14 but for the in-vivo compressed DBT simulation experiment.....	143
5.19 Noisy forward projections. (a)-(c): Forward projections of the fixed images. (d)-(f): Forward projections of the corresponding moving images. The images present different noise levels.	146
5.20 Plot of the relative error against different levels of noise using the toroid phantom.	146
5.21 As Figure 5.20 but for the uncompressed breast MRI experiment.	147
5.22 As Figure 5.20 but for the in-vivo compressed DBT simulation experiment.....	147
5.23 Experiment on different initial displacements (rotation levels) and TRE (on \log_2 scale). (a), (c), and (e): Test on the toroid phantom image showing initial and final TRE with respect to the various initial rotation levels; (b), (d), and (f): The same test on the breast MRI images. 149	
5.24 Experiment on different initial displacements (rotation levels) and SSD error (on \log_2 scale). (a), (c), and (e): Test on the toroid phantom image showing initial and final SSD with respect to the various initial rotation levels; (b), (d), and (f): The same test on the breast MRI images. 150	
5.25 Magnified results of the three tests above. (a), (b) and (f) of figures 5.13, 5.15 and 5.17. Left to right: Original fixed image f_1^g ; Results of the sequential method f_1^s ; Results of the iterative method f_1^i . Only one of the out-of-plane slices have been shown accordingly.	153

6.1	<i>2D results of the interpolation operation and its transpose. First row: Forward interpolation with deformed grid on; Second row: transpose of the interpolation. From left to right: Original image; Implementation using C with Matlab MEX interfaces; Implementation using Matlab; Difference images between two implementations. The results have shown that our C implementation is faster and accurate.</i>	162
6.2	<i>3D results of the interpolation operation (Left) and its transpose (Right).</i>	163
6.3	<i>B-spline transformation example. Top Row: Regular grid (Left) and B-spline transformed grid (Right) of the x-y plane centre slice; Bottom Row: Original mesh (Left) with control points and its B-spline transformation (Right). The original 3D Shepp-Logan phantom image has $65 \times 65 \times 65$ voxels, and there are $9 \times 9 \times 9$ control points (red points) placed equidistantly along each dimension.</i>	166
6.4	<i>Toroid phantom test case 1. (a)-(c): Fixed image; (d)-(f): Moving image; (g)-(i): Sequential result, i.e., transformed moving image reconstruction $\mathcal{T}_\zeta^* f_2^*$; (j)-(l): Simultaneous result. (Left: Coronal view; Middle: Transverse view; Right: Sagittal view.)</i>	168
6.5	<i>Plot of the mean and standard deviation of the absolute error between the recovered and the ground truth transformation parameters for 20 different randomly generated affine transformations. The 12 parameters are calculated using Equation 4.10, which combines rotation, scaling, shearing and translation. In other words, these 12 parameters are the 12 entries of the affine transformation matrix. In the plot, parameters number 4, 8, 12 are the translations along each direction, and other parameters are obtained from the multiplication of the rotation matrix and matrices of the scaling and shearing.</i>	169
6.6	<i>Difference images. (a)-(c): Differences between the fixed and the moving images; (d)-(f): Differences between the fixed image and the sequential result; (g)-(i): Differences between the fixed image and the simultaneous result.</i>	170
6.7	<i>Reconstruction using two acquisitions p_1 and p_2 without registration. (a)-(c): Fixed image reconstruction; (d)-(f): Moving image reconstruction.</i>	171
6.8	<i>Breast MRI test case 8. (a)-(c): Fixed image; (d)-(f): Moving image; (g)-(i): Sequential result, i.e., transformed moving image reconstruction $\mathcal{T}_\zeta^* f_2^*$; (j)-(l): Simultaneous result. The transverse view has been rotated 90° clockwise for the purpose of better display. (Left: Coronal view; Middle: Transverse view; Right: Sagittal view.)</i>	173

6.9	<i>Difference images.</i> (a)-(c): Differences between the fixed and the moving images; (d)-(f): Differences between the fixed image and the sequential result; (g)-(i): Differences between the fixed image and the simultaneous result.	174
6.10	<i>As Figure 6.5, plot of the mean and standard deviation of the absolute error between the recovered and the ground truth transformation parameters of 15 different affine transformations.</i>	175
6.11	<i>Line profiles of the three views of the breast MRI test case 8. (The line profiles were drawn between the two arrows of each view as seen in Figure 6.8 (a)-(c) as an example, and they were at the same positions for other corresponding images.)</i>	177
6.12	<i>Line profiles of the reconstruction results without registration. (The line profiles were drawn at the same positions as Figure 6.11 showed.)</i>	178
6.13	<i>Experiment on different initial displacements (rotation levels) with final TRE and SSD error (on log₂ scale). (a), (c), and (e): Test on the toroid phantom image showing initial and final TRE and SSD with respect to the various initial rotation levels; (b), (d), and (f): The same test on the breast MRI images.</i>	179
6.14	<i>Two DBT simulations were created using in-vivo MR acquisitions of a breast with two different real plate compressions to mimic the temporal imaging (Images have been segmented and mapped to effective X-ray attenuation). (a)-(c): Fixed image; (d)-(f): Moving image; (g)-(i): Sequential result, i.e., transformed moving image reconstruction $T_\zeta^* f_2^*$; (j)-(l): Simultaneous result. (Left: Transverse view; Middle: Coronal view; Right: Sagittal view.)</i>	181
6.15	<i>Difference images. (a)-(c): Differences between the fixed and the moving images; (d)-(f): Differences between the fixed image and the sequential result; (g)-(i): Differences between the fixed image and the simultaneous result.</i>	182
6.16	<i>Line profiles of the transverse view of the DBT simulations experiment. The line profiles were drawn between the two arrows of the transverse view as seen in Figure 6.14 (a) as an example.)</i>	182
6.17	<i>Displacement field. (a) Original regular grid for the central slice; (b) Deformed grid for the central slice; (c) Displacement field of the whole 3D volume. (Red cross: control points; Green arrow: displacement vector in 2D; Coloured quiver: displacement vector in 3D.)</i>	183
6.18	<i>Original fixed 3D Shepp-Logan phantom and its regular grid for the central slice.</i>	184
6.19	<i>Transformed 3D Shepp-Logan phantom and its deformed grid for the central slice, i.e., ground truth of the transformation.</i>	184

6.20 Simultaneous reconstruction and registration result and the registered control point grid for the central slice	185
6.21 Difference image between the simultaneous result (Figure 6.20) and the original fixed phantom (Figure 6.18). The registered control point grid is superimposed on the ground truth transformation and indicates that the ground truth transformation has been recovered well for the majority of control points. (Figure 6.19).....	185
6.22 A montage view of the original fixed 3D Shepp-Logan phantom.	186
6.23 A montage view of the transformed 3D Shepp-Logan phantom.	187
6.24 A montage view of the simultaneous reconstruction and registration result.	188
6.25 A montage view of the difference image between the simultaneous result (Figure 6.24) and the original fixed phantom (Figure 6.22).	189
6.26 The 3D breast phantom images. (a) In higher resolution with $260 \times 260 \times 260$ voxels; (b) The down-sampled version of (a) in lower resolution with $65 \times 65 \times 65$ voxels.	190
6.27 Original fixed 3D breast phantom image and its regular grid for the central slice.....	191
6.28 Transformed 3D breast phantom image and its deformed grid for the central slice, i.e., ground truth of the transformation.....	191
6.29 Simultaneous reconstruction and registration result and the registered control point grid for the central slice.	192
6.30 Difference image between the simultaneous result (Figure 6.29) and the original fixed phantom (Figure 6.27). The registered control point grid is superimposed on the ground truth transformation and indicates that the ground truth transformation has been recovered well for the majority of control points. (Figure 6.28).....	192
6.31 A montage view of the original fixed 3D breast phantom image.	193
6.32 A montage view of the transformed 3D breast phantom image.....	194
6.33 A montage view of the simultaneous reconstruction and registration result.	195
6.34 A montage view of the difference image between the simultaneous result (Figure 6.33) and the original fixed phantom (Figure 6.31).	196
6.35 Experiment on different initial displacements (TRE levels) with final TRE and SSD error (on \log_2 scale). (a), (c), and (e): Test on the toroid phantom image showing initial and final TRE and SSD with respect to the various initial TRE levels; (b), (d), and (f): The same test on the breast MRI images.....	197

-
- 6.36 *The 3D toroid test case 1. Comparison of the objective function of the fixed image reconstruction using the sequential method $f(f_1) = \frac{1}{2} \|Af_1 - p_1\|^2$, and the objective function of the simultaneous method $f(f, \zeta) = \frac{1}{2} (\|Af - p_1\|^2 + \|A\mathcal{T}_\zeta f - p_2\|^2)$.* 199
- 6.37 *The breast MRI test case 8. Comparison of the objective function of the fixed image reconstruction using the sequential method $f(f_1) = \frac{1}{2} \|Af_1 - p_1\|^2$, and the objective function of the simultaneous method $f(f, \zeta) = \frac{1}{2} (\|Af - p_1\|^2 + \|A\mathcal{T}_\zeta f - p_2\|^2)$.* 200

[This page intentionally left blank]

List of Tables

2.1	<i>Comparison of various physical properties in different breast imaging modalities.</i>	65
3.1	<i>DBT imaging system parameters from some of the most famous manufacturers.</i>	75
5.1	<i>Comparison of the signal to noise ratio using identity registration transformations with the same forward projections. We test on four different noise levels, i.e., 0.1%, 1%, 10%, and 100% of the maximum intensity of the forward projections. Iter: iterative method; Seqn: sequential method.</i>	136
5.2	<i>Numerical results of the three experiments. (SSD = $\ f_1^* - f_1^g\ ^2$)</i>	144
5.3	<i>Comparison of the relative error, which is defined by $\frac{\ f_1^* - f_1^g\ ^2}{\ f_1^g\ ^2}$.</i>	144
6.1	<i>Comparison of different applications of simultaneous inverse problem. (SR: super-resolution; LR: low resolution; fwdProjs: forward projections; Recon.+Regn.: reconstruction and registration; “-”: not mentioned).</i>	156
6.2	<i>Comparison of the gradient information used in the iterative and simultaneous methods.</i>	164
6.3	<i>Comparison of the SSD error and the TRE. The SSD error of the sequential method is $\ f_1^* - f_1^g\ ^2$ (Difference between the result of the transformed moving image reconstruction and the original fixed image), and the SSD error of the simultaneous method is given by $\ f^* - f_1^g\ ^2$.</i>	201
6.4	<i>Comparison of the relative error, which is defined by $\frac{\ f_1^* - f_1^g\ ^2}{\ f_1^g\ ^2}$ and $\frac{\ f^* - f_1^g\ ^2}{\ f_1^g\ ^2}$ for the sequential and simultaneous method respectively.</i>	201

[This page intentionally left blank]

Introduction

With more than 0.6 million new cases in more economically developed countries each year [4], breast cancer is the commonest non-skin malignancy carcinoma in women. It is a most baleful disease, which is also one of the leading causes of female cancer mortality. In the United Kingdom (UK), where age standardised incidence and mortality are the highest in the world [192], breast cancer is the most prevalent malignant carcinoma. In 2008, a total of 48,034 new cases have been diagnosed in the UK despite the fact that it is rare (341 cases) in around half the population (men). In addition, the lifetime risk of developing breast cancer is 1 in 8 for women and 1 in 1,014 for men using the Adjusted for Multiple Primaries (AMP) method. According to Cancer Research UK, breast cancer incidence rates in women have increased by 51% from 0.75‰ in 1977 to 1.22‰ in 2006 [4]. Moreover, incidence is strongly related to age, with 81% of cases occurring in women of 50-years-old and over. There are fewer cases within the young age groups; however, it is still the most common cancer in women under 35. By the age of 35 to 49, over 6,700 women are diagnosed with breast cancer each year [2].

The normal adult female breast (Figure 1.1) weighs from 30 grams to over 500 grams depending on personal habitus, age, pregnancy, lactation, menstruation, menopause, and other factors. It contains an inconstant composition of subcutaneous fatty tissue, fibrous septa, and fibroglandular elements. The breast is a large modified sebaceous gland that typically consists of 15 to 25 lobes. These lobes are divided into multiple lobules, and each of the lobules includes 10 to 100 terminal milk-secreting alveoli or acini. A single lactiferous duct, which exits at each lobule, is formed with many tiny milk-transporting ductules. In addition, about 15 to 25 such ducts are merged at the nipple, and the terminal duct and the acinus form the Terminal Duct Lobular Unit (TDLU, Figure 1.1). The vascularity of the intervening connective tissue is reduced in postmenopausal involution of the breast because the lobular and alveolar structures regress. Eventually only small and occasional

islands of functional breast parenchyma remain, surrounded by dense, scarred connective tissue [275] [222].

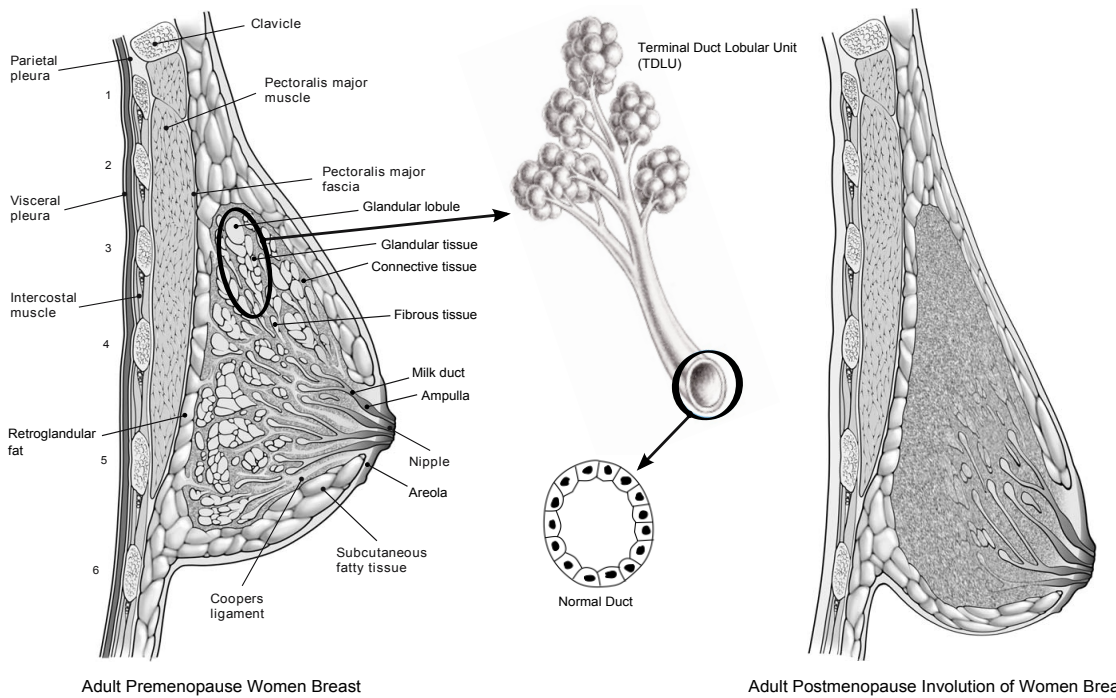


Figure 1.1: Left: The anatomy of adult premenopausal women breast. The breast itself consists mostly of fat, glandular structures and has no muscular tissue. Around 15 to 25 lactiferous ducts converge at the nipple. The ribs are numbered from 1 to 6; Middle: The Terminal Duct Lobular Unit (TDLU) and normal duct cell; Right: The anatomy of adult postmenopausal female breast. The vascularity of the intervening connective tissue is reduced due to the regression of lobular and alveolar structures. The illustration is reproduced from Jatoi et al. [129].

The breast anatomy is well documented in many research publications, but the aetiology of individual breast cancer is still a mystery. Current research has shown that the cause of the disease is strongly associated with genetic and environmental risk factors across certain populations. Most breast and ovarian cancers are sporadic, are not inherited, but a small proportion of cases are. These are the result of inherited predisposition due to mutations in the tumour suppressor genes BRCA1 and BRCA2 [149]. There is a considerable amount of literature on the relationship between mutational spectra of specific genes and breast cancer heredity. Mutations in a number of genes such as BRCA1, BRCA2, TP53, CHEK2, and PTEN are now known to cause susceptibility to breast and/or ovarian cancer [201] [79] [308]. Overall, Ford et al. [79] reported that the majority (81%) of the breast-ovarian

cancer families was due to BRCA1, with most others (14%) due to BRCA2 by mutation analysis in 237 families, each with four or more cases of breast cancer. They also claimed that the cumulative risk estimation of breast cancer reached 28% by age 50 and 84% by age 70. A recent research on 300 probands¹ by Walsh et al. [308] showed that 17% of them carried previously undetected mutations, including 12% with genomic rearrangements of BRCA1 or BRCA2, 5% with CHEK2 mutations, and 1% with TP53 mutation.

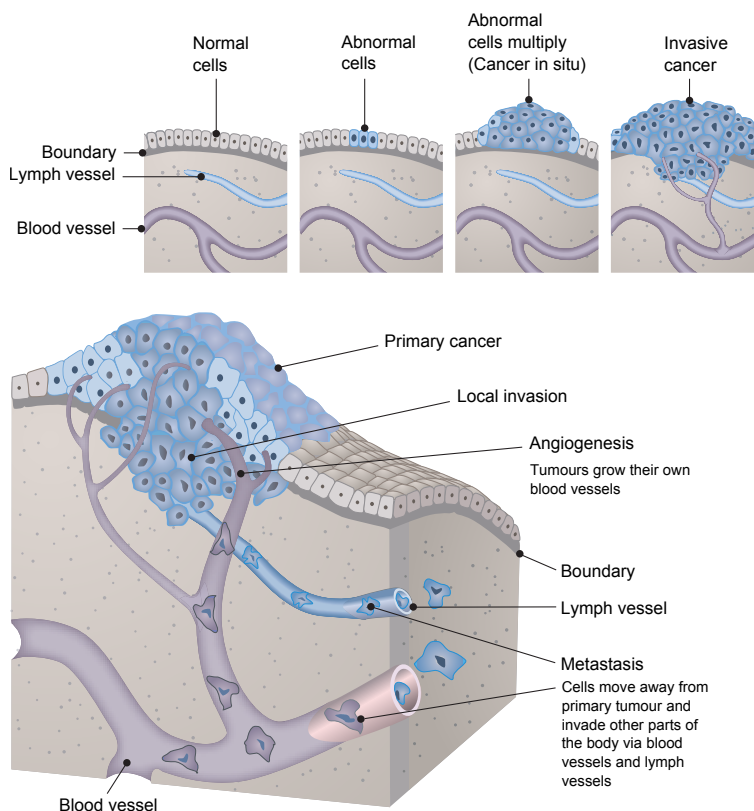


Figure 1.2: *Four sub-figures above from left to right: Illustration of the normal cells inside the breast, common microscopic abnormal variations, and breast cancer in situ leading to an invasive cancer; The sub-figure below: Metastasis of breast cancer. The illustration is reproduced from Breast Cancer Booklet by Cancer Council Victoria, Australia [8].*

Breast cancer is among the most lethal cancers. A lifetime risk of women to contract the disease is estimated to be 12.5%, higher for women born with mutations in BRCA1 or BRCA2. And many other risk factors have been studied in the last decade [145] [257] [51] [192] [189] [48] [146] [71]. Linkage and

¹ *proband*, a.k.a *propositus*, is a term used most often in medical genetics and other medical fields to denote the first member of a family to be diagnosed with a hereditary disease or trait.

mutation analysis have proved the contribution of genes to breast cancer inheritance; however, there remains largely unknown aetiology of this type of carcinoma. The magnitude of risk to women with mutated genes is controversial, and it is studied by geneticists without a verdict yet. Whereas, studies have shown that risk factors associated with breast cancer could be classified into several extensive determinants. For instance, there are age, genetic, environmental, and exogenous and endogenous hormonal factors. In addition, there are reproductive family history factors, and personal behavioural considerations, *e.g.*, diet, alcohol consumption and low physical activity. Furthermore, long latency is consistent with a late onset that always relates to chemical carcinogenesis of the human being.

Substantively, breast cancer is a disease of the cells of the breast. In other words certain genes such as the BRCA1 and BRCA2 control the process of growing new cells. These genes can replace worn-out cells and heal damaged cells of the breast. Breast cancer may be caused by the mutation of these genes. The mutation leads to an abnormality of cells growing or multiplying such as developing a lump that can be benign (not cancerous) or malignant (cancerous). Benign lumps do not propagate into other parts of the body. In contrast, malignant lumps, which are made up of cancer cells, may spread to other organs. The spread occurs if no treatment is provided when the cells can be constrained to their original place at the first developing period. This is called secondary cancer or metastasis when the cells are transferred to a new place, and continue to grow and to form another tumour (Figure 1.2). Most invasive breast cancers develop at the epithelial component of the ducts (about 86% is ductal carcinoma in 2605 cases of invasive breast cancer). And sometimes they are found at the alveoli of the lobules (about 14% lobular carcinoma in these cases) [29]. When these atypical cells multiply within the duct, called Ductal-Carcinoma-in-Situ¹ (DCIS), the risk of developing cancer is much higher [23].

There is no known cure for breast cancer; however, this carcinoma can be avoided if precautions are taken in time. Primary prevention of breast cancer, *e.g.*, hormonal control and dietary intervention, can do little help without a better appreciation of the aetiology of the disease at present. Secondary prevention, *i.e.*, screening a particular age group of women, can reduce mortality from breast cancer. However, this will not result in a decrease in incidence and prevalence. Moreover, some women will develop breast cancer even under aggressive prevention treatment. For these women, early detection is required to minimise proliferation of the disease and maximise prognosis. Currently, the detection of breast cancer is enabled using X-ray mammography, and its complements, *e.g.*, breast Magnetic Resonance Imaging (MRI) and breast ultrasound [224]. The mammogram is

¹*In situ* means to be confined to site of origin and no metastasis, *e.g.*, intra-ductal. Normally, abnormal cells of breast are confined to the ducts or lobules, and there are two types of *in situ*, *i.e.*, Ductal-Carcinoma-in-Situ (DCIS) and Lobular-Carcinoma-in-Situ (LCIS)

still considered the gold standard for breast screening because it detects both micro-calcification and masses. A breast MRI or a breast ultrasound may be done in combination with mammography; however, neither is a replacement for mammography. Recently, Digital Breast Tomosynthesis (DBT) gives us a new chance to obtain high-resolution pseudo-3D images of the breast [215]. Timely decisions can be made between benign and malignant tumours when the lesions are still small by applying DBT. On the contrary, the distinction is hard to see when the 3D layers are superimposed as seen in 2D X-ray mammography images. Therefore, DBT has potential value to be utilised as an additional imaging modality to perform the screening for patients with an abnormal mammogram.

Overall, DBT provides an insight into the fine details of the normal *fibroglandular tissues* and abnormal lesions such as *lumps, i.e., masses* in the breast cancer context, and *microcalcifications* by observing a pseudo-3D image. DBT avoids the superposition, which is usually found in X-ray mammography. In addition, the radiation dose of a single DBT scan (approx. 1.6-1.8 mGy with 25 projections) is comparable to the dose of a two-view mammogram (approx. 1-2 mGy) because the dose applied to each projection of DBT is much lower than a single mammogram employed [178].

Algorithms to aid the human observer process using DBT involve two key tasks: reconstruction and registration. Various approaches have been put forward to separate these steps, solving them sequentially. This can be effective if reconstructing using a complete set of data, *e.g.*, in cone beam CT, assuming that only simple deformation exists. Unfortunately, the sequential method suffers from misregistration, on account of the fact that there are significant artefacts associated with DBT reconstructions. Therefore, in this thesis, we hypothesise that, for DBT in particular, combining the optimisation processes of reconstruction and registration into a single algorithm will offer satisfactory for both tasks. Based on this hypothesis, we have devised a mathematical framework to combine these two tasks iteratively and simultaneously, and have implemented both affine and non-rigid B-spline registration transformation models as plug-ins. By applying our algorithm to various simulated data, we demonstrate the success of our method in terms of both reconstruction fidelity and in the registration accuracy of the recovered transformations. Furthermore, we speculate that the improved registration accuracy will significantly aid the reading process.

1.1 Problem Statement

The problem we address is to find and evaluate methods capable of allying the reconstruction and registration of DBT, which will enhance the performance of each process as a result. Consequently, we prove that the processes of reconstruction and registration of DBT are not independent but reciprocal.

We thus propose innovative numerical approaches combining reconstruction of a pair of temporal DBT acquisitions with their registration iteratively and simultaneously. To evaluate the performance of our methods we use various digital computing phantom images, 3D uncompressed MRI data sets, and simulated DBT data sets with in-vivo compression.

1.2 Research Objective

The leitmotif of this thesis is to extract more accurate reconstruction and registration results using two temporal DBT-like data sets. We show that, in comparison to the conventional sequential method, jointly estimating image intensities and transformation parameters gives superior results with respect to both reconstruction fidelity and registration accuracy using affine transformation model. In addition, we also incorporate non-rigid B-spline transformation model in our simultaneous method, which shows promising results in recovering non-rigid deformations with preservation of the reconstruction fidelity.

1.3 Contributions

The key contributions of this thesis will be:

- ⇒ a novel method that combines reconstruction and registration iteratively using two temporal DBT-like data sets [332] [333].
- ⇒ a novel method that combines reconstruction and registration simultaneously using two temporal DBT-like data sets [334] [335] [336] [337].

1.4 Thesis Structure

Chapter 2 contains clinical necessity and medical physics background on breast imaging and DBT. Chapter 3 surveys existing reconstruction methods, which are applicable in DBT, such as the Back-projection (BP) based methods, iterative Algebraic Reconstruction Techniques (ART), and Least-Squares (LS) estimation based methods. Chapter 4 outlines various aspects of image registration techniques. In Chapter 5, the method of combining reconstruction and registration iteratively is presented, with relevant tests. Chapter 6 proposes a novel approach that performs the reconstruction and registration simultaneously, with experiments and results. Chapter 7, finally, gives a conclusion of this thesis. The whole structure of this thesis is summarised in Figure 1.3. (The manuscript of this thesis was prepared using L^AT_EX 2 _{ε} ¹.)

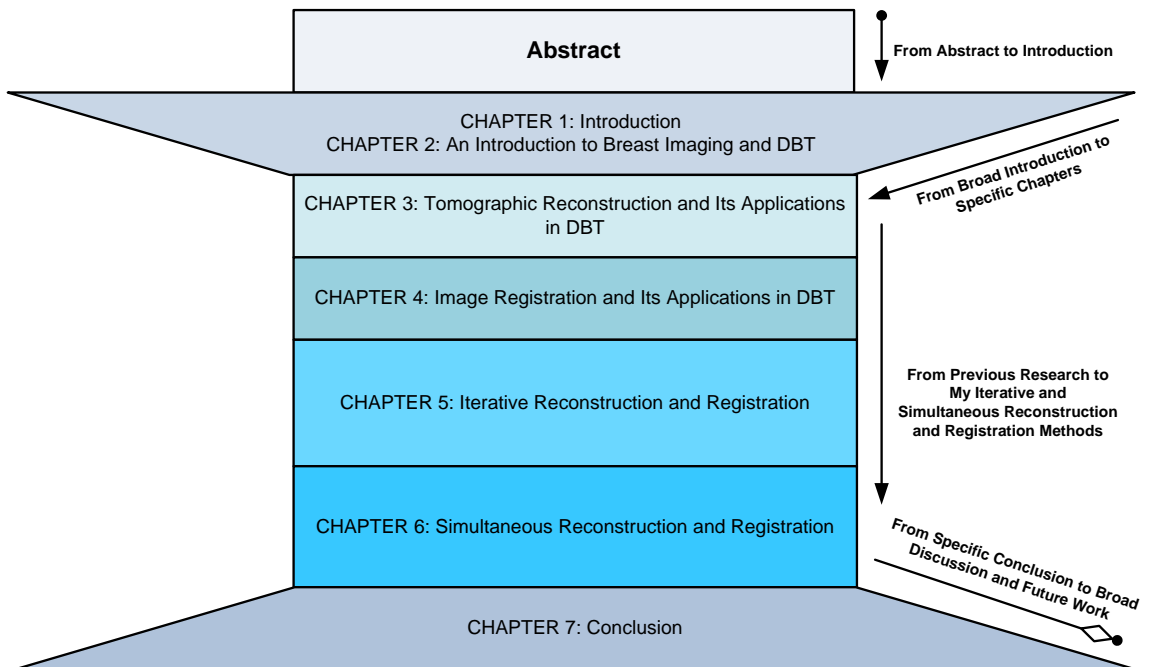


Figure 1.3: *The summarised structure of this Ph.D. thesis.*

¹L^AT_EX 2 _{ε} + PDFL^AT_EX + Texmaker 3.1 under Opensuse 11.3. Some features are only available in the electronic PDF version, *e.g.*, animation and high-resolution images. In addition, some figures were processed using Microsoft Office 2007, GraphPad Prism 5, and Inkscape 0.48.

An Introduction to Breast Imaging and DBT

The statistics of breast cancer incidence are the primary clinical motivation behind developing new and improved breast imaging techniques such as DBT. Currently, mammography is the gold standard among modalities applicable to the screening and diagnosis of breast cancer by clinicians. In addition, breast magnetic resonance imaging and breast ultrasound are prominent tools for breast cancer characterisation and staging. In this chapter, we present a comprehensive discussion on these mainstream techniques and other complementary breast imaging modalities, including breast computed tomography and breast positron emission tomography. Furthermore, previous studies on DBT demonstrate that this novel imaging technique plays an important role in evaluation and detection of breast cancer.

2.1 Breast Imaging: An Overview

Surgical treatment has a long history as an invasive cure of breast cancer, but has used imaging and screening for better investigation only since modern times. The earliest reference of surgical treatment of breast cancer is *The Edwin Smith Surgical Papyrus*, which was a series of medical case presentations written in Egypt between 3000 and 2500 BC [73]. In Europe, around the 18th and 19th centuries, surgeons proposed an aggressive operative approach to treat breast cancer. The approach removed part of the breast or the whole breast [129]. Until the beginning of the 20th century, the diagnosis of breast cancer still relied solely on clinical observations. Thus, many cancers were large at the time of diagnosis with a high spread of metastases. Without imaging and locating the breast cancer, surgery was crude, treatment was limited to surgery, and the prognosis was often poor. Nowadays, breast cancer imaging and screening, which enables us to detect the tumour at the early stage when it is small, provides guidance to the surgery procedure. We introduce several modalities

of breast imaging as follows.

2.1.1 Breast MRI

Nuclear Magnetic Resonance Imaging (NMRI) or Magnetic Resonance Imaging (MRI) has been a valuable tool of imaging structures and functional activities for many parts of the human body since the early 1980s. However, it was not widespread for breast imaging until 10 years ago. MRI is a relatively new technology, which has been around for about 40 years, compared with over 100-year history of X-ray radiography. Breast MRI, *a.k.a.*, MR Mammography (MRM), can palliate the problem of high mortality rate of breast cancer due to its sensitivity in detecting tumours as small as 3mm in diameter [136].

The full name of MRI, Nuclear Magnetic Resonance Imaging, describes the technique, which is fundamentally different from all other imaging techniques. The main concept is that if an atomic *Nucleus* is placed within a static *Magnetic* field, it *Resonates* when a oscillating Radiofrequency (RF) wave is applied at the particular frequency. In addition, an *Image* can be acquired from the resonance signals while frequency and phase encoding can demystify the space information.

Normally, MRI systems are composed of a number of components. Firstly, there is a strong and static magnetic field, which is measured by the unit of magnetic flux density, namely, Tesla. Secondly, the RF transmitter and receiver coils are embedded. Three orthogonal and controllable magnetic gradient coils, nuclear magnetic resonance spectrometer, and others are also integrated. Some of these coils are placed layers upon layers within the MRI system with a bore at the centre of the scanner. These coils create magnetic fields by passing electric currents through solenoids to detect the energy given off by magnetic induction from the precessing of the atoms. In breast imaging, optimised electrical signals are generated by tuning the specialised breast RF coils, which are always bilateral nowadays. Compared to conventional unilateral breast MRI, bilateral imaging obtains the images of two breasts in one view; thus, it facilitates the assessment of symmetry during screening. The RF coils resonate at the Larmor frequency of hydrogen at the particular field strength of the scanner. Therefore, it is not feasible to exchange the breast coil designed for a 1.5 Tesla scanner for a coil used on a 3 Tesla system [106].

X-ray mammography and breast ultrasound remain the most frequently used techniques for imaging the breast. However, MRI is a valuable addition to the diagnostic work up of a patient with a breast abnormality or biopsy-proven cancer. This is due to its high sensitivity and effectiveness in dense breast tissue. Another advantage of MRI is the validation of breast-conserving surgeries when

the size evaluation is difficult in mammographic screening or parietal involvement is suspected. High quality images of the breast can be obtained using dedicated MRI surface coils, as well. Yet the major drawbacks of breast MRI is the low-to-moderate specificity, which in combination with high sensitivity can lead to unnecessary biopsy, patient anxiety, and extra cost [205].

Additionally, contrast enhanced breast MRI, which possesses wider clinical applications as an adjunct diagnostic procedure, is becoming increasingly important [91]. It is effective for detecting the carcinoma at preliminary stage and planning early treatments for high-risk women. Also, it is superior to mammography in demonstrating diffuse and multi-focal tumours. Contrast enhanced breast MRI has been investigated since late 1980s for the patients with biopsy of proven carcinomas [226]. Consequently, breast cancer detection and diagnosis have been enhanced significantly following the intravenous administration of contrast material such as Gadolinium Diethylene-Triamine-Pentaacetic Acid (Gd-DTPA). The increased signal from the blood has been produced after the uptake within the first 5 minutes.

In 1973, Lauterbur [164] reported the first MRI results in Nature, which resolved the sources of NMR signals into images. However, the first attempt on a human took place in 1977 [90], and there have been pioneer studies on breast MRI since the 1980s. McSweeney et al. [194] have demonstrated that breast cancer significantly depends on different relaxation times in benign and malignant tissues. Kaiser [135] has reported the initial clinical results of MRI for the female breast, which has indicated that MRI allows non-invasive detection and diagnosis of benign and malignant diseases of the breast. In 1986, Dash et al. [55] showed that MRI was superior to mammography in differentiating solid from cystic lesions and equivalent to mammography in providing information regarding different parenchymal patterns. In addition, MRI correctly identified 18 of 21 surgically proven carcinomas of the breast, and mammography identified 19 of these cases. However, the major disadvantage of MRI was its inability to show calcifications, benign or malignant. The early hope of clinical breast MRI was that tumours could be discriminated from fibroglandular tissues and benign breast lesions based on their various signal intensities in T1- or T2-weighted images. Breast cancers possess higher T1 and T2 values than the normal fibroglandular tissues, and they have lower values than the benign breast lesions. Therefore, breast cancers are found to be darker than normal fibroglandular tissues in T1-weighted images but they are brighter in T2-weighted images. Furthermore, there is significant overlap between the T1 and T2 values of the tumours and benign breast lesions such as fibroadenomas [241] [68] [194] [315] [106].

Since the middle 1980s, the rare earth element gadolinium (Gd), which was chelated by a molecule to make Gd-compound non-toxic, has been employed as the contrast agent for MRI [312] [31]. In 1986,

Heywang-Köbrunner et al. [113] reported the first usage of Gd-chelates to help breast cancer detection in MRI, and diagnostically difficult cases have benefited greatly from this enhancement of MRI and its use as a supplement imaging technique [114]. In 1990, Stack et al. [273] suggested that dynamic contrast-enhanced MRI (DCE-MRI) showed promise in the further characterisation of breast tissue, particularly for the identification of breast cancer. Subsequently, Heywang-Köbrunner [111] [112] and his co-workers [115] showed that DCE-MRI could get significant diagnostic gain if it was appropriately applied and used for selected indications. In addition, the development of commercial biopsy coils was essential in order to exploit the full potential of DCE-MRI. Degani et al. [57] proposed a novel method of mapping pathophysiological features that might aid diagnosis and prognosis assessment, while the high spatial resolution improved the capacity to detect smaller lesions. Kuhl et al. [159] examined 266 breast lesions with a 2D dynamic MR imaging series and subtraction postprocessing. They concluded that the shape of the time-signal intensity curve was an important criterion in differentiating benign and malignant enhancing lesions in DCE-MRI of the breast.

Furthermore, relevant medical image processing, modelling, and analysis techniques have flourished since the development of MRI. Rueckert et al. [245] investigated the free-form deformation based registration of breast MRI. They combined a global affine model with the local breast motion modelled by B-splines, which achieved much better results than rigid or affine registration schemes. Adipose, fibroglandular and skin tissues form the most part of the breast; therefore, breast tissue deformation modelling is critical in many medical applications. In [250] Samani et al. devised a finite element based biomechanical method to model the breast, and they obtained good results with reasonable validation using breast MR images. Orel and Schnall [219] reported that the sensitivity of MR imaging for the visualisation of invasive cancer approached 100%. They also described the potential pitfalls and limitations of DCE-MRI, and in particular that it is a costly technology. Warner et al. [310] did a comparison work of breast MRI, mammography, and ultrasound for surveillance of BRCA1 and BRCA2 mutation carriers (196 women, aged 26 to 59 years). The results showed that breast MRI might be superior to mammography and ultrasound for the screening of women, who had high risk for hereditary breast cancer. Hata et al. [102] drew the conclusion that DCE-MRI could diagnose breast cancer as accurately as ultrasonography, and it was more accurate than mammography, and patterns of time-intensity curves correlated with tumour histology. Kuhl summarised the current status of the DCE-MRI, and its clinical applications [158] [157]. Saslow et al. [252] published the *American cancer society guidelines* for breast screening with MRI as an adjunct to mammography. Since 2008, several studies, for instance, [213] [170] [346] [53] [258] [214], have been conducted on tissue segmentation and lesion classification of breast MRI using statistical analysis such as fuzzy C-mean

(FCM) classification and support vector machines (SVMs). Gal et al. [81] reported a dynamic nonlocal means algorithm to denoise DCE-MRI effectively. More recent research [253] [177] [290] highlights the validation work for the registration and simulation of mammogram using breast MR images.

2.1.2 Breast Ultrasonography

Ultrasound, which is a cyclic sound pressure with a high frequency, at approximately 20 kilohertz (kHz), is greater than the upper limit of human hearing [318]. This upper limit varies in different individuals, but 20 kHz is a useful lower limit to define ultrasound. In addition, applications of ultrasound are widely used in many different fields, *e.g.*, to penetrate a medium, measure the reflection signature, supply focused energy, and others. Ultrasonography, namely sonography, is an imaging technique that uses high-frequency sound waves to outline a specific part of the body. The echo of the sound waves produces an ultrasonography sonogram. The most well known application of this technique is to image foetuses in the human womb, and there are a plenty of other applications such as breast ultrasonography. Breast ultrasound is a complementary imaging modality, which evaluates breast lumps that are found through an exam or mammogram if there are some other reasons to suspect a possible abnormality. Furthermore, it is useful to determine whether a breast lump is solid or fluid filled. Ultrasound is particularly effective in characterising lesions in dense breasts, which might not be visible using X-ray mammography. When a mammogram or MRI is not feasible for the patients with contraindications, *e.g.*, implants inside the body such as a cardiac pacemaker, ultrasonography provides another option. However, ultrasonography is not a substitutable tool of cancer screening for mammography or MRI.

Since the early 1950s, breast ultrasonography has been applied to examine and evaluate palpable breast masses. It is fast, painless, inexpensive and harmless with no radiation, and it has provided a lower rate of inadequate sample collection than clinically guided biopsy. Additionally, breast ultrasound guided fine-needle biopsy has a lower risk of pneumothorax, and the ultrasonography can guide the needle sampling for all palpable lesions.

Despite this, the sensitivity and specificity of breast ultrasonography can vary enormously depending on the experience of the operator and the equipment used. Moreover, about 1% to 2% of palpable lesions may not be identified [64]. Small lesions close to the chest wall have been found more difficult to perceive because of the backscatter from the underlying lung. These lesions may also be masked by the acoustic shadows of a large amount of sound-absorbing fibrous tissue among the glandular tissue.

2D ultrasonography has suffered from several disadvantages. For example, 2D ultrasound imaging requires that users mentally combine many images to form an impression of the 3D anatomy and pathology. Moreover, it has been difficult to relocate anatomic positions and orientations of the patient. In the past decade, advances in high-performance computing and graphics processing unit based visualisation make 3D ultrasound imaging (in real time or near real time) a viable technology [282]. There are four 3D ultrasound imaging methods, namely, mechanical scanning, free-hand scanning with and without position sensing, and 2D array scanning for dynamic 3D ultrasonography, *i.e.*, 4D ultrasound imaging [282]. An ultrasound-imaging prototype consists of a data acquisition, a preprocessing step, a segmentation process, a shape descriptor, and diagnosis results. Figure 2.1 shows a typical procedure of 3D ultrasound imaging.

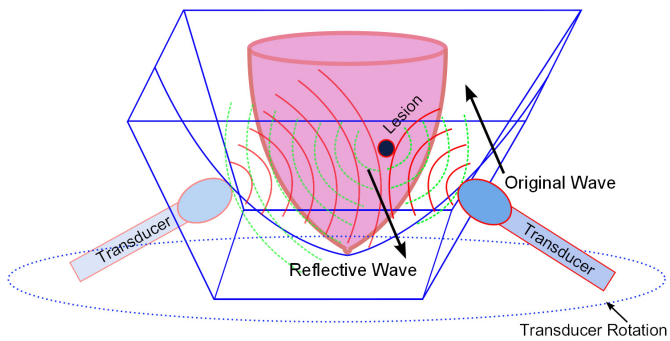


Figure 2.1: *The image acquisition process is performed by rotating the transducer 360°, and the full 3D volume of the breast is covered. Two images, which are acquired 180° apart, are registered to represent the same 2D image plane in the 3D volume.*

In 1951, Wild and Reid [319] employed ultrasonography to detect palpable lumps of the breast using an A-mode apparatus. They demonstrated the potential usage of ultrasonography for the differentiation of cystic from solid lesions. From 1970s to 1980s, several researchers such as Jellins et al. [130], Kobayashi [151], and Cole-Beuglet [49] reported the innovation of small hand-held transducers with a high frequency range from 7.5mHz to 12mHz. The hand-held transducers enabled rapid real-time examination of the whole breast. In addition, these studies improved ultrasonography quality, which allowed the visualisation of impalpable tumours, and distinguished benign lumps from malignant carcinomas. In the mid-1980s, McSweeney and Murphy [193] proposed the developments of B-mode scanning and dedicated automated water path scanners. Further research, which was carried by Stavros et al. [274], showed promising details by analysing the ultrasound features of both benign lumps and malignant breast carcinomas. Two famous review papers were published by

Nelson and Pretorius [212], and Fenster et al. [74], which summarised the feasibility and utility of 3D ultrasonography. Many publications showed prominent results on 3D breast ultrasound (BUS) imaging. The 3D reconstruction, in particular parallel planar reformatted sections, represented a valuable adjunct to the characterisation of breast masses [242] [313] [10].

Both *inter- and intra-modality registration* are critical steps for the automatic analysis of 3D BUS data. Firstly, artefacts and speckle interfere with the automatic analysis of the 3D data, and preclude the visualisation and volume estimation of internal 3D structures. Secondly, 3D compound imaging of images from multiple views can improve the data quality and enable high spatial resolution. However, large distortion significantly limits resolution during the summation of images. Moreover, hand-induced transducer motion is another reason for artefacts in breast ultrasound images [63]. Furthermore, as breast ultrasound is a complementary technique, it is always combined with other imaging modalities such as mammography [20] and breast MRI [228] [287]. Therefore, intra-modality registration is necessary for the correction of motions, which often occur during the imaging of the breast *in vivo*. Moskalik et al. [206] presented an early work on the motion correction for the 3D compound breast ultrasound. Rohling and Berman [240] proposed a fully automatic registration method, which was robust and accurate using *in-vivo* 3D BUS data. In [155] Krücker et al. applied global full affine and local thin-plate warping based registration for both phantom and *in-vivo* data, and achieved 0.31mm and 0.65mm average error. Furthermore, Xiao et al. [325] described a B-spline registration method for 3D free-hand ultrasound data, and the registration accuracy (about 0.19mm) was evaluated using phantom data. More recent research has focused on sequential registration of 2D slices of a 3D BUS image (about 0.14mm misregistration) [26] and spatial registration of temporally separated 3D greyscale and Doppler BUS images [210].

Segmentation plays an important role in breast cancer characterisation, classification, and it further assists detection and diagnosis. Gefen et al. [84] applied receiver operating characteristic (ROC) analysis to ultrasound tissue characterisation, which greatly reduced the need to perform biopsies of benign breast tumours. In [183] Madabhushi and Metaxas proposed an automated segmentation scheme for ultrasonic breast lesions. Noble and Boukerroui [216] surveyed segmentation methods for B-mode ultrasound images. Several studies, for example, [124] [65] [179] [181] [42] [180], have been carried out into automated methods for computer-aided detection and diagnosis (CAD) in breast ultrasound.

2.1.3 X-ray Mammography

Electron kinetic energy, which is converted into electromagnetic radiation, produces X-rays. Figure 2.2 is a schematic diagram of an X-ray tube with the basic components. In a vacuum envelope, a high voltage source is applied to the two electrodes, namely the cathode and anode. The cathode is negatively charged, and is the source of electrons. The anode is positively charged, and is the target of electrons. The electrons, which travel from the cathode to the anode to acquire kinetic energy, are accelerated by the electrical potential difference, *i.e.*, the voltage measured in Volts (V). The kinetic energy attained by an electron is proportional to the voltage between the cathode and the anode [34]. Coulombic forces attract and decelerate the electron, which produce a significant loss of kinetic energy, and change the trajectory of the electron. Consequently, an X-ray photon, which is produced according to the conservation of energy, possesses the energy equal to the kinetic energy lost by the electron. This radiation is also known as *bremstrahlung*, a German word for *braking radiation*.

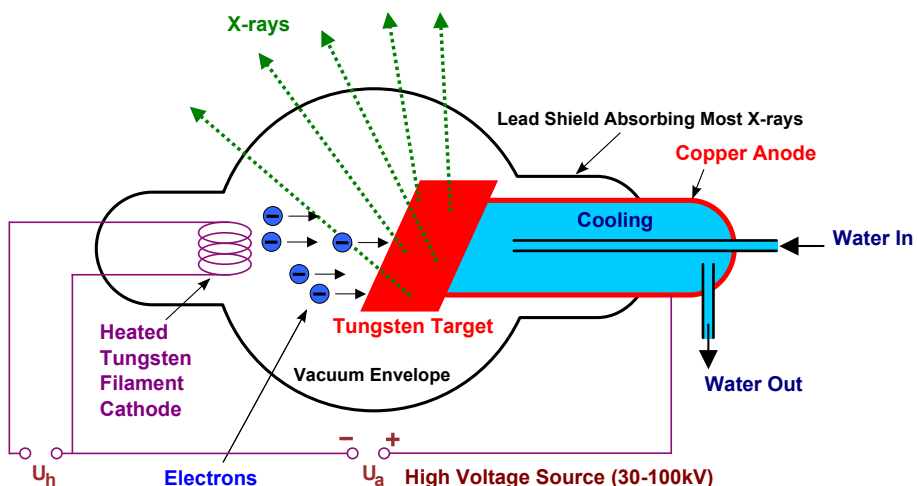


Figure 2.2: Scheme of a basic X-ray tube consists of a source and target of electrons, a vacuum envelope, and connection of the electrodes to a high-voltage source.

The wavelength of an X-ray is of the order of an Ångström ($10^{-10}\text{m} = 0.1\text{nm}$). The corresponding photon energies, which are usually measured in electron Volts (eV) or Joules (J), are of the order of keV ($1\text{eV} \approx 1.602 \times 10^{-19}\text{J}$) [280]. The energy E of a photon with frequency freq and wavelength w_L is

$$E = h \times \text{freq} = \frac{hc}{w_L}, \quad (2.1)$$

where h is Planck's constant (6.626×10^{-34} Js) and c is the speed of light in vacuum (2.998×10^8 m/s), and $hc = 1.2397 \times 10^{-6}$ eVm [280].

Figure 2.3 shows the basic principle of mammography through a simple model of a breast [229]. The breast model consists of normal breast tissue and a structure of interest, *e.g.*, a tumour, a microcalcification, or a normal breast anatomy.

Therefore, the intensities of the X-rays transmitted along the two paths are n_A and n_B , which are defined by two X-ray attenuation coefficients μ and μ' via

$$n_A = n_0 e^{-\mu z} \quad (2.2)$$

$$n_B = n_0 e^{-\mu(z-a)-\mu'a}, \quad (2.3)$$

in which n_0 expresses the intensity of the incoming beam, and the relevant radiation contrast C is

$$C = \frac{n_A - n_B}{n_A + n_B} \quad (2.4)$$

$$= \frac{1 - e^{(\mu-\mu')a}}{1 + e^{(\mu-\mu')a}}. \quad (2.5)$$

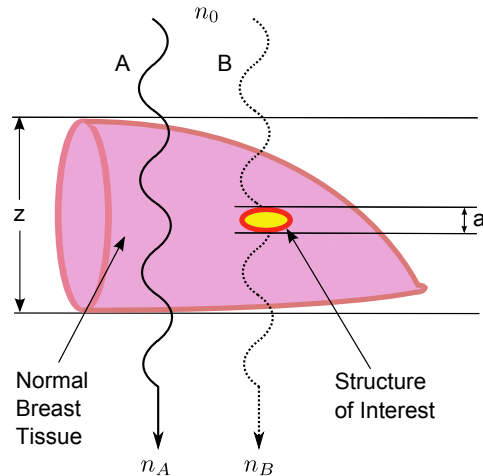


Figure 2.3: A simple model of breast, which contains normal breast tissue and a structure of interest, shows various X-ray transmissions in two different paths A and B. The mean number of X-rays transmitted along the two paths are n_A and n_B . The thickness of the breast and the structure of interest are denoted by z and a . Light travels in straight lines in a material of constant refractive index.

The apparatus of mammography has evolved over the last 40 years. Figure 2.4 illustrates a typical

state-of-the-art prototype system of mammography. It shows the common features of the standard characteristics that may vary from one manufacturer to another. The mammographic X-ray tubes use a rotating anode design, and molybdenum is the most common anode material in order to generate soft X-rays. However, rhodium and tungsten targets are also used. Characteristic X-ray production is the major reason of using molybdenum and rhodium. The characteristic radiation occurs at 17.5keV and 19.6keV for molybdenum, and at 20.2keV and 22.7keV for rhodium. In addition, the orientation of the cathode-anode axis is along the chest wall to nipple direction because the anode self-filtration results in the heel effect. This causes a significant drop in X-ray intensity on the anode side. Thus, the chest wall of the breast (the thicker part of the breast) is placed on the cathode side to help equalise the X-ray transmission with greater penetration.

Focal spots, ranging from 0.3mm to 0.4mm, are applied for non-magnification contact imaging when the objects are close to the sensor surface without intervening optics. On the other hand, magnification imaging uses a smaller size of the focal spot, *e.g.*, 0.1-0.15mm. The source to image distance (SID) and source to object distance (SOD) determine the magnification factor (1.5x to 2.0x) (Figure 2.4). Longer SIDs reduce the influence of the focal spot size on resolution [34].

Normally, filters are used in a mammographic system. For instance, a 0.03mm thick molybdenum filter with a molybdenum target is named Mo/Mo, or a 0.025mm thick rhodium filter with a rhodium target is denoted by Rh/Rh. A molybdenum target with a rhodium filter, *i.e.*, Mo/Rh, can be used as well, but there is generally no Rh/Mo filter combination. The filter reduces unnecessary exposure, and enhances the contrast sensitivity, and it is tuned to produce an optimised spectrum for specific breast conditions.

A compression is applied to the breast in order to reduce motion blurring and scattered radiation. This reduces radiation dose and visibility issues due to overlapping breast tissue. A 10 to 20 Newtons (22 to 44 pounds) force is typically applied for the compression, and is the main reason for patient discomfort and concern during mammography scanning.

An anti-scatter grid absorbs the scattered radiation and improves contrast sensitivity, but increases dose. Phosphor screen and film receptor, or digital detector can be deployed for the mammography system. For example, a typical screen-film cassette, which has a sandwich structure, includes two intensifying screens that are placed inside leaves of both the top and the bottom cassette. In addition, there is a sheet of film base at the centre with emulsion coated between the base and the screens. Many different types of detectors are used for digital mammography. Figure 2.5 shows an illustrative plot of the phosphor flat panel detector system based on a large glass plate. The scintillator, which is a key component of the detector, is made of a material that exhibits scintillation.

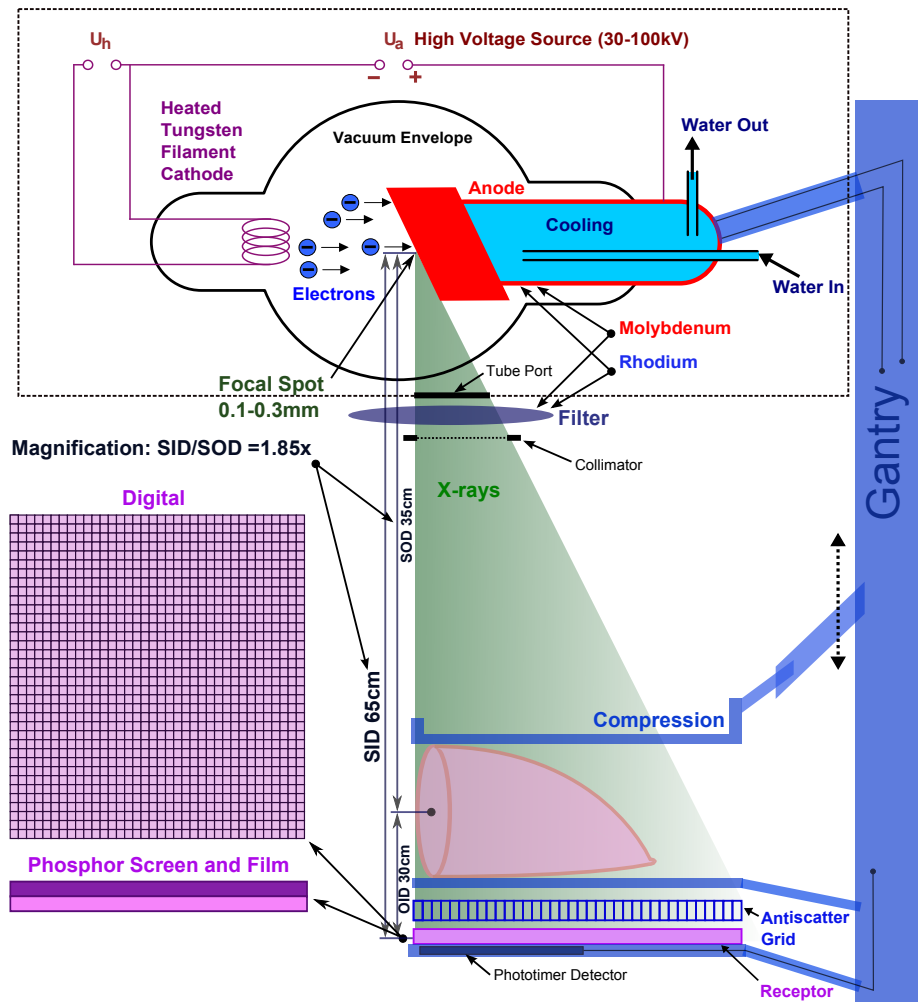


Figure 2.4: An illustration of a typical mammography system with gantry. From top to bottom, it consists of an X-ray tube anode, the focal spot, a filter, a compression paddle, an anti-scatter grid, and a receptor. Firstly, the X-ray tube anode of the mammography apparatus is made of molybdenum material, or a dual material anode with an additional rhodium track. Most X-ray tubes have a tungsten material anode; however, materials such as molybdenum and rhodium are used because they yield a nearly optimal characteristic radiation spectrum for breast imaging. Secondly, a typical x-ray tube for mammography has two selectable focal spots for contact imaging and magnification imaging. The nominal size 0.1mm is small in order to reduce the geometric blurring caused by the magnification. Thirdly, most of the X-ray machines use aluminium to filter the x-ray beam to reduce unnecessary exposure to the patient. However, mammography uses molybdenum or rhodium filter to optimize the spectrum for specific breast conditions. Next, the compression is essential to reduce the radiation dose and overlapping breast tissues. Furthermore, an anti-scatter grid is applied to absorb the scattered radiation, and improves the contrast sensitivity. Lastly, phosphor screen and film receptor, or digital receptor is employed for the mammography system.

Scintillation is the property of luminescence when the scintillant material is excited by ionising radiation such as X-ray [317]. CsI(Tl), *i.e.*, caesium iodide doped with thallium, which is one of the brightest scintillators, absorbs the X-ray photons, and converts their energy into light photons emission. There are many other materials, which can be used as scintillators such as CdWO₄, *i.e.*, cadmium tungstate, xenon gas and others.

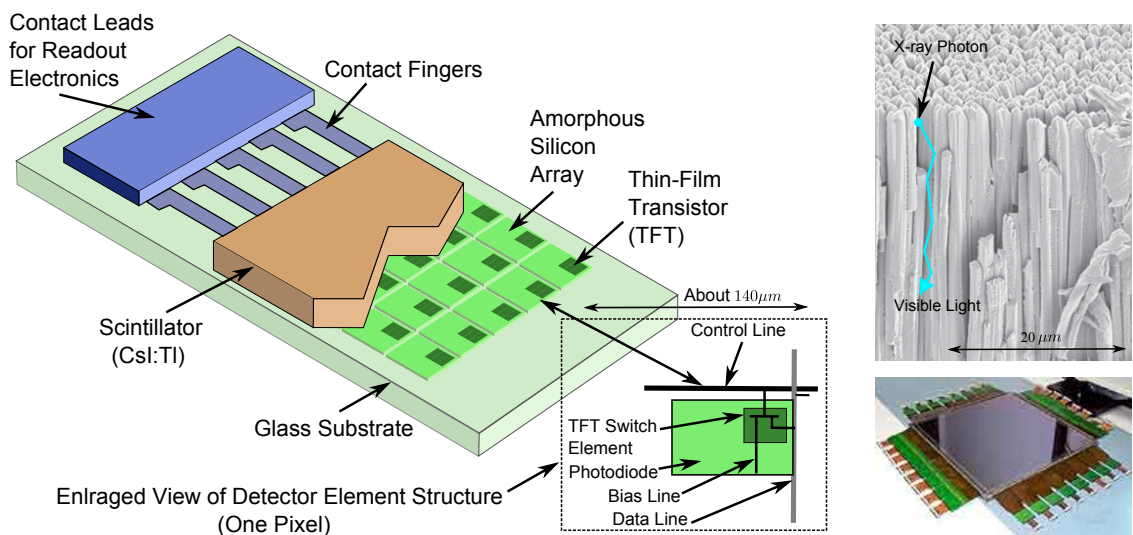


Figure 2.5: *Left:* Schematic of a flat panel detector with CsI(Tl) scintillator, and the amorphous silicon detector array (*a*-Si sensor matrix). The individual detector element is optimised for high photon detection efficiency, and the structure with a Thin-Film Transistor (TFT) readout element is enlarged as illustrated in the details. *Top right:* An electron microscope view of the CsI(Tl) needles that constitute the scintillator layer [83]. The X-ray photons are produced by the X-ray tube, and they go through the patient and the scintillation layer converts them to visible light photons. Then these visible photons reach the array of photodiodes or Charge-Coupled Devices (CCDs), and output the electrons. Amorphous silicon or a selenium layer receives these electrons, and generates the electronic image data. An Analog-to-Digital Converter (ADC), which converts the voltage to a digital number, is used to produce the digital image. *Bottom right:* Photo of a flat panel detector [83].

On the 8th November, 1895, Wilhelm Conrad Röntgen, a German professor at the Julius-Maximillan University, discovered the *X-ray*. His original manuscript *On a New Kind of Ray* (Über eine neue Art von Strahlen) was published a few days later outlining the essential features of X-ray, and he was awarded the 1st Nobel Prize for physics in 1901. The first attempt on *X-ray examinations for breast cancer* was published in 1913, when a surgeon, Salomon realised a roentgenological and histological study on 3,000 amputated breasts following mastectomies at Charité University Hospi-

tal in Berlin [249]. The work demonstrated invasive characteristics of breast cancer including breast calcifications and occult cancers [101]. This is the fundamental work of mammography, and only few studies were carried out without much improvement until the 1940s.

From 1947 to 1970, progress was made on roentgenological results associated with clinical correlation. Leborgne [166] did the first accountable research for the wide development of this method. Many American and European radiologists contributed from 1951, and this is known as the second period of mammography development. The first article on X-ray breast examinations was published nearly a hundred years ago. However, the *mammography* we understand nowadays, using a dedicated X-ray unit with a molybdenum target and breast compression devices, was developed in 1967 by Gros and his co-workers in France [93].

During the last 40 years, the third period of mammography development emphasised the value of this technique for the detection of breast cancer. Since 1970, various breast-screening groups have been set up [225]. From 1973 to 1978, cosponsored by the American Cancer Society (ACS) and the National Cancer Institute (NCI), the Breast Cancer Detection Demonstration Project (BCDDP) has screened asymptomatic volunteer women with mammography and clinical breast examinations. The project has involved 27 sites in the United States of America (USA). The Bureau of Radiologic Health has developed protocols to monitor radiation exposure during mammography. Shortly thereafter, the American College of Radiology (ACR) established the first guidelines for mammography of asymptomatic women in 1976. In Sweden, two screening programs in Falun and in Malmö started in 1977 [285]. The Canadian randomised controlled clinical trial was begun to determine if screening mammography would be beneficial for women under the age of 50 [101]. In the UK, the National Health Service Breast Screening Programme (NHSBSP) was initiated pursuant to the Forrest Report published in 1986 [2]. The report recommended NHSBSP to offer three-yearly mammography to women aged 50 to 64. The routine has established the capability of mammographic screening to detect more cancers than using physical examination alone. In 1988, the world's first national breast screening programme was set up in England. The programme has invited more than 110,700 women between the ages of 50 and 64 for screening. Since 2004, all UK women aged 50 to 70 who have registered with a GP are invited for screening every three years. The screening process is organised by dedicated professionals at special screening sites. Women are offered two view mammography, both Cranio-Caudal (CC) and Medio-Lateral Oblique (MLO) views, which are now used at every screen since 2003 [4].

There are on-going discussions and arguments about the limitations of mammography since its development a century ago. A major limitation is that the detection of breast cancer is not

trustworthy by mammography, particularly for women with heterogeneously dense breasts. Full-Field Digital Mammography (FFDM) is a recent development of conventional screen-film X-ray mammography almost exactly 10 years ago [22]. Compared to traditional Screen-Film Mammography (SFM), FFDM promises improved image quality with enhanced contrast of dense areas of the breast. FFDM also facilitates different aspects of medical information technology in mammography such as image viewing, and the use of Picture Archiving and Communications Systems (PACS). In addition, FFDM allows the application of Computer-Aided Detection (CAD), and enables the optimisation of image acquisition, image processing and image viewing steps separately. On the other hand, in SFM, the film serves simultaneously as the image receptor, display medium and long-term storage [297]. Furthermore, combining FFDM and SFM using double imaging and double reading can improve the cancer detection. Kopans [153] showed that double reading could reduce the oversight rate by 5%-15%. In [171] Lewin et al. suggested that combining double imaging and double reading was able to detect 39% more cancers than applying single imaging or single reading mammography.

Studies of the comparison between FFDM and SFM have shown that there is no statistical significance in cancer detection observed between the two methods, and the recall rate of FFDM and SFM has been noted with various results by different researchers [173] [58] [148] [339] [100]. Lewin et al. [173] reported that no obvious difference in cancer detection rate was observed between FFDM and SFM according to the results of 4,945 paired examinations. Additionally, FFDM led to a significantly lower recall rate than SFM (11.5%, 568 of 4,945 for FFDM in comparison to 13.8%, 685 of 4,945 for SFM with $P < 0.001$ by McNemar's χ^2 tests). Both FFDM and SFM encountered false-negative and false-positive findings with similar ROC analysis curves (The positive biopsy rate for cancer detection is 30%, 21 of 69 for FFDM in comparison to 19%, 22 of 144 for SFM). More publications, for example, [174] [266] [265] [267] [264], showed analogous results in further population-based studies. Skaane et al. confirmed that cancer conspicuity analysis was equal with both modalities. Nevertheless, they also observed that the recall rate for digital mammography was slightly higher than that for conventional mammography. This observation was attributed to a learning curve effect. In 2005, Pisano et al. [230] compared the diagnostic performance of FFDM and SFM for 49,528 asymptomatic women. Their results showed that the overall diagnostic accuracy of FFDM and SFM is comparable. In addition, although FFDM provided only a modest improvement over SFM, FFDM obtained better accuracy in some subgroups, for example, women under the age of 50, women with dense breasts, and young premenopausal women. In the UK, between January 2006 and June 2007, a London population-based screening centre performed 8,478 FFDM and 31,720 SFM examinations [301]. The results showed that FFDM yielded detection rates at least as high as those for SFM. One recent

paper by Karssemeijer [142] concluded that a FFDM-CAD combination performed almost as well as SFM. Furthermore, FFDM-CAD significantly improved the detection of DCIS and microcalcification clusters ($P < 0.01$ by Pearson's χ^2 tests), while the recall rate increased. So far, all these studies have suggested that FFDM can be safely implemented in breast cancer screening programs. FFDM is a fast-developed imaging modality including emerging tomographic techniques such as DBT.

2.1.4 Other Breast Imaging Modalities

There are many other less widespread methods of breast imaging, *e.g.*, nuclear imaging, breast Computed Tomography (CT), thermography, and transillumination, which bring alternative options for clinical usage in screening, diagnosis, and functional information observation.

Two main nuclear imaging modalities have been applied to the breast, namely scintimammography and Positron Emission Tomography (PET). Scintimammography involves injection of a γ -ray emitting compound (^{99m}Tc Sestamibi), which selectively accumulates in breast cancer cells. In addition, a gamma camera is used to detect gamma rays emission when the radionuclide ^{99m}Tc spontaneously decays. In the preliminary study of Taillefer et al. [286], scintimammography showed a high diagnostic accuracy in detecting breast cancer. It also demonstrated the potential to detect axillary lymph node involvement as concomitant information. In [147] Khalkhali et al. reported that the diagnostic accuracy of scintimammography was not affected by breast density; however, the sensitivity was lower (71%). Development of dedicated high-resolution gamma cameras for breast imaging may improve the detection of small lesions, but there is no clinical test as yet.

PET imaging utilises short-lived positron emitting compounds, which are some biologically active molecules. In particular, the 2- ^{18}F -flouro-2-deoxy-D-glucose (FDG), which is an analogue of glucose (a sugar), is chosen for PET. FDG traces the tissue metabolic activity in terms of regional glucose uptake in order to produce an image. FDG spontaneously emits positrons, which then interact with electrons. The encounter annihilates both positron and electron, producing two 511 keV photons, at 180 degrees from each other. The PET scanner can measure the absorption of the photons. In addition, subtle timing in detection can determine the location of the positron emission. Therefore, the distribution of FDG is resolved in 3D within the patient. In 1991, Wahl et al. [306] published the first study on PET imaging in breast cancer detection, and reported 100% sensitivity in 10 breast cancer carriers. However, in this study, all the tumours were larger than 5cm. Other relative studies conducted by Avril et al. [7] and Wahl et al. [307] using PET in breast cancer detection showed that it obtained the sensitivities of 80% to 96% and specificities of 83% to 100%. The mean tumour size was smaller but not comparable to the tumour size detected by mammography or breast ultrasonography. There are plenty of small-scale studies using scintimammography and PET imaging, especially for women with known breast carcinomas.

CT is a major tool in diagnostic imaging, but breast CT scanning is inappropriate as a primary screening test, mainly because there are high radiation dose and intravenous iodide administration applied. It is a costly examination, as well. Moreover, some studies show that there is no difference in

breast cancer detection between breast CT and mammography because of the learning curve effect. However, Boone et al. [27] investigated the dedicated breast CT, which has renewed interest in this technology.

Thermography, which measures temperature directly to form a thermal map image, has been investigated extensively for breast cancer detection. Thermography possesses high diagnostic accuracy for advanced breast cancer; however, it is not sensitive in detecting impalpable carcinomas. Breast cancer detection by transillumination is a historic method, and it is useful in distinguishing cystic from solid lesions. Nevertheless, a shortcoming is its incapability in detecting deep lesions and small tumours [1].

In summary, nuclear imaging and thermography have not contributed significantly to either breast cancer detection or characterisation, and transillumination is still in the experimental stage. Breast CT, which demands high levels of ionising radiation dose, is unacceptable for annual screening. Therefore, mammography is still the most accurate and most widely used modality for breast imaging and screening with complementary breast MRI and breast ultrasonography.

2.2 Digital Breast Tomosynthesis

Digital Tomosynthesis (DTS), a refinement of conventional geometric tomography, is a technique that relies upon the reconstruction of a volumetric image from the acquisition of multiple projections over a limited angular range. Imaging 3D anatomy via a 2D planar image has obvious defects because overlapping tissues degrade cancer detection quality by decreasing sensitivity and specificity. In conventional geometric tomography proposed in the 1930s, a focal plane of interest is produced. The focal plane is formed by moving the screen film (or the detector) and X-ray tube oppositely across the patient about a fulcrum in between. Consequently, the visibility of structures outside a planar region of focus, controlled by the location of the fulcrum, is minimised. Any planes above or below the focal plane are blurred due to the movement of the X-ray tube and detector, yielding a film presents the least amount of radiographic motion using a linear, circular, or hypocycloidal geometry. A restriction of conventional geometric tomography is that only a single slice can be acquired per scan. As a result, the overdosage of radiation makes this impractical to obtain a volume of tomography.

In the early 20th century, Johann Radon [232] [233], an Austrian mathematician, proposed the mathematical groundwork for a transform consisting of the integral of a function over straight lines. The transform, named after Radon, has been generalised to three-dimensions, and prompted consideration of non-Euclidean manifolds and higher dimensional space, as well. The Radon transform

is widely applicable to tomography, and it represents scattering data as an output image associated with cross-sectional scans of an object. Hence, the inverse Radon transform can reconstruct the original density of the object from the scattering data, to formulate the tomographic reconstruction. From 1921 to 1932, Ziedses des Plantes [347], a Dutch researcher, introduced planar tomographic imaging (Planigraphy) to obtain sections of the body in order to eliminate superimposed shadows. The technique was popularised by a German researcher Grossmann [94], who invented a commercial apparatus and successfully applied it to the study of the anatomy of the lungs. In the UK, Barclay and Twining of Manchester made their contributions to the clinical prominence of tomography [294] [255]. However, it was not until 1969 that Garrison et al. [82] completed the first full implementation of Ziedses des Plantes's concepts by developing a 3D tomography device. Planar tomography has continued its medical examinations to date, but the introduction of CT has reduced the number of applications considerably. In [202] Miller et al. concluded that a high quality tomosynthesis image must be obtained from at least eight different views of forward projections. Further research, which was carried out by Grant [92] who named the new circular backprojection device *tomosynthesis*, implied generating an infinite number of arbitrary tomograms. These authors demonstrated that it is possible to use film as the detector. However, the film-based tomosynthesis system is too cumbersome for clinical usage, and the development of a tomosynthesis system with an electronic image is necessary.

Through the 1970s and 1980s, Baily, Crepeau, Lasser, et al. [162] [13] [11] [14] [12] advocated the use of an image intensifier and a television camera to obtain tomographic images. Different planes of an object could be displayed on an electronic storage tube by altering the shape and position of the television raster for each successive television frame. Subsequently, Maravilla et al. [187] [188] designed an apparatus, which included an analog-to-digital converter and a micro data processing computer, to obtain tomographic images through retrospective reconstruction. Chakraborty et al. [37] suggested using a one-dimensional unsharp masking technique to suppress the blur inherent in tomosynthesis slice reconstructions. This spatial frequency filtering method was implemented more carefully by Sone et al. [269]. The filter functions were modified to adjust the low frequency and high frequency residual image information content. Consequently, they evaluated the clinical usage with various applications such as enhancement of arthrography, angiography, small anatomic structures imaging, and chest and pulmonary imaging [270] [271]. Changing the detector from screen-film-based to electronic-based had considerably reduced the engineering requirements of implementing tomosynthesis systems. However, commercial apparatuses still suffered from noise and distortion at the edge of the image. Moreover, post-processing was hampered by the analog acquisition system

and ineffective computing power.

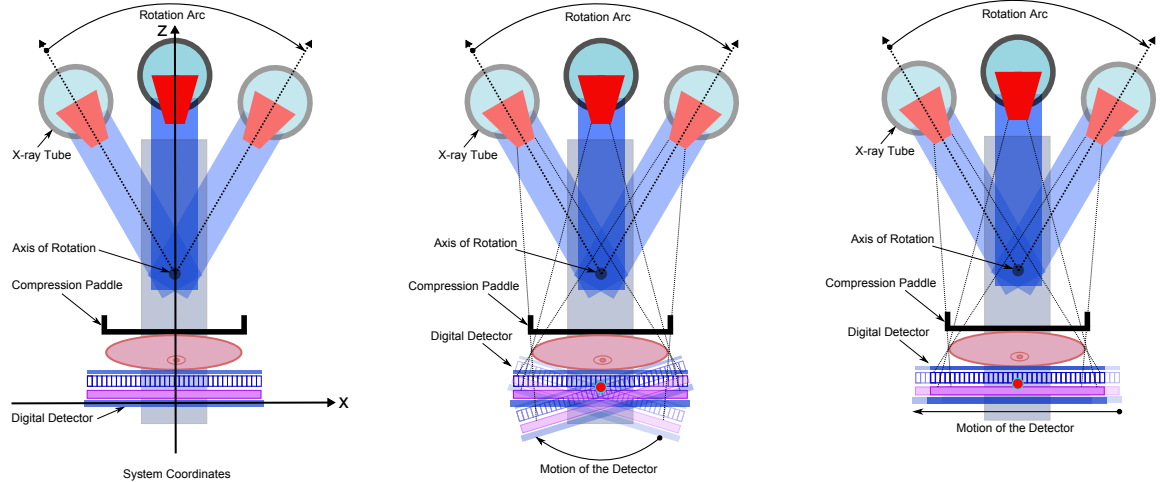


Figure 2.6: *Left:* DBT system geometries use isocentric motion and the coordinates; *Middle:* Both the x-ray source and detector move in an arc shape oppositely (Grossman geometry); *Right:* the x-ray source and detector move parallel to the in-focus tomographic plane oppositely (Twinning geometry).

For many years, tomosynthesis failed to make an impact on the clinical environment. The technique was hindered by the lack of a large area digital flat-panel detector, which should be capable of rapid image readout. With the introduction of flat-panel digital imaging systems, in 1997, Niklason et al. [215] published a landmark work on digital tomosynthesis. They used a digital detector that was composed of caesium iodide phosphor on an amorphous silicon transistor-photodiode array (CsI on a-Si). This detector was developed by General Electric (GE) Corporate Research and Development at Schenectady, NY. The basic system was a mammographic system (model DMR; GE Medical Systems, Milwaukee, WI) with the full-field digital image receptor. In addition, results on breast imaging showed that their DBT system could produce high-quality breast tomosynthesis images. The DBT system improved the specificity of mammography with visual enhancement for lesion margin. The conclusion was that digital mammographic systems made DBT feasible to be implemented, and DBT might improve early breast cancer detection, especially in women with radiographically dense breasts. The invention of digital detectors has finally satisfied all the necessary properties of clinically practicable DBT. In addition, these detectors were investigated thoroughly, for instance, [328] [298] [343] [168] [24], and they could produce high readout rates and exceptional detective quantum efficiency (DQE). Figure 2.6 shows a schematic illustration of a typical DBT prototype with different acquisition geometries. It is feasible and straightforward to modify the existing mammography

system to adapt the DBT function (Figure 2.7).

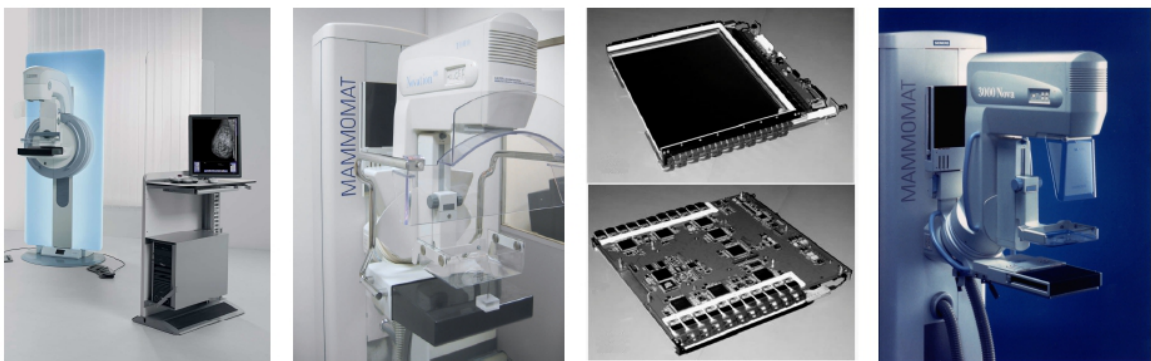


Figure 2.7: The most left: Photograph of the latest development of MAMMOMAT® Inspiration (Siemens) with a 3D tomosynthesis option. Left: One of the earlier developed digital mammography machines (Siemens) with a tomosynthesis facility. Right: Top view and bottom view of an amorphous selenium detector used for tomosynthesis imaging. The most right: A FFDM machine (Siemens) with no tomosynthesis function.

A key component in the clinical utility of DBT is the reconstruction algorithm, which can suppress most of the tissue overlap effect. The overlap effect is the major reason for recalls and additional imaging in 2D mammography examinations. Furthermore, reconstruction of DBT subsequently reinforces the object of interest on the focal plane, and occult cancers in mammography can be differentiable through the elimination of structure noise. In Chapter 3, the detailed survey of various reconstruction algorithms will be given, and many reviews have been published, for example, [283] [62] [322] [344]. In [17] Baldwin reported a working on DBT for the educational purpose. Optimisation of DBT reconstruction is an important ongoing work, and several optimisation strategies will be outlined in this thesis.

X-ray mammography and DBT are the most suitable techniques for *nonpalpable breast cancers detection*, but the risk of *carcinogenesis* from the *radiation dose* is of the primary concern. There are a great number of women receiving mammographic examinations. Therefore, monitoring the dose is crucial and is required yearly by the federal Mammography Quality Standards Act (MQSA) of Food and Drug Administration (FDA), USA. The quantity absorbed dose (D) captures the energy (E) deposited by ionising radiation per unit mass of material (M)

$$D = \frac{E}{M}. \quad (2.6)$$

In addition, the *absorbed dose* is defined for all types of ionising radiation. The System International

(SI) unit of absorbed dose is the *gray* (Gy). One gray is equal to 1J/kg. The traditional unit of absorbed dose is the rad (an acronym for radiation-absorbed dose). One rad is equal to 0.01J/kg. Thus, there are 100rads in a gray and 1rad = 10mGy. For X-rays and γ -rays, the absorbed dose can be calculated from the mass energy absorption coefficient and the energy influence of the beam [34].

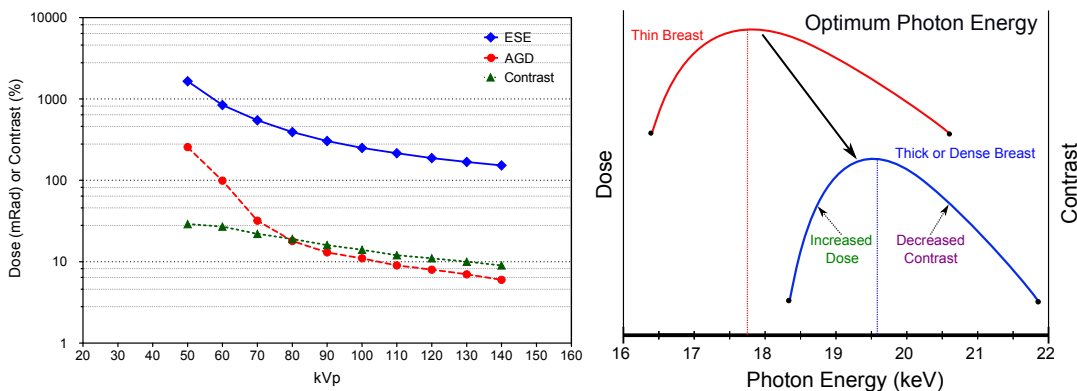


Figure 2.8: Left: Contrast and dose as a function of kVp (the plot is based on the data published in [34]). Right: Optimum photon energy (spectrum) of mammography depends on the size and density of the breast (this plot is reproduced from [272]).

The glandular tissue is the most predisposed site of carcinogenesis; therefore, the preferred dose index is the Average Glandular Dose (AGD). The amount is dependent upon the depths of glandular tissues from the entrance of the X-ray beam on the skin. The mid-breast dose, which is the dose delivered to the plane of tissue in the middle of the breast, was the radiation dosimetry benchmark until the late 1970s. However, nowadays, the AGD is the standard because the mid-breast dose, which is normally lower than the AGD, does not account for the variation in breast tissue composition. The AGD, denoted by D_g , is calculated by

$$D_g = \nu_f X, \quad (2.7)$$

where X is the Entrance Skin Exposure (ESE) in roentgens (R), and ν_f is the ESE to average glandular dose conversion factor with units of mGy/R or mrad/R. In addition, ν_f is determined by experimental and computer simulation methods. It depends on radiation quality (kVp and *Half Value Layer* (HVL)¹), materials of the x-ray tube target, filter material, breast thickness, and tissue composition. An air-filled ionisation chamber measures

¹The HVL depicts the penetrability of the photons. It is defined as the thickness of material required to reduce the intensity of an X-ray or γ -ray beam to be one-half of its initial value.

the ESE for a given kVp, mAs, and beam quality [34]. In practice, the ESE is measured at each kVp with the requirement to deliver an exposure of 0.6mRad to the screen-film detector system. Figure 2.8 shows the correlations between ESE and kVp, AGD and kVp. Heddson et al. [105] performed a study from January 2000 to February 2005 at the Helsingborg Hospital, which noted that the AGD was 1.1mGy for SFM, and 0.28mGy for FFDM. In 2004, Wu et al. [322] showed that the ESE was 1.27 times more for DBT than SFM. In addition, the AGD was 1.45 times more for DBT than SFM with various breast thickness (from 3cm to 8cm) and tube voltage (from 25kVp to 33kVp). In [184] Maidment et al. reported that the AGD of their tomosynthesis scanning was about 1.5mGy at 35kVp. Furthermore, Diekmann et al. [61] demonstrated a comparable result that there were 1.33 times more doses for tomosynthesis in comparison to a normal digital mammography.

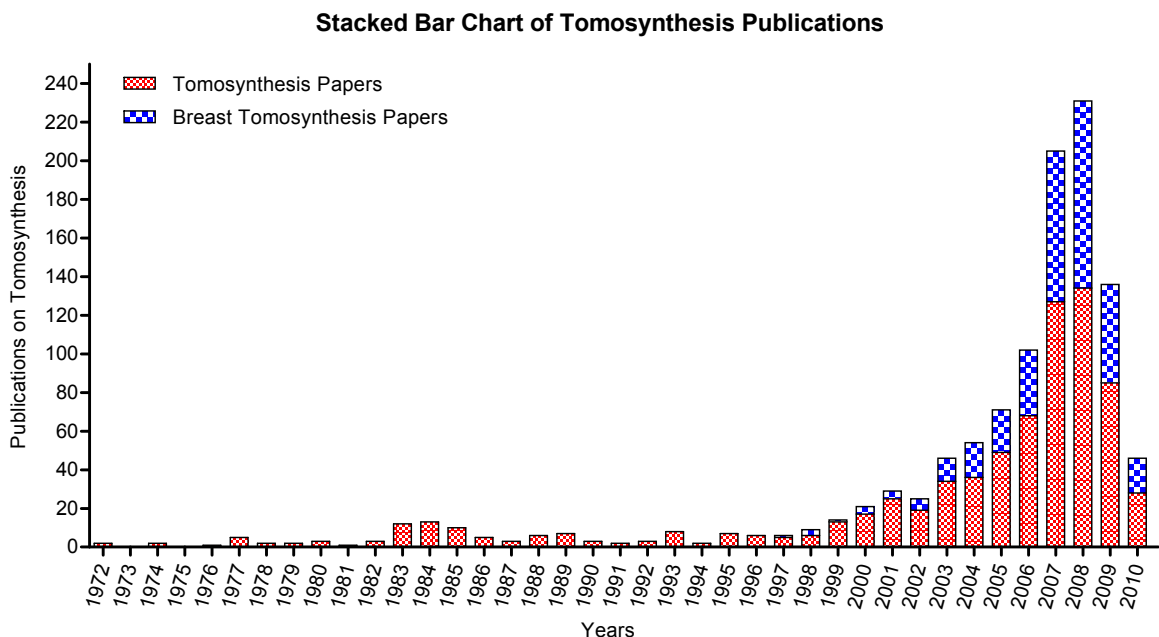


Figure 2.9: Statistics of scientific publications on tomosynthesis research field indexed by ISI Web of Knowledge and PubMed. Actually, there are some papers on tomosynthesis before 1972 when Grant defined the term 'tomosynthesis'.

In 2007, Poplack et al. [231] reported that subjectively DBT scans could have comparable or superior image quality to that of SFM in the diagnostic setting. In addition, DBT possessed the potential to decrease the recall rate when used adjunctively with FFDM. About half (52 in 99; 52%) of the findings would not have been recalled when FFDM was supplemented with tomosynthesis. Gur [96] published a commentary paper that confirmed the clinical potential of DBT. In [221] Park et

al. showed that DBT could reduce recall rates and improve the selection of patients for biopsy. The cancer detection rates could be increased using DBT, especially in patients with dense breasts. In addition, recent research carried out by Good et al. [87] and Gur et al. [97] also found similar results that DBT could reduce recall rates. However, more research is necessary before defining the optimal role of DBT in the clinical environment. Recently, Svahn [284] published an article, which indicated that there were significant differences between the combined modality (DBT with the contralateral FFDM view) and dual-view FFDM. However, no differences were found between single-view DBT and dual-view FFDM or between single-view DBT and the combined modality. DBT has been used in research for many years, yet the first Food and Drug Administration (FDA) approval was issued in February 2011 (Hologic Selenia® Dimensions™ system). Therefore, unlike FFDM, there are only few population-based studies on ergonomic and diagnostic performance of DBT.

Furthermore, Contrast Enhanced Digital Breast Tomosynthesis (CE-DBT) is potentially integrating the strengths of both FFDM and DBT imaging techniques ([40] [60] [172]). In addition to the clinical potential of DBT and CE-DBT, Dedicated Breast Computed Tomography (DBCT) could also have a role in detecting breast cancer. In [141] Karella et al. suggested that both of DBCT and DBT were nascent technologies and there would be many possibilities for improvements.

In order to take a panoramic view of the research on DBT, we have gathered the statistics of scientific publications indexed by ISI Web of KnowledgeSM, Thomson Reuters[©] and PubMed, National Center for Biotechnology Information[©] (Figure 2.9). The registered papers have started from 1972, when the terminology of *tomosynthesis* has been defined. Papers, which have been published or will be published after March of 2010, have not been included due to less accumulated citations and lower impact. In addition, the statistics have illustrated how the interest on tomosynthesis has increased over the years. Since 2004, DBT has dominated the scientific publications in the tomosynthesis research field. In total, *breast tomosynthesis* accounted for 349 (46.3%) of all the 754 released *tomosynthesis* papers.

2.3 Conclusions and Discussion

For many years, a number of medical imaging modalities have been investigated to detect and diagnose breast cancer. However, unclear aetiology of breast cancer and drawbacks of the conventional screening methods force us to develop novel medical imaging techniques such as DBT. The objective is to detect and demonstrate malignant carcinomas at the early stage in a 3D distinct manner. Table 2.1 compares various physical properties of different breast imaging modalities.

Table 2.1: Comparison of various physical properties in different breast imaging modalities.

<i>Features \ Modalities</i>	<i>MRI</i>	<i>Ultrasound</i>	<i>PET</i>
Signal Basis	Proton NMR ²	Cyclic sound pressure	Gamma rays emitting ³
Format	3D Multi-slice	2D or 3D	3D or 4D
Breast Compression	Mild ⁴	Mild ⁵	Mild
Contrast Injection Required	Yes	Sometimes	Yes
Examination Time	Long (30-45min)	Long (15-30min)	Long (Approximate 45min)
Demonstrates Calcifications	No	No ⁶	No (PET can detect DCIS)
Effective in Dense Breast	Yes	No	Yes ⁷
<i>Features \ Modalities</i>	<i>CT</i>	<i>Mammography</i>	<i>Tomosynthesis</i>
Signal Basis	X-ray	X-ray	X-ray
Format	3D	2D projection	Pseudo-3D
Breast Compression	Mild	Yes	Yes (Less than mammography)
Contrast Injection Required	No	No	No
Examination Time	Short (17sec-5min)	Short (5-10min)	Short 12.5/39sec (25/49views) ⁸
Demonstrates Calcifications	Yes	Yes	Yes
Effective in Dense Breast	Yes	No	Yes

Firstly, detection and diagnosis of breast cancer by using MRI has been investigated with plentiful results. Breast MRI has merits in 3D tomographic results, including sensitivity to tumours inside dense tissue, and lack of radiation. It is applicable to young premenopausal women. Some advantages of MRI are offset by its undesirable effects such as low spatial resolution of around 1mm and the requirement of contrast agent injection, *e.g.*, Gadolinium DTPA. It is complicated to estimate the rate of uptake of the contrast agent.

Secondly, conventional 2D ultrasound can be targeted or focused on the symptomatic lesion, but this limits the use of ultrasound and its applications. In addition, it is possible to miss impalpable lesions. 3D ultrasonography is rapidly gaining popularity, and it offers several distinct advantages over conventional ultrasonography. Conventional ultrasonography is very useful for distinguishing breast

¹ The data of MRI and mammography were collected from Morris et al. [205] published in 2005. The data of DBT were obtained from Bissonnette et al. [24] published in 2005. PET data were collected from Kaul and Daguilh [144] published in 2002 and Pio et al. [227] published in 2006. Breast CT data were summarised according to Yang [338] published in 2007 and breast ultrasound data were obtained from Park et al. [220] published in 2005.

² There is mainly water proton with nuclear magnetic resonance.

³ The system detects pairs of gamma rays emitted indirectly by a positron-emitting radionuclide.

⁴ Mild compression can be used to stabilise the breast.

⁵ An appropriate amount of breast compression is given. It is varied to see if the lesion will alter in shape, or slip away from under the probe (commonly happened for fibroadenomas).

⁶ Ultrasonography is very sensitive in detecting cystic lesions, but it is not as useful in detecting lesions that are less than 1cm in diameter.

⁷ PET scanning may be useful in assessing patients with difficult-to-evaluate breasts, *e.g.*, women with dense breasts, previous surgery or radiation, and breast implants.

⁸ This typical setting is obtained from [24] with a Siemens DBT apparatus.

cysts, but 3D ultrasonography has the capacity to demonstrate lesion margins and tomography. 2D ultrasound merges 3D data into 2D overlapping images. In contrast, 3D images can be reconstructed from data obtained with a single sweep of the 3D ultrasonography beam across the involved organ. However, the 3D ultrasonography is more complicated than the conventional ultrasound system, and it is hard for the operators to manipulate. Moreover, the reconstruction of 3D ultrasonography is time-consuming because it requires a considerable amount of image manipulations to obtain high quality results. The data archiving and communication are also more challenging. Compared with other modalities, ultrasonography provides high specificity, easy manipulation for both operators and patients, no radiation, low cost and tomographic screening (For 3D ultrasonography only). The drawbacks are mainly about the low sensitivity and the operator dependency.

Next, the detection and diagnosis of breast cancer have primarily relied on conventional mammography for about forty years. Conventional mammography is the most accurate and most widely used of all the breast imaging modalities. Conventional mammography or SFM exhibits high sensitivity in fatty breasts, high resolution up to $50\mu\text{m}$ and low cost. However, limitations of a mammogram include low sensitivity in dense glandular breast tissue, and low specificity, and they are represented by both considerable false negatives and false positives. The rate of missed cancers is measured by the false negatives, which are common in detections of dense breast with low signal-to-noise ratio. Meanwhile, the cost of high sensitivity of mammography is a relatively large number of results, which could be regarded as suspicious in patients without disease. In addition, the radiation dose limits the applicability of mammography, and especially it poses a potential risk for young women with a genetic predisposition.

Digital mammography or FFDM has been tested extensively for clinical use, and many manufacturers have been approved to produce digital units for both clinical screening and diagnosis. Several research groups have compared SFM with FFDM, and many studies have concluded that digital mammography offers a significantly lower recall rate. Yet some studies have obtained a higher recall rate for FFDM because of the learning curve effect. However, FFDM has gained better accuracy in some subgroups such as women with dense breasts. In addition, the FFDM-CAD combination has significantly improved the detection of DCIS and microcalcification clusters. Until now, all the research shows that FFDM can be safely implemented in breast cancer screening programs. FFDM is a fast-developed imaging modality including novel techniques and detectors, which enable a technical leap of inspiring tomographic techniques such as DBT. Other less widespread breast imaging modalities, *e.g.*, nuclear imaging, breast CT, thermography, and transillumination provide alternative options for clinical use in screening, diagnosis, and functional information observation.

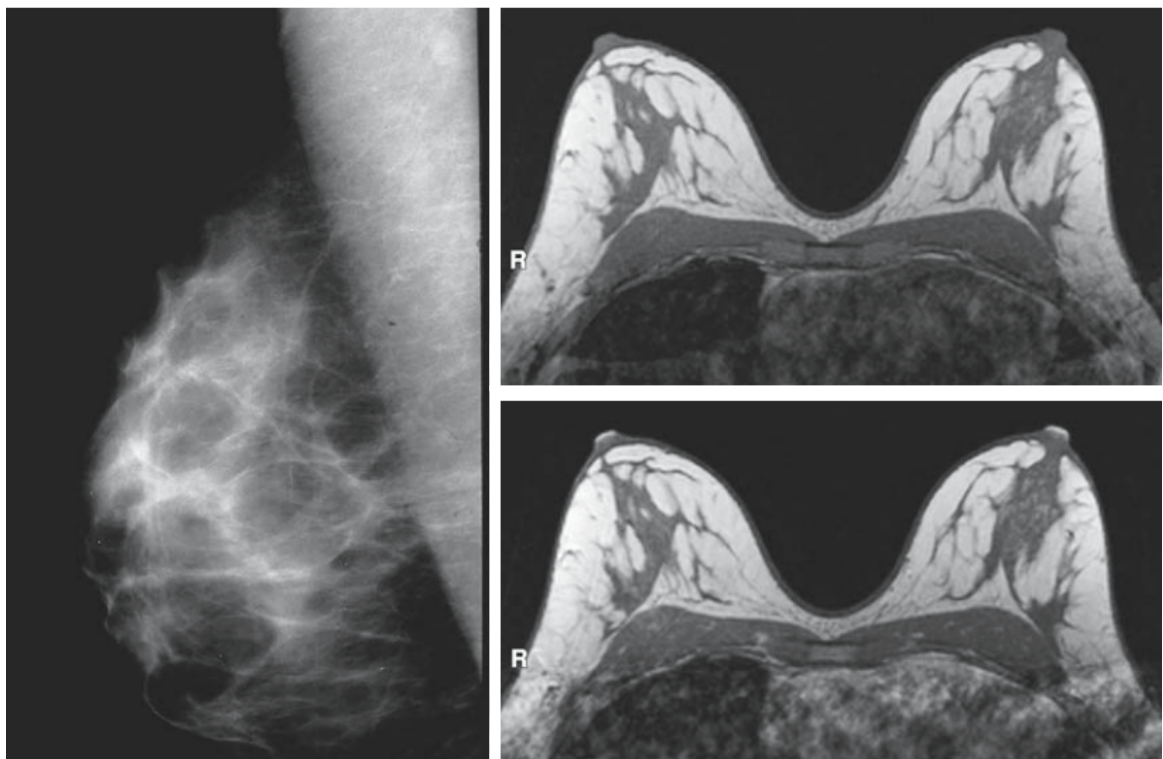


Figure 2.10: Comparison between mammography and breast MRI for the same 33-year-old patient with documented *BRCA1* mutation. Left: Screening mammogram (MLO view of the right breast); Upper right: Pre-contrast T1-weighted breast MRI; Lower right: First post contrast of the dynamic series. The images are taken from Morris et al. [205].

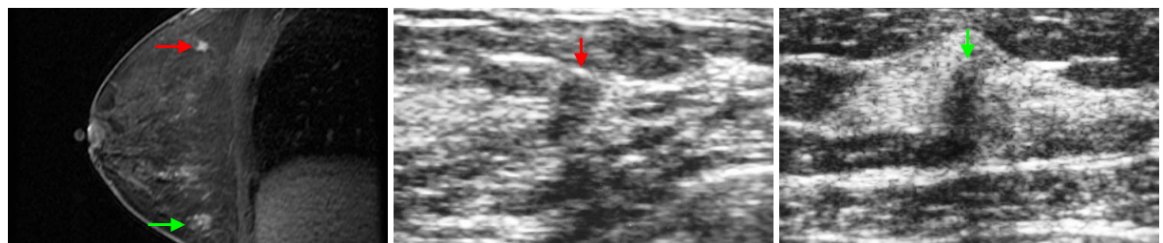


Figure 2.11: Comparison between breast MRI and breast ultrasound for the same 47-year-old patient. Left: T1-weighted breast MRI in sagittal view showing two lesions (red and green arrows); Middle: Breast ultrasound shows a hypoechoic mass that is taller than wide (red arrow), corresponding to the superior MRI lesion; Right: Breast ultrasound shows a hypoechoic mass that is taller than wide (green arrow), corresponding to the inferior MRI lesion. The images are taken from Morris et al. [205].

Furthermore, there are numerous benefits offered by DBT, *viz.*, 3D tomographic demonstration for breast, compatible for mammography specifications, high sensitivity and specificity, high resolution, and small acquisition lag in compared to mammography. However, prolonged imaging time of DBT introduces patient motion blur on the images. Additionally, gantry motion leads to a larger effective x-ray focal spot size, which may degrade the image quality. Moreover, the DBT reconstruction is an inherent ill-posed inverse problem because of the incomplete sampling of tomosynthesis scan. Well-posed problems are more common, which means the model parameters and the material properties are known. On the other hand, inverse problems, which derive these parameters and properties from observations, are typically ill-posed. We can draw a conclusion that DBT is a promising breast imaging modality, whereas its reconstruction is still a complicated ill-posed inverse problem.

In summary, developments of prominent digital detectors of FFDM permit the growth of DBT. Advantages of DBT are concluded as follows. Firstly, DBT eliminates overlapping structures of the standard digital mammography. Three-dimensional screening brings a much clearer view of lesions within the breast, and it locates the potential cancer more accurately than SFM or FFDM. Previous research proves that DBT can make cancer lesions easier to see among dense fibro-glandular tissues [271]. In addition, DBT combines various forward projections into a pseudo-3D reconstruction that brings structures into relief. Radiologists can navigate the breast using a 3D image for a more careful examination [66]. Secondly, DBT needs no longer examination time than normal mammography for most diagnostic requirements. Actually, the examination time is decreased since only one acquisition, *i.e.*, CC or MLO, is necessary (two acquisitions might be required at some sites). Furthermore, due to the interpretation criteria are the same for both mammography and DBT, any radiologist who is skilled at reading mammography will be able to read DBT studies. The reading is also less complicated for the radiologist because the superimposed structures are removed. Next, research also confirms that sensitivity (the ability to detect breast cancers) and specificity (the differentiation between benign and malignant cancers) are both improved by using DBT. Other merits of DBT are well addressed in previous studies. For example, the cost of screening (primary and secondary) is decreased while DBT increases the cancer detection rate. DBT can be utilised as the base platform for registering and developing other breast imaging studies [154]. It makes a huge improvement for breast cancer detection and diagnosis, as well. We show some example results of various breast imaging modalities (Figures 2.10 and 2.11) to provide an intuitive understanding of the advantageous gain of DBT imaging (Figures 2.12 and 2.13). Eventually, development of DBT could represent a success in the field of breast cancer imaging in the future. In next two chapters, we will survey two key components in DBT applications, *i.e.*, tomographic reconstruction and medical image registration.

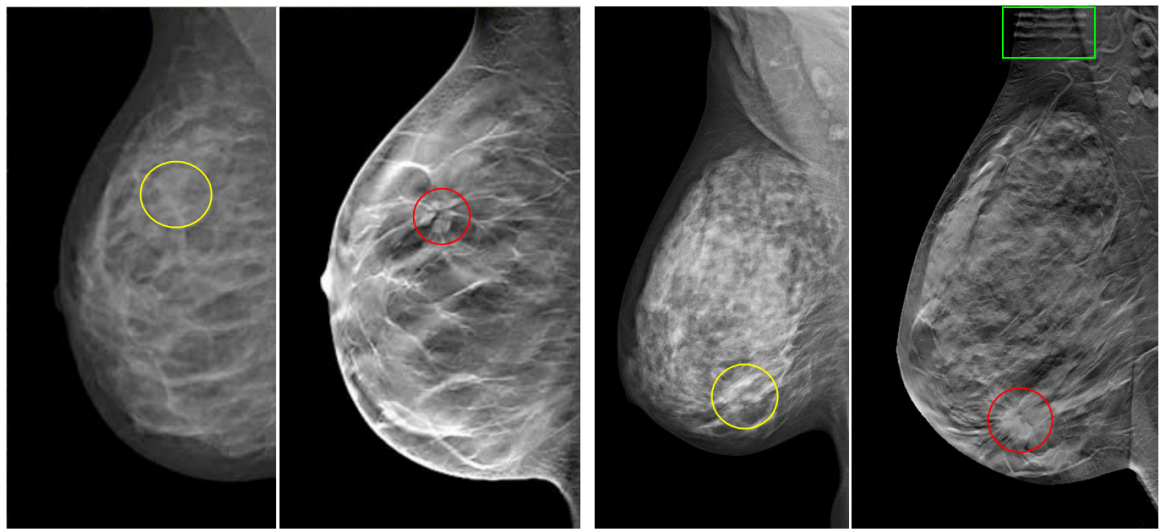


Figure 2.12: Comparison between mammography and DBT for the two different patients. Two sub-figures on the left hand side: Original mammography with in-plane artefacts caused by breast tissues overlapping (yellow circle) vs. a selected DBT slice (reconstructed) and the lesion is clearly shown in the DBT reconstruction (red circle); Two sub-figures on the right hand side: Original mammography showing overlapped breast tissues (yellow circle) vs. a selected DBT slice (reconstructed) showing the lesion clearly (red circle) and the in-plane streak artefacts are shown (green square). The images are taken from Bick and Diekmann [22].

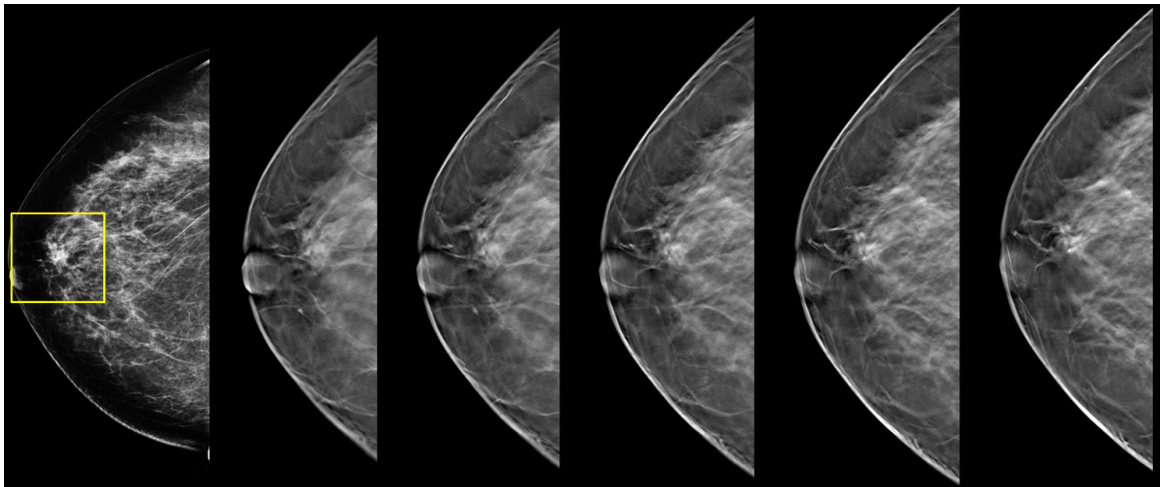


Figure 2.13: Comparison between mammography and DBT slices. The sub-figure on the left hand side: Original 2D mammography showing a potential lesion (yellow square); Other sub-figures: The individual structures that make up the potential lesion can be clearly seen on the separated slices (No. 14, 18, 22, 26 and 30) of 3D DBT, and no lesion is presented in fact. The images are taken from Dallessio [54].

Tomographic Reconstruction and Its Applications in DBT

Tomographic image reconstruction is a crucial problem in current research on medical image processing. The DBT imaging procedure, which depends on the specified *geometry*, is considered as a *forward problem* to get the DBT data. On the other hand, the reconstruction is an *inverse problem*. Essentially, all the tomographic image reconstruction algorithms are applicable to DBT. In this chapter, we investigate some widely used reconstruction algorithms based on X-ray tomography with *non-diffracting* sources. The image reconstruction algorithms can be coarsely divided into two categories, *i.e.*, the analytical and the iterative methods (Figure 3.1). We provide a brief discussion on DBT geometry and hardware specifications following by detailed reviews on several analytical and iterative reconstruction algorithms.

3.1 Forward Problem: Imaging

3.1.1 Forward Radon Transform

Mammography, breast CT, and DBT apparatus utilise X-ray radiation, which is of an electromagnetic nature, as the energy source. Thermal electrons, which escape from a cathode filament heated to approximately 2100 °C, generate radiation energy following their entry into the rotating anode. The energy of the braking radiation in turn depends on the acceleration voltage, U_a , between cathode and anode, and relates to the electron kinetic energy as

$$\frac{1}{2}m_e v^2 = eU_a \quad (3.1)$$

in which the mass of electrons $m_e = 9.109 \times 10^{-31} \text{ kg}$ and the charge of electrons $e = 1.602 \times 10^{-19} \text{ C}$. Thus, the electron velocity v can be determined. In medical imaging applications, the value of U_a falls between 25kV and 150kV.

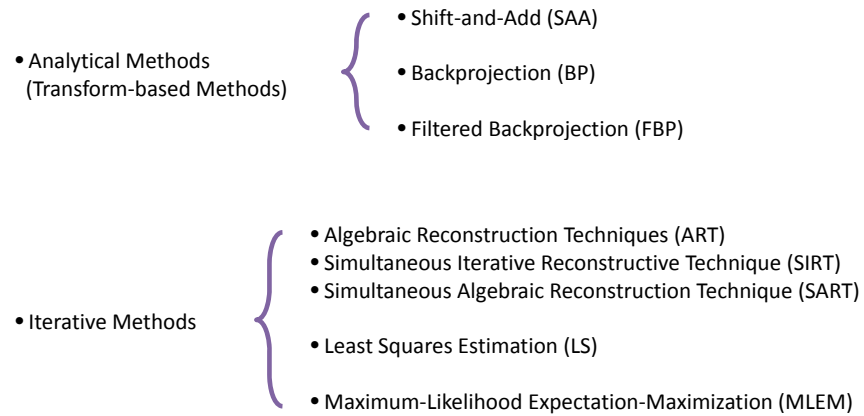


Figure 3.1: Detailed classification of the reconstruction algorithms.

The physical mechanism leading to X-ray breast imaging is based on the Lambert-Beer's Law, which states the attenuation property of light when it travels through certain material (Figure 2.3). However, there are two problems with Lambert-Beer's Law, *viz.*, we need a logarithmic transform for the X-ray attenuation model and the model consists of numerous inhomogeneous attenuation coefficients. Firstly, Equations 2.2 and 2.3 can be rewritten as

$$I_A = I_0 e^{-\mu z} \quad (3.2)$$

$$I_B = I_0 e^{-\mu(z-a)-\mu'a}, \quad (3.3)$$

where I_0 is the incident intensity, and I_A and I_B are transmitted intensities without and with a lesion, *e.g.*, a tumour or a microcalcification. z and a are the approximate thickness of the whole breast and the lesion respectively. In addition, μ and μ' are the attenuation coefficients of the breast tissue and lesion. If the inhomogeneous X-ray attenuation is discretely modelled using multiple attenuation coefficients, that is

$$I_T = I_0 e^{-\sum_{i=1}^n \mu_i z_i}, \quad (3.4)$$

and the measured projection is not linearly related to these attenuation coefficients. Therefore, we

need to perform the logarithmic transform for the X-ray attenuation model and the result is

$$\ln \frac{I_0}{I_T} = \sum_{i=1}^n \mu_i z; \quad (3.5)$$

however, in this case, we assume that the X-ray source is monoenergetic and the beam is ideally small, which can not be true in real applications. Therefore, the Hounsfield unit (HU) scale is applied to derive linear attenuation coefficients, *e.g.*, 0HU is assigned to water ($\mu_{\text{water}} = 0.21\text{cm}^{-1}$) and -1000HU is assigned to air ($\mu_{\text{air}} = 0.0\text{cm}^{-1}$) on this scale [35]. Secondly, as there are multiple unknown coefficients along the X-ray beam within the breast object, the inhomogeneous attenuation is modelled by a sequence of discrete partitions. If the breast object is rasterised, *i.e.*, sampled into discrete rows and columns, we can use a 3D matrix to store the attenuation coefficients (Figure 3.2). In fact, there are many factors, which affect X-ray attenuation including wavelength of the incident beam, atomic number, mass density, and thickness of the medium [35].

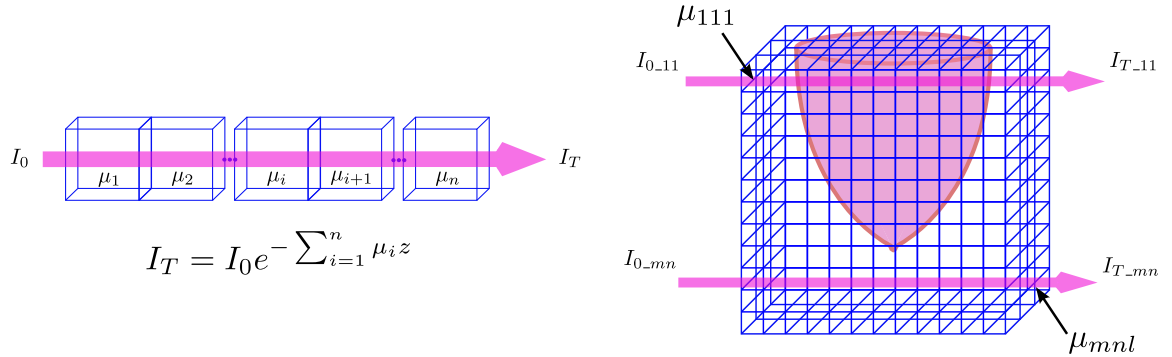


Figure 3.2: *Left:* A single X-ray beam is passing through a segment of breast tissue with multiple inhomogeneous attenuation coefficients; *Right:* A 3D matrix of discrete attenuation coefficients can be created.

After the interaction between X-ray photons and breast matter, attenuation can occur. The same interaction principle can be applied between the radiation and the detector. Therefore, we measure the X-ray quanta via their interaction products, *e.g.*, emitted photoelectrons, ionised gases. Many types of detectors have been developed for X-ray imaging such as film cassettes, computed radiography cassettes, image intensifiers, gas detectors, and digital flat-panel X-ray detectors. The product of the geometric efficiency and the quantum efficiency gives the overall detection efficiency. Geometric efficiency is the percentage of the X-ray sensitive area of the detector over the total exposed area. In addition, the quantum efficiency measures the fraction of absorbed photons and the ones that contribute to the signal [32].

The signals, which are measured by the detector, generate the forward projection images in an analogue or a digital form. In addition, the forward projection can be modelled by the forward Radon transform, which calculates the line integral of an X-ray beam at a particular angle. We use $f(x, y)$, which is defined in a limited 2D plane, to describe a 2D distribution of one physical quantity. Therefore, (x, y) are the points on the 2D plane, and $f(x, y)$ is an arbitrary function in the \mathbb{R}^2 region. If L is an arbitrary straight line on the plane, the integration of $f(\cdot)$ along this line L can be written as follows.

$$P = \int_L f(x, y) d\sigma \quad (3.6)$$

where P is defined as the projection of the $f(\cdot)$ function. $d\sigma$ is the increment along the straight line L . Furthermore, this straight line L can be determined by two parameters: one is the distance from the origin to the line L , namely ρ , and the other one is the angle θ between the distance line ρ and the x coordinate (Figure 3.3). Thus, L can be represented by using

$$L : \begin{cases} x = \rho \cos \theta - \sigma \sin \theta \\ y = \rho \sin \theta + \sigma \cos \theta \end{cases}, \quad (3.7)$$

and the integration, *i.e.*, 2D forward Radon transform, can be represented by

$$P(\rho, \theta) = \int_L f(x, y) d\sigma = \int_{-\infty}^{\infty} f((\rho \cos \theta - \sigma \sin \theta), (\rho \sin \theta + \sigma \cos \theta)) d\sigma. \quad (3.8)$$

In addition, Equation 3.8 can be written in a *vector* form if we define $(x, y) = \rho\Theta^\perp + \sigma\Theta$, in which $\Theta^\perp = (\cos \theta, \sin \theta)$, and $\Theta = (-\sin \theta, \cos \theta)$. $P(\rho, \theta)$ can be represented by

$$P(\rho, \theta) = \int_{-\infty}^{\infty} f\left(\rho \cdot \begin{pmatrix} \cos \theta \\ \sin \theta \end{pmatrix} + \sigma \cdot \begin{pmatrix} -\sin \theta \\ \cos \theta \end{pmatrix}\right) d\sigma = \int_{-\infty}^{\infty} f(\rho\Theta^\perp + \sigma\Theta) d\sigma. \quad (3.9)$$

where the $\sigma\Theta$ is perpendicular to the vector Θ^\perp , and $d\sigma$ is the increment along the Θ direction. Therefore, the Equation 3.9 can be rewritten as

$$P(\rho, \theta) = \int_{\Theta} f(\rho\Theta^\perp + \sigma) d\sigma. \quad (3.10)$$

Consequently, in the 2D plane, the integration of the arbitrary function $f(\cdot)$ along the straight line is equal to its Radon transform. If we know $P(\rho, \theta)$ for all ρ and θ , $P(\rho, \theta)$ is the 2D Radon

transform of $f(x, y)$. On the other hand, $P(\rho, \theta)$ is the sample of the Radon transform of $f(x, y)$ if we know $P(\rho, \theta)$ for subset of ρ and θ .

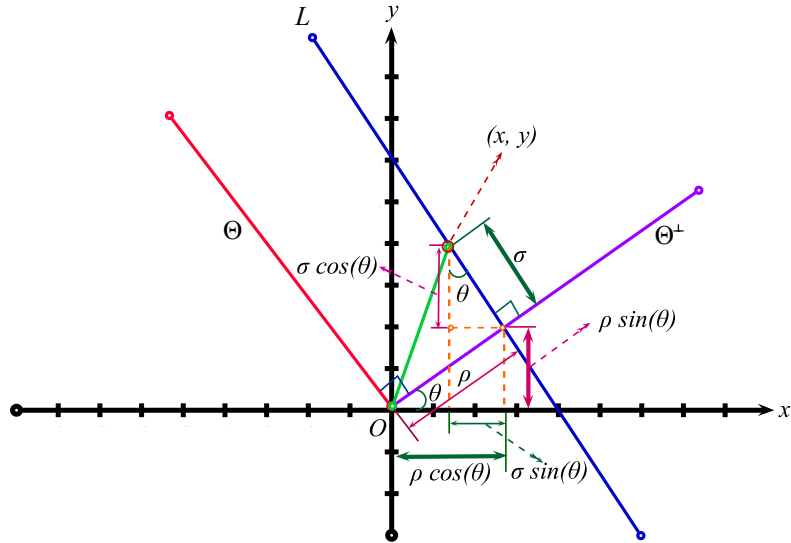


Figure 3.3: Schematic illustration of the relationship between x , y , ρ , σ and θ .

Furthermore, if we parameterise the function using x , y instead of σ in Equation 3.8, we can prove (Details in Appendix A)

$$\begin{aligned} P(\rho, \theta) &= \int_{-\infty}^{\infty} f((\rho \cos \theta - \sigma \sin \theta), (\rho \sin \theta + \sigma \cos \theta)) d\sigma \\ &= \int_{-\infty}^{\infty} \int_{-\infty}^{\infty} f(x, y) \delta(\rho - (x \cos \theta + y \sin \theta)) dx dy, \end{aligned} \quad (3.11)$$

in which the $\delta(\cdot)$ function is the Dirac delta function, and it is defined by

$$\delta(x) = \begin{cases} +\infty, & \text{for } x = 0 \\ 0, & \text{otherwise} \end{cases}, \quad (3.12)$$

and

$$\int_{-\infty}^{\infty} \delta(x) dx = 1. \quad (3.13)$$

To sum up the 2D based discussion of the forward Radon transform, the forward problem of DBT imaging can be modelled using the X-ray attenuation function and the forward Radon transform with 3D extension of the hardware geometry (More discussion in Section 5.2.1).

3.1.2 DBT Geometry and Hardware Parameters

The geometry of the DBT hardware system defines the size of the forward projections and the number of rays, which in turn will determine the appearance of the reconstruction. Most modern DBT machines use Grossman geometry or Twinning geometry (Figure 2.6), and both of them are cone-beam based geometries (details in Section 5.2.2).

In addition, similar to mammography, mild breast compression is necessary via two parallel acrylic plates when acquiring the tomosynthesis scan. Two different views are commonly used, namely Cranio-Caudal (CC: images are taken from a head-to-toe view) and Medio-Lateral Oblique (MLO: images are taken from an oblique or angled view).

Furthermore, we provide an overview of the hardware parameters of various DBT systems from some of the most famous manufacturers in Table 3.1. Most of the prototype DBT systems use 0.3mm X-ray focal spot size, and there are mainly two types of gantry motion (rotation), *i.e.*, continuous rotation and step-and-shoot rotation. In the continuous rotation type, the gantry possesses a constant speed of rotation during the whole imaging process, leading to an enlarged X-ray focal spot size along the rotation direction. On the other hand, in the step-and-shoot rotation type, there is a full stop whilst acquiring a forward projection. The system developed by University of North Carolina (UNC) has employed a stationary array of X-ray sources, which avoids the gantry motion.

Table 3.1: DBT imaging system parameters from some of the most famous manufacturers.

	<i>Siemens: Mammomat Novation¹</i>	<i>GE: Senograph 2000D²</i>	<i>Dexela UVA system³</i>
X-ray kVp, mA	$\approx 28\text{kVp}$, $\approx 180\text{mA}$	$25\text{-}30\text{kVp}$, $\approx 130\text{mA}$	32kVp , 150mA
Focal spot size	0.3mm+blur due to gantry motion	0.3mm+blur due to gantry motion	0.3mm
Gantry motion	Continuous	Step and shoot	Step and shoot
View numbers	25/49	11	13
Imaging time	20s/39.2s	7s	30s
<i>XCounter system³</i>		<i>UNC: Argus⁴</i>	<i>Hologic: Selenia⁵</i>
X-ray kVp, mA	N/A	$\approx 28\text{kVp}$, 10mA	$24\text{-}39\text{kVp}$, $\approx 28\text{mA}$
Focal spot size	N/A	0.2mm	0.3mm+blur due to gantry motion
Gantry motion	Continuous	Stationary	Continuous
View numbers	48	25	11
Imaging time	30s	11.2s	18s

¹ Data were collected from Bissonnette et al. [24] published in 2005.

² Data were collected from Wu et al. [321] published in 2003.

³ UVA: University of Virginia. Dexela and XCounter data were collected by Mr. Spencer Gunn via collaboration between our UCL CMIC lab and Dexela Ltd. and XCounter AB in 2010. Also refer to Varian MAM-RAD70.

⁴ Data were collected from Yang and Zhou [331] published in 2008.

⁵ Data were collected from Ren et al. [235] published in 2005.

3.2 Inverse Problem: Reconstruction

Image reconstruction of DBT is an inverse problem from a mathematical point of view. In DBT, a pseudo-3D image of the breast is obtained by acquiring a number of low radiation projection images. The X-ray tube, which is mounted on a rotating gantry, moves in an arc above the breast. The individual images are reconstructed into a series of high-resolution slices. Lesions, which are invisible using conventional mammography due to overlying of dense breast tissue, can become visible in the DBT reconstruction. In this section, we give an overview on analytical, ART and least squares based iterative methods of the tomographic reconstruction and its application in DBT.

3.2.1 Analytical Methods

Reconstruction is the soul of the DBT technique. The motivation for developing DBT from digital mammography is that of superior 3D reconstruction results. The considerable weight of research into 3D DBT reconstruction has generated multifarious analytical methods, which include traditional Shift-and-Add (SAA), Image-Stretching-Shift-and-Add (ISSAA) [215], Filtered Backprojection (FBP) [92] [190] [156] [163] [276] [47], and Convolution Backprojection (CBP) [195] [59]. Although many reconstruction algorithms have been proposed in the last three decades, few of them have been as widely implemented and used in real applications as FBP.

3.2.1.1 Shift-And-Add (SAA) and Back-projection (BP) Methods

As mentioned, most modern DBT machines use Grossman geometry or Twinning geometry (Figure 2.6). However, conventional geometry, in which the motion of the X-ray focal-spot is parallel to the detector, can demonstrate the principle of DBT (Figure 3.4). According to the illustration, DBT allows us to obtain an arbitrary number of slices of sections through the breast within a relatively limited number of projection images. After obtaining several individual images, we get the projected positions on the detector from central points on each image. In addition, we calculate the relative shift required to bring an object of interest into focus at a certain depth of a section under the breast surface. A synthetic image of such a section is produced by adding these shifted images together. Structures on the particular section are reinforced by adding these shifted images and blurring away structures elsewhere. Essentially, we apply the procedure to all the sections through the whole breast. This is the principle of the traditional Shift-and-Add (SAA) algorithm [154] and its modified version, *i.e.*, Image-Stretching-Shift-and-Add (ISSAA) algorithm [215].

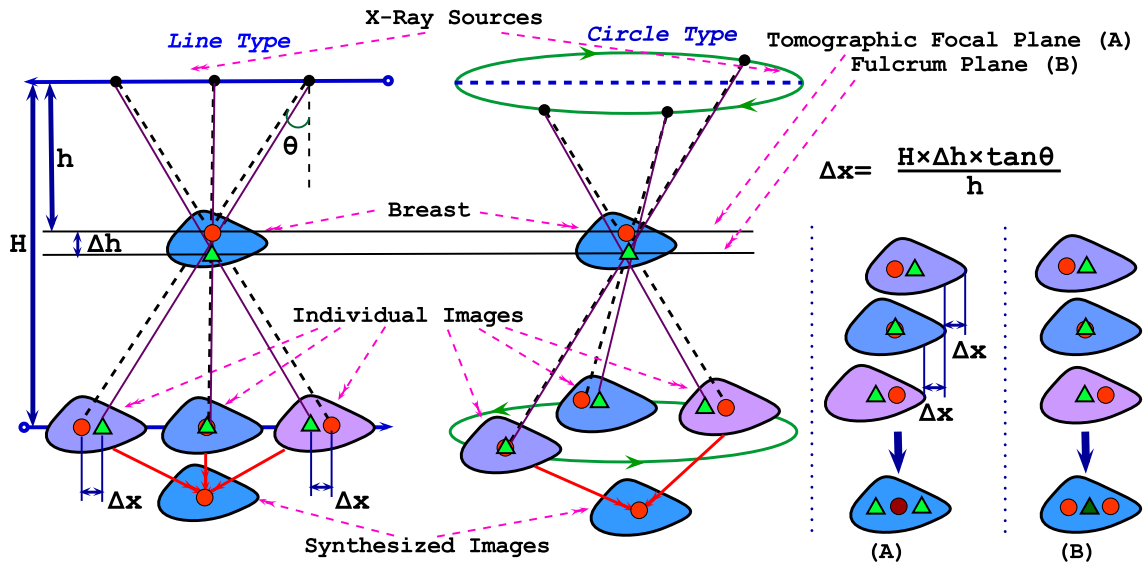


Figure 3.4: Left, line type X-ray source; Middle, circle type X-ray source; Right, schematic of DBT synthesis (A) and conventional summing up (B). For example, we focus on the red circular object on the tomographic focal plane. By shifting and adding synthesis method, DBT imaging increases the visibility of objects by blurring out objects (e.g., the green triangle) from other planes.

The SAA algorithm is valid only when the motion of the x-ray focal-spot is parallel to the detector, e.g., a linear motion at a fixed height above the detector. It is equivalent to a simple backprojection [322]. A BP algorithm can accurately incorporate the imaging geometry wherever the x-ray tube is moved. Both SAA and BP methods are based on the Radon transform. Consequently, both SAA and BP methods employ the backprojection, which smears back the X-ray acquisitions, i.e., line integral, back to the image space represented by pixels or voxels (Figure 3.5).

Mathematically, the backprojection $\hat{f}(x, y)$ with full range of angle can be modelled by

$$\begin{aligned}\hat{f}(x, y) &= \int_{-\infty}^{\infty} \int_0^{\pi} P(\rho, \theta) \delta(\rho - (x \cos \theta + y \sin \theta)) d\rho d\theta \\ &= \int_0^{\pi} P(x \cos \theta + y \sin \theta, \theta) d\theta.\end{aligned}\quad (3.14)$$

Inter-plane artefacts (Figure 3.10), which are caused by the interferences of features located in other planes, are usually observed in a tomosynthetic reconstruction plane using SAA and BP algorithms. In addition, the out-of-plane artefacts (refer to Hu et al. [122]) caused by limited-angle acquisition are inevitable. The Equation 3.14 of the simple backprojection intuitively reverses the

forward projection process; however, the equation results in undesirable distribution of attenuation values. The non-negative line integration $P(\rho, \theta)$ smears back non-negative values not only to the object but also to the whole image. In other words, areas outside of the object have some positive values, which cause the inter-plane blurring artefacts. Previous studies, *e.g.*, [152] [8], have proposed some approaches to remove the inter-plane artefacts. In 2003, Dobbins III and Godfrey [62] summarised the SAA method in use of digital x-ray tomosynthesis. Research carried out by Zhang et al. [344] [345] performed the comparison between SAA and BP methods with iterative reconstruction approaches using DBT data. Although many attempts have been done with various clinical data sets using SAA or BP method, the major drawback is the *blurring* those applications suffer from.

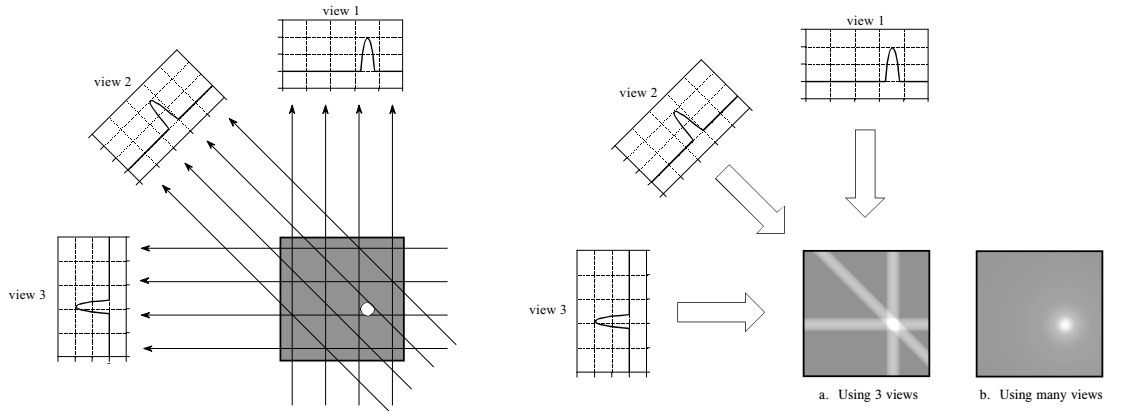


Figure 3.5: *Left:* Three sets of line project the target to three projection views. While only three views are shown above, a typical CT scan uses hundreds of views at slightly different angles. *Right:* Backprojection reconstructs an image by taking each view and smearing it along the path it was originally acquired; however, the resulting image is a blurry version of the original image. These images are copied from Steven W. Smith [268].

3.2.1.2 Filtered Back-projection Method (FBP)

The *Fourier Slice Theorem* is the fundamental to the FBP [138]. It calculates the Fourier transform of a parallel projection of an image $f(x, y)$ taken at angle θ . In addition, it gives a slice of the 2D Fourier transform $F(\mu, v)$, which is subtending an angle θ with the μ -axis. In other words, the Fourier transform of $P(\rho, \theta)$ gives the values of $F(\mu, v)$ along a radial line B (Figure 3.6). Therefore, if we change the (x, y) coordinates into (ρ, σ) coordinates, the projection along the σ direction with the distance ρ is

$$P(\rho, \theta) = \int_{-\infty}^{\infty} f(\rho, \sigma) d\sigma. \quad (3.15)$$

The Fourier Transform of Equation 3.15 is

$$S_\theta(\omega) = \int_{-\infty}^{\infty} P(\rho, \theta) e^{-i2\pi\omega\rho} d\rho. \quad (3.16)$$

We can combine Equations 3.15 and 3.16 as follows

$$S_\theta(\omega) = \int_{-\infty}^{\infty} \left[\int_{-\infty}^{\infty} f(\rho, \sigma) d\sigma \right] e^{-i2\pi\omega\rho} d\rho. \quad (3.17)$$

From the Equation A.2 we can derive that

$$S_\theta(\omega) = \int_{-\infty}^{\infty} \int_{-\infty}^{\infty} f(x, y) e^{-i2\pi\omega(x \cos \theta + y \sin \theta)} dx dy, \quad (3.18)$$

because the determinant of the transform Jacobian is 1 and $d\rho d\sigma = dx dy$ [121]. If we set $\mu = \omega \cos \theta$ and $v = \omega \sin \theta$ then

$$S_\theta(\omega) = F(\mu, v) = F(\omega \cos \theta, \omega \sin \theta). \quad (3.19)$$

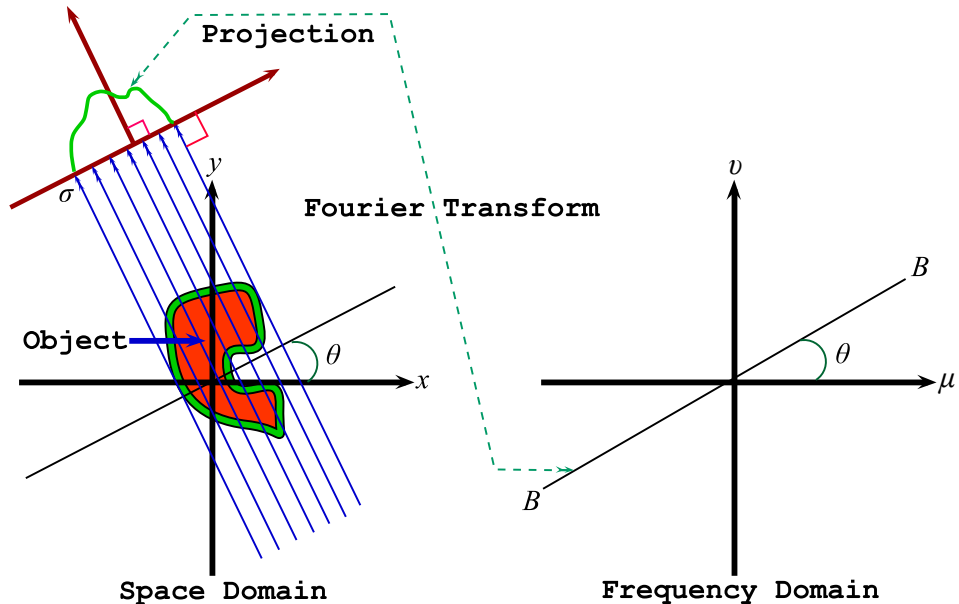


Figure 3.6: Illustration of the Fourier Slice Transform.

Therefore, from the Fourier Transform of one function $f(x, y)$ at $\theta_1, \theta_2, \theta_3 \dots \theta_n$ we can get the 2D Fourier Transform $F(\mu, v)$ of the function $f(x, y)$ on the entire (μ, v) domain (Figure 3.7).

$F(\mu, v)$ can be obtained using these $F(\omega \cos \theta, \omega \sin \theta)$ values. Furthermore, $f(x, y)$ can be derived from the inverse Fourier Transform of $F(\mu, v)$ that is

$$f(x, y) = \int_{-\infty}^{\infty} \int_{-\infty}^{\infty} F(\mu, v) e^{i2\pi(\mu x + vy)} d\mu dv. \quad (3.20)$$

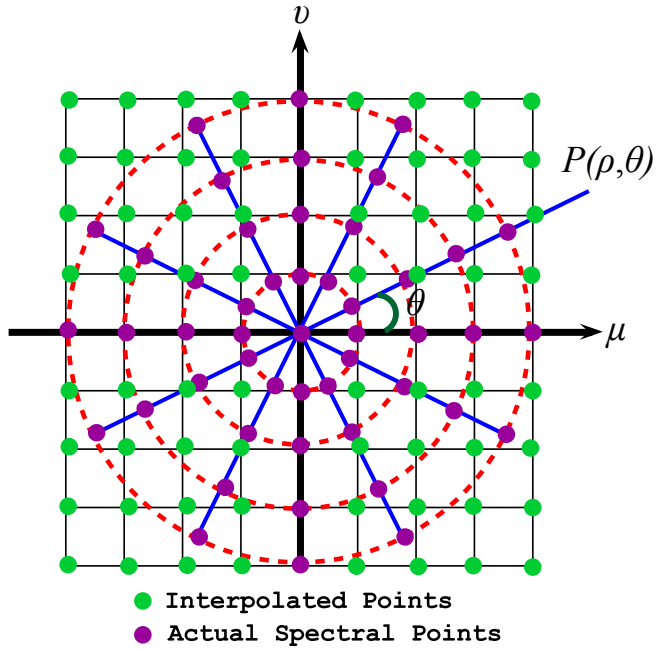


Figure 3.7: Samples in the μ, v domain and the interpolation to the Cartesian coordinates.

In addition, the discrete form of the Equation 3.20 can be represented as the following if $x, y \in (-G/2, G/2)$ and G is a constant

$$f(x, y) = \frac{1}{G^2} \sum_m \sum_n F\left(\frac{m}{G}, \frac{n}{G}\right) e^{i2\pi\left(\frac{mx}{G} + \frac{ny}{G}\right)}. \quad (3.21)$$

In practice, we can only get limited Fourier components, thus

$$f(x, y) \approx \frac{1}{G^2} \sum_{m=-N/2}^{N/2} \sum_{n=-N/2}^{N/2} F\left(\frac{m}{G}, \frac{n}{G}\right) e^{i2\pi\left(\frac{mx}{G} + \frac{ny}{G}\right)} \quad (3.22)$$

In order to apply the Equation 3.22 we must interpolate these radial points to the points on a square grid, i.e., Cartesian coordinates (Figure 3.7). N could be arbitrarily defined by an even

integer, and the spatial resolution in the reconstructed image is determined by the value of N . Theoretically, by providing as many values of $F(\mu, v)$ that are known on some radial lines (Figure 3.6), we can determine the N^2 coefficients that Equation 3.22 requires. Furthermore, the calculation involves solving a large set of simultaneous equations often leading to unstable solutions. It is more common to determine the values on the square grid using nearest neighbour or linear interpolations from the radial points. Since the density of the radial points becomes sparser as one gets farther away from the centre, the interpolation error also becomes larger. In addition, there is a greater error in the calculation of the high frequency components than the low frequency ones in an image, and the error results in some image degradation [138].

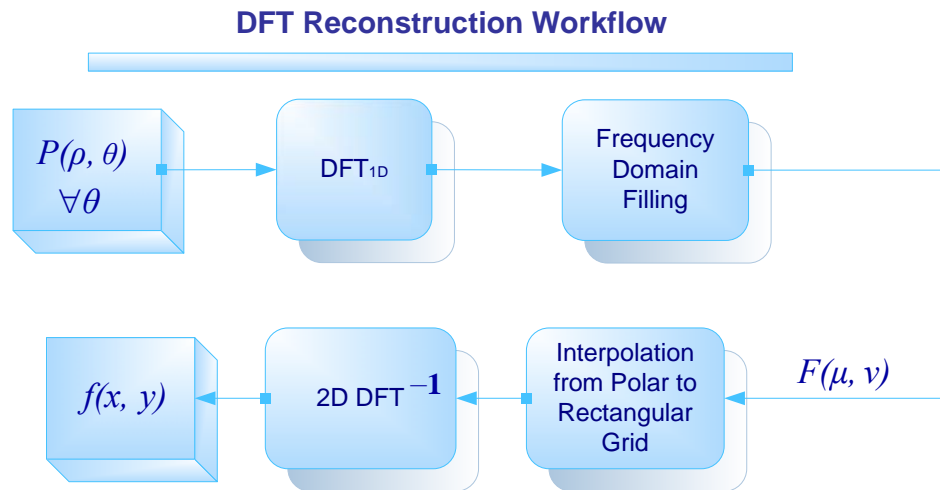


Figure 3.8: Flow chart of the DFT reconstruction procedure in 2D.

Furthermore, the Discrete Fourier Transform (DFT) and its inverse form can be represented as follows [126]

$$F(\mu, v) = \sum_{x=0}^{M-1} \sum_{y=0}^{N-1} f(x, y) e^{-i2\pi(\frac{\mu x}{M} + \frac{v y}{N})}, \quad (3.23)$$

and

$$f(x, y) = \frac{1}{MN} \sum_{\mu=0}^{M-1} \sum_{v=0}^{N-1} F(\mu, v) e^{i2\pi(\frac{\mu x}{M} + \frac{v y}{N})}, \quad (3.24)$$

and the flow chart of the DFT reconstruction procedure is illustrated in Figure 3.8.

Although the Fourier Slice Theorem provides a straightforward solution for tomographic reconstruction, it presents some challenges in actual implementation. Firstly, it produces samples in the Fourier domain, which is not coincident with Cartesian coordinates [121]. These samples have to be

interpolated or re-gridded to the Cartesian coordinates. Moreover, in the temporal domain, the interpolation error is localised to the small region where the pixel is located. However, each sample in a 2D Fourier space represents certain spatial frequencies both in the horizontal and vertical directions. Therefore, an interpolation of one sample affects the appearance of the entire image after the inverse Fourier transform, and the Fourier domain interpolation is highly sensitive. Another disadvantage of the direct Fourier space reconstruction is the difficulties of performing targeted reconstruction, which is used to exam fine details of a small region in the object [121]. Because there are some obvious drawbacks to the direct reconstruction from Fourier space, it is desirable to investigate alternative implementations of the Fourier slice theorem. The most widely used implementation is the *filtered backprojection algorithm*.

Furthermore, while backprojection is conceptually simple, it does not correctly solve the problem. A single point in the true image is reconstructed as a circular region that decreases in intensity from the centre. In other words, the point spread function of the backprojection is circularly symmetric, and it decreases as the reciprocal of its radius. Filtered backprojection is a technique to correct the blurring encountered in simple backprojection [268].

Figure 3.9 provides an intuitive description of the FBP algorithm, whereby each view is filtered before the backprojection to counteract the blurring effects. That is, each of the one-dimensional views is convolved with a one-dimensional filter kernel to create a set of filtered views. These filtered views are backprojected to provide the reconstructed image, which is a close approximation to the original image. Kak and Slaney [138] summarised the FBP algorithm as follows

- Sum for each of the K angles (assuming we have K forward projections) between 0 and 180 degrees to measure the projection $P(\rho, \theta)$;
- Fourier transform it to find $S_\theta(\omega)$;
- Multiply it by the weighting function $\frac{2\pi|\omega|}{K}$;
- Sum over the image plane the inverse Fourier transforms of the filtered projections, *i.e.*, the backprojection process.

Mathematically, we can prove that FBP can be represented by (Details in Appendix A)

$$f(x, y) = \frac{1}{2\pi^2} \int_0^\pi \int_{-\infty}^\infty \left[\frac{\partial P(\sigma, \theta)}{\partial \sigma} \right] \frac{1}{x \cos \theta + y \sin \theta - \sigma} d\sigma d\theta. \quad (3.25)$$

Many studies have been done on the selection of the filters in FBP algorithm. The filtering procedure can be applied in the temporal domain or the frequency domain. Some filters such as the Ram-Lak filer, the Shepp-Logan filter and low-pass cosine filters are widely used for the FBP

algorithm. In practice, we need to use the Fast Fourier Transform (FFT) to calculate the DFT. Furthermore, the discussion above is based on parallel projections, and the reconstruction algorithm can apply to the fan-beam or cone-beam geometry. Feldkamp et al. [72] solved an approximation of the FBP based on the 3D cone-beam geometry in 1984. However, the reconstruction results were too noisy to demonstrate the structure details visually.

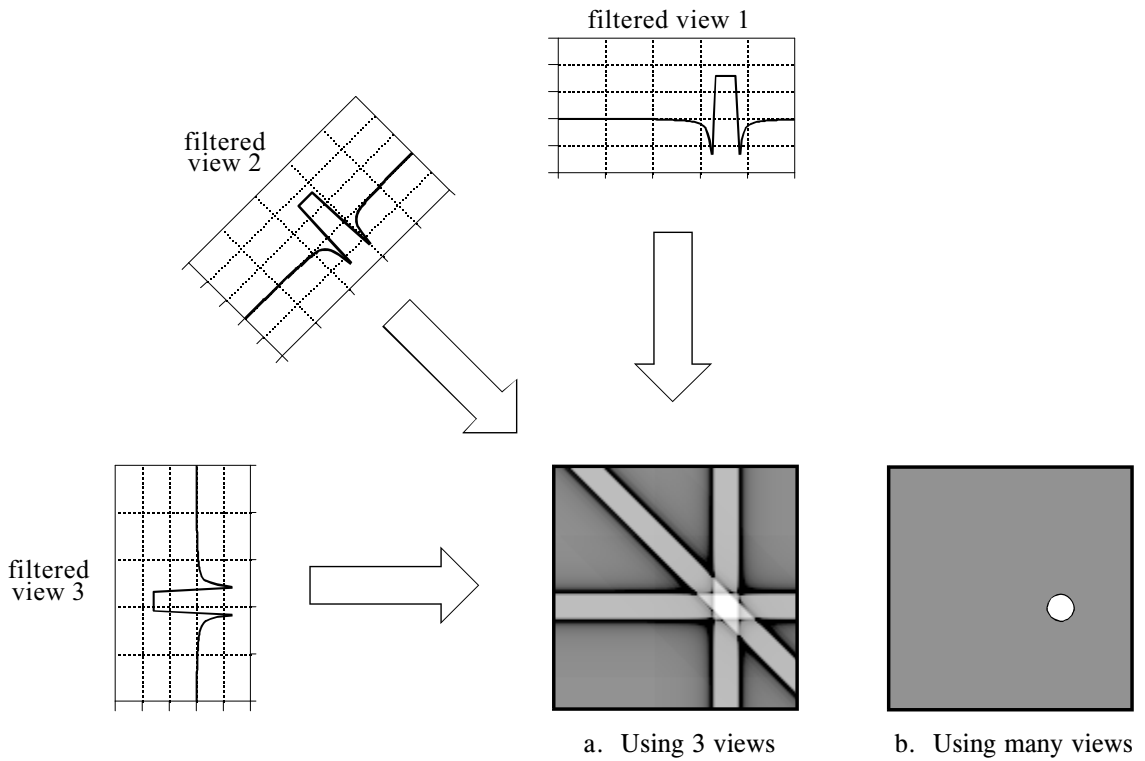


Figure 3.9: *Filtered backprojection reconstructs an image by filtering each view before backprojection. This removes the blurring effects in the simple backprojection, and the results in a mathematically exact reconstruction of the image. Filtered backprojection is the most commonly used algorithm for CT scanner.* [268]

Recent studies on FBP are mainly divided into two categories: new filters design and hardware acceleration, *e.g.*, field-programmable gate array (FPGA), graphics processing unit (GPU) and others. DeRose and Clack [56] proposed a shift-variant FBP method, which reconstructed cone-beam data. In 2003, Louis [182] reported a general approach to derive inversion formulae for 3D cone beam tomography, and tuned the filtering to reduce the data noise. Mertelmeier et al. [196] published a paper on the filter design for their FBP reconstruction of DBT. In [327], Xu and Mueller [326] suggested a GPU implementation of the FBP for CT reconstruction. Leeser et al. [167] conducted research into

an FPGA implementation for parallel-beam backprojection. Kachelrieß et al. [133] showed their work on a hyperfast parallel-beam and cone-beam backprojection using the cell general purpose hardware, which might be applicable for tomosynthesis and SPECT reconstruction. Recently, in [329] Yan et al. adopted GPU programming for high performance DTS reconstruction using commercial PC graphics hardware. Chen [41] carried out a comparative study on SAA, BP and FBP using DBT data sets (Figure 3.10).

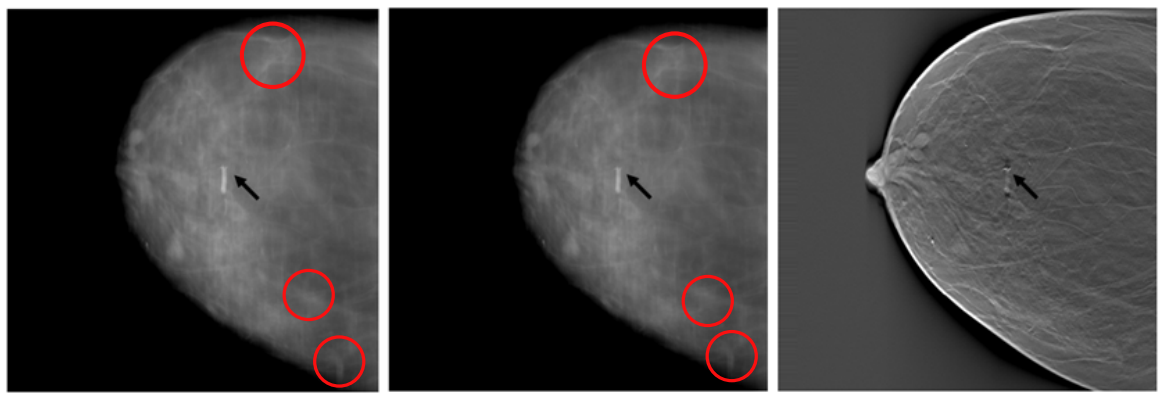


Figure 3.10: A human breast demonstrating a solitary calcification. Left: Traditional SAA. Middle: BP. Right: FBP (Hamming and Gaussian filters). The in-plane slices shown here are 7.5mm above the surface plate. There are some inter-plane artefacts shown in both SAA and BP reconstructions. These artefacts, which due to the interferences of features in other planes, form the suspicious masses (red circles) and they are eliminated using the FBP method. Results are collected from Chen's thesis [41]

In other methods based on transfer functions, particular impulse response functions or point spread functions are designed according to the imaging geometry and the application. When we employ the Fourier transform, the convolution process changes into simple multiplication. Therefore, inversion filtering or its matrix form is applied to reconstruct the whole volume in continuous function or discrete arrays, and to suppress the inter-plane blurring.

In the early 1990s, Matsuo et al. [190] proposed a reconstruction method that utilised a 3D convolution process with an inverse filter function. It was derived from the point spread function of the projection and backprojection geometry analytically. They also designed a digital photosynthesis system, which was adapted for both phantom experiments and clinical evaluations. Their system demonstrated superior reconstruction results with fewer artefacts from the outside of the focused plane. Many studies, *e.g.*, [24] [196], also obtained promising results for DBT reconstruction using inverse filtering approaches.

3.2.2 ART Based Iterative Methods

Iterative reconstruction methods provide alternative choices, and they include Algebraic Reconstruction Technique (ART, Kaczmarz method [134] [88] [109] [137] [67] [5] [132] [299] [150] [138]), Simultaneous Iterative Reconstruction Technique (SIRT) [85] [109] [108] [161] [123] [279], Simultaneous Algebraic Reconstruction Technique (SART) [6] [207] [131], Multiplicative Algebraic Reconstruction Technique (MART) [300] [36]. Moreover, Maximum-Likelihood Expectation Maximization (MLEM) and Ordered Subsets Expectation Maximization (OSEM) [107] [123] [323] have been employed and accompanied with reconstruction techniques. The maximum likelihood method is a general method of solving reconstruction problems, assuming any distribution of the errors; however, if errors are normally distributed then the maximum likelihood method is equivalent to least squares. Therefore, in this thesis, we only considered the simplified model that experimental errors follow a normal distribution and leave out more general discussion of maximum likelihood techniques. In addition, we provide a review of ART based reconstruction methods in this section and we will also survey the reconstruction method based on the least squares estimation in the next section.

3.2.2.1 Algebraic Reconstruction Technique (ART)

In order to clarify the principle of the ART, we superimposed a square grid on an image, *i.e.*, a target (Figure 3.11). Firstly, f_1 to f_n represent values of the cells on the square grid, and we need to reconstruct the values of the cells inside the target. Secondly, p_m describes a ray that goes through the target with a particular view angle. However, the *rays*, which are different from the rays in the transform-based method, are lines with a width of τ . In addition, the line integral is named as a *ray-sum* in the ART context [138], and p_m is the ray-sum measurement of the m -th ray. The relationship between f_n and p_m can be expressed as

$$\sum_{n=1}^N a_{mn} f_n = p_m, \quad (3.26)$$

in which $n = 1, 2, \dots, N$, $m = 1, 2, \dots, M$, and M is the total number of rays that go through the target at one angle of view. Furthermore, a_{mn} is defined as the weight of the each line with width τ

$$a_{mn} \text{ for this cell} = \frac{\text{Area of the black triangle}}{\delta^2}. \quad (3.27)$$

In other words, the a_{mn} is the weighting factor representing the contribution of the n -th cell

to the m -th line integral. Most of the values of a_{mn} are zero since only a small number of cells contribute to a given ray-sum.

If M and N are small, we could use conventional matrix theory to invert the system denoted by Equation 3.26. However, in practice N may be large as 65,536 for an image sized 256×256 , and the typical size of DBT is much larger. M is also of the same magnitude. Then the size of the a_{mn} matrix will be $65,536 \times 65,536$, which precludes any possibility of using direct matrix inversion. Furthermore, it costs about 512GB to save the full matrix; even though the matrix is sparse, it still needs huge storage to save the data.

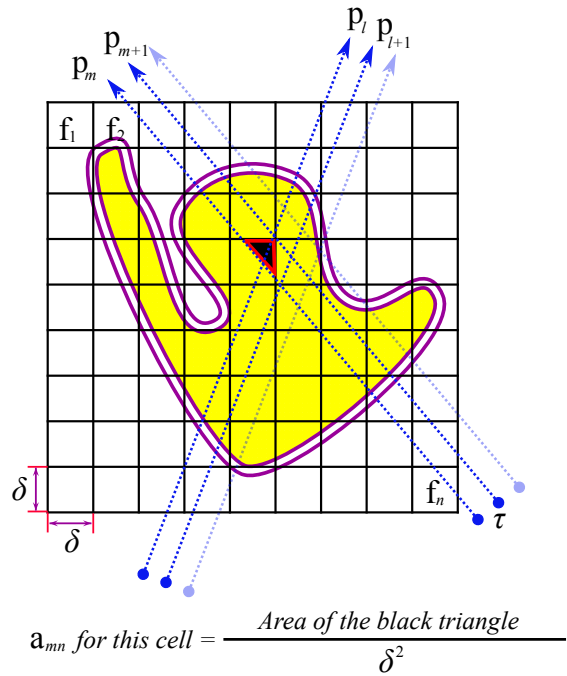


Figure 3.11: Square grid on the image.

For large values of M and N , there are attractive iterative methods for solving Equation 3.27. These iterative methods are based on the *vector resolute*, i.e., the *method of projections*, which was firstly proposed by Kaczmarz [134]. In addition, we can prove that the formula of ART is

$$f^k = f^{k-1} - \frac{f^{k-1} \cdot a_m - p_m}{a_m \cdot a_m} a_m, \quad (3.28)$$

in which $a_m = (a_{m1}, a_{m2}, \dots, a_{mN})$, and $a_m \cdot a_m$ is the inner product (or dot product/scalar product)

of the a_m with itself. Alternatively, the formula can be rewritten as

$$f_n^k = f_n^{k-1} + \frac{p_m - q_m}{\sum_{n=1}^N a_{mn}^2} a_{mn}, \quad (3.29)$$

in which

$$q_m = f^{k-1} \cdot a_m = \sum_{n=1}^N f_n^{k-1} a_{mn}. \quad (3.30)$$

The Equations 3.29 and 3.30 suggest that when we project the $(k-1)$ -th solution onto the k -th hyperplane, the gray level of the n -th element, whose current value is f_n^{k-1} , is obtained by correcting its current value by

$$\Delta f_n^{k-1} = f_n^k - f_n^{k-1} = \frac{p_m - q_m}{\sum_{n=1}^N a_{mn}^2} a_{mn}. \quad (3.31)$$

Note that while p_m is the measured ray-sum along the m -th ray, q_m is considered to be the computed ray-sum for the same ray based on the $(k-1)$ -th solution for the image gray levels. The correction Δf_n of the n -th cell is obtained by calculating the difference between the measured ray-sum and the computed ray-sum. In addition, it normalises the difference by $\sum_{n=1}^N a_{mn}^2$. Next, we assign this value to all the image cells in the m -th ray, and each assignment is weighted by the corresponding a_{mn} [138].

3.2.2.2 Simultaneous Iterative Reconstruction Technique (SIRT)

According to the Equations 3.29 and 3.31, the ART method can be generally expressed as

$$f_n^k = f_n^{k-1} + \lambda \Delta f_n^{k-1}, \quad (3.32)$$

which can be expanded as

$$\begin{aligned} f_n^k &= f_n^{k-1} + \lambda \Delta f_n^{k-1} \\ &= f_n^{k-1} + \lambda \frac{p_m - \sum_{n=1}^N f_n^{k-1} a_{mn}}{\sum_{n=1}^N a_{mn}^2} a_{mn}. \end{aligned} \quad (3.33)$$

The λ is an ad hoc *relaxation factor*, which is used to limit large model *perturbations*, and m is the iteration number. This type of additive ART method is named Simultaneous Iterative ART

(S-ART). Similarly, the Multiplicative ART (M-ART) can be formulated as

$$f_n^k = f_n^{k-1} \left(\frac{p_m}{\sum_{n=1}^N f_n^{k-1} a_{mn}} \right)^{\lambda a_{mn}}. \quad (3.34)$$

Instead of updating the n -th cell using the m -th equation information (each row of the matrix a consist of a_{mn}) in the ART, SIRT method goes through all the equations and then updates the n -th cell at the end of each iteration. This update for the n -th cell is the average value of all the computed changes for that cell. Furthermore, the SIRT approach, which possesses the expense of slower convergence, usually leads to better reconstructions than those produced by the ART. The SIRT method is expressed as

$$f_n^k = f_n^{k-1} + \lambda \frac{1}{M_n} \sum_{m=1}^M \Delta f_n^{k-1}. \quad (3.35)$$

It can be expanded as

$$\begin{aligned} f_n^k &= f_n^{k-1} + \lambda \frac{1}{M_n} \sum_{m=1}^M \Delta f_n^{k-1} \\ &= f_n^{k-1} + \lambda \frac{1}{M_n} \sum_{m=1}^M \frac{p_m - \sum_{n=1}^N f_n^{k-1} a_{mn}}{\sum_{n=1}^N a_{mn}^2} a_{mn}, \end{aligned} \quad (3.36)$$

in which M represents that the projection data can be assembled into an M -dimensional column vector p , with the element of p_m , and $m = 1, 2, \dots, M$ in the Equation 3.26. In addition, M_n is the number of non-zero elements in the column vector a_n . McGaughey and Young [191] made a conclusion that SIRT generally outperformed ART in providing a match between model and data by the study of the model estimation as a function of iteration number. They also indicated that ART was comparable to SIRT with very low relaxation factors. However, ART was found inferior to the initial backprojection at high relaxation factors, *e.g.*, $\lambda \approx 0.1$. Thus, SIRT would be favoured over ART if an iterative inversion scheme were warranted for an application. Furthermore, the update was performed after all projection views were processed in SIRT, which could improve the reconstruction results. In [25] Bleuet et al. attempted to use an iterative algebraic reconstruction method for linear tomosynthesis reconstruction with the adapted fan volume sampling scheme, with the X-ray source moving along a finite straight line. The quality of their reconstructed object was conserved while the computation time was considerably reduced without any parallelisation of the algorithm. Wang et al. [309] proposed a fast and memory-saving ART method for DTS reconstruction, which performed a one step ART iterative reconstruction than two step reconstruction and deblurring

processes. The weight matrix of ART was calculated offline, and it was saved in a look-up-table to accelerate the reconstruction. In addition, a Bessel-Kaiser function was applied as the pixel basis function to improve the reconstruction quality, and the simulation showed that their ART implementation obtained accurate 3D reconstruction results. Zhang et al. [344] mentioned that ART had fast convergence speed since only a single projection value was used to update the linear attenuation coefficients at a time. However, it converged to a least squares solution, which could be very noisy for severely ill-posed inverse problems, *e.g.*, limited-angle DBT reconstruction.

3.2.2.3 Simultaneous Algebraic Reconstruction Technique (SART)

SART, which combines the best of ART and SIRT, produces a superior reconstruction result with a fast convergence. The general SART is expressed as

$$f_n^k = f_n^{k-1} + \lambda \frac{\sum_{m=1}^M \Delta f_n^{k-1}}{\sum_{m=1}^M a_{mn}}, \quad (3.37)$$

which can be expanded as

$$\begin{aligned} f_n^k &= f_n^{k-1} + \lambda \frac{\sum_{m=1}^M \Delta f_n^{k-1}}{\sum_{m=1}^M a_{mn}} \\ &= f_n^{k-1} + \lambda \frac{\sum_{m=1}^M \left(\frac{p_m - \sum_{n=1}^N f_n^{k-1} a_{mn}}{\sum_{n=1}^N a_{mn}^2} \right) a_{mn}}{\sum_{m=1}^M a_{mn}}. \end{aligned} \quad (3.38)$$

In 2006, Zhang et al. [344] [345] published some work on limited-angle cone-beam DBT reconstruction. They compared the BP method, the SART algorithm, and the maximum likelihood method using phantoms to evaluate the image quality and reconstruction artefacts. All the experiments were performed on the second-generation GE DBT prototype system. The system possessed a stationary CsI phosphor/a:Si active matrix flat panel digital detector with a pixel size of 0.1 mm by 0.1 mm. In addition, there were 21 projections acquired over $\pm 30^\circ$ in less than 8secs. The voltage ranged from 26kVp to 33kVp, and the total mAs of the various views ranged from 44mAs to 150mAs. The system used an Rh-target/Rh-filter X-ray source at 29kV with no anti-scatter grid, and the AGD was about 250mrad. The predefined test volume was 14cm by 23cm in area and 5cm in thickness, and the out-of-plane resolution was set to 1mm. They employed the Contrast-to-Noise Ratio (CNR), the line profile of features, the Artefact Spread Function (ASF), the Noise Power Spectrum (NPS), and the Line Object Spread Function (LOSF) to evaluate the contrast, sharpness, and artefacts quantitatively. They found that the BP method resulted in less noisy tomosynthesis images and

higher CNR values for masses than the SART. However, the two iterative methods provided greater contrast enhancement for masses and calcifications and sharper LOSF. In addition, they reduced inter-plane blurring and artefacts with better ASF behaviours for masses. Furthermore, the BP method obtained strong blurring artefacts along the X-ray source motion direction and it obscured the contrast-detail objects. The SART method could remove the superimposed breast structures and significantly improved specificity of the object with BP results as initialisation.

Van de Sompel and Brady [295] reported a SART reconstruction on basic ellipsoids in 2D and MR-derived breast phantom in 3D initialized by three different initial guesses, namely Unfiltered Backprojection (UBP), Filtered Backprojection (FBP), and the Zero Image (ZI). Chan [38] summarised the Computer-Aided Diagnosis (CAD) in breast tomosynthesis and chest CT and compared conventional mammography with the SART reconstruction of DBT at the 1mm slice intervals.

3.2.3 Least Squares Estimation

Many studies into DBT reconstruction show that the ART-based iterative methods present many advantages over transform-based methods; however, these iterative algorithms may not be ideally suitable for the DBT reconstruction. In principle, these iterative algorithms are seemly designed for reconstructing complete and noisy projection data sets, *e.g.*, in many medical imaging applications like CT, the forward projection data, which are fully sampled and noisy, can be *exactly inverted* in theory, and these iterative algorithms are also able to remove the additive noise. Conversely, tomosynthesis systems obtain projection data with low noise [261], but they are highly incomplete. Therefore, many various attenuation distributions should be compatible to the observed forward projections, and ART-based iterative algorithms make little effort in this situation.

3.2.3.1 Least Squares Approximation

Consider the problem of reconstructing an unknown image f from noisy data p satisfying,

$$p = Af + \epsilon, \quad (3.39)$$

where $A \in \mathbb{R}^{m \times n}$ describes the forward projection process with noise ϵ . Here A is also known as the system matrix or forward projection matrix, and Equation 3.39 expresses the fundamental forward problem.

Apply a least-squares based unconstrained minimisation approach for the estimate f ,

$$\begin{aligned} f^* &= \arg \min_f \left(f(f) = \frac{1}{2} \|Af - p\|^2 \right) \\ &= \arg \min_f \left(\frac{1}{2} (Af - p)^T (Af - p) = \frac{1}{2} (f^T A^T - p^T)(Af - p) \right) \\ &= \arg \min_f \left(\frac{1}{2} (f^T A^T Af - f^T A^T p - p^T Af + p^T p) \right), \end{aligned} \quad (3.40)$$

in which $\|\cdot\|^2$ denotes the Euclidean norm that is the L^2 -norm.

p^T and Af are vectors and the dot product is commutative, and $p^T Af = p^T(Af)$ according to matrix associative law, we can simply prove there always holds the equivalent of $f^T A^T p \equiv p^T Af$; therefore, Equation 3.40 is rewritten as follows,

$$\begin{aligned} f^* &= \arg \min_f \left(f(f) = \frac{1}{2} (f^T A^T Af - f^T A^T p - p^T Af + p^T p) \right) \\ &= \arg \min_f \left(\frac{1}{2} (f^T A^T Af - 2f^T A^T p + p^T p) \right). \end{aligned} \quad (3.41)$$

The gradient $g(f)$ of the objective function in Equation 3.41 is derived as below.

$$g(f) = \frac{\partial f(f)}{\partial f} = A^T Af - A^T p. \quad (3.42)$$

According to the first-order necessary conditions (as seen in Appendix B), we can equate the gradient of the objective function to zero, *i.e.*, $A^T Af - A^T p = 0$. Therefore, the minimum norm solution f^* is

$$f^* = (A^T A)^{-1} A^T p = A^\dagger p \quad (3.43)$$

in which $A^\dagger = (A^T A)^{-1} A^T$ is the Moore-Penrose pseudo-inverse. In addition, A^\dagger is equivalent to the proper inverse of matrix A if it is square and non-singular, *i.e.*, it is invertible; however, we can always construct the pseudo-inverse regardless if A is not square and/or rank-deficient.

Furthermore, we can define any linear operator using the singular value decomposition (SVD). Therefore, any matrix A can be written as a product

$$A = U \Sigma V^T, \quad (3.44)$$

where the columns of U and V are orthonormal, and the number of non-zeros in the diagonal part of Σ is equal to the rank r of the matrix A . Thus, if A is square and full-rank, we can rewrite f^* using SVD as follows

$$f^* = A^{-1}p \quad (3.45)$$

$$= V\Sigma^{-1}U^T p \quad (3.46)$$

$$= \sum_{i=1}^r \frac{\mathbf{u}_i \cdot p}{\varsigma_i} \mathbf{v}_i, \quad (3.47)$$

in which A^{-1} is the proper inverse of matrix A , and \mathbf{u}_i , ς_i , and \mathbf{v}_i are the column vectors of matrix U , Σ , and V . In addition, the pseudo-inverse A^\dagger can be expressed by

$$A^\dagger = U\Sigma^\dagger V^T = \sum_{i=1}^r \frac{\mathbf{v}_i \mathbf{u}_i^T}{\varsigma_i}. \quad (3.48)$$

Regularisation, which was inspired from filtering the contribution of the singular vectors in the inverse, yields operator approximations to the SVD of the pseudo-inverse. For example,

$$A_\lambda^\dagger = V\Sigma_\lambda^\dagger U^T \quad (3.49)$$

$$= \sum_{i=1}^{\lambda} \frac{\mathbf{v}_i \mathbf{u}_i^T}{\varsigma_i} \approx V\Sigma^\dagger U^T \quad (3.50)$$

in which Σ_λ^\dagger is

$$\Sigma_\lambda^\dagger = \begin{cases} 1/\varsigma_i & \text{if } \varsigma_i > \lambda \\ 0 & \text{otherwise} \end{cases} \quad (3.51)$$

and λ is a small threshold. This is also known as truncated SVD (TSVD), in which only the λ column vectors of U and λ row vectors of V^T corresponding to the λ largest singular values Σ^\dagger are calculated, and the rest of the matrix is discarded. Therefore, the filter in TSVD method is

$$q_\lambda(\varsigma_i^2) = \begin{cases} 1 & \text{if } \varsigma_i > \lambda \\ 0 & \text{otherwise} \end{cases} \quad (3.52)$$

We also define the condition number $\kappa(A)$ of the matrix A as follows

$$\kappa(A) := \frac{\varsigma_{max}(A)}{\varsigma_{min}(A)}, \quad (3.53)$$

where $\kappa(A)$ measures the sensitivity of $A^\dagger p$ to perturbations in p and A , and for large $\kappa(A)$ (above a few thousand) A is called ill-conditioned which is the case for most of the real applications. Small errors in the data Δp can be magnified by small singular values ς_i (as seen in Appendix C).

Another filter we can apply is

$$q_\lambda(\varsigma_i^2) = \frac{\varsigma_i^2}{\varsigma_i^2 + \lambda}, \quad (3.54)$$

which is known as Tikhonov filtering, and the corresponding regularised inverse is

$$A_\lambda^\dagger = (A^T A + \lambda I)^{-1} A^T. \quad (3.55)$$

It is usually impractical to construct the SVD explicitly for a large system; however, we can obtain the solution using a variational form as follows

$$f_\lambda^* = A_\lambda^\dagger p = (A^T A + \lambda I)^{-1} A^T p, \quad (3.56)$$

and we can also address the problem as an unconstrained optimisation process, that is

$$f_\lambda^* = \arg \min_{f \in \mathbb{R}^n} \left(f(f) = \frac{1}{2} \|Af - p\|^2 + \lambda \|f\|^2 \right). \quad (3.57)$$

More generally we can consider an optimisation problem with

$$f_\lambda^* = \arg \min_{f \in \mathbb{R}^n} \left(f(f) = \mathcal{D}(Af, p) + \lambda \mathcal{R}(f) \right), \quad (3.58)$$

in which \mathcal{D} and \mathcal{R} can be any data discrepancy and regularisation functionals based on a L^1 -norm, a L^2 -norm, a L^p -norm, or a statistical measurement, and λ is the regularisation parameter or damping factor.

In particular, when

$$\mathcal{R}(f) = \frac{1}{2} \|f\|^2, \quad (3.59)$$

it is called Tikhonov (Tychonov) regularisation, which can be any quadratic functional

$$\mathcal{R}(f) = \frac{1}{2} \|f\|_\Gamma^2 = \frac{1}{2} f^T \Gamma f, \quad (3.60)$$

where Γ is a matrix. We can consider using the derivative of f in order to impose a penalty on the

oscillations in the solution, rather than use f to penalise only the magnitude of the solution, that is

$$\mathcal{R}(f) = \frac{1}{2} \|f'\|^2, \quad (3.61)$$

or in discrete form

$$\mathcal{R}(f) = \frac{1}{2} \|Df\|^2 = \frac{1}{2} f^T D^T D f, \quad (3.62)$$

in which D is a finite difference matrix implementing the derivative f' of f .

One of the drawbacks of using a Tikhonov regularisation is the fast quadratic growth of the penalty term, which leads to an undesirable solution. Total variation, which is based on the L^1 -norm, is an alternative penalty functional

$$\mathcal{R}(f) = |f'|, \quad (3.63)$$

and we can implement this in the discrete setting as follows

$$\mathcal{R}(f) = |Df| = \sum_{n=1}^{N-1} |f_{n+1} - f_n|. \quad (3.64)$$

Although iterative reconstruction methods tend to handle noise better than analytical methods such as FBP, the reconstruction process itself can amplify the noise gradually [256] even though tomosynthesis projection data possess low noise. Therefore, the merit of total variation regularisation is that it can suppress the noise in the reconstruction with sharp edges, but there is no direct matrix inversion as in Equation 3.56.

3.2.3.2 Numerical Optimisation

Optimisation is ubiquitous, and it has been used in many areas including engineering, economics, operations research, and others. Essentially, the numerical optimisation is a mathematical problem identifying optimum or optima, which may be expressed in calculus-based formulas. There are plenty of choices of numerical optimisation schemes, which includes line search methods, trust-region based methods, gradient (steepest) descent method, conjugate gradient methods, Levenberg-Marquardt algorithm, Gauss-Newton algorithm, quasi-Newton methods, the simplex method, and other variants of existing methods. A thorough investigation on numerical optimisation algorithms [21] [304] [30] [217] showed that the conjugate gradient method, quasi-Newton method and trust-region types of methods are suitable for solving the large-scale reconstruction problem in Equation 3.56. However,

line search method, steepest descent method, and Nelder-Mead method are suitable for small-scale or medium-scale reconstruction problems.

We emphasise the conjugate gradient method and quasi-Newton method in this thesis. The performance of the linear conjugate gradient method is determined by the distribution of the eigenvalues of the coefficient matrix. By transforming, or preconditioning the linear system, we can make this distribution more favourable and improve the convergence of the method significantly. The linear conjugate gradient method was proposed by Hestenes and Stiefel in the 1950s [110]. It is an iterative method, which was motivated by the alternative to Gaussian elimination that was well suited for solving large problems. In addition, Fletcher and Reeves [78] introduced the first nonlinear conjugate gradient method in 1964. It was one of the earliest known techniques for solving large-scale nonlinear optimisation problems. Over the years, many variants of this original scheme were proposed, and some were widely used in practice. The key features of these algorithms were that they required no matrix storage, and they were faster than the steepest descent method [217]. Vogel [304] has shown that for extremely large and highly structured linear systems, the conjugate gradient method provided a very efficient solution. In addition, the conjugate gradient method could also be adapted to solve non-quadratic optimisation problems, and a general non-linear conjugate gradient algorithm is summarised in Appendix D.

Furthermore, the motivation to develop the quasi-Newton method was the attempt of solving a long optimisation calculation in the mid 1950s. The quasi-Newton method is one of the most creative ideas in nonlinear optimisation [217]. Similar to Newton's methods and the steepest descent method, the optimisation is supplied with the *gradient information* of the objective function as the guidance of the searching direction. The advantages of the quasi-Newton method are: firstly, it possesses rapid *superlinear convergence*; secondly, it is designed to prevent the calculation of the Hessian matrix or its inverse at each iteration that happens in other Newtons methods; thirdly, due to the efficiency of the quasi-Newton, it makes the development and solution of the *large-scale optimisation problems* became reality. Thus, the core of the quasi-Newton theory is the approximation of the inverse Hessian matrix. The most popular approximation methods used in quasi-Newton algorithms are DFP and BFGS methods (Appendix D), named using the acronymic combinations of the scientists' names: Davidon-Fletcher-Powell and Broyden-Fletcher-Goldfarb-Shanno. In addition, the limited-memory quasi-Newton methods use a few vectors instead of manipulating fully dense approximation of the inverse Hessian matrix. There are various limited-memory methods, and the one based on BFGS is named L-BFGS. Based on the description of the BFGS method, the L-BFGS method, which has been used in our application, is outlined as follows.

The objective of BFGS method is to find an appropriate approximation for the inverse Hessian matrix, that is

$$H_{k+1} = V_k^T H_k V_k + \alpha_k s_k s_k^T, \quad (3.65)$$

in which

$$\alpha_k = \frac{1}{z_k^T s_k}, \quad V_k = I - \alpha z_k s_k^T, \quad (3.66)$$

and

$$s_k = f_{k+1} - f_k, \quad z_k = g(f_{k+1}) - g(f_k). \quad (3.67)$$

In addition, the updating at k -th iteration can be formulated using

$$\begin{aligned} H_{k+1} = & V_k^T V_{k-1}^T \cdots V_0^T H_{\text{initial}} V_0 \cdots V_{k-1} V_k \\ & + V_k^T \cdots V_1^T \alpha_0 s_0 s_0^T V_1 \cdots V_k \\ & \vdots \\ & + V_k^T V_{k-1}^T \alpha_{k-2} s_{k-2} s_{k-2}^T V_{k-1} V_k \\ & + V_k^T \alpha_{k-1} s_{k-1} s_{k-1}^T V_k \\ & + \alpha_k s_k s_k^T \end{aligned} \quad (3.68)$$

In order to circumvent storing all these vector pairs of $\{s_k, z_k\}$, L-BFGS method only use information from last m iterations that is

$$\begin{aligned} H_{k+1} = & V_k^T V_{k-1}^T \cdots V_{k-\hat{m}}^T H_{\text{initial}} V_{k-\hat{m}} \cdots V_{k-1} V_k \\ & + V_k^T \cdots V_{k-\hat{m}+1}^T \alpha_{k-\hat{m}} s_{k-\hat{m}} s_{k-\hat{m}}^T V_{k-\hat{m}+1} \cdots V_k \\ & \vdots \\ & + \alpha_k s_k s_k^T \end{aligned} \quad (3.69)$$

where m is defined by the user according to empirical. In addition, a typical value $3 \leq m \leq 20$ could produce satisfactory results, and $\hat{m} = \min\{k, m-1\}$. Therefore, when $k > m$ we can discard the vector pair $\{s_{k-m}, z_{k-m}\}$ from storage that is the main difference between L-BFGS and its parent form BFGS.

3.3 Conclusions and Discussion

In this chapter, we have surveyed various classical and novel reconstruction methods, which can be applied to reconstruct DBT volumes with particular geometric setup. The reconstruction algorithms can be coarsely divided into two categories, namely analytical and iterative methods.

SAA and BP are straightforward reconstruction algorithms, which mathematically line up the in-focus structures along the X-ray tube motion direction. SAA and BP can reconstruct mass clearly but with serious blurry artefacts, especially for the edges of the mass. FBP is based on the traditional SAA algorithm, which obtains breast structures with deblurring techniques. However, the FBP method is always restricted by the imaging geometry, and the reconstruction efficacy depends on the filter design for limited angle DBT reconstruction problem with highly incomplete sampled spatial frequency domain. FBP contains an inverse filtering procedure for the forward projected images including sampling density information in the frequency domain, and back projects the filtered images to the spatial domain to create the reconstructed slice. Compared to SAA and BP algorithms, FBP suppresses out-of-plane blurring with a comparatively fast reconstruction. FBP is superior for reconstruction of low frequency contents. In addition, it possesses a fast reconstruction, which is feasible for clinical usage, and currently most industrial vendors use FBP to reconstruct DBT volumes.

Iterative methods based on ART technique show their promise in reconstructing DBT volumes, and they are not limited by the imaging geometry. In many studies, SART is favoured for DBT reconstruction because this block-action strategy has a moderate trade-off between ART and SIRT. In the traditional ART method, the measurement noise is considerably amplified due to the continual updating and the intrinsic ill-posed property of this kind of inverse problem. In contrast, the convergence speed is relatively slow using SIRT reconstruction, which averages over all the rays in all projections, and the reconstructed results are always over smoothed. Least squares estimation with proper numerical optimisation provides an alternative way of performing iterative reconstruction. ART based methods are suitable to reconstruct complete and noisy data sets like fully sampled CT projection data with noise; however, DBT systems produce highly incomplete projections with low noise. Therefore, least squares estimation based algorithms outperform ART based methods for DBT reconstruction in theory. However, in real applications, regularisation is necessary when the data are not ideal. Many regularisation schemes are well studied in CT, PET and optical tomography reconstructions, and various Total Variation like (TV-like) regularisation methods [143] [260] [261] are proposed for DBT reconstruction. Furthermore, there is a trade-off between the data fidelity and

the regularisation terms, which are represented by data error and image regularity metric respectively (as seen in Figure 3.12). When the regularisation is small, the reconstruction is close to the available data but may contain evident artefacts because of the noisy or inconsistent data, whereas large regularisation term outputs smooth images at the expense of fidelity to the data.

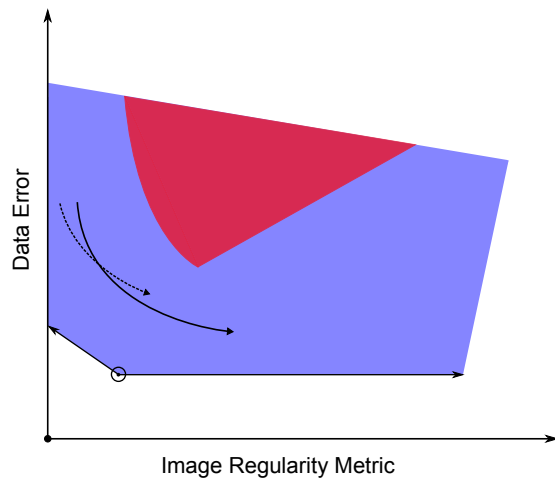


Figure 3.12: *Diagram of the trade-off between the data fidelity and the regularisation terms represented by data error and image regularity metric respectively. The plot shows the fidelity and regularity plane for an undersampled (blue area) versus a completely sampled tomographic system (red area). For completely sampled systems, a unique image minimises the data error because only one value of the regularity is possible, whereas many possible candidate volumes correspond to the situation of minimum data error for undersampled systems. The two curves represent a generic behaviour of standard iterative algorithms for the case of no regularisation (solid curve) and with regularisation (dashed curve).*

In summary, compared to the analytical methods, the iterative methods are conceptually simple with milder assumptions for the missing data, but always converge slowly and may be trapped by local minima. On the contrary, FBP method presents fast reconstruction, but the filter design, parameters tuning are complicated. In our DBT registration and reconstruction framework, we develop a least squares based approach, which is simple to combine with existing numerical optimisation techniques, and it could also incorporate different image constraints and various regularisation schemes.

Image Registration and Its Applications in DBT

Registration is a major field of research in medical image processing. It searches for the best geometrical transformation mapping points from one image to the corresponding points in another image [19]. Intra-subject registration maximises correspondences of two or more images, which are acquired using various imaging modalities or at different time points, from the same subject. Whereas, inter-subject registration aim to align images of multiple subjects in order to perform population-based studies on the anatomical variability.

Medical image registration has been used in many clinical and research applications [33] [70] [277] [185] [169] [18] [116] [348] [223] [292], *e.g.*, image registration can eliminate the effect of patient position and motion artefacts. Thus, it is often used throughout the imaging, screening and treatment process to capture, visualise and quantitatively analyse the development of disease.

There are several significant concepts, which must be considered when developing image registration algorithms. These include image interpolation, the transformation model used, similarity metric or distance measurement, optimisation, and validation. Firstly, the image processing algorithms often utilise image interpolation. Particularly, in image registration, interpolation contributes in data preparation, image resampling, and transformations. Secondly, the transformation model, including rigid, affine and deformable transforms, parameterises the geometrical deformation field. Distance measurement provides the metric of similarity between the images, and is the registration basis. Many criteria are proposed as the basis of aligning two images, and a common classification is as landmark-based, segmentation-based or intensity-based registration [311] [281]. Next, the registration process can be viewed as an optimisation problem, and the goal is to minimise an associated objective function modelled by the distance measurement. Finally, the validation evaluates the accuracy, robustness, and clinical utility of the registration results. However, the evaluation is difficult because the correct transformation, *i.e.*, the ground truth, is usually unknown in a real application.

4.1 Forward Problem: Warping

4.1.1 Image Interpolation

Medical image registration, especially breast image registration using mammography or DBT reconstructions, seeks align images before their subtraction, for example, in order to find where and how they differ. To reveal this alignment from the observed images is an inverse problem, and the forward problem is the image warping between these images. Image warping, which implies a particular transformation model computed during registration, can be validated via comparison with a known a ground truth. However, in real applications, as a result of different conditions of acquisition, *e.g.*, various imaging modalities and temporal variances, normally we have no ground truth.

Interpolation plays an important role in registration. Firstly, it determines the accuracy of my transformation model, which is essential in the simulation process of the forward problem and in the recovery steps of the inverse problem. For example, a deficient interpolation can create degenerate simulations and corrupt the unprocessed raw data (processed mammogram data is ready for display) [291]. Secondly, an ideal interpolator must be self-consistent, differentiable, and short in spatial extent. Therefore, a good quality approximation of the ideal interpolator can ease the optimisation procedure of the registration. In addition, we can apply multi-scale and multi-resolution methods to avoid local minima. In these methods, we use appropriate interpolation to obtain downsampled and smoothed images in a pyramid model and step back to the original scale with full resolution as the registration proceeds.

Essentially, the interpolation represents a continuously defined function using the summation of discrete weighted and shifted basis functions [291]. It is equivalent to a low-pass filtering process. In addition, a more generalised interpolation consists of an extra prefiltering step, which allows us to use many potential basis functions. One definition of interpolation is

$$\mathcal{I}(x) = \sum_{k \in \mathbb{Z}^n} f_k \varphi_{\text{int}}(x - k) \quad \forall x = (x_1, x_2, \dots, x_n \in \mathbb{R}^n), \quad (4.1)$$

in which $\mathcal{I}(x)$ is an interpolated value at coordinate x in n dimensional space. Furthermore, $\mathcal{I}(x)$ is equal to the linear combination of samples f_k at integer coordinates $k = (k_1, k_2, \dots, k_n) \in \mathbb{Z}^n$. From signal processing theory, the perfect recovery of signal $\mathcal{I}(x)$ only occurs when $\mathcal{I}(x)$ is band-limited and its sampling rate satisfies Nyquist-Shannon theorem to avoid aliasing [291]. In addition, the *sinc* function, which vanishes at all integers except at the origin, can be used as an ideal basis function,

i.e., φ_{int} , to obtain the exact interpolation. However, in real applications, image signals are not exactly band-limited, *sinc* interpolation requires infinite samples, and is computationally expensive. Therefore, we seek an appropriate approximation to the ideal *sinc* interpolation.

Many interpolation schemes have been proposed in previous studies, *e.g.*, nearest neighbour, linear, polynomial, and spline-based interpolation. Nearest neighbour and linear interpolation are described respectively by

$$\varphi^0(x) = \begin{cases} 1, & \text{for } -\frac{1}{2} \leq x < \frac{1}{2}, \\ 0, & \text{otherwise} \end{cases}, \quad (4.2)$$

$$\varphi^1(x) = \begin{cases} 1 - |x|, & \text{for } |x| < 1 \\ 0, & \text{otherwise} \end{cases}. \quad (4.3)$$

Interpolation that is more complex can be modelled using polynomials and splines. For example, the cubic polynomial interpolation kernel is

$$\varphi^3(x) = \begin{cases} 1 - \frac{5}{2}|x|^2 + \frac{3}{2}|x|^3, & \text{for } |x| \leq 1 \\ 2 - 4|x| + \frac{5}{2}|x|^2 - \frac{1}{2}|x|^3, & \text{for } 1 < |x| < 2 \\ 0, & \text{otherwise} \end{cases}. \quad (4.4)$$

Furthermore, spines are piecewise polynomials, which are smoothly connected by joining points, *i.e.*, knots. In [203] Mitchell and Netravali formulated the spline family using a 2-parameters model. The cubic interpolation spline family (φ_F) are defined by various ϱ_1 and ϱ_2 :

$$\varphi_F^3(x) = \frac{1}{6} \begin{cases} (12 - 9\varrho_1 - 6\varrho_2)|x|^3 + (-18 + 12\varrho_1 + 6\varrho_2)x^2 \\ \quad + (6 - 2\varrho_1), & \text{for } |x| \leq 1 \\ (-\varrho_1 - 6\varrho_2)|x|^3 + (6\varrho_1 + 30\varrho_2)x^2 \\ \quad + (-12\varrho_1 - 48\varrho_2)|x| + (8\varrho_1 + 24\varrho_2), & \text{for } 1 < |x| < 2 \\ 0, & \text{otherwise} \end{cases}, \quad (4.5)$$

$$\varphi_F^3(x) := \begin{cases} \text{Cubic B-spline,} & \varrho_1 = 1, \varrho_2 = 0 \\ \text{Duff?''s Tensioned B-splines,} & \varrho_1 > 0, \varrho_2 = 0 \\ \text{Catmull-Rom Spline,} & \varrho_1 = 0, \varrho_2 = 0.5 \\ \text{Cardinal Splines,} & \varrho_1 = 0, \varrho_2 < 0 \end{cases}. \quad (4.6)$$

The B-spline, which is short for basis spline, has minimum support at a certain order of degree, *i.e.*, the B-spline has non-zero values for the minimum range of abscissa [247]. Specifically, the B-spline kernel β^n of order n is the n -fold convolution of the B-spline of order 1, *i.e.*,

$$\beta^n = \beta_1 \otimes \beta_{n-1}, \quad (4.7)$$

in which

$$\beta^0(x) = \begin{cases} 1, & \text{for } |x| < \frac{1}{2} \\ \frac{1}{2}, & \text{for } |x| = \frac{1}{2} \\ 0, & \text{otherwise} \end{cases}. \quad (4.8)$$

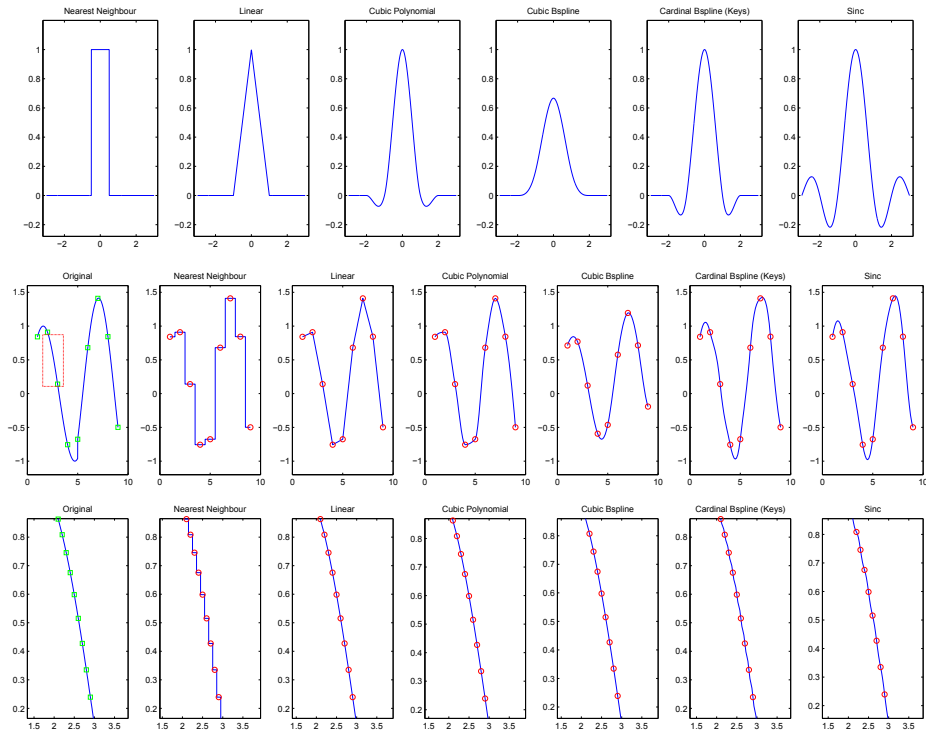


Figure 4.1: Interpolation examples using a 1D signal. First row: Various interpolation kernels; Second row: Coarse interpolation using samples (green square) on the original signal; Third row: Fine interpolation using more samples (zoomed in area of the red box).

Compare with Equation 4.2, $\beta^0(x)$ is almost identical to the $\varphi^0(x)$ except $\beta^0(x)$ is symmetrical. In addition, $\beta^1(x)$ is the same as $\varphi^1(x)$ in Equation 4.3, and $\beta^n(x)$ approaches a Gaussian distri-

bution when n becomes larger. A generalised version of B-splines is Duff's Tensioned B-splines. Furthermore, if we employ an additional step of calculating the interpolation coefficients instead of using f_k directly, we can derive the cardinal splines. The Catmull-Rom spline is a particular case of the cardinal splines, which converge to the *sinc* function at high orders. Examples of different interpolation kernels and the results on a simple 1D signal are shown in Figure 4.1.

4.1.2 Transformation Models

In the forward problem of image warping, a transformation model mathematically describes the transformation between two or more images. In addition, the inverse problem, *i.e.*, registration, aims to find the transformation mapping any point in the source (or floating or moving) image into the corresponding point in the target (or reference or fixed) image. In many real applications, a single transformation model is insufficient to recover all the deformation. However, the combination of transformations can approach the correct alignment. Parameterised transformation models, which describe the Degrees of Freedom (DoF) associated with a certain number of parameters, can be classified as rigid, affine and non-rigid deformable transformations (Figure 4.2). In general, the more DoF a transform contains, the more complex it is to solve the optimisation problem of registration.

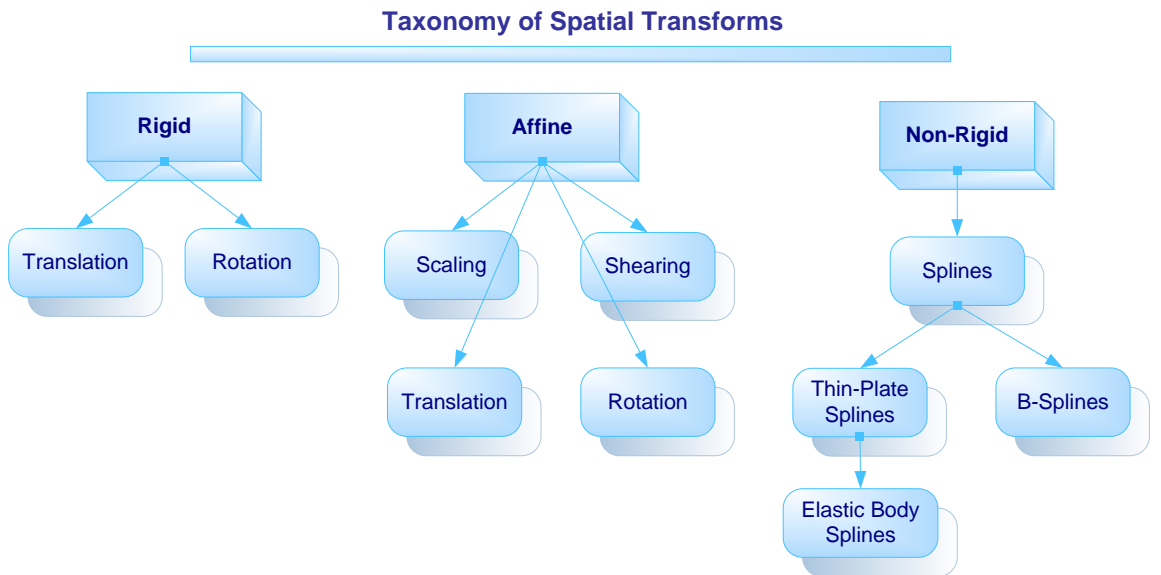


Figure 4.2: Illustration of the taxonomy of spatial transforms.

Rigid transformation, which contains only rotations and translations, is suitable when there are no

changes in the shape of the structure between the source and the target images. Affine transformation allows scaling and shearing, which can model more complex problems where the imaging scaling factors are unknown. In addition, non-rigid transformations define free-form mappings that are typically constrained by regularisation to a limited and feasible solution space. Rigid and affine registration is well-validated but non-rigid registration is more complex and difficult to validate [342].

Transformation models can also be defined as *global* or *local transformations* (Figure 4.3). A transformation is called global if it applies to the entire image, and it is local if each subsection of the image has its own transformation [185].

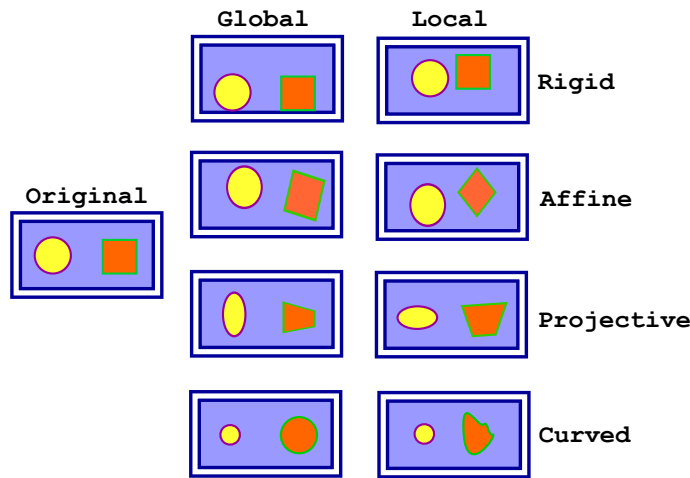


Figure 4.3: Examples of 2D transformations.

Mathematically, we can define the rigid transformation using homogeneous coordinates and argument matrix as

$$\mathcal{T}_{\text{rigid}}(x, y, z) = \begin{bmatrix} x' \\ y' \\ z' \\ 1 \end{bmatrix} = \begin{bmatrix} r_{11} & r_{12} & r_{13} & t_x \\ r_{21} & r_{22} & r_{23} & t_y \\ r_{31} & r_{32} & r_{33} & t_z \\ 0 & 0 & 0 & 1 \end{bmatrix} \begin{bmatrix} x \\ y \\ z \\ 1 \end{bmatrix}, \quad (4.9)$$

in which t_x , t_y and t_z are the translation along each axes of the 3D coordinate system. r_{ij} are the rotation coefficients, which are calculated by the multiplication of three separate rotation matrices.

In the 3D affine model, there are 12 parameters, which combine the rigid transformation with shearing and scaling, that is

$$\mathcal{T}_{\text{affine}}(x, y, z) = \mathcal{T}_{\text{shearing}} \cdot \mathcal{T}_{\text{scaling}} \cdot \mathcal{T}_{\text{rigid}} \cdot [x, y, z, 1]^T \quad (4.10)$$

where $[\cdot]^T$ is the transpose of the matrix. The shearing and scaling matrices are

$$\mathcal{T}_{\text{shearing}} = \begin{bmatrix} 1 & h_x & h_y & 0 \\ 0 & 1 & h_z & 0 \\ 0 & 0 & 1 & 0 \\ 0 & 0 & 0 & 1 \end{bmatrix}, \quad \text{and} \quad \mathcal{T}_{\text{scaling}} = \begin{bmatrix} s_x & 0 & 0 & 0 \\ 0 & s_y & 0 & 0 \\ 0 & 0 & s_z & 0 \\ 0 & 0 & 0 & 1 \end{bmatrix}. \quad (4.11)$$

There are other high order global transformations, which are more complex, e.g. the tri-linear transformation has 24 DoF and the quadratic transformation has 30 DoF. In addition, non-rigid deformable transformations can model subtle changes between images. These deformable transformations are described using a linear combination of basis functions or using splines. In particular, the use of Free-Form Deformations (FFD) based on B-splines for image registration, which was proposed by Rueckert et al. [245], has been successfully applied to many medical image registration problems. B-splines are locally controlled, *i.e.*, changing one control point only affects the transformation within a local neighbourhood or region. Therefore, it is more efficient than thin-plate splines and elastic-body splines. In [245] Rueckert et al. formulated the FFD using a 3D tensor product of 1D cubic B-splines as

$$\mathcal{T}_{\text{FFD-B-spline}}(x, y, z) = \sum_{l=0}^3 \sum_{m=0}^3 \sum_{n=0}^3 B_l(u) B_m(v) B_n(w) \phi_{i+l, j+m, k+n}, \quad (4.12)$$

in which $i = \lfloor \frac{x}{\delta} \rfloor - 1$, $j = \lfloor \frac{y}{\delta} \rfloor - 1$, $k = \lfloor \frac{z}{\delta} \rfloor - 1$, $u = \frac{x}{\delta} - \lfloor \frac{x}{\delta} \rfloor$, $v = \frac{y}{\delta} - \lfloor \frac{y}{\delta} \rfloor$, $w = \frac{z}{\delta} - \lfloor \frac{z}{\delta} \rfloor$, and $\phi_{i+l, j+m, k+n}$ are the control points with uniform spacing δ . Furthermore, $\lfloor \cdot \rfloor$ denotes a floor operation, which maps a real number to the largest previous integer.

In addition, B_l is the l -th basis function of the cubic B-spline

$$B_0(u) = (1 - u)^3 / 6 \quad (4.13)$$

$$B_1(u) = (3u^3 - 6u^2 + 4) / 6 \quad (4.14)$$

$$B_2(u) = (-3u^3 + 3u^2 + 3u + 1) / 6 \quad (4.15)$$

$$B_3(u) = u^3 / 6. \quad (4.16)$$

4.2 Inverse Problem: Registration

Registration is also called *image fusion* or *matching* [76]. The goal of registration is to determine a spatial transformation that brings homologous points among images being registered into correspondence. From the geometrical point of view, image registration uncovers the *alignment* of two or more images of the same objects taken at *different views*, *different times* or captured by *different modalities*.

There are plenty of investigations into rigid registration methods such as [185] [116]. Many studies have been carried out into non-rigid registration techniques, as well, *e.g.*, [86] [169] [348] [52] [204] [89] [281] [119]. These studies proposed elastic and fluid models, function expansions and splines, B-splines and wavelets, radial basis functions, landmark based methods, level sets registration, and the numerical solution of registration problems. In [33] Brown summarised that there are *four* key components in the development of a registration algorithm. Firstly, a *feature space*, where features to be matched, are selected in the image pair. Secondly, we have a search space, *i.e.*, range of *transformations* to be used. In addition, we need a *search strategy* to find the optimum transformation within the search space. Lastly, a *similarity metric* estimates the optimality of a transformation for the selected feature set. For instance, the edges in both images are generally good features; the rotation transformation could be the search space; there are many search strategies such as exhaustive search; and correlation could be employed as the similarity metric. These four key components can be modified as necessary for a more complex situation such as changing the rotation transformation to affine transformations. The choice of the four key components will exercise a great influence on the consequences of the registration and with many options for each available, the number of combinations is virtually endless.

4.2.1 Category of the Image Registration

In previous studies, many criteria, *i.e.*, landmark-based, segmentation-based and intensity-based methods, were employed as the basis for aligning source and target images. In addition, from the transformation point of view, the registration can be categorised into parametric image registration (PIR) and nonparametric image registration (NPIR).

4.2.1.1 Landmark-Based Image Registration

Landmark-based registration (or feature-based registration) uses salient features defined by the user. The selected features are structures such as points, lines, corners, crossings, and surfaces. The great advantage of landmark-based registration is the fast registration speed because the selected landmarks are sparse in the feature space. However, the non-deterministic user defined landmarks affect the accuracy of the registration results.

4.2.1.2 Segmentation-Based Registration

Segmentation-based methods register the binary structures such as curves, surfaces and volumes, which are obtained by segmentation. Segmentation-based methods are faster than methods using full image content because of the reduction of information. Nevertheless, the registration is based on segmentation pre-processing step, which undermines the precision of alignment results.

4.2.1.3 Intensity-Based Registration

Intensity-based methods deal with image intensity directly. Intensity-based methods require the full range of image content. Therefore, they are more time-consuming, whereas these intensity-based methods are generally robust, and involve no user interaction or pre-processing. The cost function of intensity-based methods is constructed using image intensity of homologous points within source and target images, and raw intensities of medical images are often smoothed and re-sampled. In contrast, landmark-based and segmentation-based methods minimise the distance between physical points.

The merit of landmark-based or segmentation-based methods is the capability of dealing with both intra-modality and inter-modality registration. However, any errors in feature extraction and segmentation will propagate through the registration process, and they are inevitable and unrecoverable. On the other hand, intensity-based methods form the similarity measurement according to

the level of shared information between the image intensities [243]. Combinations of landmark-based, segmentation-based and intensity-based methods have also been proposed.

4.2.1.4 Parametric Image Registration

PIR refers to registration via a specific class of transformation models. For a typical 3D problem, we have six parameters for the rigid transformation and twelve for the affine transforms. There are many more parameters associated with B-spline based registration, which are determined by the number of control points used. In real clinical applications, rigid and affine transforms are applicable to the registration of anatomical structures such as brain and bones. However, it is insufficient to describe complex deformation of soft tissues like liver and breast, where we need deformable registration. Although the affine registration has limited capability to recover significant non-rigid deformation, it is beneficial in modelling and testing a registration framework using simulated data. In practice, combining global affine and local non-rigid transformations is generally suitable for tackling most real registration problems. In summary, parametric models with affine transformations could be a good starting point for my research on combining reconstruction and registration in DBT, and deformable transformations can then be substituted at a later date once the framework has been developed.

4.2.1.5 Non-Parametric Image Registration

In the case of NPIR, we have a dense displacement field, which describes the transformation at every intensity point [243]. Additionally, in NPIR, we could use both small and large deformation models, which involve solving Partial Differential Equations (PDEs) that are associated with the displacement field. For instance, the large deformation models, the displacements can be described using a time dependent velocity field [243]. Thus, the forces, which govern the physical process of mimicking stretch of an elastic material, relax over time. Optical flow [120] and elastic models [15] are widely used small deformation models. The viscous fluid model [44], which is a typical large deformation model, enforces the topological properties on the deformation by constraining the transformation to be smooth. In contrast, the PIR model is controlled by a set of parameters, which possess much fewer dimensions in the search space. To sum up, the NPIR has plenty of flexibility to describe the transformations, but it is generally computationally expensive compared to the PIR model.

4.2.2 Solving the Image Registration Problem

4.2.2.1 Distance Measures

The similarity criterion measures differences in values at specific pixel/voxel locations between the two images. Brown [33] reported that the differences were measured as *volumetric* differences. Typically, value changes are the differences in intensity or radiometry. However, more generally, the concept of volumetric is proposed in order to include the wide variety of existing sensors whose values are not intensities.

Intensity-based methods minimise a cost function that measures the similarity between the image intensity of corresponding points of source and target images. The similarity computation is straightforward for the registration between source and target images, which are acquired by using the same imaging modality. However, it is more complex to deal with multi-modality image registration. The most commonly used similarity measurements are Squared Sum of Intensity Differences (SSD), Correlation Coefficient (CCoe), Mutual Information (MI), and Normalised Mutual Information (NMI), which are represented as follows.

$$\text{SSD} = \sum (\mathbf{R}(x, y, z, t_0) - \mathbf{T}(\mathcal{T}(x, y, z), t_1))^2; \quad (4.17)$$

$$\text{CCoe} = \frac{\sum (\mathbf{R}(x, y, z, t_0) - \bar{\mathbf{R}}(t_0))(\mathbf{T}(\mathcal{T}(x, y, z), t_1) - \bar{\mathbf{T}}(t_1))}{\sqrt{\sum (\mathbf{R}(x, y, z, t_0) - \bar{\mathbf{R}}(t_0))^2 \sum (\mathbf{T}(\mathcal{T}(x, y, z), t_1) - \bar{\mathbf{T}}(t_1))^2}}, \quad (4.18)$$

in which $\mathbf{R}(\cdot)$ and $\mathbf{T}(\cdot)$ are the fixed and moving images, and $\bar{\mathbf{R}}(\cdot)$, $\bar{\mathbf{T}}(\cdot)$, \mathcal{T} , t_0 , and t_1 represent the average image intensities, spatial transformation, and imaging time respectively. In addition, x , y , and z are the 3D coordinates of the image pixels.

Mutual information is based on the concept of information theory and expresses the amount of information that one image \mathbf{R} contains about a second image \mathbf{T} [244]

$$\text{MI}_{\text{Similarity}}(\mathbf{R}, \mathbf{T}) = H(\mathbf{R}) + H(\mathbf{T}) - H(\mathbf{R}, \mathbf{T}), \quad (4.19)$$

where $H(\mathbf{R})$, $H(\mathbf{T})$ denote the marginal entropies of \mathbf{R} , \mathbf{T} . $H(\mathbf{R}, \mathbf{T})$ denotes their joint entropy, which is calculated from the joint histogram of \mathbf{R} and \mathbf{T} . If both images are aligned, the mutual information is maximised. Because the mutual information depends on the overlap between two

images, normalised mutual information is advocated as [244]

$$\text{NMI}_{\text{Similarity}}(R, T) = \frac{H(R) + H(T)}{H(R, T)}. \quad (4.20)$$

In 1981, Horn and Schunck [120] proposed the original optical flow registration method, which assumed that the changes in image intensities are only due to motion. SSD possesses the same basic assumption that both images are identical when they are registered. It is the optimum measure if the images are varied by Gaussian noise only [303] [302]. However, SSD is sensitive to outliers, and it is inappropriate, for instance, when intensities have changed due to the injection of contrast agent. MI, which is a symmetric similarity measurement, was proposed by Viola and Wells III [303], and Collignon et al. [50] independently in 1995. Previous research showed that MI was very general because it made an assumption that a predictable relationship existed between the intensities of the two images. Additionally, Studholme et al. [277] [278] showed that NMI is more robust than MI for intermodality brain registrations when overlap changes are substantial.

4.2.2.2 Numerical Optimisation

Medical image registration algorithms usually estimate the transformation either following a *data-driven flow* or *minimising a certain cost function* [76]. Flow methods are very similar to approaches called optical flow in computer vision, which estimate motion in an image sequence such as a video. Here, we will focus on registration via optimisation. Generally, the cost function consists of a similarity measure expressed as follows

$$\zeta^* = \arg \min_{\zeta} \left(f(\zeta) = \mathcal{S}[T[\mathcal{T}_\zeta(x)], R(x)] = \mathcal{S}[\mathcal{I}_{\text{Int}_1}[\mathcal{T}_\zeta(x)], \mathcal{I}_{\text{Int}_2}(x)] \right), \quad (4.21)$$

in which $T[\mathcal{T}_\zeta(x)]$ and $R(x)$ denote the source image and the target image; however, there are interpolation operators, *i.e.*, $\mathcal{I}_{\text{Int}_1}$ and $\mathcal{I}_{\text{Int}_2}$, processing the images. Here x represents a pixel/voxel location or coordinates described using lexicographical ordering, and $f(\zeta)$ denotes the cost function. In addition, \mathcal{S} is an appropriate similarity measure or distance measure, and \mathcal{T}_ζ is the transformation. We minimise the cost function with respect to the transformation parameters ζ . Therefore, the desired transformation is a solution of this optimisation problem. More accurately, the transformation parameters ζ should be constrained in an admissible region Ω_ζ [76]. Furthermore, due to the ill-posedness inherent in the registration, proper regularisation and additional penalty terms

have been introduced to alleviate unstable and unfeasible solutions. Consequently, the registration problem in Equation 4.21 becomes one of minimising the joint functional

$$\begin{aligned}\zeta^* = \arg \min_{\zeta} & \left(f(\zeta) = \mathcal{S}[T[\mathcal{T}_\zeta(x)], R(x)] + \lambda \mathcal{R}(\mathcal{T}_\zeta(x)) + \xi \mathcal{P}(\mathcal{T}_\zeta(x)) \right), \\ s.t. & \quad \zeta \in \Omega_\zeta \in \mathbb{R}^n\end{aligned}\quad (4.22)$$

where the λ and ξ are the parameters of the regularisation (\mathcal{R}) and penalty (\mathcal{P}) functions. We can use any non-linear optimisation techniques (as seen in Section 3.2.3.2 and Appendix D to solve this problem.

4.2.2.3 Ill-Posed and Regularisation

As mentioned before, registration is an inherently ill-posed inverse problem. Because for every spatial location $x \in \Omega \in \mathbb{R}^n$, we try to obtain a vector $y_\zeta = \mathcal{T}_\zeta(x) \in \mathbb{R}^n$ with only scalar information $T(y_\zeta)$ and $R(x)$ provided. Normally, we use the L^2 -norms of derivatives of the displacement field $u = y_\zeta$ to express the regularisation term $\lambda \mathcal{R}(y_\zeta)$ in Equation 4.22. However, other regularisation schemes such as L^1 -norm based methods can also be applied. Therefore, let \mathcal{K} denote a numerical operator (e.g., a differential operator), and we can use the L^2 -norm $\|\cdot\|_2^2$ to describe the regularisation as

$$\mathcal{R}(y_\zeta) = \int_{\Omega} \|\mathcal{K}[y_\zeta(x)]\|_2^2 dx, \quad (4.23)$$

in which Ω is a feasible spatial boundary of the image. We can use the norm operator, the partial derivatives based diffusion operator, the gradient and divergence based elastic operator, and the curvature operator to model the regularisation functional. For example, in 2D, $n = 2$, and let $\mathcal{K}[y_\zeta] = y_\zeta$ and $y_\zeta = [y_\zeta^1; y_\zeta^2]$, then the norm of y_ζ is

$$\mathcal{R}(y_\zeta) = \int_{\Omega} (y_\zeta^1(x))^2 + (y_\zeta^2(x))^2 dx. \quad (4.24)$$

This is the well-known Tikhonov (Tychonov) regularisation.

The diffusion operator, which groups partial derivatives $\nabla y_\zeta^n(x)$, measures the variation of y_ζ , and the operator has been used in optical flow and demons algorithms, that is

$$\mathcal{R}(y_\zeta) = \int_{\Omega} (\nabla y_\zeta^1(x))^2 + (\nabla y_\zeta^2(x))^2 dx. \quad (4.25)$$

In addition, if we define the divergence as $\nabla \cdot y_\zeta(x)$, the elastic operator is

$$\mathcal{R}(y_\zeta) = \int_{\Omega} \iota \langle \nabla y_\zeta, \nabla y_\zeta \rangle + (\iota + \varsigma)(\nabla \cdot y_\zeta(x))^2 dx, \quad (4.26)$$

in which ι and ς are the Lamé constants [204].

By introducing the second order derivatives $\Delta y_\zeta^n(x)$, we can derive the curvature based regulariser as

$$\mathcal{R}(y_\zeta) = \int_{\Omega} (\Delta y_\zeta^1(x))^2 + (\Delta y_\zeta^2(x))^2 dx. \quad (4.27)$$

Furthermore, the penalty term $\mathcal{P}(y_\zeta)$ could contain additional constraints including the deviation from user-supplied landmarks, volume preservation, and local rigidity [76].

Although the concept of regularisation and penalty terms, which changes the ill-posed problem into a solvable one, is easy to understand, the implementation needs to be deliberated. Firstly, the discretisation of the operators needs to be conceived. Secondly, the derivative of the operators needs to be deduced before substituting them into the optimisation process. In addition, the operators in higher-dimensional space may require more computational time. The choice of the parameters (λ and ξ) of these operators considerably affects the results of registration.

4.2.2.4 Validation Methods

In real clinical applications, the ground truth or the real transformations are generally unknown. However, a registration is not feasible for clinical usage without an effective validation. Maintz and Viergever [185], and Jannin et al. [127] reported that the registration validation criteria include accuracy, reliability, robustness, fault detection, functional complexity, and clinical use. Commonly used evaluation schemes are Target Registration Error (TRE), Consistency Registration Error (CRE), visual inspection, image matching criteria, and clinical usefulness. The TRE is expressed as follows.

$$TRE(x) = \|T(x) - T_{warp}(x)\|, \quad (4.28)$$

in which TRE is calculated at the corresponding anatomical positions of interest [99], *i.e.*, manually selected landmarks, in the source image $T(x)$ and transformed target image $T_{warp}(x)$. In addition, TRE represents the distance after registration between corresponding points or landmarks, which are not used for calculating the registration transformation [77]. TRE spatially varies across the image except for simple translational errors. The error images show the spatial TRE distribution, which is useful in analysing registration achievements. The accuracy can then be expressed by the

mean, median, Root Mean Square (RMS), 95% or maximum of the regional TRE distribution.

4.3 Registration Algorithms in Breast Imaging and DBT

Registration is widely applied for a better visualisation of lesions on pre-contrast and post-contrast breast MRI; speckle tracking and image compounding in breast ultrasound images; alignment of breast PET; and standard mammography images on hybrid machines [95] [263]. Image registration is a prerequisite to align images taken at different times to isolate small breast lesions, and it is useful in monitoring breast cancer therapy. Recent research has focused on the more complex voxel based automatic registration techniques, which can replace semi-automated control point based methods. In this section, we survey previous registration techniques for breast images and their novel applications on DBT.

Early breast cancer detection, which requires identification of fine details of temporal pathological changes, compares the current image with images captured years before. In addition, diagnostic breast imaging is a multimodality task because various imaging modalities provide different biomedical information. For example, digital mammography is preferred to detect subtle breast lesions such as microcalcifications, breast ultrasound can distinguish cysts from solid lesions, and breast MRI may offer functional information. Recent studies have proposed several 3D X-ray breast imaging techniques such as breast CT and DBT, and the latter modality combines the pre-eminence of digital mammography and 3D image visualisation.

For pre-contrast and post-contrast breast MRI registration, in 1996, Zuo et al. [349] reported a voxel based automated rigid registration method minimising the variance ratio between the two images using a Newton type of optimisation. Kumar et al. [160] proposed an optical flow based affine registration algorithm, which minimised the sum of squared intensity difference using gradient descent method. In [103] Hayton et al. used an optical flow based nonlinear registration to consider both global and local transformations. Rueckert et al. [245] published a nonlinear registration method, which employed FFDs using B-splines, and they used the normalised mutual information and smoothness penalty within a multi-resolution hierarchical framework, as well. In 2000, Tanner et al. [288] investigated a non-rigid registration algorithm to register time-series MRI of the breast, which could result in finding significant volume changes in the region of enhanced lesion. They also indicated that the contrast-enhanced lesions shrunk substantially in contrast enhanced breast MRI. Later, Tanner et al. [289] employed Rueckert's method to assess the registration accuracy using biomechanical breast models based on Finite Element Method (FEM), and this model could

predict the displacements of tissue within the breast. Various biomechanical models were selected by changing the process of mesh generation, boundary condition definition, and tissue elastic property assumptions. The non-rigid registration performed on the MRI volumes before and after a compression in a controlled manner, identifying corresponding landmarks that estimated the displacements independently. In 2003, Rohlfing et al. [239] did some modifications to Rueckert's work, which contained a regularisation term to preserve volume. However, Rueckert et al. solved a problem incorporating global affine transformation with local transformations.

For breast ultrasound registration, Moskalik et al. [206] proposed an affine registration for compound images using control points. Meyer et al. [199] reported a semi-automated method that iteratively registered images using user specified control points, and maximised the mutual information using the Nelder-Mead simplex algorithm. In 2002, Xiao et al. [325] proposed a voxel based nonlinear registration method with block sampling and matching, which could only deal with local transformations. In 2004, Neemuchwala et al. [211] published a paper on an affine registration method, which identified higher-level invariant features that compared with the minimal spanning trees.

For intra-modality X-ray mammography registration, Yin et al. [341] presented an automated method for bilateral breast images alignment, in which a least squares matching method was used. It contained segmentation procedures for the breast region, the breast border and the nipple that then served as control points. Image subtraction was applied to evaluate the registration results. In 1997, Vujovic and Brzakovic [305] described a control point based approach, which determined several control points on the current and prior mammograms according to the intersection points of prominent anatomical structures in the breast. They determined the correspondence between these control points by searching in a local area around the control points of interest. In addition, three observers evaluated their registration results, one of which was an experienced radiologist. In 1999, Sanjay-Gopal et al. [251] published a paper on an automated regional registration algorithm, which identified corresponding lesions on temporal pairs of mammograms. The registration accuracy was assessed by comparing the average distance with respect to the centroid of the radiologist-identified regions. In [248] Sallam and Bowyer developed a warping technique for mammographic registration based on the manually identified control points. In 2001, Hadjiiski et al. [98] improved Sanjay-Gopal's regional registration algorithm by introducing a local alignment step. Wirth et al. [320] proposed a mutual information based method that identified the control points in mammogram pairs, and they also employed image subtraction to assess the performance of their registration method. In 2003, Engeland et al. [296] noted that mutual information based registration was superior to nipple

location or centre of the mass based alignment. The mutual information based method also performed better than the thin-plate spline surface technique and the warping based method that identified control points on the breast contour and the pectoral muscle. Richard and Cohen [237] reported a multi-resolution registration method that combined feature based and intensity based constraints in one mathematical model using free boundary condition. In [118] Hipwell et al. described a novel validation method for X-ray mammogram registration using real breast MRI, from which convincing pseudo-mammograms were generated with known 3-D deformations. They illustrated the method by computing the accuracy for two conventional non-rigid 2D registration algorithms applied to the pseudo-mammograms. In addition, they showed that the accuracy of these algorithms was close to the best achievable using a 2D one-to-one correspondence model. However, the new algorithms incorporated more representative transformation models, which were required to achieve sufficiently accurate registrations for this application.

Inter-modality (or multi-modality) registration fuses complementary image information, which can be advantageously used to assist radiologists and clinicians in the diagnostic procedure and assessment of therapy. Many studies have been proposed to solve multi-modality registration and invent co-registered multi-modality acquisition systems for breast screening application. Jansson et al. [128] proposed a method based on the PET instrument, and concluded that PET had clinical potential in predicting response to chemotherapy in patients with locally advanced breast cancer. It detected metastatic disease earlier than any other methods. In 2000, Murthy et al. [208] [209] developed a Positron Emission Mammography (PEM) system, which could produce high-resolution metabolic images of breast cancer. The system acquired PET images after mammographic imaging, and accurately co-registered images of these two modalities. Malur et al. [186] studied the efficacy of combining FFDM with free-hand breast ultrasound, and concluded that the combination of mammography and breast ultrasound was more effective in detecting breast cancer than using mammography alone especially for the dense breast. In 2004, Elbakri et al. [69] invented a FFDM/ultrasound system, in which the ultrasound transducer scanned along the X-ray camera to generate a 3D reconstruction of the compressed breast volume that precisely co-registered with the digital mammogram. Piron et al. [228] presented a hybrid biopsy system combining pre-biopsy MRI with real-time breast ultrasound, which contained a control point based rigid registration of breast MRI and ultrasound. In [200] Miga presented preliminary work in elastography using an iterative non-rigid registration method with mutual information to recover the tissue elastic properties. Ruiter et al. [246] proposed an automated algorithm to register mammograms with breast MRI volumes using a biomechanical model based on the FEM. The algorithm could recover the 3D position of a lesion

in the MRI from the lesion location information of mammograms. Based on the studies by Hipwell et al. [117] [118], Mertzanidou et al. [197] [198] developed an intensity-based approach for registering mammography and breast MRI, which attained a re-projection error of 3.83mm.

DBT is promising to replace the current gold standard mammography in future screening procedure, because the geometries of these two modalities are similar and the total X-ray dose usage of DBT is comparable to mammography. However, it is necessary for radiologists to compare DBT results with previous mammographic records, which needs a 2D-3D registration of the DBT reconstructions with earlier mammographic images of the same patient. Furthermore, recent research on contrast enhanced DBT provides the possibility of capturing functional information [28], and many reconstruction algorithms are reported, including filtered backprojection (FBP) and more complicated iterative methods. Thus, registration of different temporal DBT reconstruction data and registering DBT to other breast imaging modalities are also necessary in real clinical applications.

DBT offers the benefits of providing a pseudo-3D reconstruction instead of 2D images using digital mammography. Therefore, the registration of DBT images with previous mammograms is necessary. In addition, the temporal intra-modality DBT registration is also crucial in order to determine breast cancer development, radiotherapy progress, and prognosis. Different image processing methods of DBT are dependent upon accurate temporal registration. For example, Chan et al. [39] employed a 3D processing method for breast cancer detection using DBT data sets, while Reiser et al. [234] manipulated 2D source images separately. Kapur et al. [139] [140] investigated the registration of cross-sectional images of DBT and breast ultrasound, and this work achieved high co-registration accuracy. In 2006, Bakic et al. [16] performed the registration on 15 pairs of mammograms and central tomosynthesis projections of the same breast. The registration compensated for 94% of the per-pixel intensity differences that existed between the two images before alignment. In [16] Bakic et al. also developed a multimodality registration method to register a mammogram with individual DBT source projection images. They analysed the results of registering an MLO mammogram to nine tomosynthesis source projection images of the same breast, and they achieved 90% compensation of the per-pixel intensity differences. Although the investigations of Bakic et al. were preliminary, they showed the success of registering DBT projections with corresponding digital mammograms. Ren et al. [236] reported a hybrid multi-resolution rigid-body registration method. The method automatically registered reference chest DTS with on-board¹ chest DTS images, in order to guide patient positioning in radiation therapy, and it might be easily applied to DBT registration. Sinha et al. [262] published a paper on a 3D alignment technique to register two DBT mammographic

¹*On-board* imaging technology allows the patient to be imaged on the treatment table by a device, which is built into the radiation therapy apparatus, to ensure the patient and tumour are consistently positioned for treatment.

volumes using mutual information. They obtained an average misregistration error of 1.8 ± 1.4 mm. In comparison to the in-plane tomosynthesis resolution of 0.1mm, the average registration error of ≈ 2 mm was relatively large. However, it was much smaller compared with the mean and median sizes (20.2mm and 15mm) of malignant tumours detected in a population-based mammography study and compares favourably with the out-of-plane resolution of DBT [259].

4.4 Conclusions and Discussion

In this thesis, we have reviewed the key components of medical imaging registration, and have provided a survey of many significant aspects on breast imaging registration. To summarise, medical imaging registration can be classified into different categories (Figure 4.4).

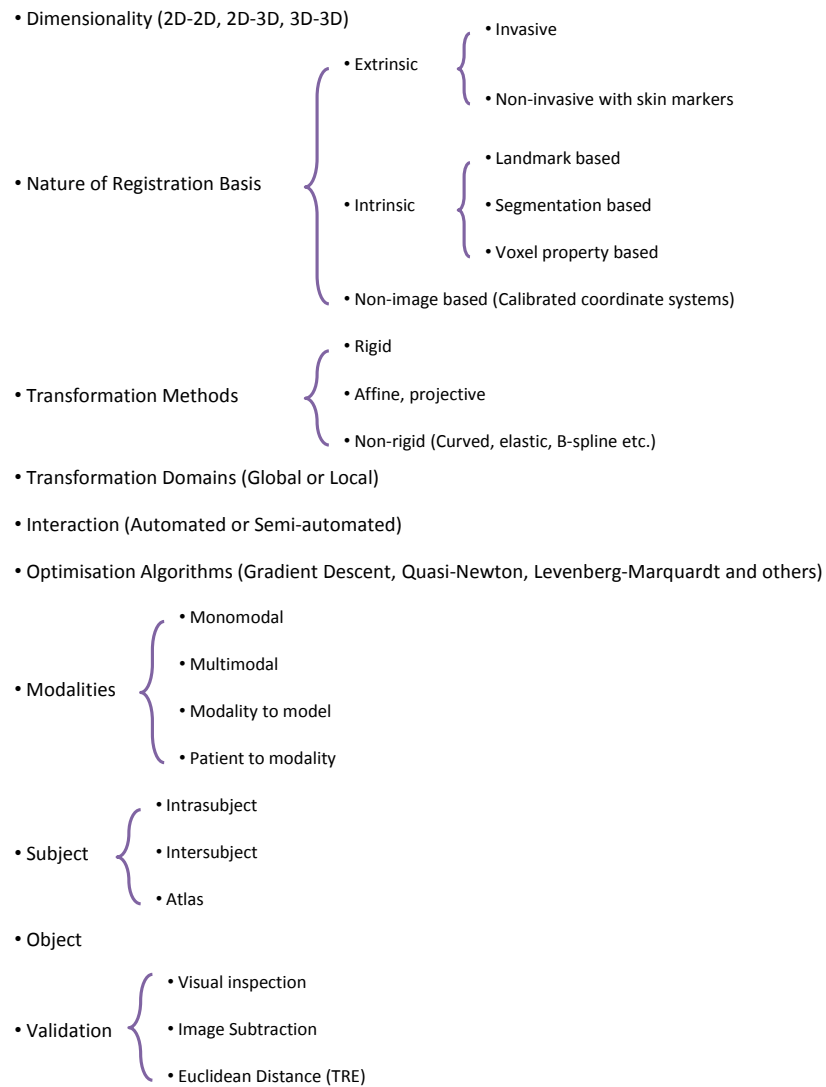


Figure 4.4: *Summary of image registration key components and categories.*

There are thorough investigations on intra-modality registration methods, and the inter-modality registration of mammography with other breast imaging modalities are of increasing interest. Inter-

modality registration improves the accuracy of breast diagnosis using the alignment of visible structures in different modalities. In addition, it can integrate distinct valuable information from various modalities. For example, mammography possesses high sensitivity, yet has relatively low specificity, and we can gather information from other modalities with high specificity such as breast ultrasound. In recent years automated intensity based registration methods have proved popular for breast image registration. A prime example is the free-form deformation based non-rigid registration; however hybrid registration techniques, which use control points, tissue features and breast boundary, are also promising. For DBT applications, three types of alignment are necessary including intra-modality, inter-modality registrations, and the registration of 2D and 3D images. Validation, which is significant in the assessment of registration algorithms, is an on-going requirement. Currently, the validation procedures are mainly based on the distance between geometrical features or manually selected landmarks, and visual inspection.

In conclusion, breast-imaging registration has a wide variety of clinical applications including better breast lesion detection and visualisation, tracking breast cancer development, and combining multi-modality information. However, it is still a challenging task because of the natural non-rigid property of the breast, the motion and compression during breast imaging acquisition, and the specificity of different modalities. Moreover, there are two obvious DBT characteristics, which complicate their registration. The first comprises the reconstruction “streak” artefacts in the in-plane direction (Figure 2.12). The second is the overall shape of the reconstructed breast, which is imposed by the compression plates. The compression produces a conflict between aligning the global *box-like* shape of the breast and attempting to deform the internal structure to account for rolling of the breast. Therefore, these factors may create local minima and confound the search for the global minimum solution. This reinforces my strategy to combine registration and reconstruction iteratively or simultaneously, which are two novel techniques we are actively pursuing, and they will be introduced in the next two chapters.

Iterative Reconstruction and Registration

In this chapter, we present a new method of performing reconstruction and registration iteratively in order to use two sets of X-ray (DBT) acquisition data. The iterative process leads to an improvement in the reconstruction, and enables a superior registration of the reconstructed volumes. Using synthetic images, uncompressed breast MRI, and DBT simulations with in-vivo breast compressions, we demonstrate that this combined iterative reconstruction and registration approach produces improvements in both the reconstructed volumes and the estimated transformation parameters when in comparison to perform the tasks sequentially. Work from this chapter is based on and extends [332] [333].

5.1 Motivation

In Chapters 1 and 2, we have discussed the clinical potential of DBT, which can be used to enhance breast cancer detection by reducing the confounding effect of superimposed tissue associated with conventional mammography. In addition, the increased volumetric information should enable temporal data sets to be more accurately compared, a task that radiologists routinely apply to conventional mammograms to detect the changes associated with malignancy.

Reconstructed 3D DBT images have high in-plane resolution but low out-of-plane resolution and exhibit reduced superposition of overlying tissue structures as in comparison to conventional X-ray mammography. Whilst the added depth information offered by DBT has the potential to enhance detection and diagnosis of breast cancer [154]; the greater volume of data, relative to X-ray mammography, increases the need for automated tools to aid the reading process. This is of particular importance if DBT is to be adopted in the high-workload screening context.

There are many tomographic reconstruction techniques, which are applicable to DBT such as

those discussed in Chapter 3. In addition, we have elaborated on registration methods for DBT in Chapter 4. However, there is no research combining these two tasks using limited angle DBT. In this chapter, we address the problem of comparing DBT data by combining reconstruction of a pair of temporal volumes with their registration iteratively. This is a challenging task due to the significant artefacts associated with DBT reconstructions. These are generated by the limited field of view of the acquired images and the correspondingly large null-space in the frequency domain. Rather than registering the images after reconstruction, we investigate the benefits of combining both reconstruction and registration, and test the hypothesis that the performance of each task will be enhanced as a result. Therefore, we propose an iterative method of least squares optimisation for our combined reconstruction and registration scheme. This also avoids the implicit assumption of missing data being equal to zero in algorithms such as in FBP.

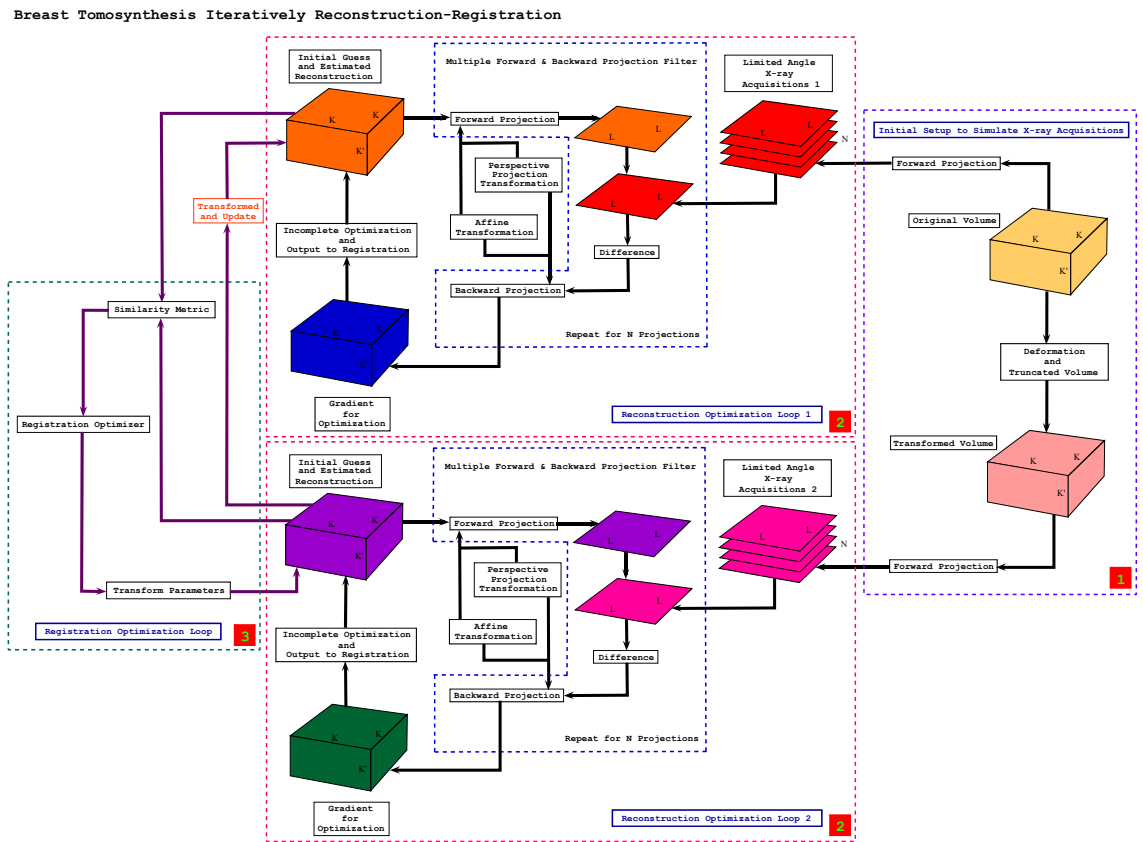


Figure 5.1: Flow chart of breast tomosynthesis iterative reconstruction-registration method. Blocks from right to left: 1. Initial setup to simulate X-ray acquisitions; 2. Perform two incomplete reconstruction loops; 3. Register for the reconstructed volumes and return the transformation parameters to update the fixed volume.

5.2 Problem Outline

We treat the task of combining reconstruction and registration iteratively as two general inverse problems, for which we solve the reconstruction by a generic optimisation approach such as the conjugate gradient algorithm, and we use a non-linear conjugate gradient or an L-BFGS solver for the registration problem. An overview of this iterative method is shown in Figure 5.1.

5.2.1 Forward and Inverse Problems

5.2.1.1 Reconstruction Part

In Chapter 3, we have discussed the forward and inverse problems of image reconstruction in 2D space; however, our problem, which combines reconstruction and registration using DBT settings, is in 3D.

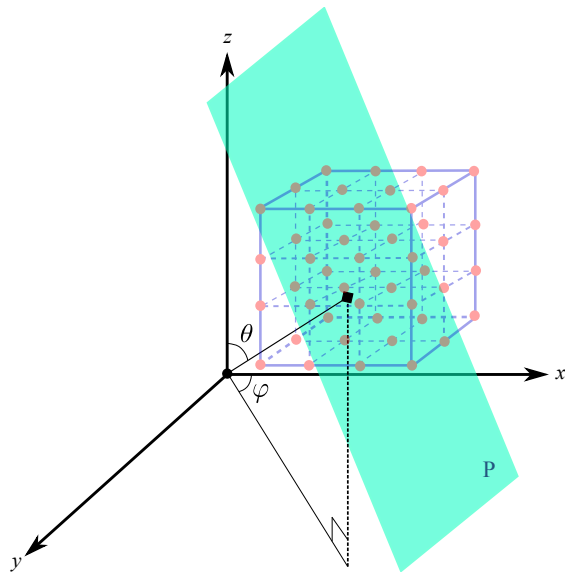


Figure 5.2: *Forward projection geometry in 3D.*

Radon transform based FBP is straightforward to extend to 3D. For example, according to the 3D projection geometry in Figure 5.2, the 3D Radon transform is

$$P(\rho, \theta, \varphi) = \iiint_{-\infty}^{\infty} f(x, y, z) \delta(\rho - (x \cos \varphi \sin \theta + y \sin \varphi \sin \theta + z \cos \theta)) dx dy dz, \quad (5.1)$$

in which θ is the elevation angle and φ is the azimuth angle. In addition, we can derive the inversion formula for the 3D Radon transform, *i.e.*, filtered backprojection, as

$$f(x, y, z) = \frac{-1}{8\pi^2} \int_0^\pi \int_0^{2\pi} \left[\frac{\partial^2 P(\rho, \theta, \varphi)}{\partial \rho^2} \Big|_{\rho=(x \cos \varphi \sin \theta + y \sin \varphi \sin \theta + z \cos \theta)} \right] \sin \theta d\varphi d\theta. \quad (5.2)$$

However, in this thesis, we use least squares estimation based iterative methods to solve the reconstruction because they are straightforward to combine with various optimisation schemes and regularisation techniques. Therefore, the forward problem of the reconstruction is expressed in Equation 3.39 that is

$$\mathbf{p} = A\mathbf{f} + \boldsymbol{\epsilon}. \quad (5.3)$$

In addition, we can model the reconstruction problem as Equation 3.58 that is

$$\mathbf{f}^* = \arg \min_{\mathbf{f} \in \mathbb{R}^n} \left(f(\mathbf{f}) = \mathcal{D}(A\mathbf{f}, \mathbf{p}) + \lambda \mathcal{R}(\mathbf{f}) \right). \quad (5.4)$$

5.2.1.2 Registration Part

Essentially, the forward problem of image registration can be modelled by image warping, which includes a transformation operation \mathcal{T}_ζ and an interpolation operation \mathcal{I} . Therefore, we can model the registration procedures as a nonlinear least squares optimisation problem as Equation 4.22 that is

$$\zeta^* = \arg \min_{\zeta \in \mathbb{R}^n} \left(f(\zeta) = \mathcal{S}[\mathcal{T}_\zeta(\mathbf{x}), \mathbf{R}(\mathbf{x})] + \lambda \mathcal{R}(\mathcal{T}_\zeta(\mathbf{x})) \right) \quad (5.5)$$

if no additional penalty constraints \mathcal{P} are taken into account, and it is an unconstrained optimisation problem. In addition, ζ is a vector that describes transformation parameters or deformation fields, and the problem is nonlinear with respect to ζ . In this Chapter, we use the affine transformation; however, using our framework it is straightforward to incorporate other high order transformations. Further investigations for our particular DBT application are discussed in the methodology part of Sections 5.4.1 and 5.4.2.

5.2.2 Forward and Backward Projectors

According to the flow chart of our reconstruction and registration framework (Figure 5.1), the X-ray acquisitions are simulated from the forward projections of the test volumes. Three types of test volumes are employed for our experiments, they are a toroid phantom volume, an uncompressed MRI

volume, and a DBT volume simulated from an in-vivo compressed breast MR image. Therefore, we need a 3D to 2D forward projector, which is capable of creating limited angle projections of the tested volumes. Furthermore, in the reconstruction process, both forward (3D to 2D) and backward (2D to 3D) projectors are used.

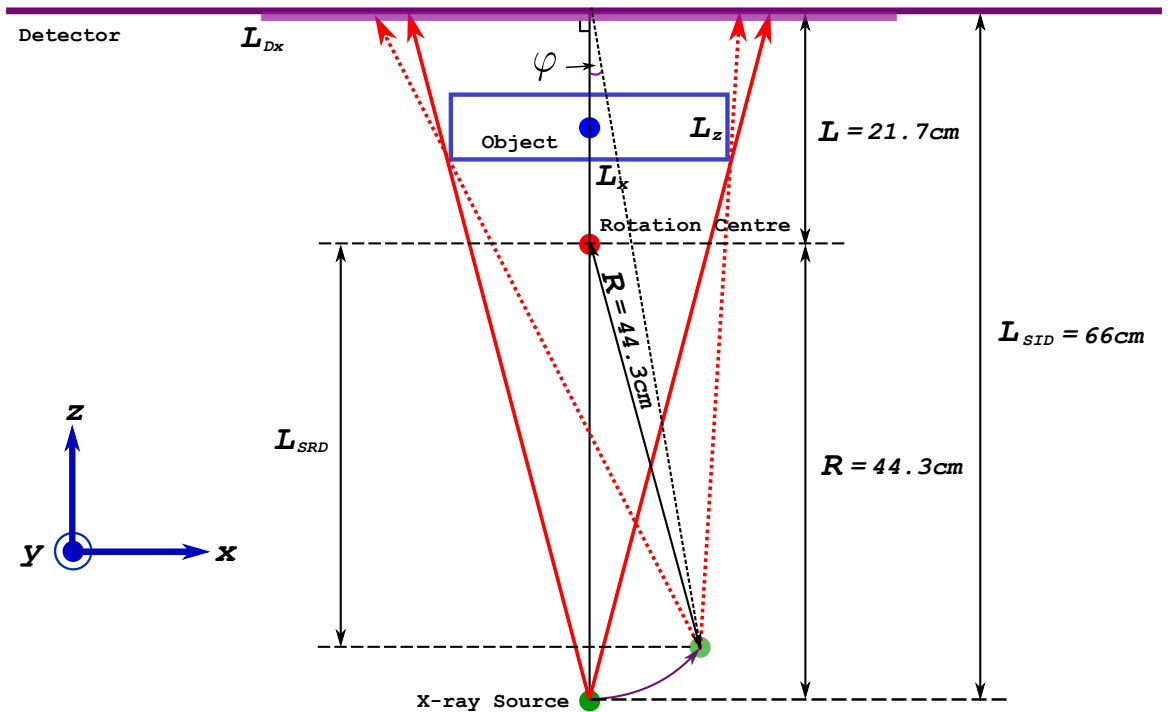


Figure 5.3: A 2D schematic illustration of the DBT geometry. Firstly, we define the X-ray source to detector distance L_{SID} to 66cm, and the length of the rotation arm R is 44.3cm and the distance L between the rotation centre of the X-ray source and the detector is 21.7cm. L_z is the depth of the object, which is around 3cm to 8cm in real applications. In addition, L_{Dx} is the width of the forward projection images, which depends on the width L_x of the object, and L_{SRD} defines the X-ray source to its rotation centre distance.

In this set-up, we have defined the geometry the same as a typical DBT employed (details is described in this patent by Wu et al. [324]). The X-ray source rotates in a limited angle arc, and 11 projections are produced covering ± 25 degrees. The rotation arm R is 44.3cm in length, and L is 21.7cm from the rotation centre to the detector (Figure 5.3). The initial X-ray source to detector distance L_{SID} is 66cm when the X-ray source moves to $\varphi = 0$ degree¹.

¹Draw a line from the X-ray source to the centre of the detector, and φ is the complementary angle of the inclination between this line and the detector plane (Figure 5.3). In real simulation, we use eleven angles $[-25 - 20.32 - 15.59 - 10.82 - 5.99 - 1.09 3.9 8.99 14.19 19.52 24.98]$ in degree, which are $[-0.4363 - 0.3547 - 0.2721 - 0.1888 - 0.1045 - 0.0190 0.0681 0.1569 0.2477 0.3407 0.4360]$ in radian.

In our task, we do not need to obtain the full range of projections. Therefore, rather than form the 3D forward Radon transform and the corresponding backward projection, we use a ray-casting based method, which is a discrete representation of the continuous formula of the Radon transform and the backprojection.

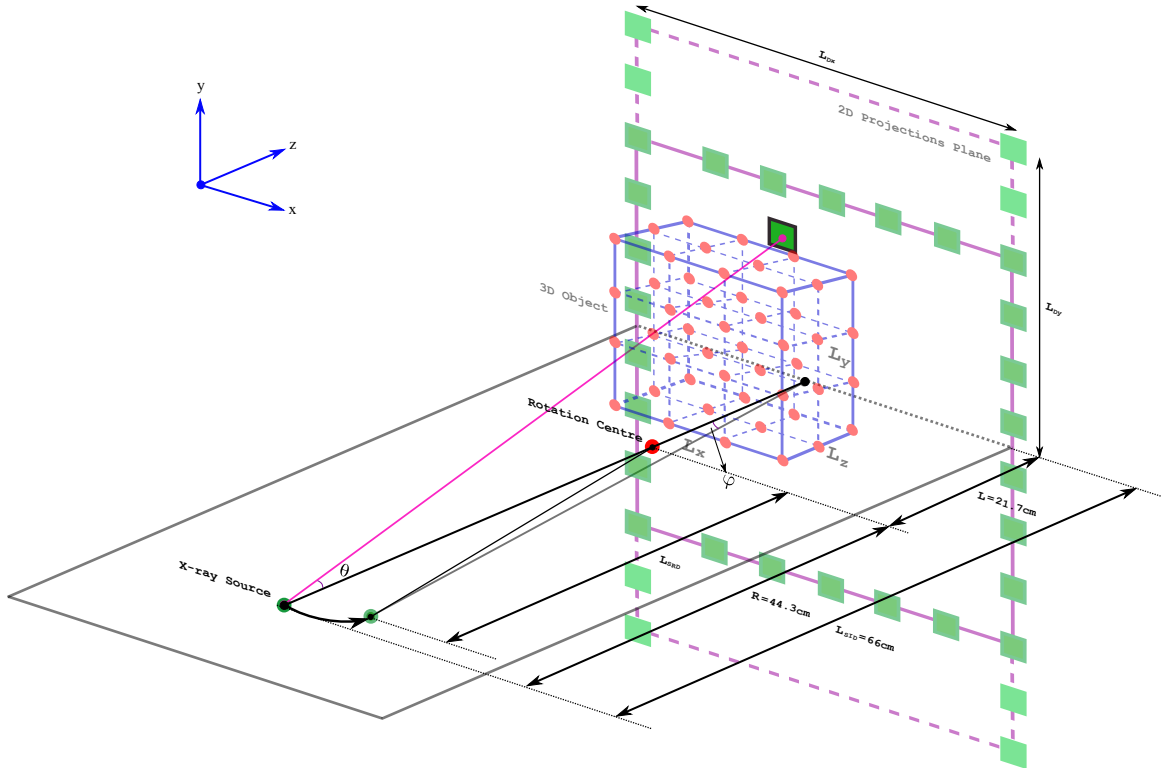


Figure 5.4: Schematic illustration of the ray-casting method.

Ray-casting is an image order algorithm [9] [80], which can render 3D scenes to 2D screens, *i.e.*, 2D forward projections. It integrates rays of a light from observer or detector point to the light source (Figure 5.4). It consists of four components, *viz.*, rays generation, line integrals, interpolations, and a perspective transformation, which is necessary for a cone-beam based geometry.

In particular, there are many line-integration schemes associated with various interpolation schemes (Figure 5.5). First, Siddons method calculates the length of intersection between two slices in the x - y plane, and the length defines the contribution of a voxel to the line-integral. Second, Josephs method finds the intersections between a ray and the slices of the x - y plane, and only bilinear interpolation is required to calculate the points on the ray, which will contribute to the line-integral. Furthermore, both equal sampling approach and Köhler's method use trilinear interpolation. The

equal sampling approach calculates the interpolated points with equidistance h . In contrast, Köhler's method only interpolates once between two slices of the x - y plane. According to Turbell's research [293], Joseph's method with bilinear interpolation performs similarly as Köhler's method, and they are both better than Siddon's method. The performance of the equal sampling approach depends on the oversampling factor. Similar results are produced by the equal sampling approach and Köhler's method when the oversampling factor is large enough. However, the computing time is dramatically increased when this factor becomes large. Therefore, Joseph's method with bilinear interpolation can produce an efficient line-integration with accurate results for our ray-casting implementation. Details of interpolation schemes are discussed in Section 4.1.1.

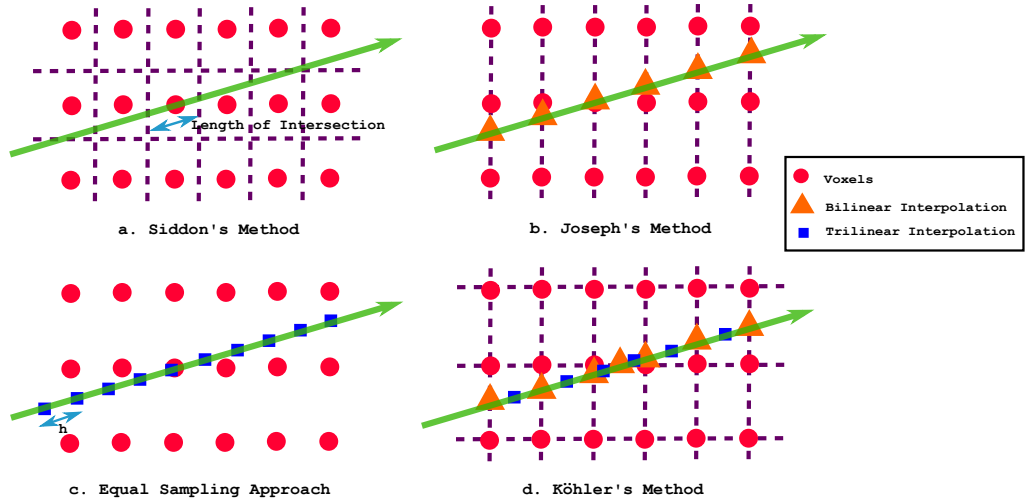


Figure 5.5: Different line-integration schemes of the ray-casting method. Vertical dash lines are slices of the x - y plane. Siddon's method is only defined by the length of intersection between two adjacent slices; In Joseph's method, only bilinear interpolation is required on the x - y plane; Equal sampling approach employs trilinear Interpolation with equidistance along the line and there might be more than one interpolations between two adjacent slices; Köhler's method finds the bilinear interpolations on both x - y and x - z planes, and then applies the trilinear interpolation according to the position of the bilinear interpolations.

For the implementation of the backprojection, the integrated voxel values are smeared back to the volumes along each ray. We also use Joseph's method with bilinear interpolation for the backward projector. Essentially, the backprojection process reverses the forward projection process using ray-casting. Firstly, according to the DBT geometry, we define the rays between the X-ray source and each pixel on the forward projection plane. Secondly, we find the intersections between a ray and slices of x - y plane. Then we equally divide the pixel value by the number of intersections, and we

use this average value to increment the four voxels surrounding each intersection according to its bilinear coefficients. In this way back-projection is the exact inverse of forward projection, subject to errors introduced by discretisation/interpolation process. The backprojection process is repeated 11 times and the value for a voxel is accumulated.

In summary, the ray-casting algorithm is an efficient discrete implementation for the forward Radon transform and backprojection process under limited-angle DBT settings. It implements the *forward projectors* for particular *DBT geometries*, and has been modified to implement the complementary *backward projectors*.

5.3 Materials

5.3.1 DBT Simulation Using Synthetic Toroid Phantom

A toroid phantom volume has been created for our first experiment. The toroid is a doughnut-shaped object visually. Topologically, the *toroid* is a closed surface defined as the product of two circles [316].

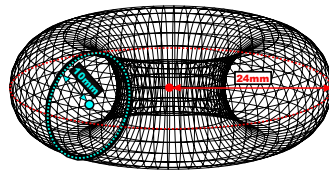


Figure 5.6: Red circle: Define the major radius of the toroid (24mm). Blue circle: Define the minor radius of the toroid (10mm).

The toroid (Figure 5.6) is embedded in a volume of $70 \times 70 \times 70\text{mm}^3$ with 1mm resolution in each dimension. The original toroid is our fixed image and its affine transformed volume is the moving image (Figure 5.7). In addition, we can perform the forward projection for both of our fixed and moving image in order to generate simulated X-ray acquisitions (Figure 5.8).

We assign intensities from 1 to 999 to the digital toroid phantom, in which the background is assigned to 1 and the highest intensity 999 is assigned in the centre of minor radius of the toroid object. The intensities of the cross section with minor radius, is a bell-shaped function that is determined by $(999 - \tau_1 k_{mr}^2)$, in which τ_1 is a coefficient describing the sharpness of the changes of intensities. In addition, k_{mr} are integers from 1 to the value of the minor radius, and we apply linear interpolation for various minor radius.

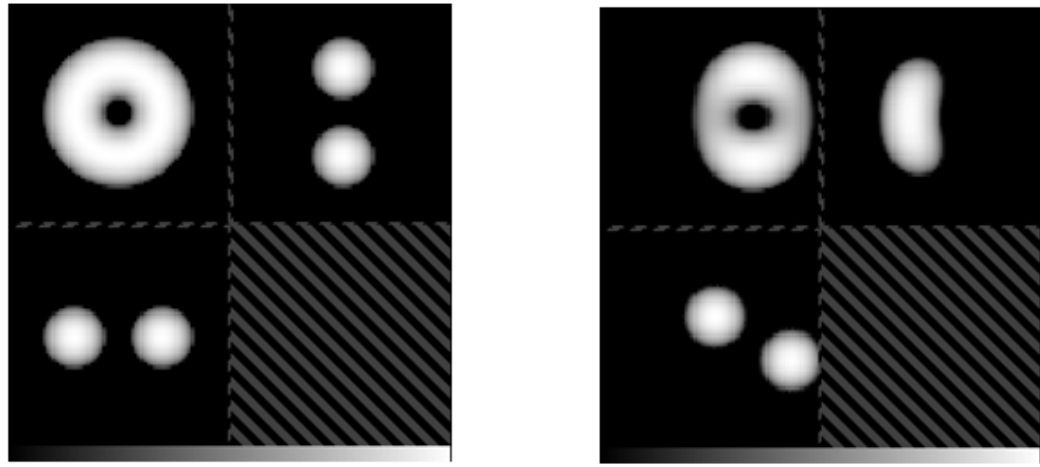


Figure 5.7: *Left: Fixed (target) image; Right: Moving image.* The transformations R_ζ between the target and the moving images contain a translation of $\mathcal{T}_{\text{translation}} = [10, 0, -20]\text{mm}$ and a rotation about the y axis of -30 degrees. Intensities have been normalised into the range of 0 to 1.

Figure 5.8: *Left: Projection of the fixed image. Right: Projection of the moving image.*

5.3.2 DBT Simulation Using Uncompressed MRI

The uncompressed MRI volume is $140 \times 128 \times 60$ in voxels with $1.328 \times 1.328 \times 2.5\text{mm}$ resolution in each dimension. The original MRI volume is our fixed image and its affine transformed volume is the moving image (Figure 5.9), and the forward projections of them are shown in Figure 5.10. The original MRI data is provided by UK MR Breast Screening Study (MARIBS) by Leach et al. [165].

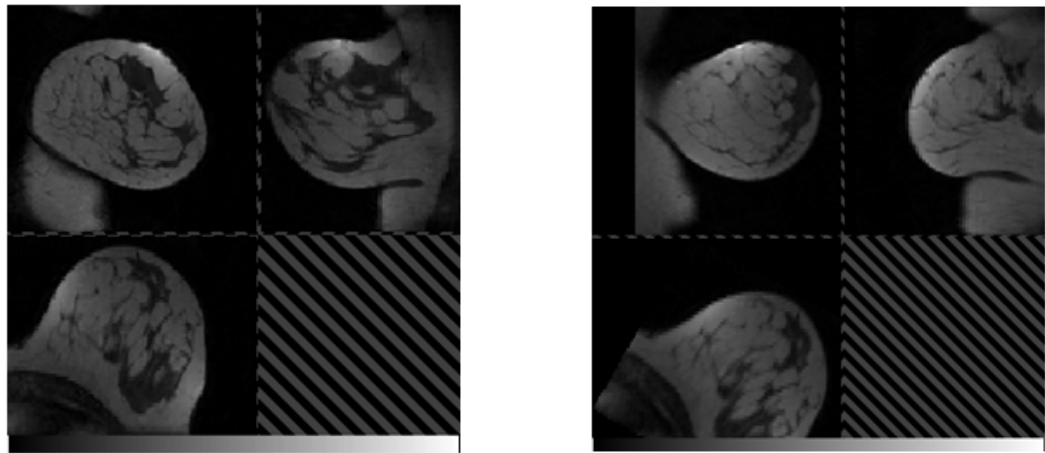


Figure 5.9: *Left: Fixed (Target) Image; Right: Moving Image.* The transformations R_ζ between the target and the moving images contain a translation of $\mathcal{T}_{\text{translation}} = [10, 0, -20]\text{mm}$ and a rotation about the y axis of -30 degrees.

Figure 5.10: *Left: Projection of the fixed image. Right: Projection of the moving image.*

5.3.3 DBT Simulation Using In-Vivo Compressed Breast MRI

We use in-vivo compressed breast MRI to simulate our DBT data set. The simulated DBT volume is $160 \times 80 \times 160$ in voxels, and the resolution is $1 \times 2.5 \times 1\text{mm}$ in each dimension. The two sets of the DBT simulation are segmented using an Expectation-Maximization (EM) algorithm, with a Markov Random Field (MRF) regularisation, namely EM-MRF based breast tissue classification [198]. There is an unknown non-rigid deformation between fixed and moving images, which we try to recover using affine transformation, and the forward projections of the fixed and moving images are shown in Figure 5.11.

Figure 5.11: *Left: Projection of the fixed image. Right: Projection of the moving image.*

5.4 Sequential Method versus Iterative Method

A 3D image, $R(x) \in \mathbb{R}^{D_3}$, two sets of temporal data, $p_1, p_2 \in \mathbb{R}^{p_{\text{num}} \times D_2}$, the parametric transformations, \mathcal{T}_ζ , and the system matrix, $A \in \mathbb{R}^{p_{\text{num}} \times D_2 \times D_3} : \mathbb{R}^{D_3} \rightarrow \mathbb{R}^{D_2}$, can be related via

$$p_1 = AR(x) = Af_1^g, \quad (5.6)$$

$$p_2 = AT[\mathcal{T}_\zeta(x)] = Af_2^g. \quad (5.7)$$

In particular, R and T represent the interpolation operation \mathcal{I} in Equation 4.1, and x is the regular coordinate in lexicographical ordering. Additionally, f_1^g and f_2^g are the intensities of the ground truth of our fixed and moving images.

5.4.1 Sequential Method

Forward projections, *i.e.*, p_1, p_2 , are acquired using a limited angle DBT geometry with $p_{\text{num}} = 11$ projections covering $\pm 25^\circ$. The forward model is described by the system matrix A , which can mimic the X-ray attenuation or absorption properties of the breast. In the conventional sequential method, the reconstruction of equations 5.6 and 5.7 can be solved by minimising

$$f_1^* = \arg \min_{f_1} \left(f(f_1) = \frac{1}{2} \|Af_1 - p_1\|^2 \right); \quad (5.8)$$

$$f_2^* = \arg \min_{f_2} \left(f(f_2) = \frac{1}{2} \|Af_2 - p_2\|^2 \right). \quad (5.9)$$

Following reconstruction, volumes f_1^* and f_2^* , *i.e.*, the fixed and moving images, are registered

with respect to the registration parameters ζ :

$$\zeta^* = \arg \min_{\zeta} \left(f(\zeta) = \frac{1}{2} \|\mathcal{T}_\zeta(f_2^*) - f_1^*\|^2 \right) \quad (5.10)$$

$$= \arg \min_{\zeta} \left(f(\zeta) = \frac{1}{2} \|T^*[\mathcal{T}_\zeta(x)] - R^*(x)\|^2 \right). \quad (5.11)$$

5.4.2 Iterative Method

In our novel iterative reconstruction and registration method, we solve equations 5.6 and 5.7 with respect to estimates f_1 and f_2 of f and the registration parameters ζ , by alternating an incomplete optimisation (i.e. j iterations) of the reconstructed volumes \hat{f}_1 and \hat{f}_2 :

$$\hat{f}_1 = j \text{ STEPS of } \arg \min_{f_1} \left(f(f_1) = \frac{1}{2} \|Af_1 - p_1\|^2 \right) \quad (5.12)$$

$$\hat{f}_2 = j \text{ STEPS of } \arg \min_{f_2} \left(f(f_2) = \frac{1}{2} \|Af_2 - p_2\|^2 \right) \quad (5.13)$$

with the registration of the current estimates \hat{f}_1 and \hat{f}_2 with respect to the registration parameters ζ :

$$\hat{\zeta} = \arg \min_{\zeta} \left(f(\zeta) = \frac{1}{2} \|\mathcal{T}_\zeta(\hat{f}_2) - \hat{f}_1\|^2 \right) \quad (5.14)$$

$$= \arg \min_{\zeta} \left(f(\zeta) = \frac{1}{2} \|\hat{T}[\mathcal{T}_\zeta(x)] - \hat{R}(x)\|^2 \right). \quad (5.15)$$

After each registration iteration (Equation 5.15), and prior to the next iteration of the reconstructions (Equations 5.12 and 5.13), the reconstruction estimates are updated as follows (Equations 5.16 and 5.17).

$$f_1 = \hat{\mathcal{T}}_\zeta(\hat{f}_2) = \hat{T}[\hat{\mathcal{T}}_\zeta(x)] \quad (5.16)$$

$$f_2 = \hat{f}_2. \quad (5.17)$$

This “outer loop” of reconstruction followed by registration is repeated k times. The last iteration outputs $f_1^* = \hat{f}_1$, $f_2^* = \hat{f}_2$ and $\hat{\mathcal{T}}_\zeta \hat{f}_2$.

In addition, the following analytical gradients are used to calculate \hat{f}_1 and \hat{f}_2 for the reconstruction

part

$$g(f_1) = A^T(Af_1 - p_1) \quad (5.18)$$

$$g(f_2) = A^T(Af_2 - p_2). \quad (5.19)$$

Similarly, by the chain rule, the analytical gradient for the registration part is

$$g(\zeta) = (\hat{f}_1 - \mathcal{T}_\zeta(\hat{f}_2)) \frac{\partial \mathcal{T}_\zeta(\hat{f}_2)}{\partial \zeta} = (\hat{R}(x) - \hat{T}[\mathcal{T}_\zeta(x)]) \frac{\partial \hat{T}[\mathcal{T}_\zeta(x)]}{\partial \zeta} \quad (5.20)$$

$$= (\hat{R}(x) - \hat{T}[\mathcal{T}_\zeta(x)]) \frac{\partial \hat{T}[\mathcal{T}_\zeta(x)]}{\partial \mathcal{T}_\zeta(x)} \frac{\partial \mathcal{T}_\zeta(x)}{\partial \zeta}. \quad (5.21)$$

It consists of three parts, *i.e.*, image difference $(\hat{R}(x) - \hat{T}[\mathcal{T}_\zeta(x)])$, the partial derivative of the moving image $\frac{\partial \hat{T}[\mathcal{T}_\zeta(x)]}{\partial \mathcal{T}_\zeta(x)}$ evaluated at location $\mathcal{T}_\zeta(x)$, and the partial derivative of the transformation $\frac{\partial \mathcal{T}_\zeta(x)}{\partial \zeta}$. As we use the gradient information to get the updated parameters ζ , the moving image we used to calculate the partial derivative is the *original* moving image (not the updated or transformed moving image). In addition, this partial derivative, *i.e.*, spatial derivative, of the original moving image is calculated using the image gradient that is defined by

$$\nabla \hat{T}(y_\zeta) = \frac{\partial \hat{T}[\mathcal{T}_\zeta(x)]}{\partial \mathcal{T}_\zeta(x)} = \left(\frac{\partial \hat{T}}{\partial x} y_\zeta, \frac{\partial \hat{T}}{\partial y} y_\zeta, \frac{\partial \hat{T}}{\partial z} y_\zeta \right)^T, \quad (5.22)$$

in which $y_\zeta = \mathcal{T}_\zeta(x) = (x, y, z)^T$.

The preceding combined reconstruction and registration method is summarised by

Algorithm 1: Iteratively Combined Reconstruction and Registration

Input: p_1, p_2 .

Output: $f_1^*, f_2^*, \hat{\mathcal{T}}_\zeta \hat{f}_2$.

```

begin
  % Initialise  $f_1$  and  $f_2$  to vectors with all zero entries
  % Initialise  $\zeta$  to a vector of the reshaped identity matrix  $I$ 
   $f_1 := 0; f_2 := 0;$ 
   $\zeta := I;$ 

  % Calculate matrix  $A$  for the forward projection
  % Matrix  $A^T$  represents the backward projection
   $A := \text{RAYCASTING}(\text{SIZE}(f_1));$ 

  % Outer loop for the registration runs  $k$  times
  for  $k$  iterations do
    % Inner loop for the reconstruction runs  $j$  times
    for  $j$  iterations do
       $\hat{f}_1 = j \text{ STEPS of } \arg \min_{f_1} ( f(f_1) = \frac{1}{2} \|Af_1 - p_1\|^2 );$ 
       $\hat{f}_2 = j \text{ STEPS of } \arg \min_{f_2} ( f(f_2) = \frac{1}{2} \|Af_2 - p_2\|^2 );$ 
       $\hat{\zeta} = \arg \min_{\zeta} ( f(\zeta) = \frac{1}{2} \|\mathcal{T}_\zeta \hat{f}_2 - \hat{f}_1\|^2 );$ 
       $f_1 = \hat{\mathcal{T}}_\zeta \hat{f}_2;$ 
       $f_2 = \hat{f}_2;$ 

    % Output  $f_1^*$ ,  $f_2^*$ , and  $\hat{\mathcal{T}}_\zeta \hat{f}_2$ 
     $f_1^* = \hat{f}_1;$ 
     $f_2^* = \hat{f}_2;$ 
     $\hat{\mathcal{T}}_\zeta \hat{f}_2.$ 

```

At each update of the volumes after the outer loop registration, we use the transformation of f_2 to correct f_1 that is

$$f_1 = \hat{\mathcal{T}}_\zeta \hat{f}_2; \quad (5.23)$$

however, an alternative method is updating f_1 using the average of the transformed \hat{f}_2 and recon-

structed \hat{f}_1 that is

$$f_1 = \frac{1}{2}(\hat{\mathcal{T}}_\zeta \hat{f}_2 + \hat{f}_1), \quad (5.24)$$

in which we gather information of both \hat{f}_1 and \hat{f}_2 . Furthermore, we can also incorporate the inverse transformation of f_1 in the correction of f_2 , but not all transformations have an analytical inverse. To sum up, our iterative method alternately performs incomplete reconstructions for two temporal data sets, followed by a registration.

5.4.3 Validation

In order to validate the efficacy of our iterative method, we contrast the results of the sequential method and our iterative method using the image appearance, the SSD error and the TRE. Firstly, we compare the final transformed moving image $\hat{\mathcal{T}}_\zeta \hat{f}_2$ with the original fix image f_1^g , which is the ground truth of the reconstruction, to analyse the accuracy of our iterative method. Secondly, the difference image between $\hat{\mathcal{T}}_\zeta \hat{f}_2$ and f_1^g is also compared with the difference image of the conventional sequential method, *i.e.*, differences between $\mathcal{T}_\zeta^* f_2^*$ and f_1^g , in which \mathcal{T}^* is calculated using ζ^* from Equation 5.11, and f_2^* is obtained from Equation 5.9. In addition, as we used both simulated data and simulation with real compression, the TRE is either obtained by calculating the mean error (and standard deviation) for each voxel in the simulated volume or by calculating the distance between the corresponding landmarks, which are manually predefined in the simulated data with real compression (Equation 4.28).

5.4.4 Implementation

We developed a software that integrates the iterative reconstruction and registration schemes for DBT. First, we implemented both the sequential method and our iterative method in Matlab environment, which is straightforward to test with different digital phantom images, various optimisers, and Tikhonov regularisation. Second, the implementation has been done using UCLToolkit, which is an ITK based toolbox developed by our group at the Centre for Medical Image Computing (CMIC) of University College London (UCL). In addition, we can choose to use various optimisation schemes, *e.g.*, nonlinear conjugate gradient or L-BFGS, for our application. In the experimental sections of this Chapter, we display the results using our UCLToolkit implementation. In particular, we use the conjugate gradient search engine for the reconstruction, and the L-BFGS method is chosen for the registration part of our problem. Although we have implemented both updating schemes for f_1 described in Equations 5.16 and 5.24, we use the former because there is no significant improvement

when we average the transformed \hat{f}_2 and \hat{f}_1 .

5.5 Experiments and Results using Affine Model

In this thesis, we address the problem of comparing temporal DBT volumes via registration. This is a challenging task due to the significant artefacts associated with DBT reconstructions. These are generated by the limited field of view of the acquired images and the correspondingly large null-space in the frequency domain. Rather than registering the images after reconstruction, we investigate the benefits of combining both reconstruction and registration, and test the hypothesis that the performance of each task will be enhanced as a result. There are two possible reasons that our iterative method could obtain satisfied results in both reconstruction and registration at least as good as the sequential method: first, the random noise can be averaged out when we have more 2D projection data even the 2D projection data have been taken from identical geometric settings; second, due to moving between two time points, there is a potentially enlarged angular range of data acquisition that can alleviate the null-space problem. Therefore, we performed two hypothetical experiments in order to confirm the rationalisation of our iterative method. In addition, we have performed four experiments to compare the sequential and iterative reconstruction and registration using three sets of simulated data with increased realism introduced before, and the results are shown as follows.

5.5.1 Hypothetical Experiment HA1: Test on the Identity Registration Transformations with the Same Projections

Hypothesis 1: The random noise can be averaged out when we have more 2D projection data even the 2D projection data have been taken from identical geometric settings.

Experiment: We test on identity registration transformations with the same forward projections, *i.e.*, there is no moving between two time points and the forward projections are taken from exactly the same position for both two data sets. However, we simulate different random noise for these two forward projections, and we test with our three DBT simulation data sets with different noise levels (details of the noise, which follows a normal distribution, are described later in Section 5.5.6). Eventually, we compare the signal to noise ratio (SNR) of the results of the sequential and iterative methods. The SNR can be calculated using Equations 5.25 and 5.26, in which $\frac{A_{\text{signal}}}{A_{\text{noise}}}$ is the amplitude ratio in digital signal processing context, and we can use the maximum, minimum and standard

deviation of the image to calculate the SNR in decibel (dB) of a given image.

$$\text{SNR}_{\text{dB}} = 20 \log_{10} \left(\frac{A_{\text{signal}}}{A_{\text{noise}}} \right) \quad (5.25)$$

$$= 20 \log_{10} \left(\frac{\max(\text{Image}) - \min(\text{Image})}{\text{std}(\text{Image})} \right) \quad (5.26)$$

Results: Figure 5.19 (a)-(c) shows the noisy forward projections of the fixed images with different levels of added noise. In this experiment the fixed and moving images are identical; however, there are different random noise has been added. In Table 5.1, we compare the SNR of the reconstructed moving image ($\hat{T}_C \hat{f}_2$) using the sequential and iterative methods. The results of SNR consistently show that our iterative method obtained larger SNR than the sequential method at the same noise level. As the added noise increased, the SNR of both methods converged to similar values.

Table 5.1: *Comparison of the signal to noise ratio using identity registration transformations with the same forward projections. We test on four different noise levels, i.e., 0.1%, 1%, 10%, and 100% of the maximum intensity of the forward projections. Iter: iterative method; Seqn: sequential method.*

DBT Simulations \ SNR	0.1% noise	1% noise	10% noise	100% noise
Toroid Phantom (Iter)	41.61	27.98	18.06	7.34
Toroid Phantom (Seqn)	29.51	20.71	14.63	6.90
Uncompressed Breast MRI (Iter)	29.45	24.37	19.90	12.86
Uncompressed Breast MRI (Seqn)	25.75	22.51	18.14	12.37
In-vivo DBT simulation (Iter)	29.61	20.03	9.30	8.12
In-vivo DBT simulation (Seqn)	26.30	14.87	8.48	6.73

Conclusion: The results suggest that for more forward projection data with random noise our iterative method is capable of increasing the SNR combining all the data acquired at different time points.

5.5.2 Hypothetical Experiment HA2: Test on the Different Forward Projections with Known Registration Parameters

Hypothesis 2: Due to moving between two time points, there is a potentially enlarged angular range of data acquisition that can alleviate the null-space problem.

Experiment: In this experiment, we test on the digital toroid phantom images. We simulate a simple affine transformation, which has been applied to the fixed image to create the ground truth moving image, with a translation of $\mathcal{T}_{\text{translation}} = [10, 0, -20]\text{mm}$ and a rotation about the y axis of -30 degree. Instead of running registration after finish reconstruction in the sequential method or iteratively performing registration and reconstruction in our iterative method, we provide the correct ground truth of the transformation for the registration step. Therefore, in this experimental setting, the reconstruction quality is only depending on the angular range of data acquisition, and it will not be degraded due to any registration error.

Results: Figure 5.12 shows that the image appearance of the results of our iterative method with correct registration transformations is superior than the results produced using the sequential method.

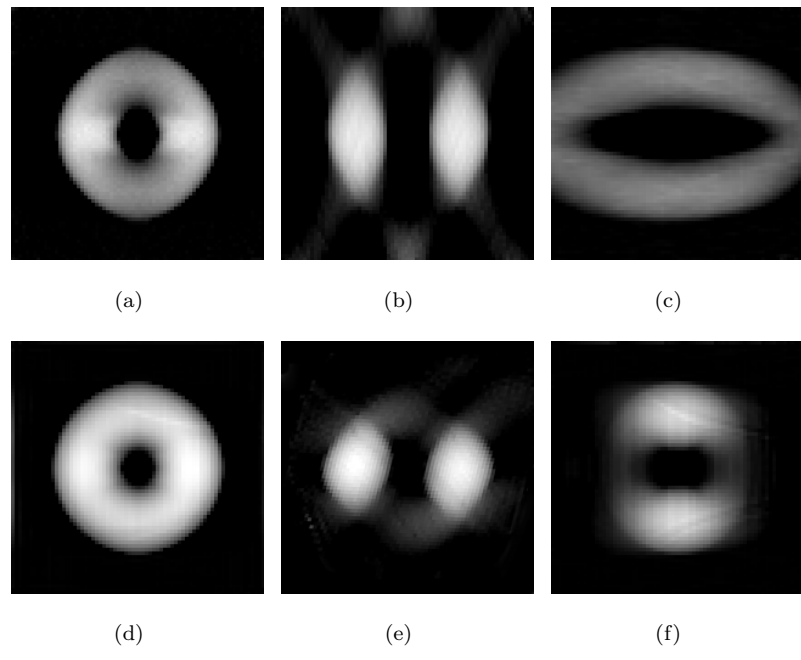


Figure 5.12: Results of the sequential method and the iterative method when the correct registration transformations have been provided. (a)-(c): Results of the sequential method; (d)-(f): Results of the iterative method. (Left: Coronal view; Middle: Transverse view; Right: Sagittal view. Original ground truth of the fixed and moving images are shown below in Figure 5.13 (a) and (e))

Conclusion: There are many possible reasons of enlarging the view angles, *e.g.*, rotation, shearing, and compression of the object; however, most of the enlargement is gained from the rotation of the

object imaged between two time points. The potentially enlarged angular range of data acquisition can reduce the null-space, and therefore reduce the out-of-plane artefacts and produce a more compact reconstruction.

5.5.3 Experiment IA1: Test on the DBT Simulation Using Synthetic Toroid

In the first set of two experiments a 3D toroidal phantom image was created and rigidly transformed via parameters R_ζ using a translation of $\mathcal{T}_{\text{translation}} = [10, 0, -20]\text{mm}$ and a rotation about the y axis of -30 degree (Figure 5.13). As seen in Figure 5.13. (f) and (h), the *iterative* results are more compact and accurate than the *sequential* results Figure 5.13. (b) and (d), and the out of plane blurring is reduced (coloured squares). The sum of squared differences (SSD) $\|f_1^* - f_1^g\|^2$ is decreased by an order of magnitude (10^{11} to 10^9); however, for the *iterative* method this value of 4.32×10^9 is superior to the *sequential* result of 6.89×10^9 . Plot of the cost function $f(f_1) = \frac{1}{2} \|Af_1 - p_1\|^2$ represented in Equation 5.12 for both sequential and combined methods are shown in Figure 5.14.

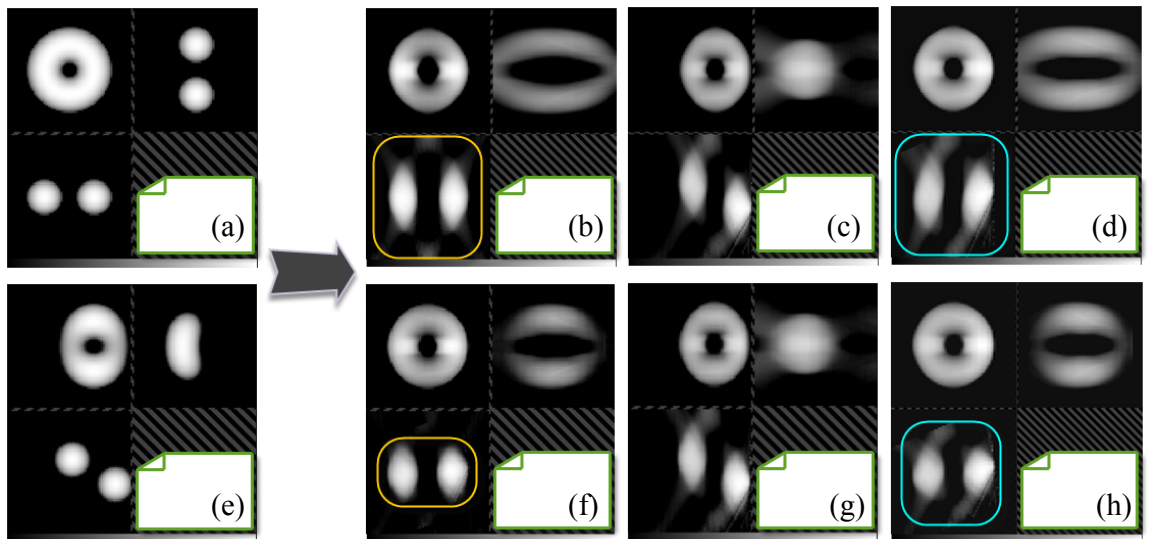


Figure 5.13: (a) Original test volume f_1^g ; (e) Transformed test volume f_2^g ; Sequential results (b)-(d): (b) reconstruction f_1^* , (c) reconstruction f_2^* , and (d) transformed reconstruction $\mathcal{T}_\zeta^* f_2^*$; Iterative results (f)-(h): (f) reconstruction f_1^* , (g) reconstruction f_2^* , and (h) transformed reconstruction $\hat{\mathcal{T}}_\zeta \hat{f}_2$.

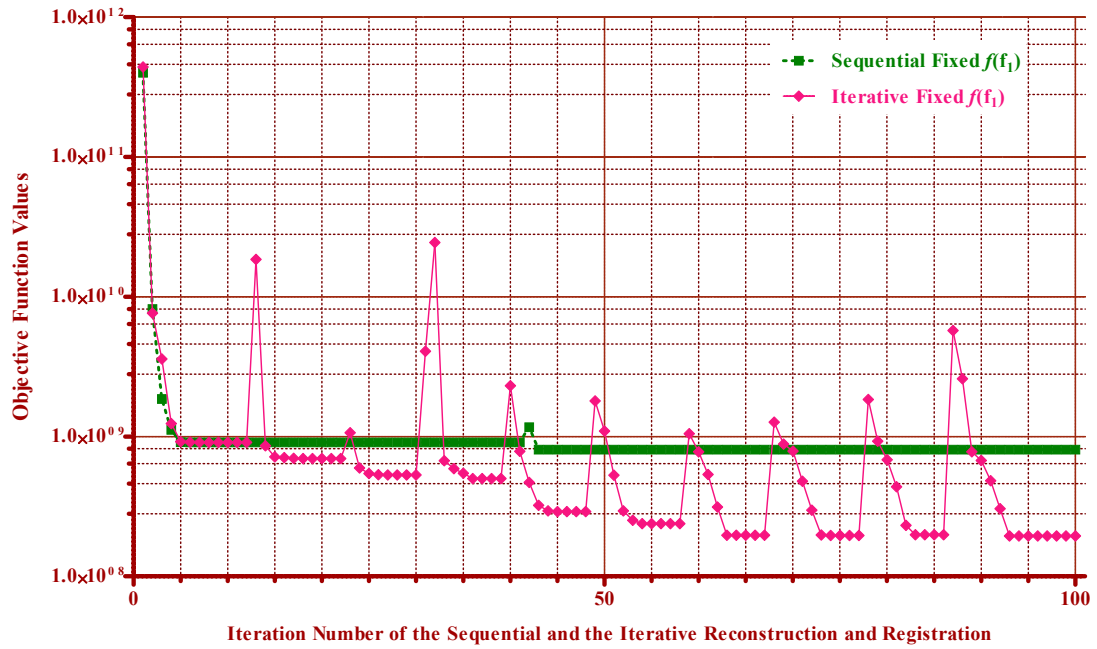


Figure 5.14: Plot of the cost function $f(f_1) = \frac{1}{2} \|Af_1 - p_1\|^2$ for the 3D toroid experiment. In this graph, we plot the cost function value with respect to the iteration number for both sequential and iterative methods. There are 100 iterations in total and the cost function values are the same for both methods at the first iteration. For the sequential method, we have got a cost function which is decreasing smoothly. In contrast, the iterative method updates f_1 with the transformation of \hat{f}_2 , i.e., $\hat{T}_\zeta \hat{f}_2$, after 10 iterations of the reconstruction and a single registration. This results in the increasing and peaks in the cost function plot of the iterative method (including the initial first iteration).

5.5.4 Experiment IA2: Test on the DBT Simulation Using Uncompressed MRI

In the second set of two experiments the same transformation was applied to a 3D breast MR image that obtained similar behaviour (the SSD comparison gives *iterative* 1.25×10^8 vs. *sequential* 1.42×10^8 decreased from 1.71×10^{11}) illustrated in Figure 5.15. There is a black region with sharp edge at the bottom of both Figure 5.15 (h) and (d) due to the transformed image Figure 5.15 (e) falling outside of the field of view. However, a better reconstruction for the missing data in Figure 5.15 (f) is obtained due to our incorporation of all the X-ray acquisitions into the reconstruction of x_1 . The corresponding cost functions are shown in Figure 5.16.

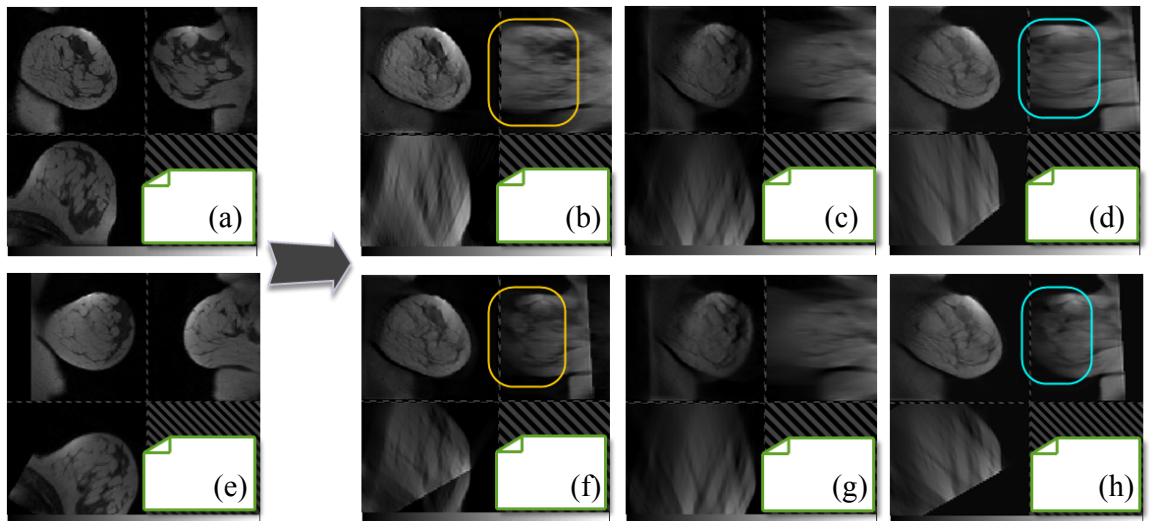


Figure 5.15: As Figure 5.13 but for a 3D uncompressed breast MR image.

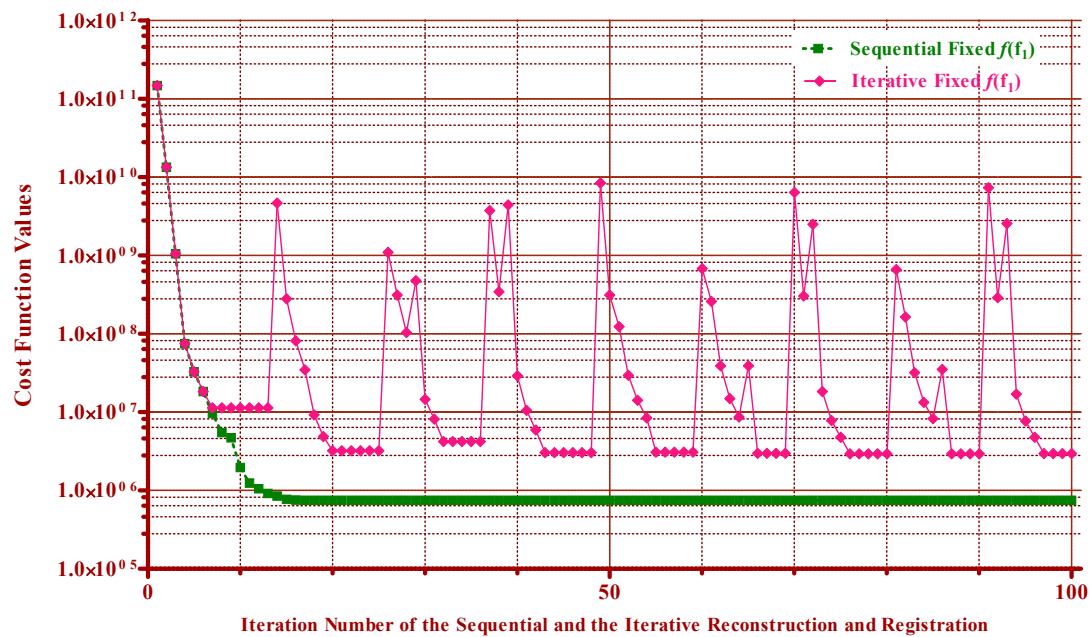


Figure 5.16: As Figure 5.14 but for the 3D uncompressed breast MR image.

5.5.5 Experiment IA3: Test on the DBT Simulation with In-Vivo Compression

In this set of two experiments we tested the methods using two MRI acquisitions obtained before and after application of a lateral-to-medial plate compression of the breast (Figure 5.17). The SSD between reconstruction, f_1^* , and the original volume, f_1^g , indicates that the *iterative* method produces a more accurate reconstruction of the data (the SSD comparison gives *iterative* 5.90×10^9 vs. *sequential* 7.60×10^9 decreased from 6.91×10^{11}). In addition, the affine transformation model is insufficient for the compression deformation, which may degrade the reconstructed results; however, measurement of the target registration error for a set of 12 user defined landmarks, indicates that the *iterative* method also produces a more accurate registration result (4.6mm vs. 8.6mm, given an initial misregistration of 23.6mm). The corresponding cost functions are shown in Figure 5.18.

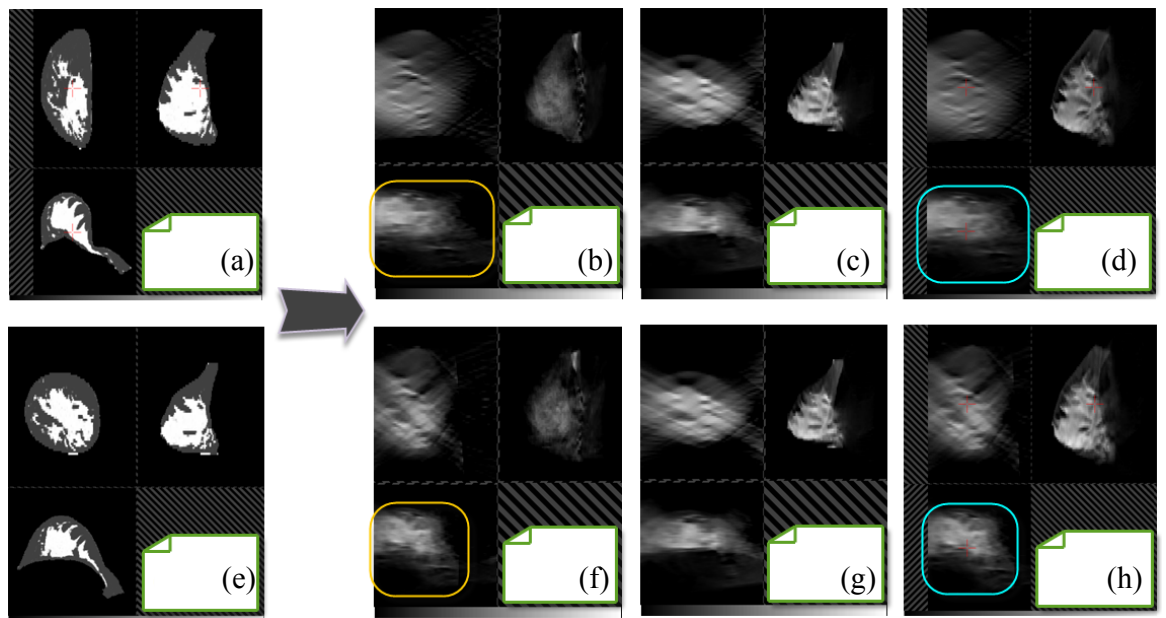


Figure 5.17: As Figure 5.13 but applied to in-vivo MRI acquisition of a breast before and after plate compression (Images have been segmented and mapped to effective X-ray attenuation).

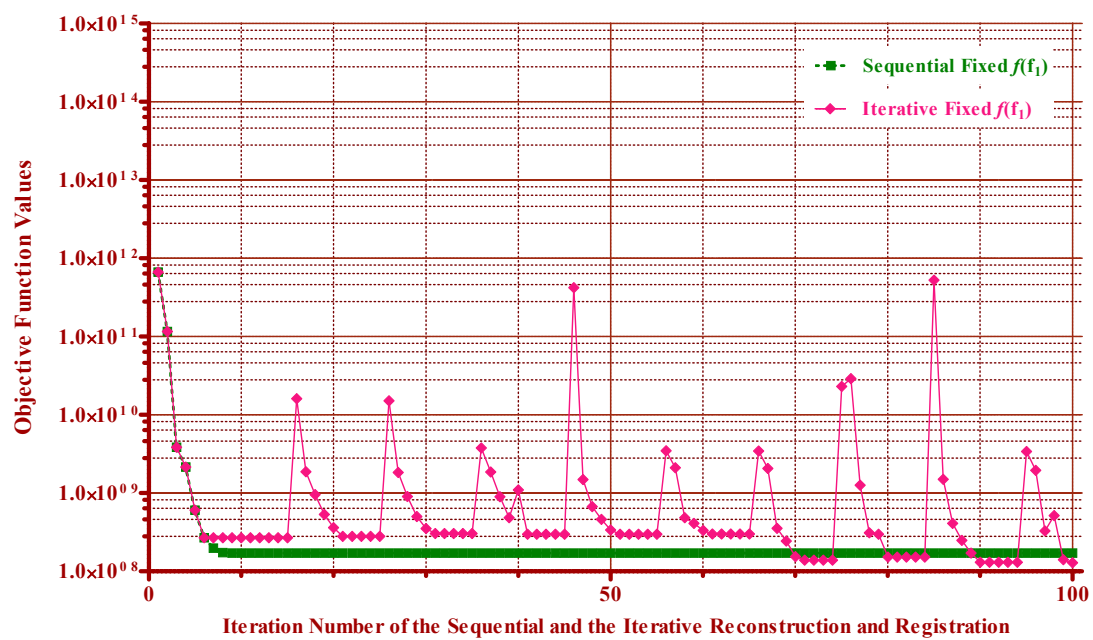


Figure 5.18: As Figure 5.14 but for the in-vivo compressed DBT simulation experiment.

All the numerical results (SSD and TRE described in the validation Section 5.4.3) of the three experiments above are shown in the Table 5.2 below. In addition, Table 5.3 shows the corresponding relative error.

Table 5.2: *Numerical results of the three experiments. (SSD = $\|f_1^* - f_1^g\|^2$)*

	Initial	Sequential Method	Iterative Method
Toroid Phantom	4.51×10^{11}	6.89×10^9	4.32×10^9
Misregistration TRE (mm)	19.6	8.6	5.1
Uncompressed Breast MRI	1.71×10^{11}	1.42×10^8	1.25×10^8
Misregistration TRE (mm)	31.2	17.4	15.2
In-vivo DBT simulation	6.91×10^{11}	7.60×10^9	5.90×10^9
Misregistration TRE (mm)	23.6	8.6	4.6

Table 5.3: *Comparison of the relative error, which is defined by $\frac{\|f_1^* - f_1^g\|^2}{\|f_1^g\|^2}$.*

	Initial	Sequential Method	Iterative Method
Toroid Phantom	1	0.0153	0.0096
Uncompressed Breast MRI	1	0.0008	0.0007
In-vivo DBT simulation	1	0.0110	0.0085

5.5.6 Experiment IA4: Test on the Noisy Data

In X-ray radiography, image quality is not only determined by spatial resolution but also affected by image contrast and hence noise. Noise is generated by many random processes in X-ray imaging. Firstly, X-ray photons leave the source in a random pattern that follows a Poisson distribution. This is generally designated quantum noise, and the Poisson distribution can be approximated using a Normal distribution if there are a large number of detected photons per pixel. Secondly, the number of photons captured by the detector creates the detector noise, which may follow a Normal distribution [35]. Furthermore, there are many other sources of noise such as the number of photons passing unaffected through the object. The difference between noise and artefacts is that the latter can be reproduced if the same scan is repeated. In addition, we can analyse the noise using *contrast to noise ratio*, or *image signal to noise ratio*.

A discrete random vector \mathbf{X} has a Poisson distribution with independent components if its multivariate PDF is

$$\mathcal{M}(\mathbf{x}; \eta) = \begin{cases} \prod_{n=1}^N \frac{e^{-\eta_n} \eta_n^{x_n}}{x_n!}, & \text{for } \mathbf{x}_n > 0 \\ 0, & \text{otherwise} \end{cases}, \quad (5.27)$$

in which the mean is η and the variance is also η , and the Poisson distribution is denoted by

$$\mathbf{X} \sim \mathcal{N}_{\text{Poisson}}(\eta). \quad (5.28)$$

A continuous random vector \mathbf{X} has a Normal distribution, or Gaussian distribution if its multivariate probability density function (PDF) is

$$\mathcal{M}(\mathbf{x}; \psi, \sigma^2) = \frac{1}{\sqrt{2\pi\sigma^2}} e^{-\frac{(\mathbf{x}-\psi)^2}{2\sigma^2}}, \quad (5.29)$$

in which the mean is ψ and the variance is σ^2 , and the Normal distribution is denoted by

$$\mathbf{X} \sim \mathcal{N}_{\text{Normal}}(\psi, \sigma^2). \quad (5.30)$$

Instead of simulating a complex noise model, we simply add noise, which follows a normal distribution, for both forward projections of the temporal data sets, *i.e.*, p_1 and p_2 in Equations 5.6 and 5.7. We defined four different noise levels, *i.e.*, 0.1%, 1%, 10%, and 100% of the maximum intensity of the forward projections (examples of noisy forward projections in Figure 5.19). Finally, we performed our iterative method on these four pair of noise data sets, and compared to the sequential alterna-

tive. Results from the noisy forward projections show that our iterative method has consistently outperformed the sequential method as seen in Figures 5.20, 5.21, and 5.22, in which we plot the relative error against four different noise levels. The relative error is defined by $\frac{\|f_1^* - f_1^g\|^2}{\|f_1^g\|^2}$ as before.

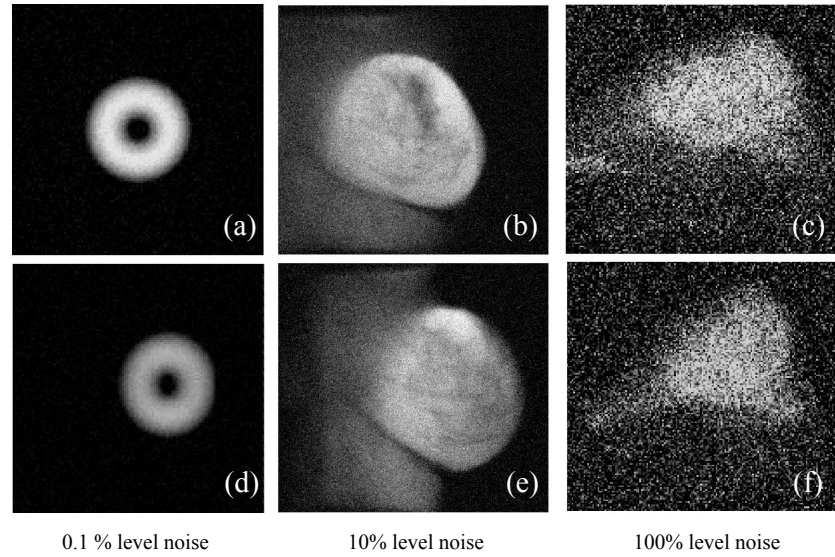


Figure 5.19: *Noisy forward projections.* (a)-(c): Forward projections of the fixed images. (d)-(f): Forward projections of the corresponding moving images. The images present different noise levels.

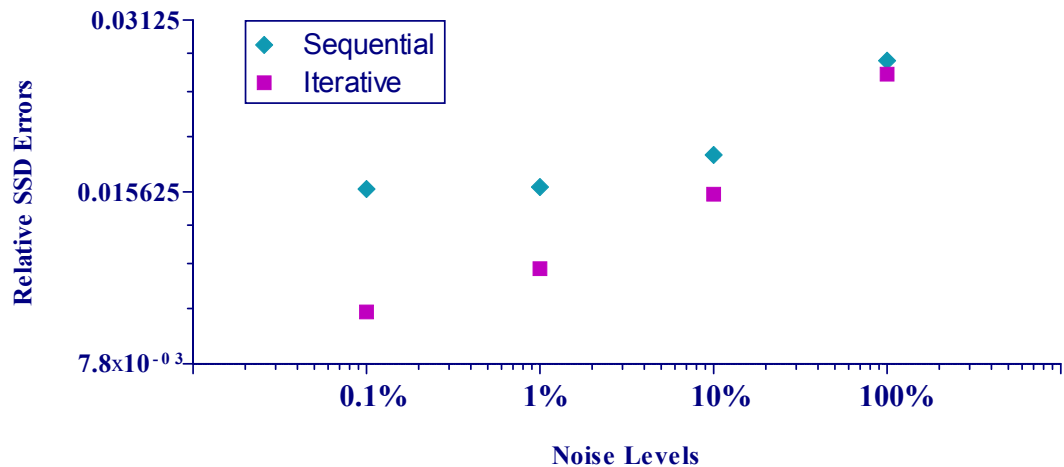


Figure 5.20: *Plot of the relative error against different levels of noise using the toroid phantom.*

From the comparison of relative errors against different levels of noises, we have confirmed that our iterative method performed at least as well as the sequential method using three various DBT

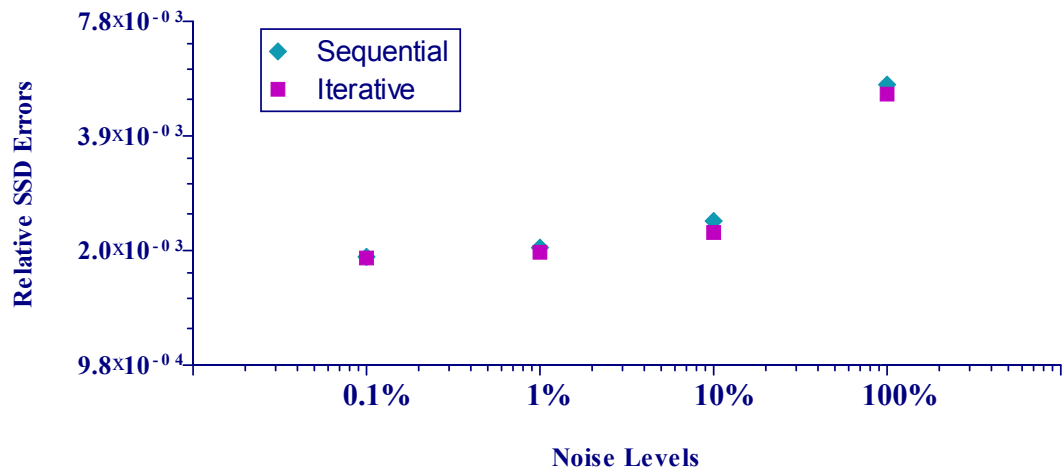


Figure 5.21: As Figure 5.20 but for the uncompressed breast MRI experiment.

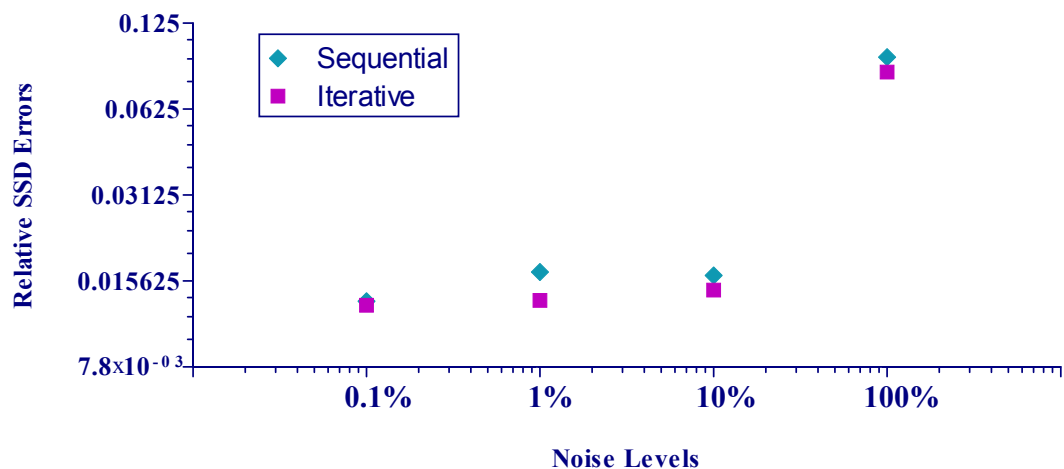


Figure 5.22: As Figure 5.20 but for the in-vivo compressed DBT simulation experiment.

simulations (Figures 5.21 and 5.22). Both iterative and sequential methods possess a certain level of noise tolerance. From the experiments on the toroid phantom images (as seen in Figure 5.20), the relative errors of the iterative method increased much more rapidly compared to the sequential method. Surprisingly, a possible argument is that the sequential method provides a more stable result than the iterative method under noisy environment that is not as we anticipated. However, we believe another rationalisation for this is that when the initial noise level is high, *e.g.*, 100% of the maximum intensity, we actually reconstruct random noise in both sequential and iterative methods, and there is a convergence of the relative error for both methods. In addition, as mentioned in Section 3.2.3 before, the DBT systems obtain highly incomplete projection data with low noise. Therefore, our test with noise level of 10% and 100% of the maximum intensity are far more crucial than the real case, and they can be considered as the extreme tests.

5.5.7 Experiment IA4: Test on Different Displacements

The objective of this experiment is to test the correlations of the reconstruction precision and registration accuracy with respect to various initial displacements. Based on the two hypothetical experiments in Sections 5.5.1 and 5.5.2, our hypothesis of this experiment is that the large initial displacement introduced by the rotation of the subject can improve the reconstruction quality by reducing the null-space problem, but the final TRE will be increased.

The main reduction of the null-space problem between two time points is introduced by the rotation of the subject; therefore, we have fixed the translation displacements ($\mathcal{T}_{\text{translation}} = [10, 0, -20]\text{mm}$) in this experiment but vary the differences by rotation angles of the subject. In addition, consider of the real case of DBT scan, there are 45 degrees rotation difference between the standard CC and MLO views. As we simulated the scans taken at different time points but with one view DBT; thus, we set the rotation angles in this experiment from -19 to 19 degrees, which is sufficiently large compared to the real situation that the breast subject need to be placed within two compress plates and calibrated before scanning.

Furthermore, we have divided the range of rotation angles into three levels, *i.e.*, low (-7 to 0 and 0 to 7 degrees), medium (-13 to -8 and 8 to 13 degrees), and high displacement (-19 to -14 and 14 to 19 degrees) levels. Also, we perform the experiments with different noise level described in Section 5.5.6 before, where there are two levels of noise has been added (1% and 10%) and compared to the situation without any noise. Results are shown in Figure 5.23, which we plot the initial and final TRE with respect to the three different initial rotation levels. Essentially, the TREs have been reduced when the initial displacement levels are decreasing in both data sets.

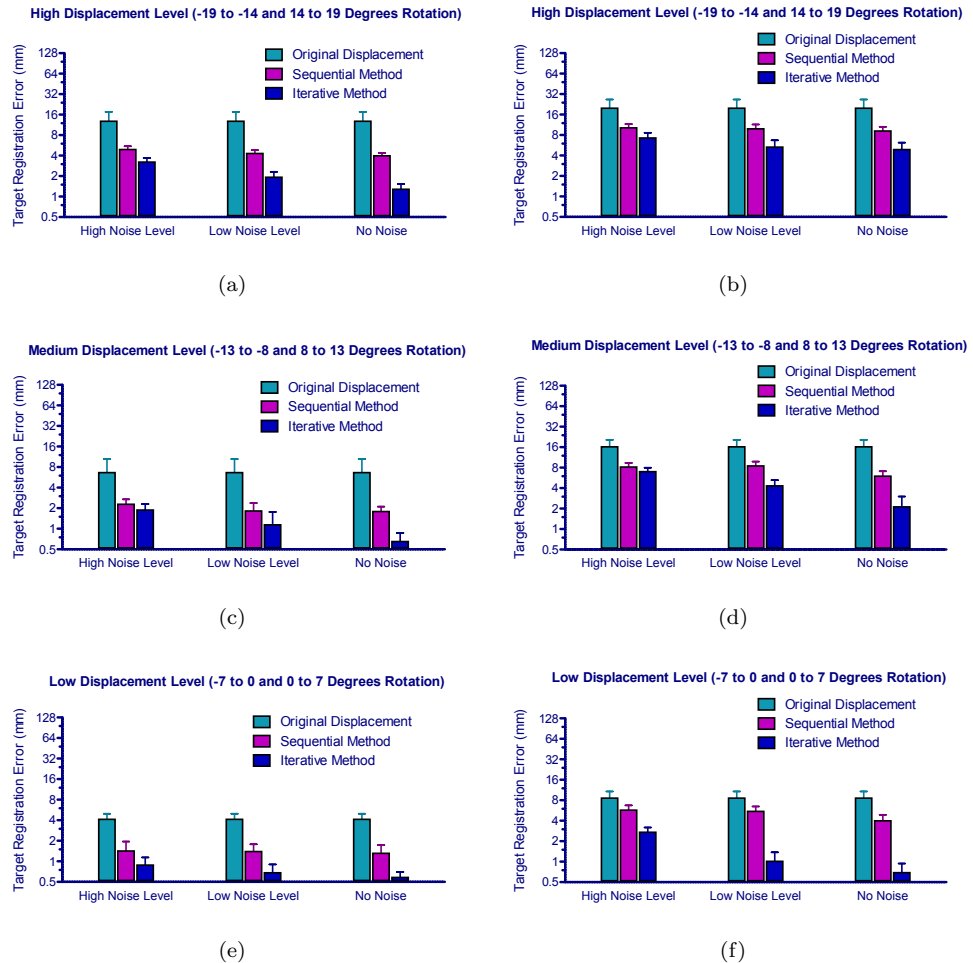


Figure 5.23: Experiment on different initial displacements (rotation levels) and TRE (on \log_2 scale). (a), (c), and (e): Test on the toroid phantom image showing initial and final TRE with respect to the various initial rotation levels; (b), (d), and (f): The same test on the breast MRI images.

In addition, we compared the final SSD errors with respect to the initial displacement (Figure 5.23), *i.e.*, different rotation levels. Results on the toroid phantom (Figure 5.23 (a), (c), and (e)) shows that the final SSD errors have been increased in both sequential and iterative methods as displacement level decreasing, but the iterative method has always outperformed the sequential method. According to the SSD error, firstly, we can demonstrate that the iterative method has obtained better reconstruction fidelity; secondly, even though the larger deformation has degraded the recovery of the registration parameters (Figure 5.23), its less null-space has improved the reconstruction results. However, the situation of the experiments on the breast MR images (Figure 5.23 (b), (d), and (f))

show that the smaller initial displacement produced superior reconstruction regarding to the SSD error. We attribute this to the fact that the transformation has moved the breast MR images to the out of FOV; therefore, smaller initial displacement retains the breast volume inside FOV and consequently outputs lower SSD. In other words, the SSD error due to out of FOV has dominated the final SSD comparison.

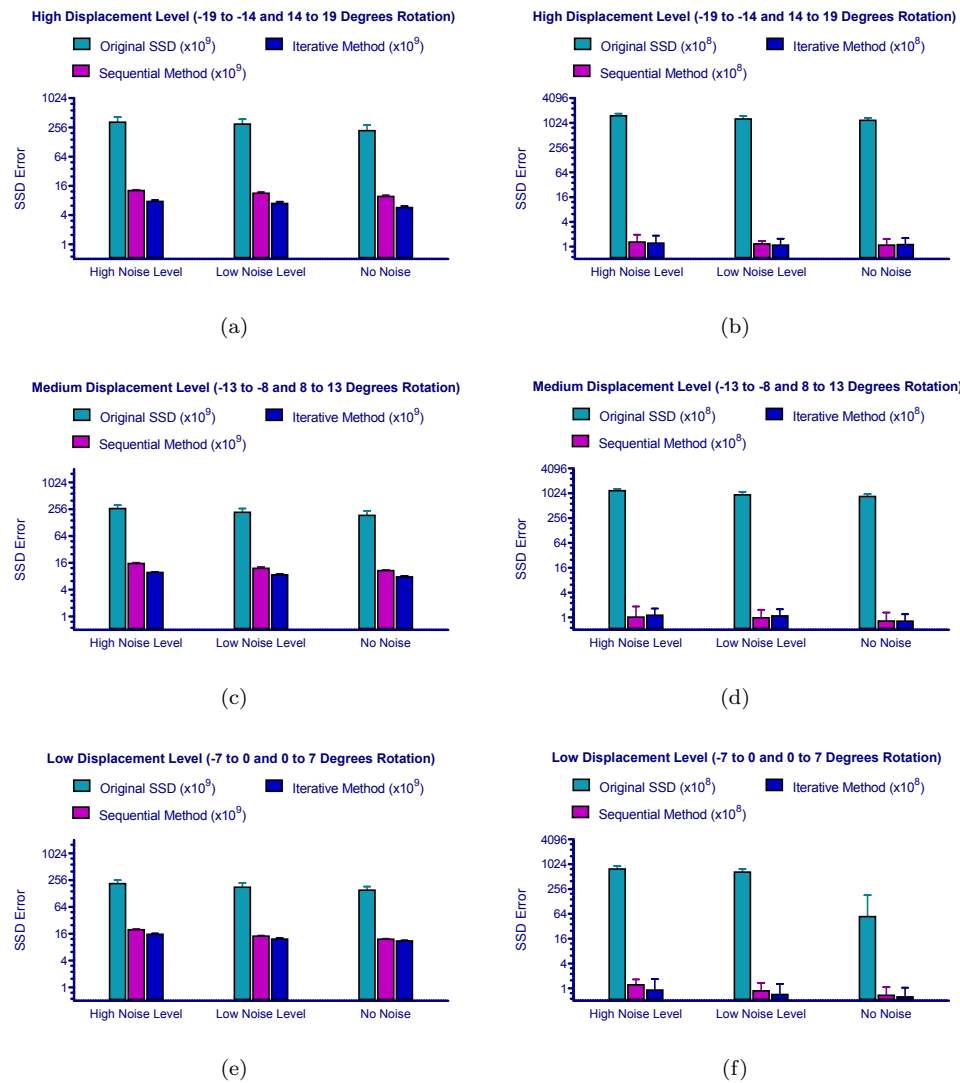


Figure 5.24: Experiment on different initial displacements (rotation levels) and SSD error (on log₂ scale). (a), (c), and (e): Test on the toroid phantom image showing initial and final SSD with respect to the various initial rotation levels; (b), (d), and (f): The same test on the breast MRI images.

5.6 Conclusions and Discussion

Our iterative method has been found to produce superior results in optimised cost function value, registration accuracy and reconstructed image appearance. This is illustrated in Figure 5.25. We attribute this to the fact that the iterative approach uses all the X-ray acquisition data (both p_1 and p_2) to reconstruct volume f_1 . This leads to an improvement in the reconstruction of f_1 which in turn enables a more accurate registration to reconstructed volume f_2 to be achieved.

An implicit assumption in this approach is that there is no change in the breast (such as the growth of a tumour or due to the differences in image acquisition parameters) between the two time-points being reconstructed and registered, justifying the use of SSD as the registration similarity metric. Given this approach, we could envisage a subsequent step where we compare reconstruction volume f_1 with the original acquisitions, p_1 and p_2 , to detect change.

The iterative method updates f_1 with the transformation of \hat{f}_2 , *i.e.*, $\hat{\mathcal{T}}_\zeta \hat{f}_2$, after 10 iterations of the reconstruction and a single registration. This results in the peaks in the cost function plot for the iterative method when compared to the smooth plot for the sequential method, Figures 5.14, 5.16 and 5.18. In Figure 5.16, the final cost function value of the sequential method is less than our iterative method because the MR volume has been transformed beyond the field of view (f_2^g in Figure 5.15). This region is visible in the simulated projection images, p_1 . The result is that the sequential method produces a lower value of the cost function, $f(f_1) = \frac{1}{2} \|Af_1 - p_1\|^2$, due to greater image overlap despite the reconstruction (and registration) being less successful.

To sum up, firstly, we have developed a method to iteratively reconstruct and register temporal DBT data sets and tested it using various DBT simulations, *i.e.*, digital toroid phantom images, breast MRI volume, and DBT simulation with real compressions. According to the test results on these DBT simulations, we can conclude that our iterative method could retain the registration accuracy while producing successful reconstruction. From the digital synthesised phantom images to DBT simulations with in-vivo plate compressions, we perform our tests on a case that is closer and closer to a real situation. Secondly, compared to the conventional sequential method, our method always produced more compact results, which significantly reduced the out-of-plane artefacts caused by the nature of the null-space problem of the limited-angle reconstruction. Our findings of comparison between our iterative method and the sequential method is consistent with all the simulation data, and they are also in accordance with the results under simulated noisy environment and various initial displacements (quantified using different rotation levels). In addition, the evidence from the study on the hypothetical experiments, *i.e.*, testing on identity registration transformations with

the same forward projections and different forward projections with known registration parameters, suggests that the iterative method should obtain superior results because of two reasons. First, more 2D forward projection data can average out random noise. Second, potentially larger angular range of data capture can alleviate the null-space problem.

However, we are aware that our research on the iterative method may have three limitations. First, the results of the combined iterative method is dependent on the original moving or overlapping between the captured data in two time points. Very small moving (large overlapping) between two time points will not be sufficient to reduce the null-space artefacts, but very small overlapping will degrade the registration accuracy. To find an optimised overlapping rate is beyond the scope of the thesis, but it is an interesting topic to explore. Moreover, currently there is no examining protocol to control the overlapping ratio in clinical environment; therefore, the effectiveness of our iterative method in real clinical case could be arbitrarily dependent on the position of breast placed on the compression plate. Second, both sequential and iterative methods produced the reconstruction of the fixed image and transformed moving image reconstruction, which could confuse the comparison in real clinical case, *e.g.*, the registration might not be perfect and there are certain differences between the fixed image reconstruction and the transformed moving image reconstruction. Third, the updating of the iterative method is not symmetric. The symmetrical attribute of similarity measurement is crucial to image registration. The symmetrical property states that the obtained transformation should be the inverse of the transformation obtained when the order of the fixed and moving images is reversed [43]. Otherwise, if the obtained transformation is asymmetrical, there are differences, which is known as the inverse inconsistency, between registration results obtained when registering images in different registration directions [238]. There are some investigations have solved the asymmetrical problem by altering the cost function to include an inverse transformation term for the registration procedure; however, it will severely increase the computational complexity especially for an iterative method as we proposed. The last two concerns of our iterative method have arisen and urged us to develop a simultaneous method of combining reconstruction and registration. In spite of the shortcomings of our iterative method, it provides a springboard for a new way to perform reconstruction and registration in DBT applications.

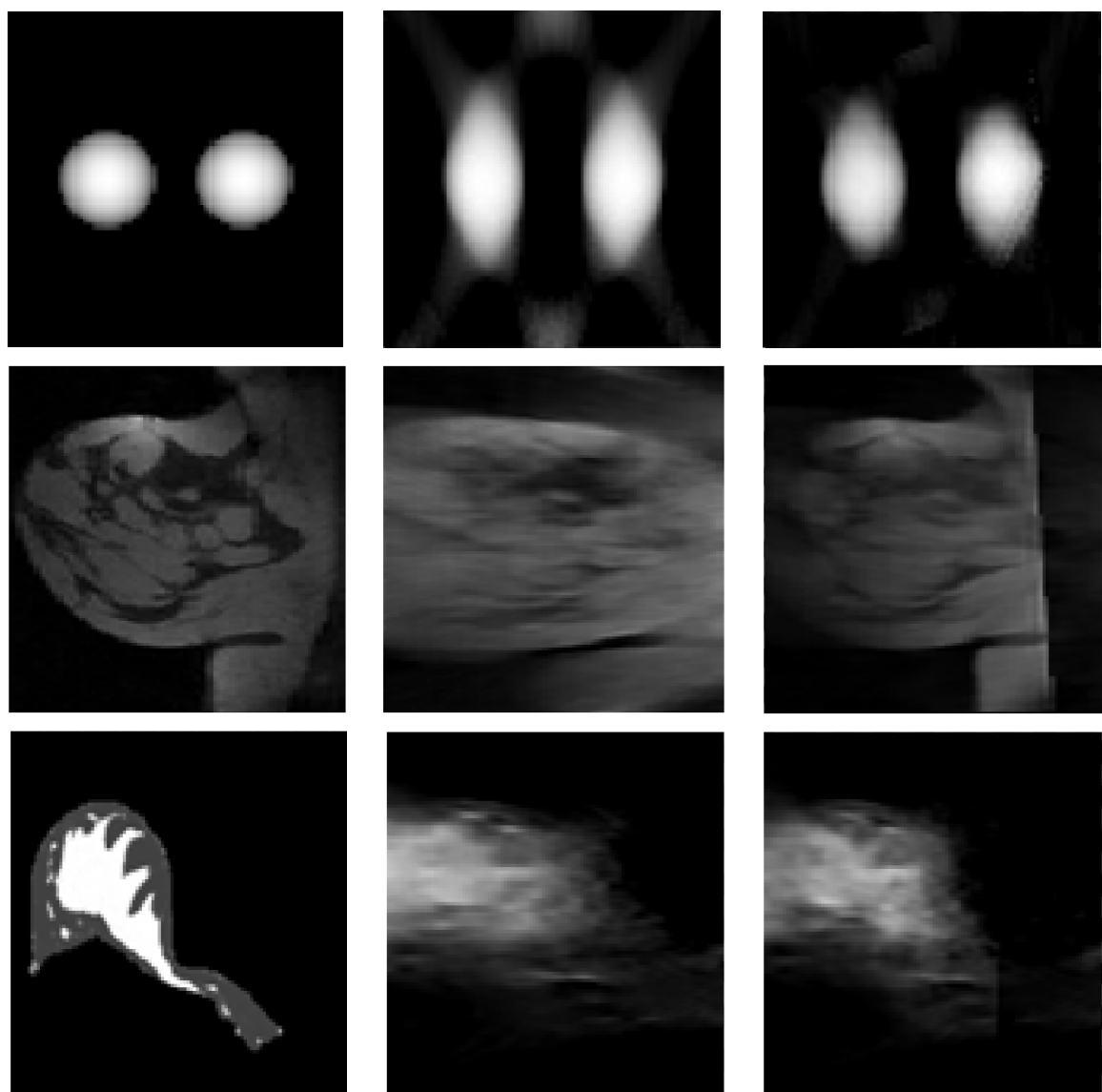


Figure 5.25: Magnified results of the three tests above. (a), (b) and (f) of figures 5.13, 5.15 and 5.17. Left to right: Original fixed image f_1^g ; Results of the sequential method f_1^s ; Results of the iterative method f_1^* . Only one of the out-of-plane slices have been shown accordingly.

Simultaneous Reconstruction and Registration

In this chapter, we present a new model for combining reconstruction and registration tasks using DBT geometry setting. Rather than perform these two tasks sequentially or iteratively, we propose an innovative model, which combines reconstruction of a pair of temporal DBT acquisitions with their simultaneous registration. In addition, we approach this nonlinear inverse problem using a decoupled optimisation scheme, and explore the suitability of the model for estimating the transformations with the image intensities. To evaluate the performance of our method we also use 3D software synthetic images, breast MR images, and DBT simulations from MRI with in-vivo breast compressions. Both affine and B-spline transformation models are studied. We show that, compared to the conventional sequential method, jointly estimating image intensities and transformations gives superior results with respect to both the reconstruction fidelity and the registration accuracy. Work from this chapter is based on and extends [334] [335] [336] [337].

6.1 Motivation

In Chapter 5, we presented a method that can find the affine registration parameters with the reconstruction iteratively. We now direct our interest more specifically towards a simultaneous method to combine these two tasks. In the conventional sequential method and our iterative method, we have two reconstructed volumes, *i.e.*, the fixed image reconstruction f_1^* and the transformed moving image reconstruction $\hat{\mathcal{T}}_\zeta \hat{f}_2$. We can compare both of these volumes to the original fixed image f_1^g ; however, this will result in ambiguity. Moreover, if we only compare the transformed moving image reconstruction to the original fixed image, the other reconstruction f_1^* is a waste.

The workflow in which DBT would be used clinically, involves two key tasks: reconstruction, to generate a 3D image of the breast, and registration, to enable images from different visits to

be compared as is routinely performed by radiologists working with conventional mammograms. Rather than separate these two tasks and perform them sequentially or iteratively, we investigate the technique of combining them simultaneously, and test the hypothesis that the performance of the joint estimation with a unified reconstruction will be of benefit to each task.

6.2 Problem Outline

Based on the motivation and hypothesis above, we have developed an algorithm, which outputs one unified result (*i.e.*, image) for the reconstruction and registration. However, the introduction of registration introduces nonlinearity of the transformation parameters making the solution of the inverse problem more complex. Although the following experiments were performed using both affine and B-spline transformation models and SSD as the objective function, other non-rigid transformations and alternative similarity measurements can naturally be substituted into our simultaneous framework. The remainder of this chapter will be organised as follows. We describe a general framework for our *simultaneous algorithm* in the context of forward and inverse problems. Subsequently, we propose a decoupled approach to solve this simultaneous reconstruction and registration problem. In addition, we also investigate previous research into combining reconstruction and registration in other applications. We devote the rest of this chapter to explaining our experiment materials, solution of the simultaneous method, and testing results with discussions.

6.2.1 Forward and Inverse Problems

According to the discussions in Chapters 3 and 4, we form the general forward and inverse models for the reconstruction and registration problems in Equations 3.58 and 4.22. The forward problem remains the same in our simultaneous framework, *i.e.*, the forward projected imaging for the reconstruction part and image warping with ground truth transformation parameters or deformation field for the registration part. Furthermore, in Chapter 5, we propose an iterative method to solve these equations. Instead of combining the two tasks iteratively, we can also create a joint functional to combine them simultaneously that is

$$\{f^*, \zeta^*\} = \arg \min_{f, \zeta \in \mathbb{R}^n} \left(f(f, \zeta) = \mathcal{D}(Af, p_1) + \mathcal{D}(A\mathcal{T}_\zeta f, p_2) + \lambda \mathcal{R}(f) \right), \quad (6.1)$$

in which f represents the unknown intensities we want to reconstruct, and ζ is the unknown transformation parameters or deformation field. The equation is optimised for a given p_1 and p_2 , which are

two temporal data sets with DBT settings. A denotes the forward projection matrix that is defined by both volume size and projection size. \mathcal{R} is an optional regularisation term with weights λ . \mathcal{T}_ζ is a nonlinear operator, which is used to describe the transformations between the temporal data sets.

6.2.2 Decoupled Approach

In Chapters 3 and 4, we have discussed tomographic reconstruction and registration with their applications in DBT separately. In this section, we give a general overview of past-to-present literatures on combining these two tasks in various applications.

Table 6.1: *Comparison of different applications of simultaneous inverse problem. (SR: super-resolution; LR: low resolution; fwdProjs: forward projections; Recon.+Regn.: reconstruction and registration; “–”: not mentioned).*

Publications	Application	Dimension	Optimisation	Optimiser	Data
Chung et al. 2006	SR	2D Affine	Decoupled	Gauss-Newton	32 LR images
He et al. 2007	SR	2D Rigid	Decoupled	Conjugate Gradient	5 LR images
Yap et al. 2009	SR	2D Rigid	Decoupled	Linear Interior Point	5 LR images
Jacobson and Fessler 2003	PET	3D Affine	Decoupled	Gradient Descent	64 fwdProjs 180°
Fessler 2010	PET	3D –	Decoupled	Conjugate Gradient	–
Odille et al. 2008	MRI	3D Affine	Decoupled	GMRES	–
Schumacher et al. 2009	SPECT	3D Rigid	Decoupled	Gauss-Newton	60 to 64 fwdProjs 360°
Yang et al. 2005	Cryo-EM	3D Rotation	Decoupled	Quasi-Newton (L-BFGS)	84 fwdProjs
Chung et al. 2010	Cryo-EM	3D Rigid	Decoupled	Quasi-Newton (L-BFGS)	799 fwdProjs
Our Recon.+Regn. Model	DBT	3D Affine & B-spline	Decoupled	Conjugate Gradient or L-BFGS	22 fwdProjs 50° ($\pm 25^\circ$)

So far, to the best of our knowledge there are little previous research have combined the reconstruction and registration (Table 6.1). There are mainly three types of applications, *i.e.*, super-resolution, motion-correction for medical imaging modalities like PET, SPECT and MRI, and 3D density map reconstruction from 2D cryo-electron microscopy (Cryo-EM) images.

First, the process of combining a set of low resolution images into a single high-resolution image is often referred to as super-resolution (SR). The SR problem involves registration and restoration (a.k.a reconstruction, but we avoid using this term in order to prevent confusion with the tomographic reconstruction of our DBT problem). Most of the previous research separated these two tasks for the SR problem. Chung et al. [45] elucidated a simultaneous mathematical framework that enabled us to combine the problem of estimating the displacements with restoring the high-resolution image.

He et al. [104] and Yap et al. [340] also proposed algorithms to integrate 2D rigid image registration into the image SR problem.

Second, due to the long acquisition times in medical imaging modalities such as PET, SPECT and MRI, patient motion is inevitable and constitutes a serious problem for any reconstruction algorithm. Many algorithms use a gating system or even breath-holding to mitigate the motion effect. In [125] Jacobson and Fessler reported a method to jointly estimate image and deformation parameters in motion-corrected PET imaging. Odille et al. [218] presented a coupled system to perform a motion-compensated reconstruction, and subsequently optimised the motion model for MRI. In 2009, Schumacher et al. [254] used the combined reconstruction and motion correction method in SPECT imaging. Recently, Fessler [75] proposed the novel idea of using an optimisation transfer, *a.k.a.*, majorise-minimise method, to find a surrogate objective function to simplify the original simultaneous functional for motion-compensated PET reconstruction.

For the Cryo-EM imaging application, Yang et al. [330] described a simultaneous method to refine a 3D density map and the orientation parameters of the 2D projections, which were used to reconstruct this map. And Chung et al. [46] furthered this idea using parallel computing to speed up the application.

There are a few difficulties when using a generic optimisation method to solve the simultaneous inverse problem *directly*. First, we do not take the algorithmic advantage of the fact that the reconstruction part of the inverse problem is linear and strongly convex in f . Subsequently, the obstacle is that, besides applying small step length due to the nonlinearity induced by ζ , it can be hard to find appropriate preconditioners for the simultaneous system which will make the solution even more computational expensive.

We therefore look at alternative techniques, *e.g.*, *the decoupled approach*, to solve this kind of simultaneous inverse problem. However, as far as we are aware, this is the first time that this technique has been applied to temporal DBT data sets. We test our algorithm with both affine and B-spline transformation models using nonlinear conjugate gradient or L-BFGS optimisers (Table 6.1).

6.3 Materials

Under the experimental settings, we test our algorithm with both affine and B-spline transformation models. Firstly, we use the same synthetic toroid phantom, uncompressed breast MRI, and DBT simulation with in-vivo compression with increased realism for the affine model (as seen in Section

5.3). Secondly, we opted for a 3D Shepp-Logan phantom to test our algorithm with the B-spline model (Figure 6.22). The 3D Shepp-Logan has been chosen because: first, it is a widely used 3D phantom image, which can be easily generated in different resolutions, to test tomographic reconstruction algorithms; second, simple but distinct structures of this 3D phantom image could demonstrate the efficacy of our simultaneous method clearly. In addition, a 3D breast phantom image was also tailored for use with the B-spline model because it is more realistic to test our algorithm under the breast imaging context (Figure 6.31).

6.4 Simultaneous Method

6.4.1 Simultaneous Method

In this section, we elaborate on our simultaneous algorithm using a *decoupled* approach to solve the inverse problem of combining reconstruction and registration. The framework can be outlined algorithmically as seen in Algorithm 2.

Algorithm 2: Simultaneous Reconstruction and Registration

Input: p_1, p_2 .

Output: f^*, ζ^* .

```

begin
    % Initialise f to a vector with all zero entries
    % Initialise  $\zeta$  to a vector of the reshaped identity matrix  $I$ 
    f := 0;
     $\zeta := I;$ 

    % Calculate matrix A for the forward projection
    % Matrix  $A^T$  represents the backward projection
    A := RAYCASTING(SIZE(f));

    % Simultaneous reconstruction and registration loop
    for  $k$  iterations do
         $\{f^*, \zeta^*\} = \arg \min_{f, \zeta} \left( f(f, \zeta) = \frac{1}{2} (\|Af - p_1\|^2 + \|A\zeta f - p_2\|^2) \right)$ 
        % Output f* and  $\zeta^*$ 
        f*;
         $\zeta^*.$ 

```

Firstly, according to Equation 6.1, the objective function is described as

$$\{f^*, \zeta^*\} = \arg \min_{f, \zeta} \left(f(f, \zeta) = \frac{1}{2} (\|Af - p_1\|^2 + \|A\zeta f - p_2\|^2) \right), \quad (6.2)$$

in which p_1 and p_2 are the two input X-ray (DBT) acquisitions, *i.e.*, forward projections. In addition, f denotes the estimation of the unknown volume, and ζ is the estimation of the parametric transformations.

A minimiser $\{f, \zeta\} \in \mathbb{R}^n$ of $f(f, \zeta)$ is characterised by the necessary condition that the partial derivative with respect to f and ζ equals zero. The partial derivative with respect to f is straightforward, and is given by

$$g(f) = \frac{\partial f(f, \zeta)}{\partial f} = A^T(Af - p_1) + \mathcal{T}_\zeta^* A^T(A\mathcal{T}_\zeta f - p_2), \quad (6.3)$$

in which $g(f)$ is the gradient with respect to f , and \mathcal{T}_ζ^* is the adjoint operator of \mathcal{T}_ζ (Section 6.4.2.1). Similarly, the corresponding Hessian can be expressed as

$$H(f) = \frac{\partial f(f, \zeta)}{\partial^2 f} = A^T A + \mathcal{T}_\zeta^* A^T A \mathcal{T}_\zeta. \quad (6.4)$$

To derive the partial derivative with respect to ζ , we apply a small perturbation to the objective function and the linearisation under the norm yields,

$$\begin{aligned} & f(f, \zeta + \Delta\zeta) \\ &= \frac{1}{2} \left(\|Af - p_1\|^2 + \|A\mathcal{T}_\zeta + \Delta\zeta f - p_2\|^2 \right) \end{aligned} \quad (6.5)$$

$$\approx \frac{1}{2} \left(\|Af - p_1\|^2 + \|A\mathcal{T}_\zeta f + A \frac{\partial \mathcal{T}_\zeta}{\partial \zeta} f \Delta\zeta - p_2\|^2 \right). \quad (6.6)$$

By taking the derivative with respect to $\Delta\zeta$, and equating the result to zero, we obtain that

$$\left(A \frac{\partial \mathcal{T}_\zeta}{\partial \zeta} f \right)^T \left(A\mathcal{T}_\zeta f + A \frac{\partial \mathcal{T}_\zeta}{\partial \zeta} f \Delta\zeta - p_2 \right) = 0; \quad (6.7)$$

and if $g(\zeta)$ and $H(\zeta)$ denote the gradient and Hessian with respect to ζ respectively then we have,

$$\left(A \frac{\partial \mathcal{T}_\zeta}{\partial \zeta} f \right)^T \left(A \frac{\partial \mathcal{T}_\zeta}{\partial \zeta} f \right) \Delta\zeta = - \left(A \frac{\partial \mathcal{T}_\zeta}{\partial \zeta} f \right)^T \left(A\mathcal{T}_\zeta f - p_2 \right), \quad (6.8)$$

and therefore, we can derive

$$\Delta\zeta = - \left[\left(A \frac{\partial \mathcal{T}_\zeta}{\partial \zeta} f \right)^T \left(A \frac{\partial \mathcal{T}_\zeta}{\partial \zeta} f \right) + \lambda I \right]^{-1} \left(A \frac{\partial \mathcal{T}_\zeta}{\partial \zeta} f \right)^T \left(A\mathcal{T}_\zeta f - p_2 \right), \quad (6.9)$$

in which,

$$g(\zeta) = \frac{\partial f(f, \zeta)}{\partial \zeta} = \left(A \frac{\partial \mathcal{T}_\zeta}{\partial \zeta} f \right)^T \left(A \mathcal{T}_\zeta f - p_2 \right) = \left(A \mathcal{T}'_\zeta f \right)^T \left(A \mathcal{T}_\zeta f - p_2 \right),$$

and

$$H(\zeta) = \left(A \frac{\partial \mathcal{T}_\zeta}{\partial \zeta} f \right)^T \left(A \frac{\partial \mathcal{T}_\zeta}{\partial \zeta} f \right) = \left(A \mathcal{T}'_\zeta f \right)^T \left(A \mathcal{T}'_\zeta f \right).$$

In order to apply a generic non-linear conjugate gradient or L-BFGS optimiser, we extract the gradients of the objective function with respect to f and ζ below

$$\begin{aligned} \nabla f(f, \zeta) = g(f, \zeta) &= \begin{pmatrix} \frac{\partial f(f, \zeta)}{\partial f} \\ \frac{\partial f(f, \zeta)}{\partial \zeta} \end{pmatrix} \\ &= \begin{pmatrix} A^T (Af - p_1) + \mathcal{T}_\zeta^* A^T (A \mathcal{T}_\zeta f - p_2) \\ \left(A \mathcal{T}'_\zeta f \right)^T \left(A \mathcal{T}_\zeta f - p_2 \right) \end{pmatrix}. \end{aligned} \quad (6.10)$$

Diagnosing the problem is one thing, solving it is another. From previous research, we find that none of these published studies solved the simultaneous reconstruction and registration directly (Table 6.1 shows). Therefore, we also opt for a decoupled approach to solve our combined problem. The reason for this approach is because the objective function in Equation 6.2 is a nonconvex function of the transformation parameters ζ and therefore very challenging to minimise. As in these previous studies we can simplify the simultaneous optimisation using the decoupled alternating minimisation technique, where we update f holding ζ fixed and vice versa, *i.e.*, the $n+1$ -th estimation can be represented by the n -th estimation that are

$$f^{n+1} = \arg \min_f f(f, \zeta^n), \quad (6.11)$$

$$\zeta^{n+1} = \arg \min_\zeta f(f^{n+1}, \zeta), \quad (6.12)$$

and the gradients become

$$g(f)^{n+1} = A^T (Af - p_1) + \mathcal{T}_{\zeta^n}^* A^T (A \mathcal{T}_{\zeta^n} f - p_2), \quad (6.13)$$

$$g(\zeta)^{n+1} = \left(A \mathcal{T}'_\zeta f^{n+1} \right)^T \left(A \mathcal{T}_\zeta f^{n+1} - p_2 \right). \quad (6.14)$$

Solving the simultaneous inverse problem using the decoupled optimisation is totally different from the sequential method or the iterative method described in [332] and [333]. First, the gradient

with respect to the image intensities is not a simple addition of the derivative in equations 5.8 and 5.9 because here we estimate only one volume rather than two as in the sequential or iterative methods. Accordingly, we have one unified result instead of two reconstructions, which need to be registered in a further step. More significantly, because of the presence of the system matrix A in the gradient formulation in equation 6.14, the simultaneous concept is more challenging than a typical image registration problem described in equation 5.11, *i.e.*, registering two complete reconstructions in the sequential method or current estimates of the two incomplete reconstructions in the iterative method.

6.4.2 Transformation Operator

6.4.2.1 Adjoint Operator

The adjoint operator of the transformation, which is denoted by \mathcal{T}^* , is used in solving our inverse problem. The definition of adjoint operator in the context of linear transformations on finite dimensional vector spaces is straightforward. As we can access the matrices of the linear transformations, the adjoint of such a matrix is the same as its transpose.

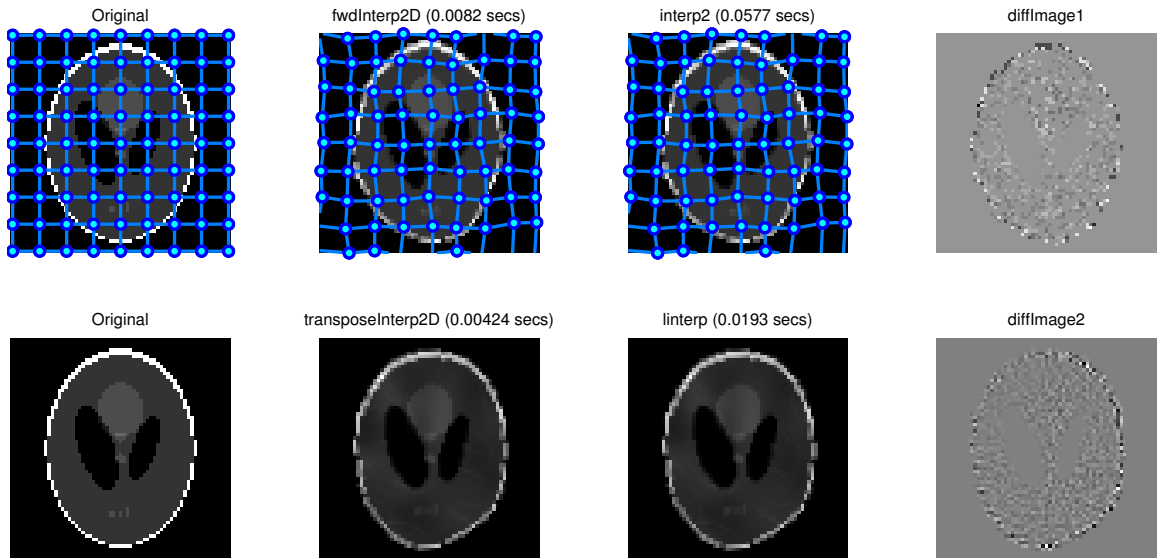


Figure 6.1: 2D results of the interpolation operation and its transpose. First row: Forward interpolation with deformed grid on; Second row: transpose of the interpolation. From left to right: Original image; Implementation using C with Matlab MEX interfaces; Implementation using Matlab; Difference images between two implementations. The results have shown that our C implementation is faster and accurate.

More generally, the adjoint operator, which is also known as the Hermitian conjugate, can be defined by

$$\langle \mathcal{T}(f_1), f_2 \rangle = \langle f_1, \mathcal{T}^*(f_2) \rangle \quad (6.15)$$

in which $\langle \cdot, \cdot \rangle$ is the inner product. In addition, f_1 and f_2 are arbitrary vectors such that $\forall f_1, f_2 \in H_s$, and H_s denotes the Hilbert space that is a vector space with an inner product with respect to the associated norm. Although \mathcal{T} is nonlinear with respect to the transformations ζ , it is linear with respect to the image intensities f . Because $\mathcal{T}_\zeta f = T[\mathcal{T}_\zeta(x)]$, and therefore

$$\mathcal{T}_\zeta^* f = \mathcal{T}_\zeta^T f = T^T[\mathcal{T}_\zeta(x)], \quad (6.16)$$

in other words, the transpose of an image transformation is the transpose of an interpolation operation. We implemented both the image interpolation (bilinear interpolation) and its transpose operation using C with Matlab MEX interfaces (2D example in Figure 6.1 and 3D example in Figure 6.2). Additionally, we validated our implementation using Equation 6.15, in which we use an arbitrary image to test various transformations, and we have always obtained the same inner product results.

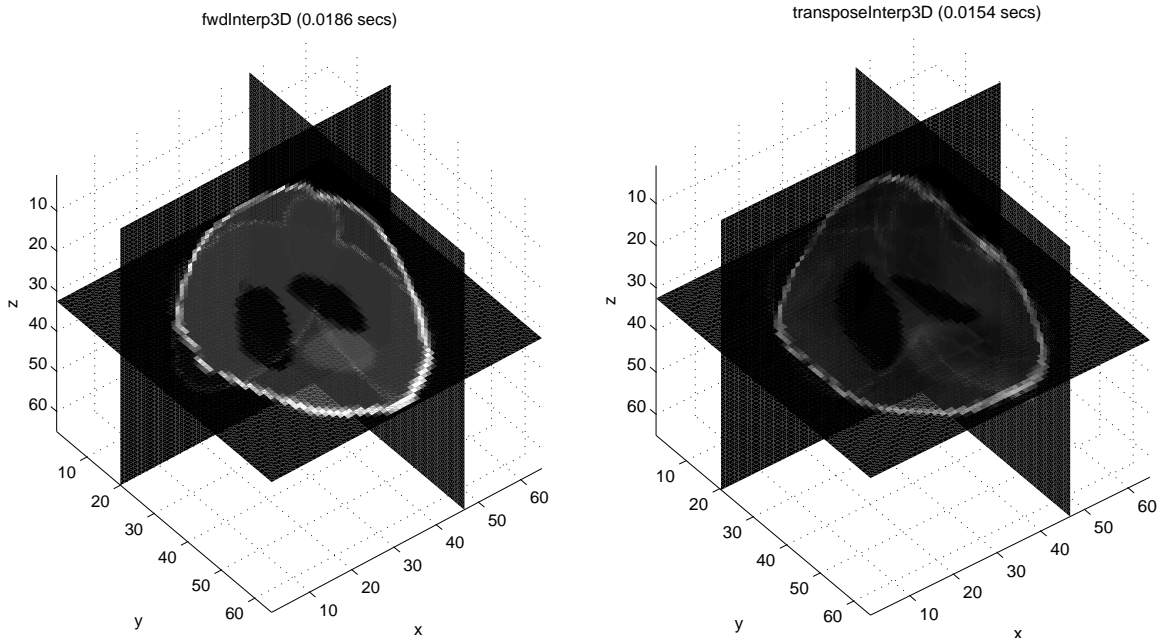


Figure 6.2: 3D results of the interpolation operation (Left) and its transpose (Right).

6.4.2.2 Derivative Operator

The derivative of the transformation is a crucial component of this method and has great impact on the result of optimisation. The analytical derivative of the transformation is fast, yet its implementation is difficult because we must first formulate the derivative of the underlying interpolation. In addition, many interpolation schemes have no analytical derivative; therefore, we can choose to use the Finite Difference Method (FDM) to approximate the derivative operation. Similarly to Equation 5.21, we can derive that the gradient with respect to the transformations is

$$g(\zeta) = \left(A\mathcal{T}'_\zeta f \right)^T \left(A\mathcal{T}_\zeta f - p_2 \right) \quad (6.17)$$

$$= \left(\frac{\partial T[\mathcal{T}_\zeta(x)]}{\partial \mathcal{T}_\zeta(x)} \right)^* \frac{\partial \mathcal{T}_\zeta(x)}{\partial \zeta} A^T (A\mathcal{T}_\zeta f - p_2). \quad (6.18)$$

In addition, we summarise the gradient information we used for the iterative and simultaneous methods in Table 6.2. Alternatively, instead of implementing the gradient using this analytical form, we can also use FDM with central difference to calculate \mathcal{T}'_ζ that is

$$\mathcal{T}'_\zeta \approx \frac{\mathcal{T}_{\zeta+\epsilon} + \mathcal{T}_{\zeta-\epsilon}}{2\epsilon} \quad (6.19)$$

given a small number ϵ .

Table 6.2: Comparison of the gradient information used in the iterative and simultaneous methods.

	Reconstruction Part	Registration Part
Iterative Method	$g(f_1) = A^T(Af_1 - p_1)$ $g(f_2) = A^T(Af_2 - p_2)$	$g(\zeta) = (\hat{R}(x) - \hat{T}[\mathcal{T}_\zeta(x)]) \frac{\partial \hat{T}[\mathcal{T}_\zeta(x)]}{\partial \mathcal{T}_\zeta(x)} \frac{\partial \mathcal{T}_\zeta(x)}{\partial \zeta}$
	Intensity Part	Transformation Part
Simultaneous Method	$g(f) = A^T(Af - p_1) + \mathcal{T}_\zeta^* A^T (A\mathcal{T}_\zeta f - p_2)$	$g(\zeta) = \left(\frac{\partial T[\mathcal{T}_\zeta(x)]}{\partial \mathcal{T}_\zeta(x)} \right)^* \frac{\partial \mathcal{T}_\zeta(x)}{\partial \zeta} A^T (A\mathcal{T}_\zeta f - p_2)$

6.4.2.3 Implementation and Experimental Settings

Our simultaneous reconstruction and registration method is implemented in the Matlab environment with several C based routines with MEX interfaces in order to speed up the application. In particular, we test with both affine and B-spline transformation models in this chapter. The affine transformation model has been described in Section 4.1.2 with 12 parameters, which globally describe the translation, scaling, rotation and shearing between the two time points. We compare the results of our simultaneous method with the sequential alternative. In addition, we opt for a transformation

depicted by uniform cubic B-splines, which are based on tensor B-spline modelling and have the uniform knot-vector, to investigate the efficacy of our method with non-rigid transformations. One of the principal merits of using the B-spline transformation model is the local support property, *i.e.*, a single span of a B-spline curve is only controlled by a limited number of control points. For the uniform cubic B-spline model, the blending function, or basis function, can be expressed by

$$\beta(x) = \begin{cases} \frac{|x|^3}{2} - |x|^2 + \frac{2}{3}, & \text{for } 0 \leq |x| \leq 1 \\ \frac{-(|x|-2)^3}{6}, & \text{for } 1 \leq |x| \leq 2 \\ 0, & \text{otherwise} \end{cases} \quad (6.20)$$

Additionally, in a real implementation, we can use the Kronecker product to compute the 3D tensor product of a 1D uniform cubic B-spline, which is defined by three sets of knots. Furthermore, the knots are placed equidistantly along each dimension, and the cubic B-spline basis function extends over 4 knot intervals in one dimension. Essentially, there are several methods to handle the boundary conditions, *e.g.*, placing 3 additional knots on top of the boundary knot or extending the knots evenly to the outside of the image. we have chosen the second method, which possesses a free boundary. Thus, we can define the displacement $\mathbf{u} = (u^1, u^2, u^3)$ as

$$u^1(\mathbf{x}) = u^1(x, y, z) = \sum_{i=1}^l \sum_{j=1}^m \sum_{k=1}^n \beta_i^1(x) \beta_j^2(y) \beta_k^3(z) q_{ijk}^1 \quad (6.21)$$

$$u^2(\mathbf{x}) = u^2(x, y, z) = \sum_{i=1}^l \sum_{j=1}^m \sum_{k=1}^n \beta_i^1(x) \beta_j^2(y) \beta_k^3(z) q_{ijk}^2 \quad (6.22)$$

$$u^3(\mathbf{x}) = u^3(x, y, z) = \sum_{i=1}^l \sum_{j=1}^m \sum_{k=1}^n \beta_i^1(x) \beta_j^2(y) \beta_k^3(z) q_{ijk}^3 \quad (6.23)$$

We use matrices to store the basis function values that are

$$\{Q^1\}_i = \beta_i^1(x); \quad \{Q^2\}_j = \beta_j^2(y); \quad \{Q^3\}_k = \beta_k^3(z), \quad (6.24)$$

and the displacement can be written in vector-matrix form by the Knnonecker product as

$$\mathbf{u}(\mathbf{q}) = Q^1 \circledast Q^2 \circledast Q^3 \mathbf{q}, \quad (6.25)$$

in which q is a vector containing all the B-spline weights, and the Knonecker product \circledast calculates the matrix of matrices of quantities obtained by multiplying each component of Q^1 with each component of Q^2 . An example of B-spline transformation and the deformed grid has shown in Figure 6.3. In addition, we also contrast the results of the sequential method and our simultaneous method using the image appearance, the SSD error and the TRE (Section 5.4.3).

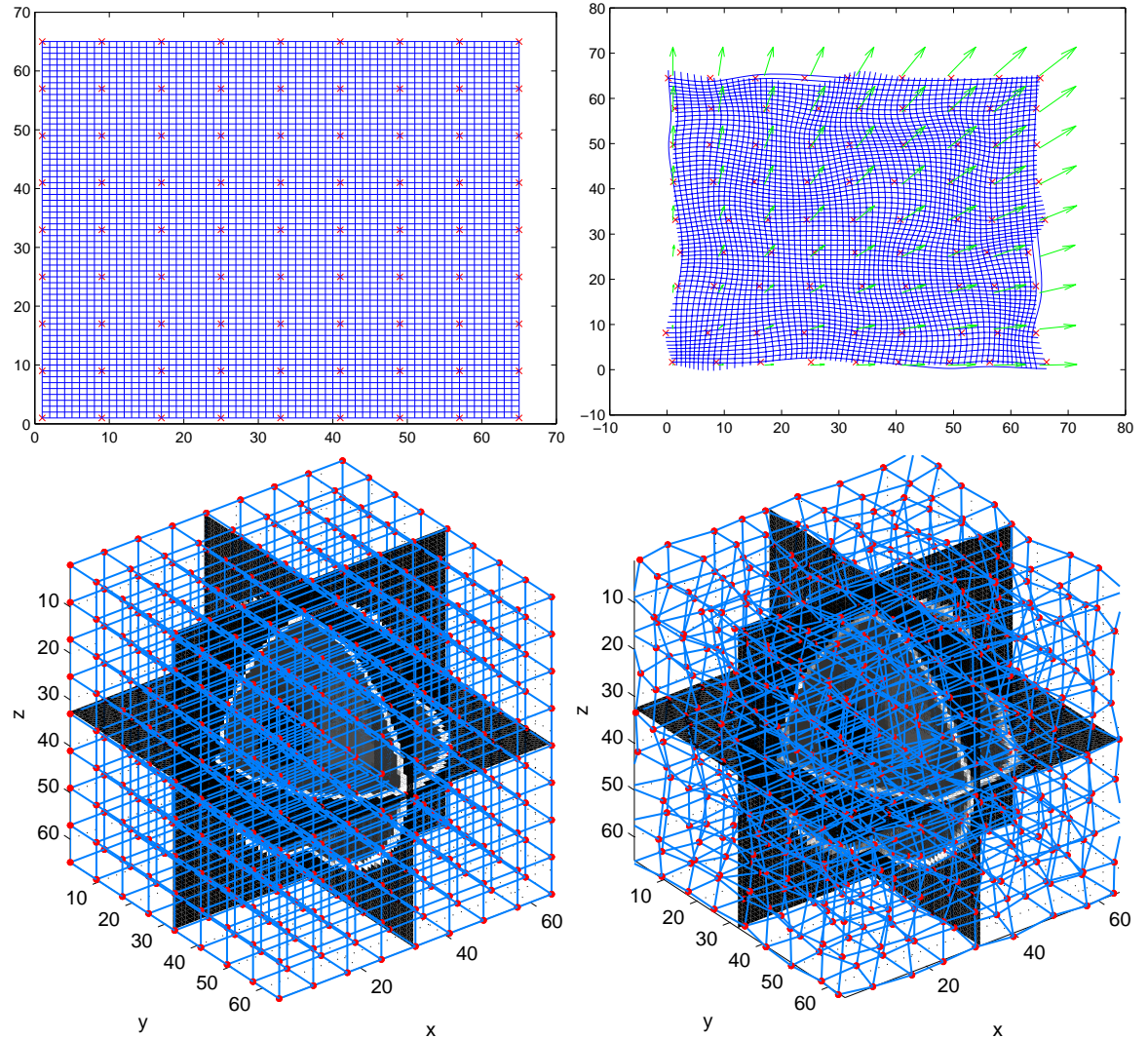


Figure 6.3: *B-spline transformation example. Top Row: Regular grid (Left) and B-spline transformed grid (Right) of the x-y plane centre slice; Bottom Row: Original mesh (Left) with control points and its B-spline transformation (Right). The original 3D Shepp-Logan phantom image has $65 \times 65 \times 65$ voxels, and there are $9 \times 9 \times 9$ control points (red points) placed equidistantly along each dimension.*

6.5 Experiments and Results using the Affine Model

6.5.1 Experiment SA1: Test on the DBT Simulation Using Synthetic Toroid

Figure 6.4 (a)-(c) shows a toroid phantom (as seen in Section 5.5.3), which was created for all the tests in this experiment. We performed 20 different sets of affine transformations to test the robustness of our simultaneous method. Affine test case 1 is presented here as an example (Figure 6.4 (d)-(f)). The results of the two different methods, *i.e.*, sequential *vs.* simultaneous, were compared. We found that there were much less artefacts in the results of our simultaneous method than the results of the sequential method (Figure 6.4 (g)-(i) *vs.* Figure 6.4 (j)-(l)); however, from the difference images in Figure 6.6 (g)-(i), we could still find small radial artefacts. From Figure 6.7 we can also compare our unified simultaneous result to the reconstruction results without registration, and it shows that our result has got benefit from using both temporal data sets. The absolute errors between the recovered parameters and the ground truth of the transformations were calculated. The results showed that the recovery of the parameters was accurate and persistent for all the 20 tests (Figure 6.5).

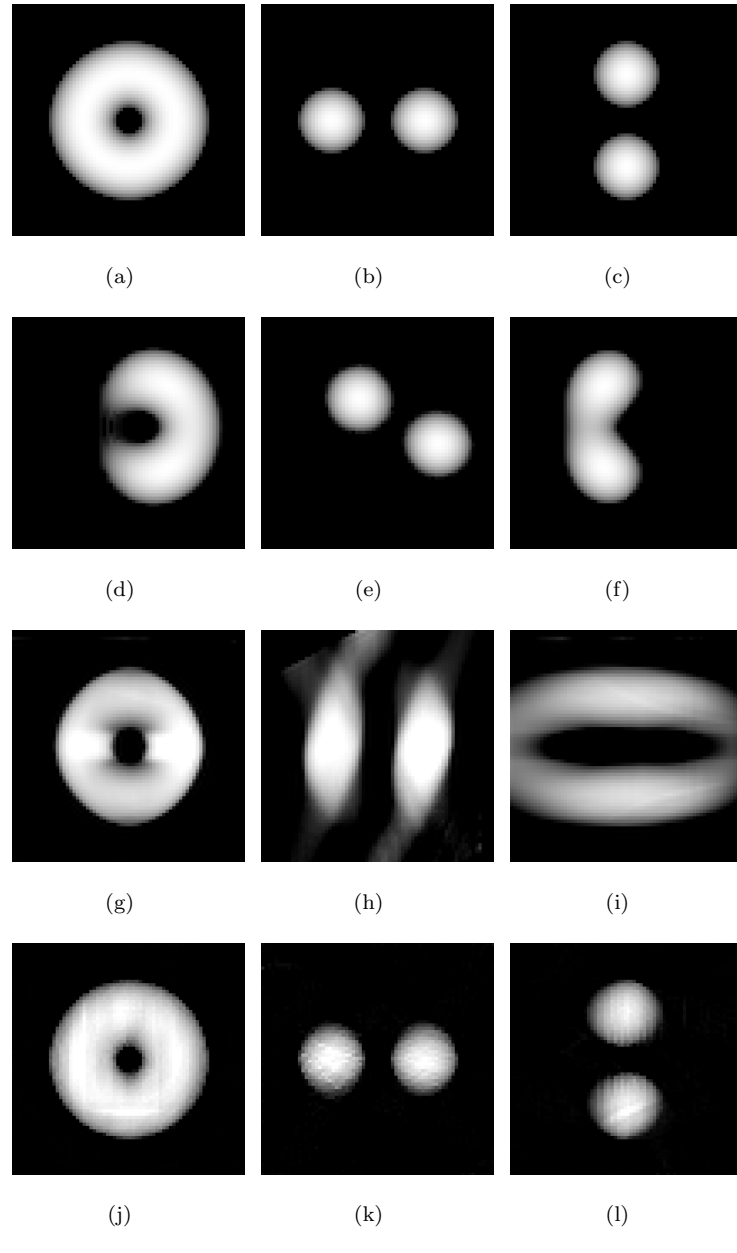


Figure 6.4: *Toroid phantom test case 1.* (a)-(c): Fixed image; (d)-(f): Moving image; (g)-(i): Sequential result, i.e., transformed moving image reconstruction $\mathcal{T}_\zeta^* f_2^*$; (j)-(l): Simultaneous result. (Left: Coronal view; Middle: Transverse view; Right: Sagittal view.)

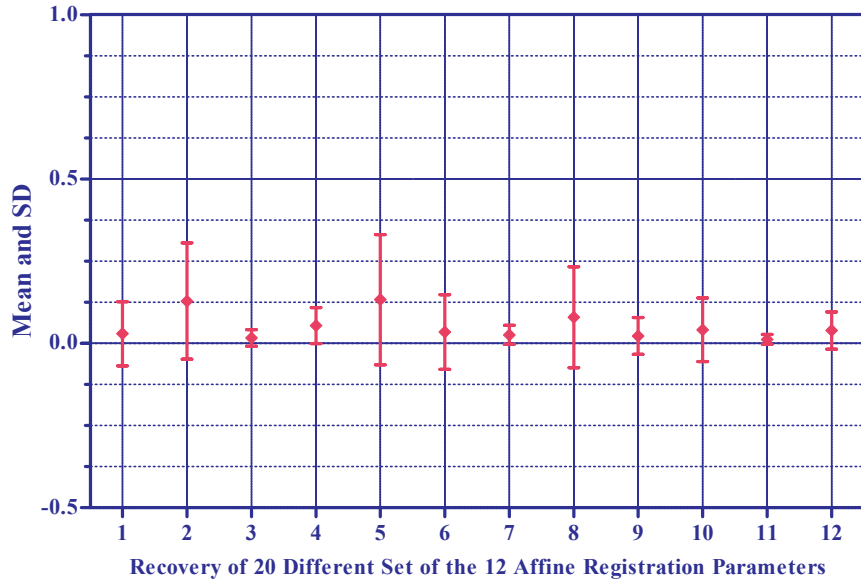


Figure 6.5: Plot of the mean and standard deviation of the absolute error between the recovered and the ground truth transformation parameters for 20 different randomly generated affine transformations. The 12 parameters are calculated using Equation 4.10, which combines rotation, scaling, shearing and translation. In other words, these 12 parameters are the 12 entries of the affine transformation matrix. In the plot, parameters number 4, 8, 12 are the translations along each direction, and other parameters are obtained from the multiplication of the rotation matrix and matrices of the scaling and shearing.

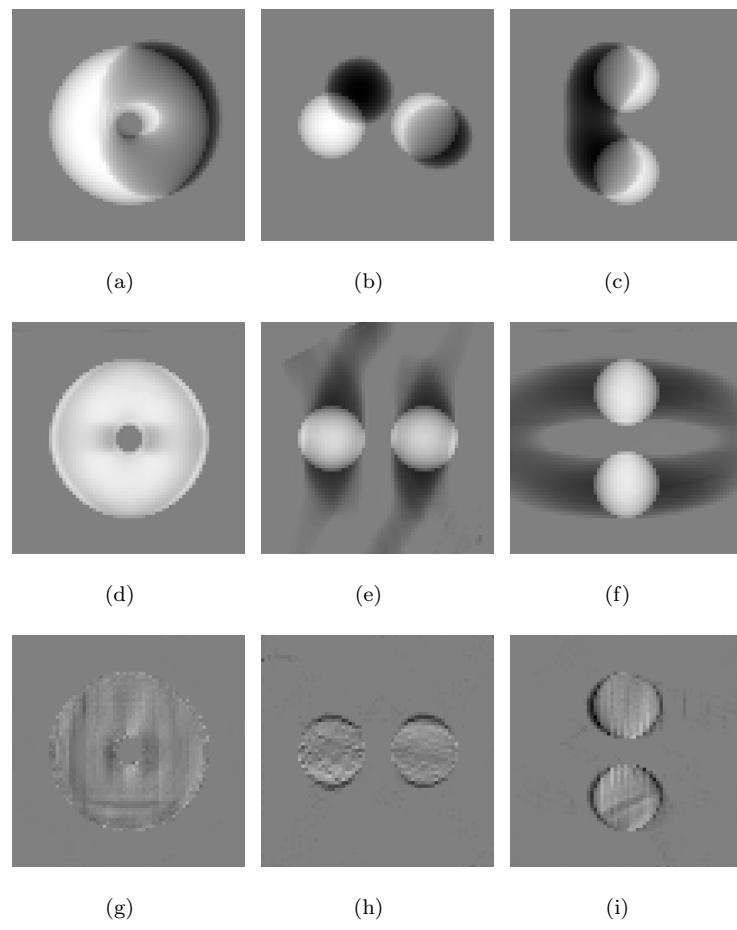


Figure 6.6: *Difference images.* (a)-(c): Differences between the fixed and the moving images; (d)-(f): Differences between the fixed image and the sequential result; (g)-(i): Differences between the fixed image and the simultaneous result.

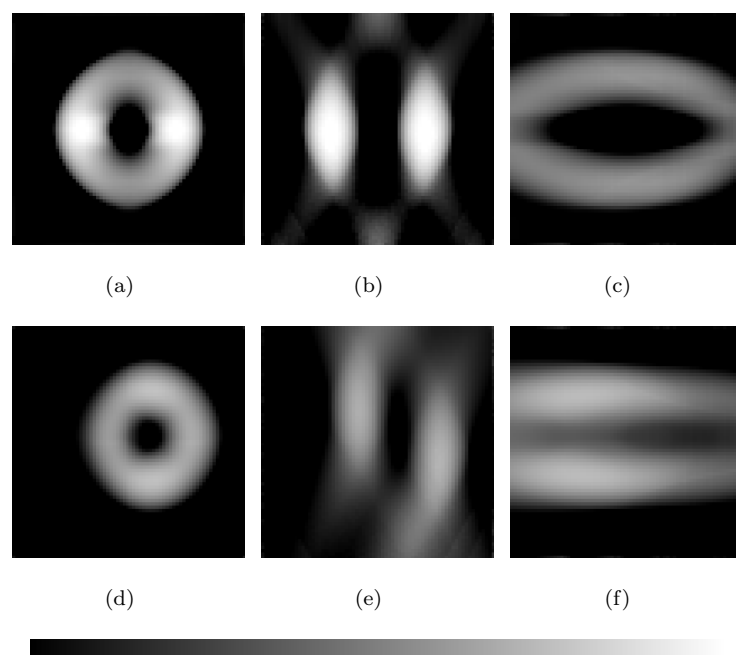


Figure 6.7: Reconstruction using two acquisitions p_1 and p_2 without registration. (a)-(c): Fixed image reconstruction; (d)-(f): Moving image reconstruction.

6.5.2 Experiment SA2: Test on the DBT Simulation Using Uncompressed MRI

The results of the experiment on the breast MR image suggest that our simultaneous method is promising (Figure 6.8 (g)-(i) *vs.* Figure 6.8 (j)-(l)). One $128 \times 140 \times 60\text{mm}^3$ breast MR image with $0.48 \times 0.48 \times 0.48\text{mm}^3$ resolution (Figure 6.8 (a)-(c)) was used for all the 15 tests (Test case 8 in Figure 6.8 (d)-(f)). Fewer out-of-plane artefacts (Refer to Section 3.2.1.1 and Hu et al. [122]) were found in the results of our simultaneous method than the results of the sequential method (Figure 6.9 (g)-(i) *vs.* Figure 6.9 (j)-(l)). Figure 6.10 shows the recovery of the transformation parameters.

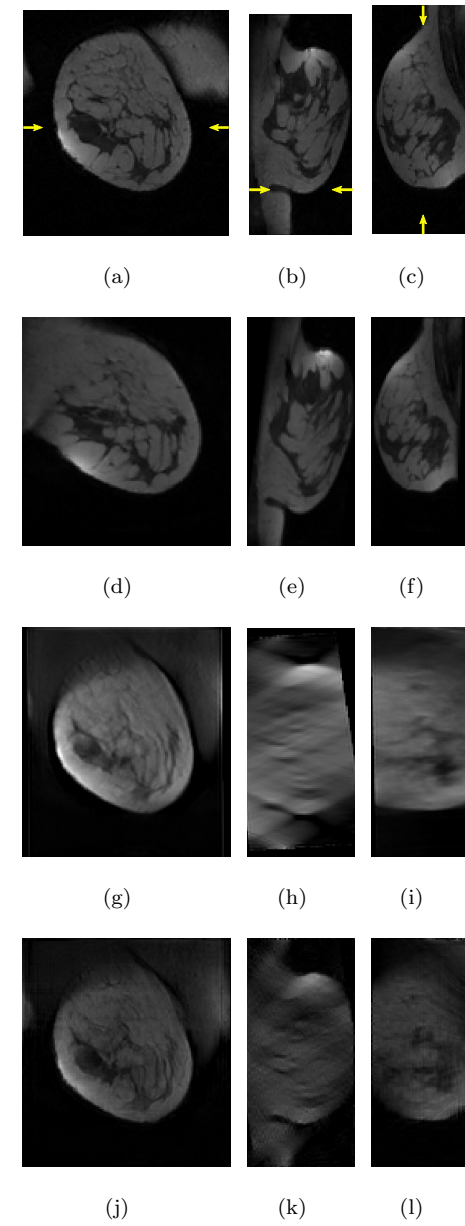


Figure 6.8: *Breast MRI test case 8.* (a)-(c): Fixed image; (d)-(f): Moving image; (g)-(i): Sequential result, i.e., transformed moving image reconstruction $\mathcal{T}_\zeta^* f_2^*$; (j)-(l): Simultaneous result. The transverse view has been rotated 90° clockwise for the purpose of better display. (Left: Coronal view; Middle: Transverse view; Right: Sagittal view.)

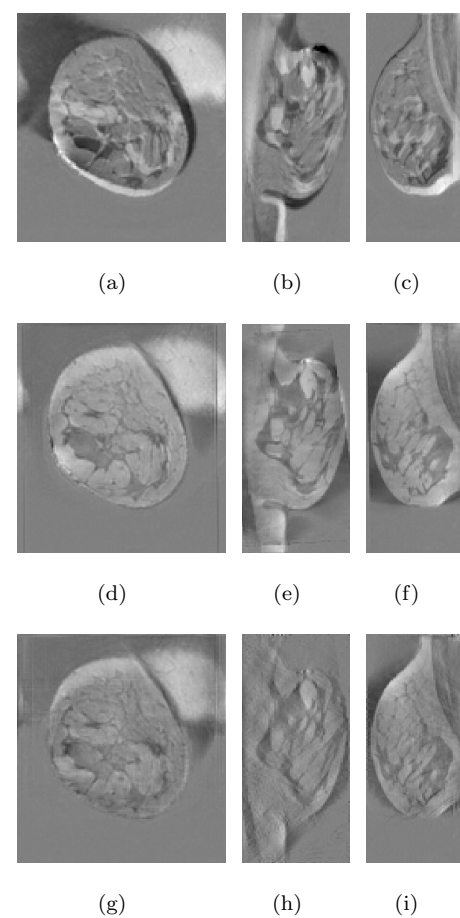


Figure 6.9: *Difference images.* (a)-(c): Differences between the fixed and the moving images; (d)-(f): Differences between the fixed image and the sequential result; (g)-(i): Differences between the fixed image and the simultaneous result.

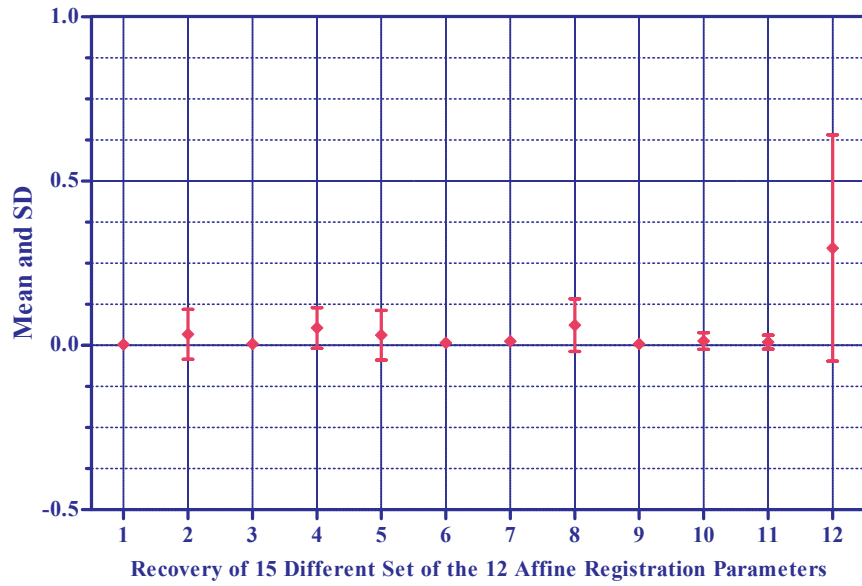


Figure 6.10: As Figure 6.5, plot of the mean and standard deviation of the absolute error between the recovered and the ground truth transformation parameters of 15 different affine transformations.

Cross-sectional line profiles in each view were plotted (Figure 6.11), *i.e.*, intensities of a horizontal line through the coronal view and intensities of a vertical line through the sagittal and transverse views respectively. By comparing the reconstruction and registration results to the original fixed image, we found that our simultaneous method produced a more accurate intensity estimation than the sequential method. In addition, the results of our simultaneous method were compared with the reconstruction results without registration using plots of the line profiles as well (Figure 6.12). From Figure 6.11, we find that the line profiles of the sequential method always have higher values than the line profiles of the simultaneous method. The reason is that we plot the line profiles of the transformation of the reconstructed moving image in the sequential method, and the original moving image has higher intensity values (Figure 6.12) and also produces higher intensities in its forward projection. In addition, the simultaneous method using the forward projections of both the fixed and the moving images that average the intensities and therefore have lower values of line profiles.

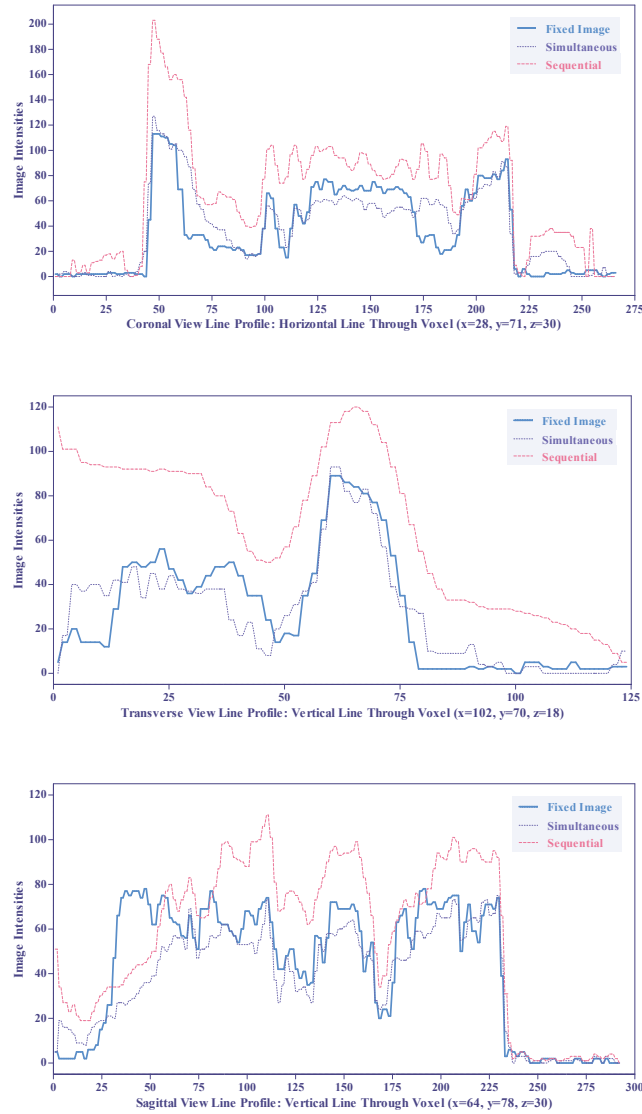


Figure 6.11: Line profiles of the three views of the breast MRI test case 8. (The line profiles were drawn between the two arrows of each view as seen in Figure 6.8 (a)-(c) as an example, and they were at the same positions for other corresponding images.)

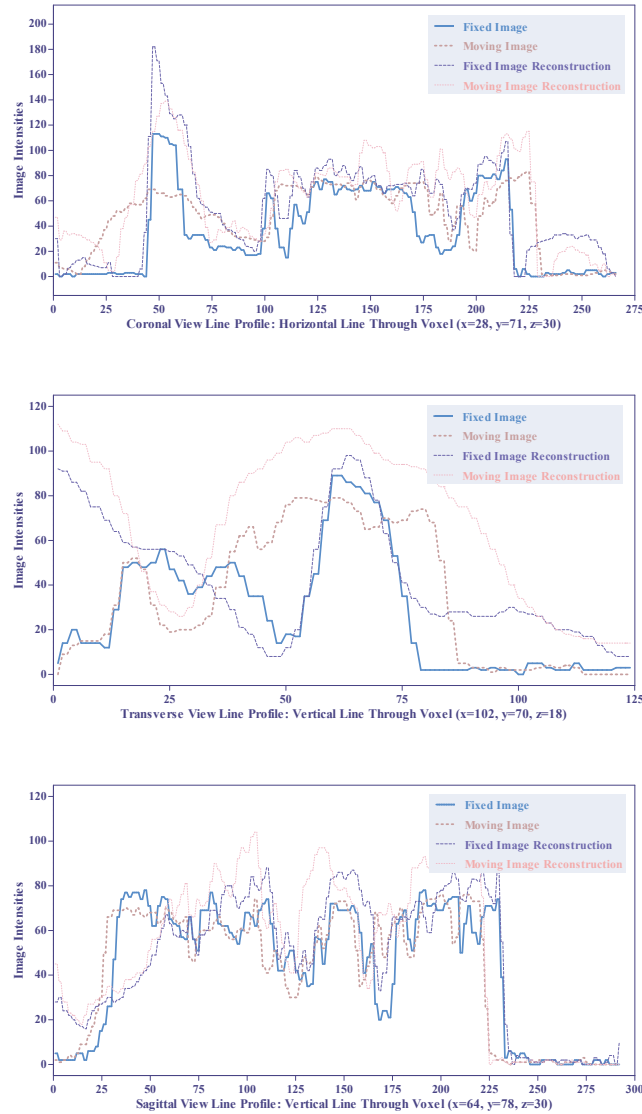


Figure 6.12: Line profiles of the reconstruction results without registration. (The line profiles were drawn at the same positions as Figure 6.11 showed.)

6.5.3 Experiment SA3: Test on Different Displacements

In this experiment, we again demonstrate the correlations between final TRE and SSD error with respect to the initial displacement. We use the same transformation settings as Section 5.5.7, and divide the initial displacement to low (-7 to 0 and 0 to 7 degrees), medium (-13 to -8 and 8 to 13

degrees), and high displacement (-19 to -14 and 14 to 19 degrees) levels; however, all the experiments in this section have not considered about any noise. Results are shown in Figure 6.13, from which we can conclude that the larger view angles enable better reconstruction quality; however, they increase the final TRE values, which represent the registration accuracy.

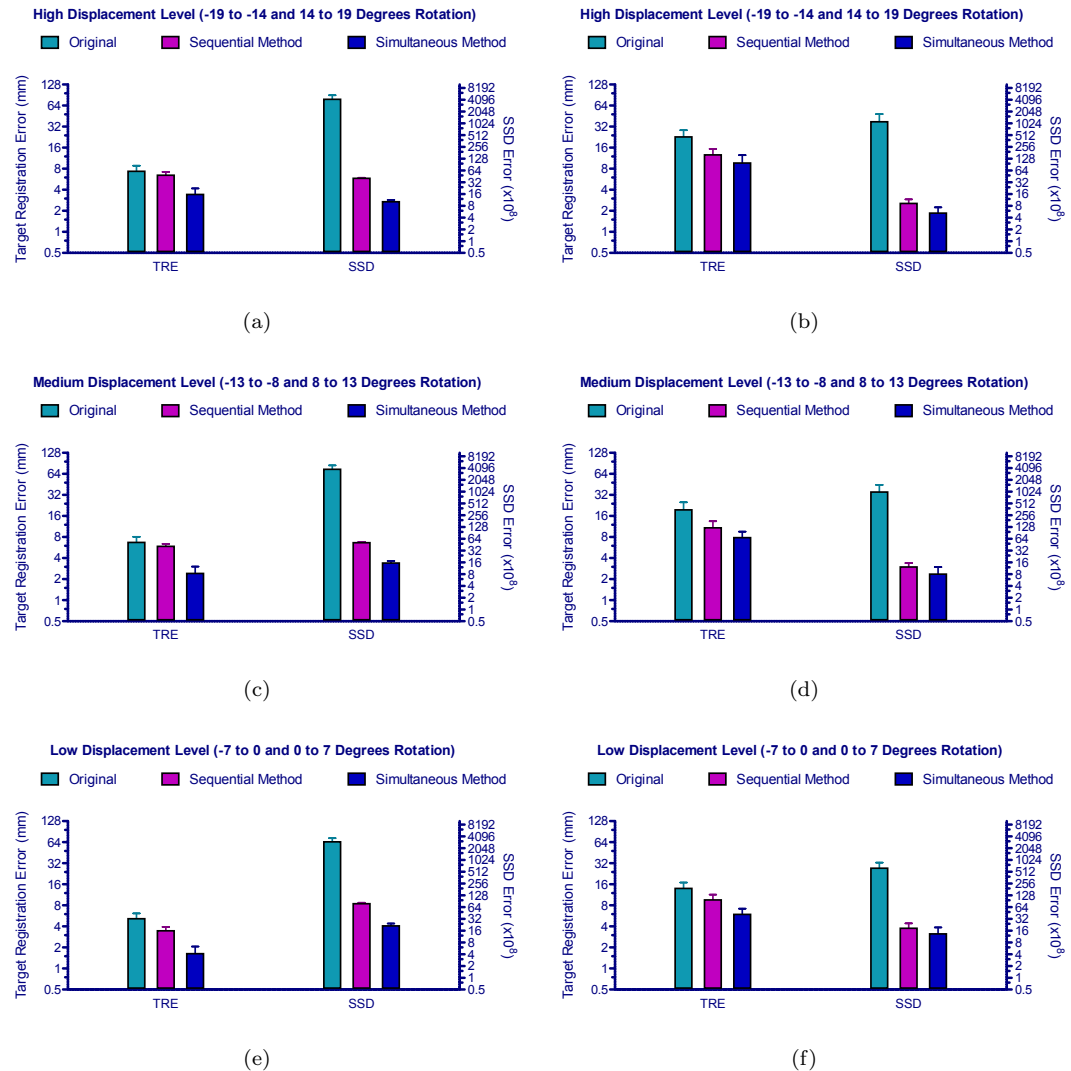


Figure 6.13: Experiment on different initial displacements (rotation levels) with final TRE and SSD error (on \log_2 scale). (a), (c), and (e): Test on the toroid phantom image showing initial and final TRE and SSD with respect to the various initial rotation levels; (b), (d), and (f): The same test on the breast MRI images.

6.5.4 Experiment SA4: Test on the DBT Simulation with In-Vivo Compression

Two temporal DBT simulations ($511 \times 208 \times 208$ voxels with a spatial resolution 0.215mm in each direction) were created for this experiment, *i.e.*, two MRI acquisitions obtained with two different real medio-lateral plate compressions of the breast (Figure 6.14 (a)-(f)). The method of DBT simulation is briefly described in Section 5.5.5, and we choose a larger data set in this experiment. From the comparison of the results (Figure 6.14 (g)-(i) *vs.* Figure 6.14 (j)-(l)), our simultaneous method outperformed the sequential method. First, the blurring effect of the sequential method was mitigated. Second, the out-of-plane structure was more compact with much less radial artefacts. Third, there was no black cutting-off artefacts near the edges. In other words, there was a recovery of the data lost due to part of the moving image falling outside of the volume field of view. There was no ground truth of the deformation because this pair of data was acquired *in vivo*. Additionally, we tried to use our affine transformation based simultaneous framework to capture the real non-rigid deformation. In practice, the affine transformation model will be insufficient to recover the real compressions, which could degrade the reconstructed results; however, the difference images in Figure 6.15 shows a fair reconstruction with appropriate registration using both methods. Accordingly, about half of the line profile (Figure 6.16) illustrated that the results of our simultaneous method fitted the original fixed image quite well, and it was superior to the sequential method. However, the other half of the line profile did not show good agreement, this can be attributed, at least in part, to the fact that the affine transformation, which is a global parametric model, is insufficient to capture such a non-rigid transformation.

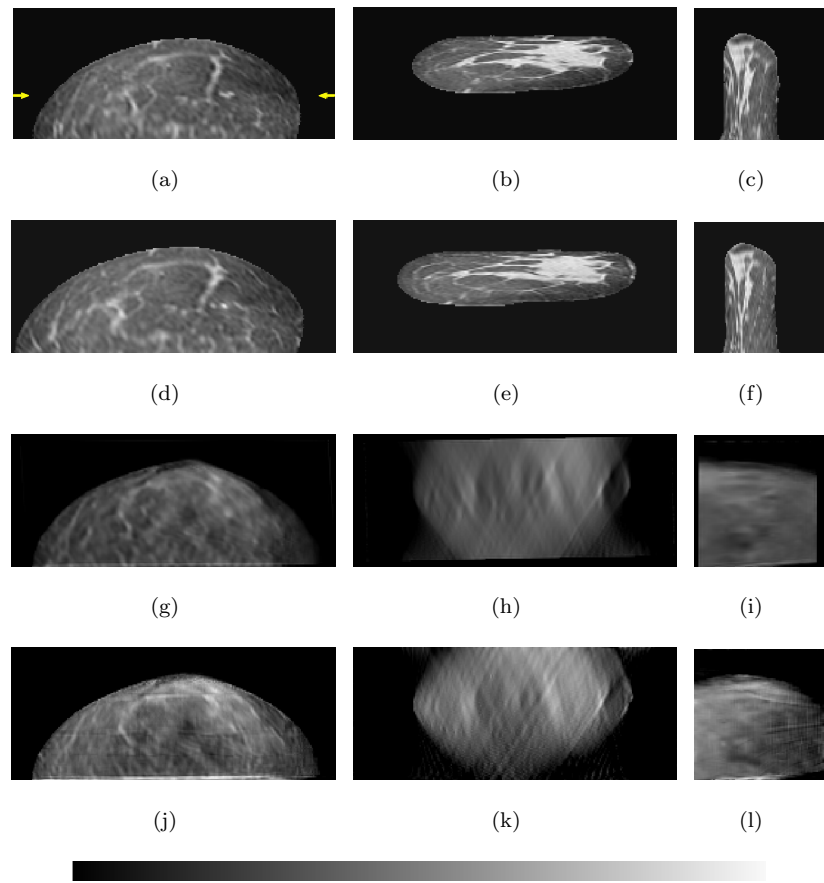


Figure 6.14: Two DBT simulations were created using in-vivo MR acquisitions of a breast with two different real plate compressions to mimic the temporal imaging (Images have been segmented and mapped to effective X-ray attenuation). (a)-(c): Fixed image; (d)-(f): Moving image; (g)-(i): Sequential result, i.e., transformed moving image reconstruction $\mathcal{T}_\zeta^* f_2^*$; (j)-(l): Simultaneous result. (Left: Transverse view; Middle: Coronal view; Right: Sagittal view.)

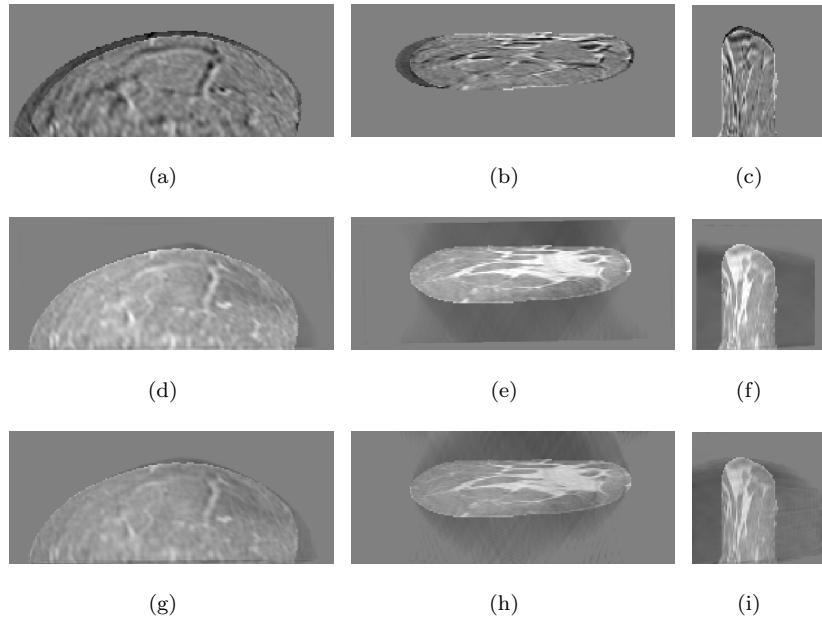


Figure 6.15: *Difference images.* (a)-(c): Differences between the fixed and the moving images; (d)-(f): Differences between the fixed image and the sequential result; (g)-(i): Differences between the fixed image and the simultaneous result.

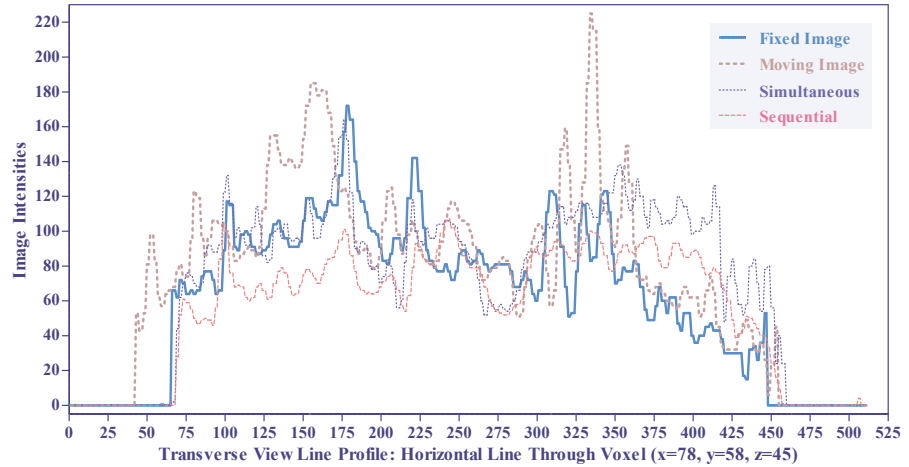


Figure 6.16: *Line profiles of the transverse view of the DBT simulations experiment. The line profiles were drawn between the two arrows of the transverse view as seen in Figure 6.14 (a) as an example.)*

6.6 Experiments and Results using the B-spline Model

6.6.1 Experiment SB1: Test on the DBT Simulation using 3D Shepp-Logan

For the B-spline transformation model, we use a 3D Shepp-Logan phantom to test our simultaneous method initially. Although the 3D Shepp-Logan phantom may not be a perfect simulation for breast structures, it is a widely used phantom image in tomographic reconstruction. Figure 6.18 shows the 3D Shepp-Logan phantom ($65 \times 65 \times 65$ in voxels), and it also shows the central slice of each plane and the regular B-spline control point grid for the central slice of the transverse plane. The transformed phantom is shown in Figure 6.19, and illustrates the ground truth of the transformation. This ground truth deformation is randomly simulated using 9 control points in each dimension with the B-spline transformation model (Figure 6.17). A random perturbation, which was created using Matlab build-in subroutine (rand) and implemented continuous uniform distribution, was applied to each control point. The subroutine generates a pseudo-random value on the open interval $(0, 1)$, and random values RV from the uniform distribution on the interval $[Range_a, Range_b]$ can be created by $RV = Range_a + (Range_b - Range_a) \times \text{rand}(\text{number of control points}, 1)$.

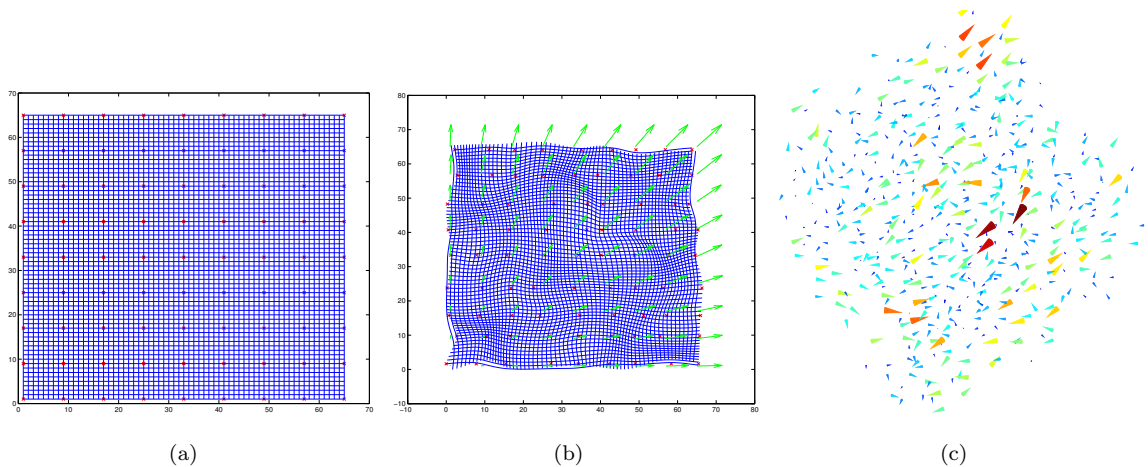


Figure 6.17: *Displacement field.* (a) Original regular grid for the central slice; (b) Deformed grid for the central slice; (c) Displacement field of the whole 3D volume. (Red cross: control points; Green arrow: displacement vector in 2D; Coloured quiver: displacement vector in 3D.)

In this experiment, we set different ranges of perturbation for each direction (x-, y- and z-axis),

e.g., $[\text{Range}_a, \text{Range}_b] = [-8, 8]$, $= [-4, 4]$, and $= [-2, 2]$ have been used respectively. Therefore, there are larger deformations for the in-plane slices and smaller ones for the out-of-plane. From the results in Figures 6.20 and 6.21, we can conclude that our simultaneous method has obtained an accurate reconstruction with a reasonable recovery of non-rigid deformations. The montage views of the fixed, transformed, recovered, and difference images are shown in Figures 6.22, 6.23, 6.24, and 6.25.

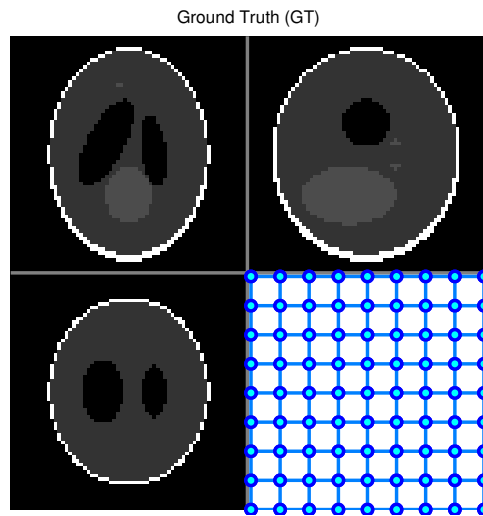


Figure 6.18: Original fixed 3D Shepp-Logan phantom and its regular grid for the central slice.

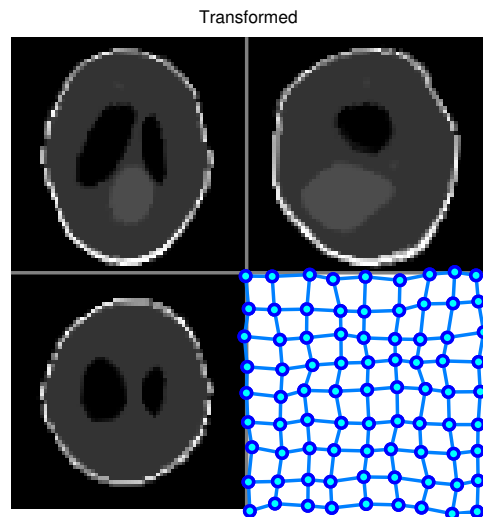


Figure 6.19: Transformed 3D Shepp-Logan phantom and its deformed grid for the central slice, i.e., ground truth of the transformation.

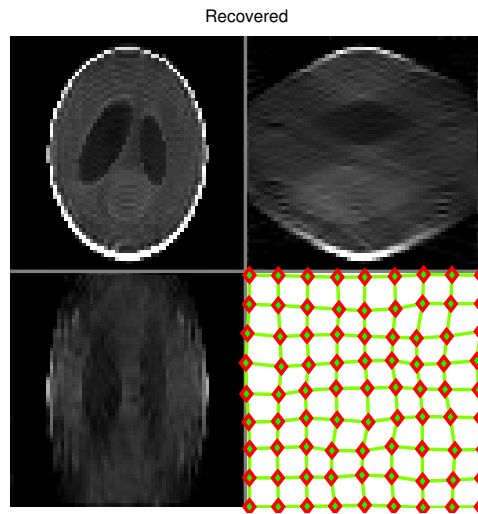


Figure 6.20: *Simultaneous reconstruction and registration result and the registered control point grid for the central slice.*

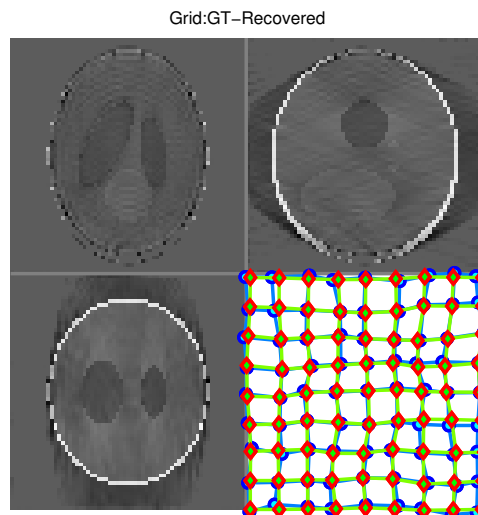


Figure 6.21: *Difference image between the simultaneous result (Figure 6.20) and the original fixed phantom (Figure 6.18). The registered control point grid is superimposed on the ground truth transformation and indicates that the ground truth transformation has been recovered well for the majority of control points. (Figure 6.19).*

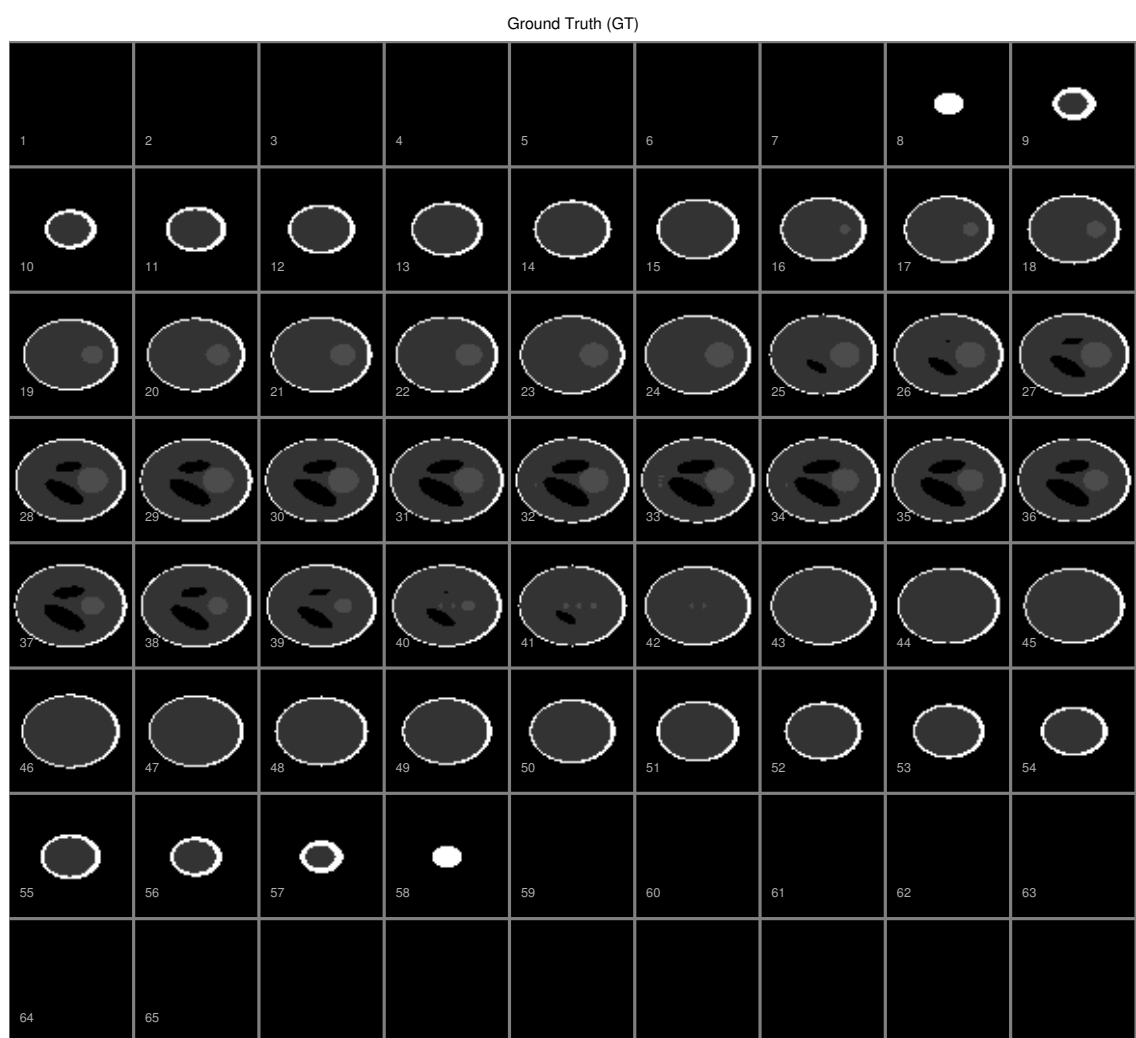


Figure 6.22: A montage view of the original fixed 3D Shepp-Logan phantom.

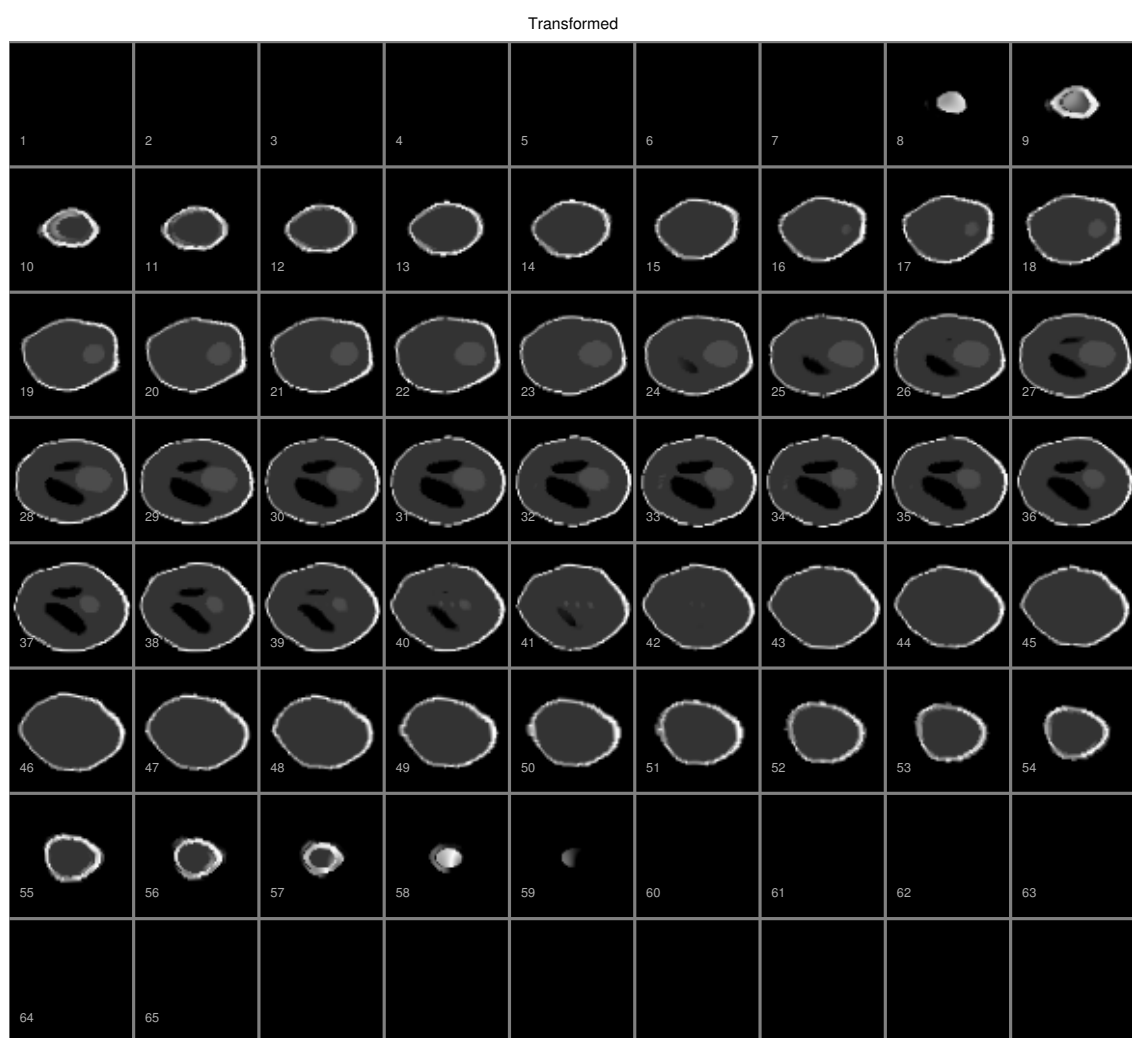


Figure 6.23: A montage view of the transformed 3D Shepp-Logan phantom.

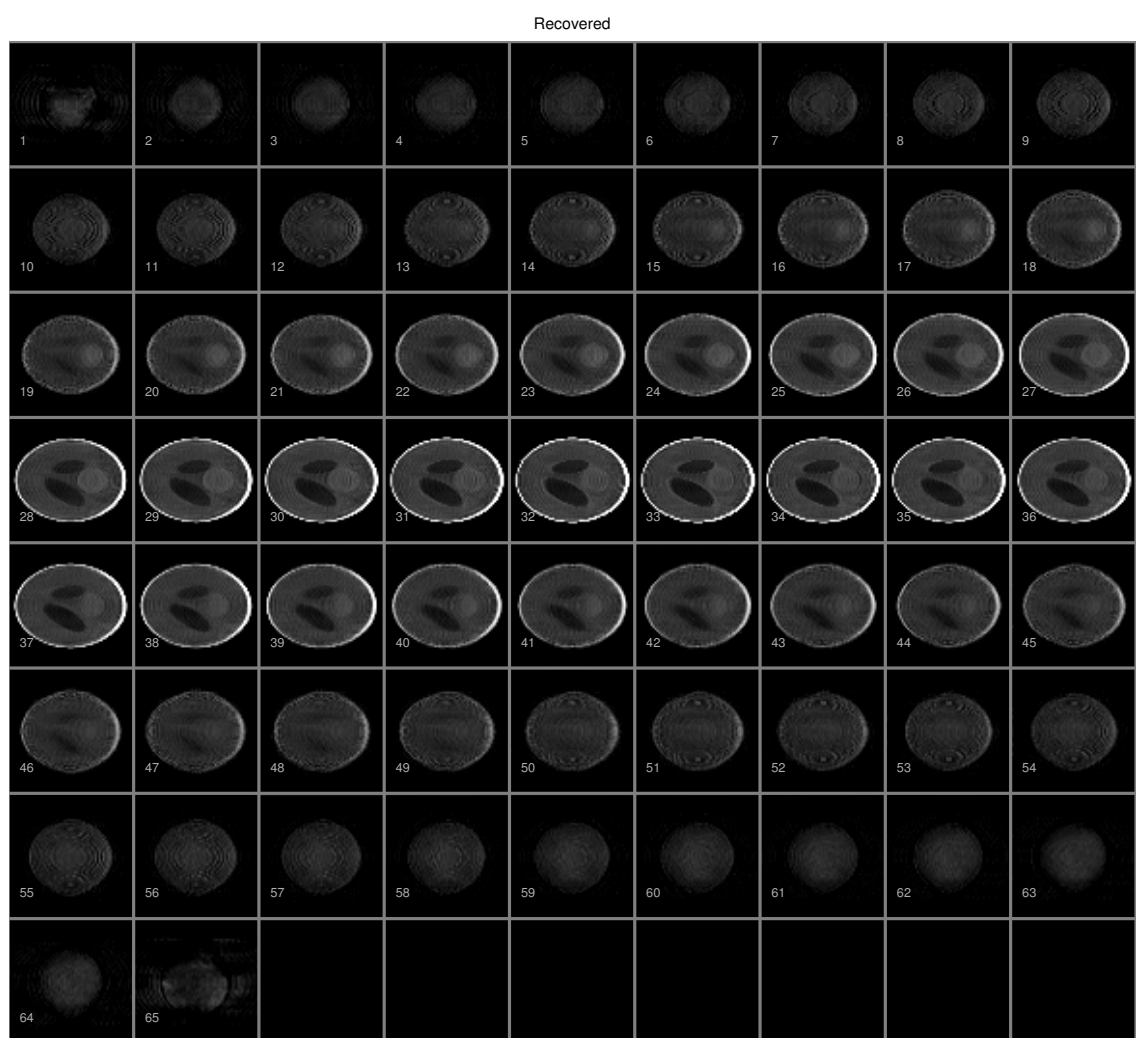


Figure 6.24: A montage view of the simultaneous reconstruction and registration result.

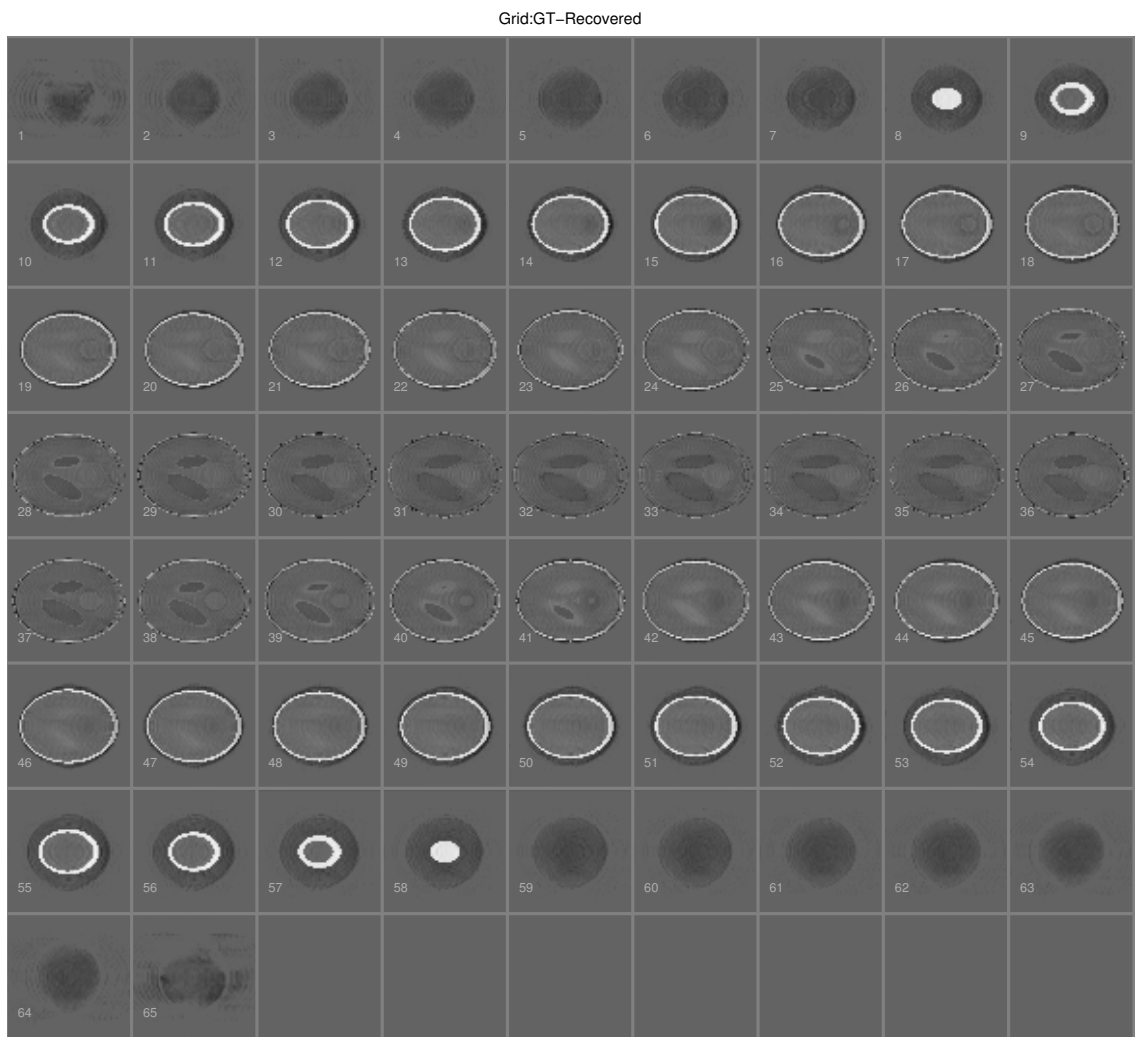


Figure 6.25: A montage view of the difference image between the simultaneous result (Figure 6.24) and the original fixed phantom (Figure 6.22).

6.6.2 Experiment SB2: Test on the DBT Simulation using 3D Breast Phantom

Additionally, we also create a 3D breast phantom image to test our simultaneous method. We use different intensities to simulate different parts of the breast phantom image, *e.g.*, calcifications possess higher intensity than fat and glandular tissue, *i.e.*, air = 1, adipose = 2, glandular = 3, lesion = 4, skin = 5, muscle = 6, and calcification = 7 (these values are simulated intensities as seen in Figure 6.26, and the original software to simulate the 3D breast phantom image [175] [176] is provided by Duke University Medical Center¹). Figure 6.27 shows a simulated 3D breast phantom image with $65 \times 65 \times 65$ voxels, in which the central slice of each plane and the regular grid for the central slice of the transverse plane are shown. The transformed phantom is shown in Figure 6.28, where we can see the ground truth of the transformation. This ground truth deformation is also randomly simulated using $9 \times 9 \times 9$ control points with the B-spline transformation model (the displacement field was randomly simulated and it was different from the last experiment).

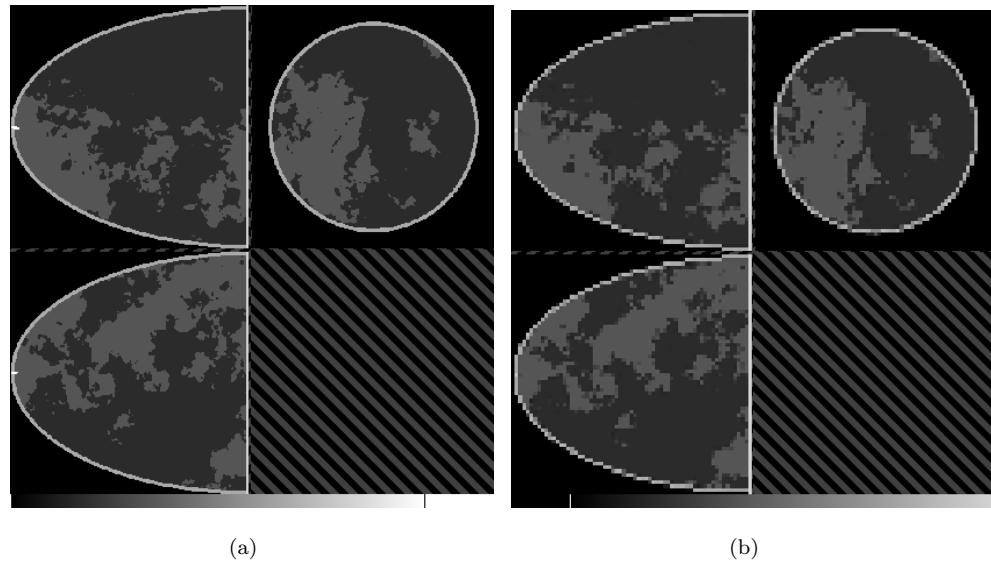


Figure 6.26: The 3D breast phantom images. (a) In higher resolution with $260 \times 260 \times 260$ voxels; (b) The down-sampled version of (a) in lower resolution with $65 \times 65 \times 65$ voxels.

From the results in Figures 6.29 and 6.30, we can conclude that our simultaneous method has obtained an accurate reconstruction with a reasonable recovery of non-rigid deformations. In addi-

¹The 3D breast phantom simulation software is provided by Dr. Christina M. Li and Dr. Paul Segars from Duke University Medical Center. However, it is an executable binary file without source files. Also, it is a simplified version with some adjustable configurations, which may not exactly follow their publications in [175] [176].

tion, the registration appears to be most accurate along the breast edge, and this is a strong feature and hence it has a significant influence on value of the cost function in this region. The montage views of the fixed, transformed, recovered, and difference images are shown in Figures 6.31, 6.32, 6.33, and 6.34.

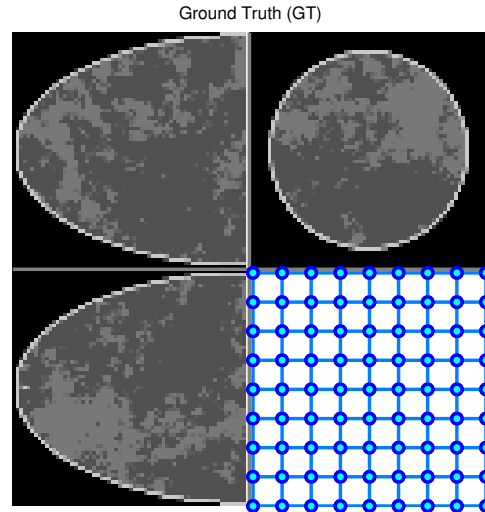


Figure 6.27: *Original fixed 3D breast phantom image and its regular grid for the central slice.*

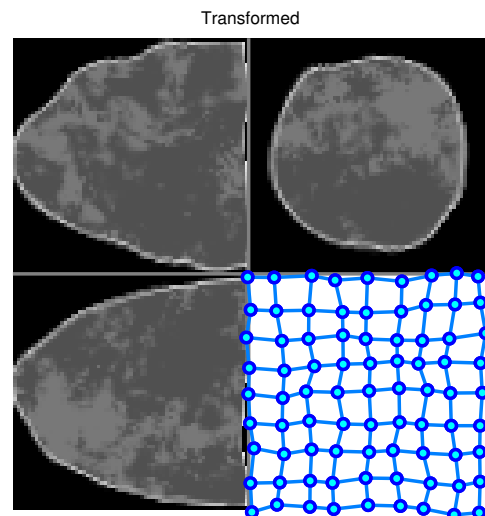


Figure 6.28: *Transformed 3D breast phantom image and its deformed grid for the central slice, i.e., ground truth of the transformation.*

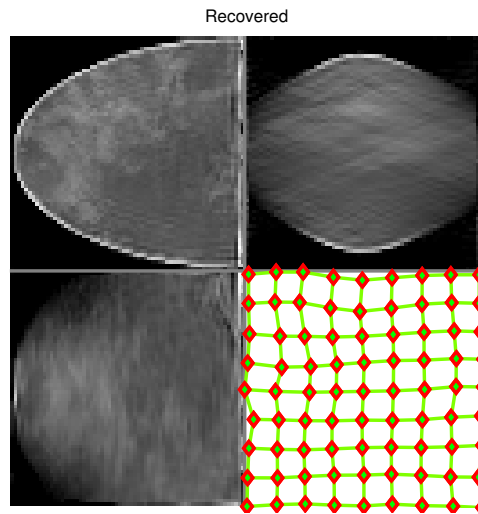


Figure 6.29: *Simultaneous reconstruction and registration result and the registered control point grid for the central slice.*

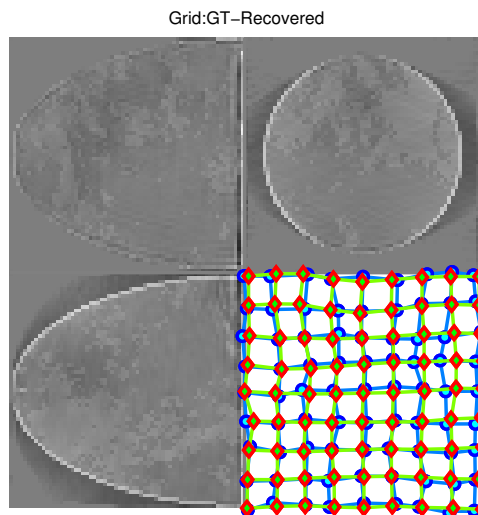


Figure 6.30: *Difference image between the simultaneous result (Figure 6.29) and the original fixed phantom (Figure 6.27). The registered control point grid is superimposed on the ground truth transformation and indicates that the ground truth transformation has been recovered well for the majority of control points. (Figure 6.28).*

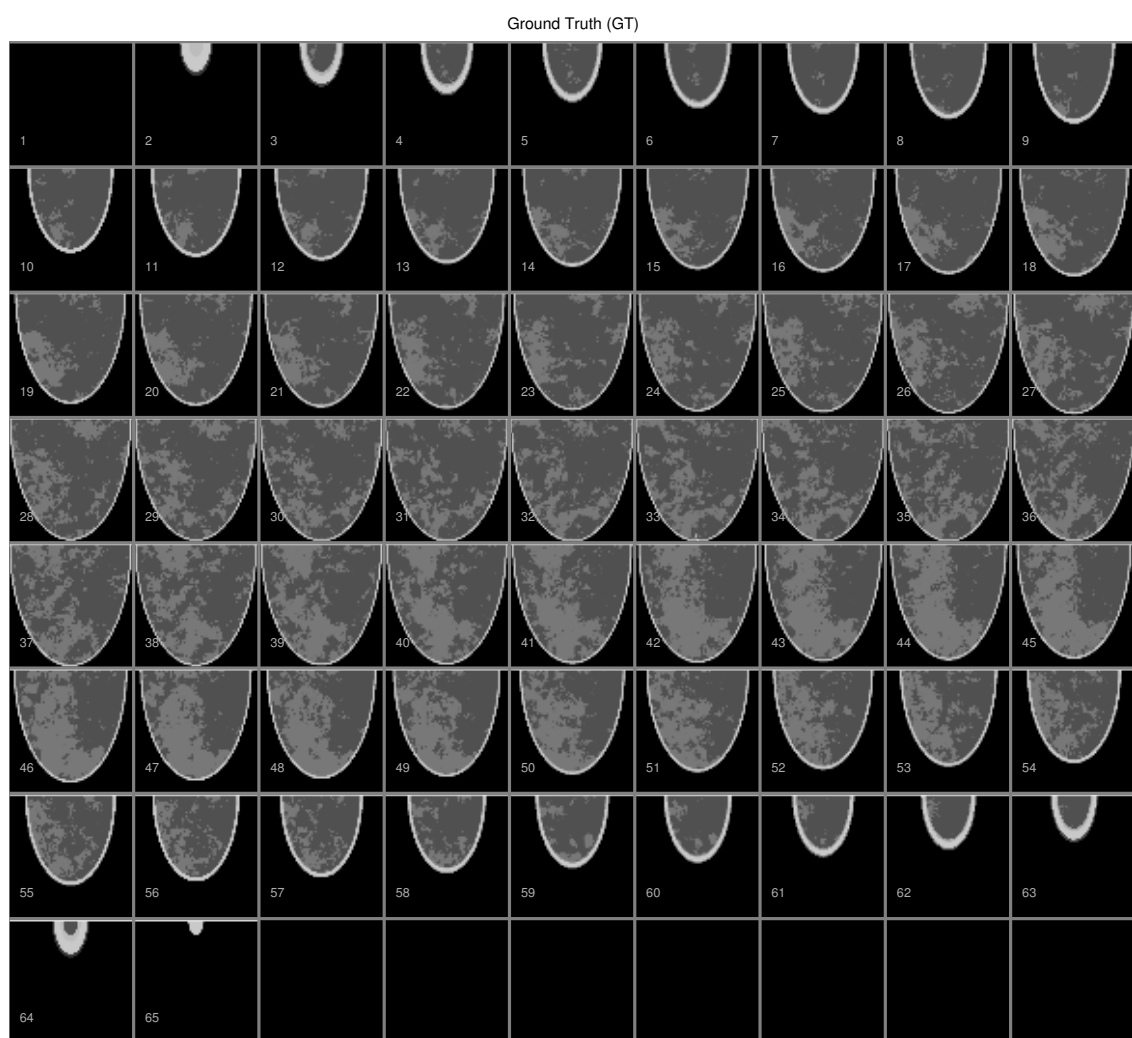


Figure 6.31: A montage view of the original fixed 3D breast phantom image.

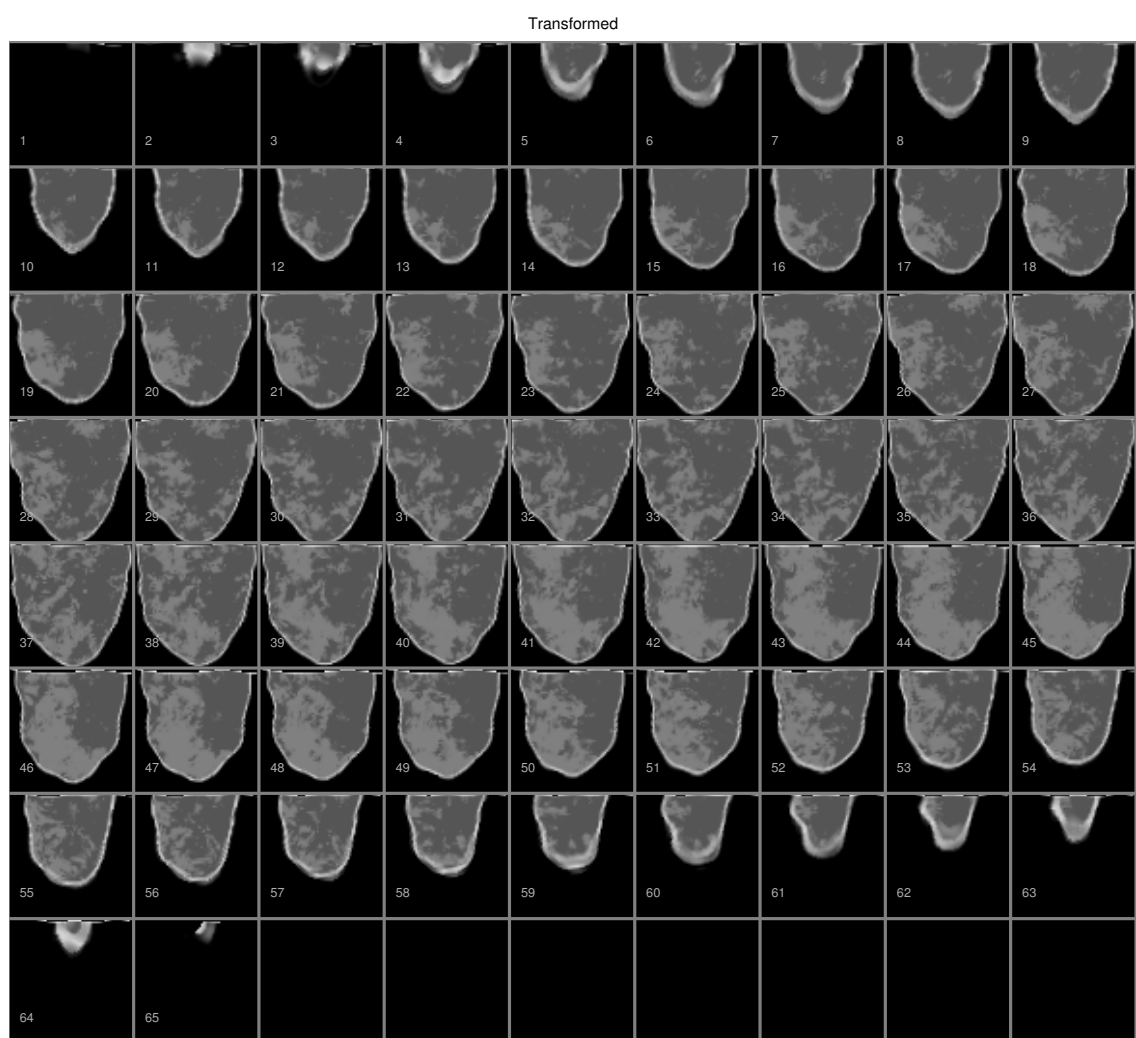


Figure 6.32: A montage view of the transformed 3D breast phantom image.

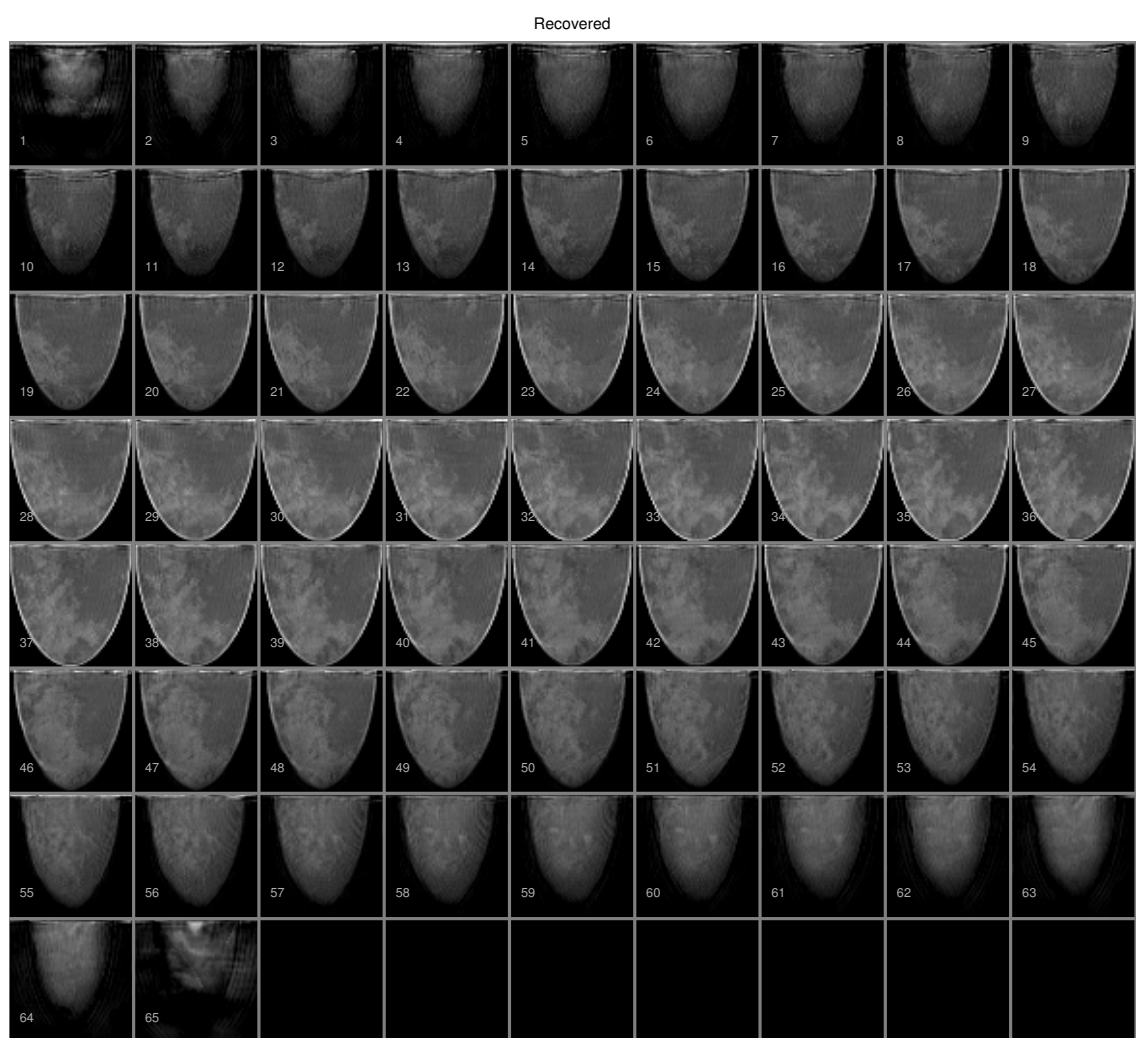


Figure 6.33: A montage view of the simultaneous reconstruction and registration result.

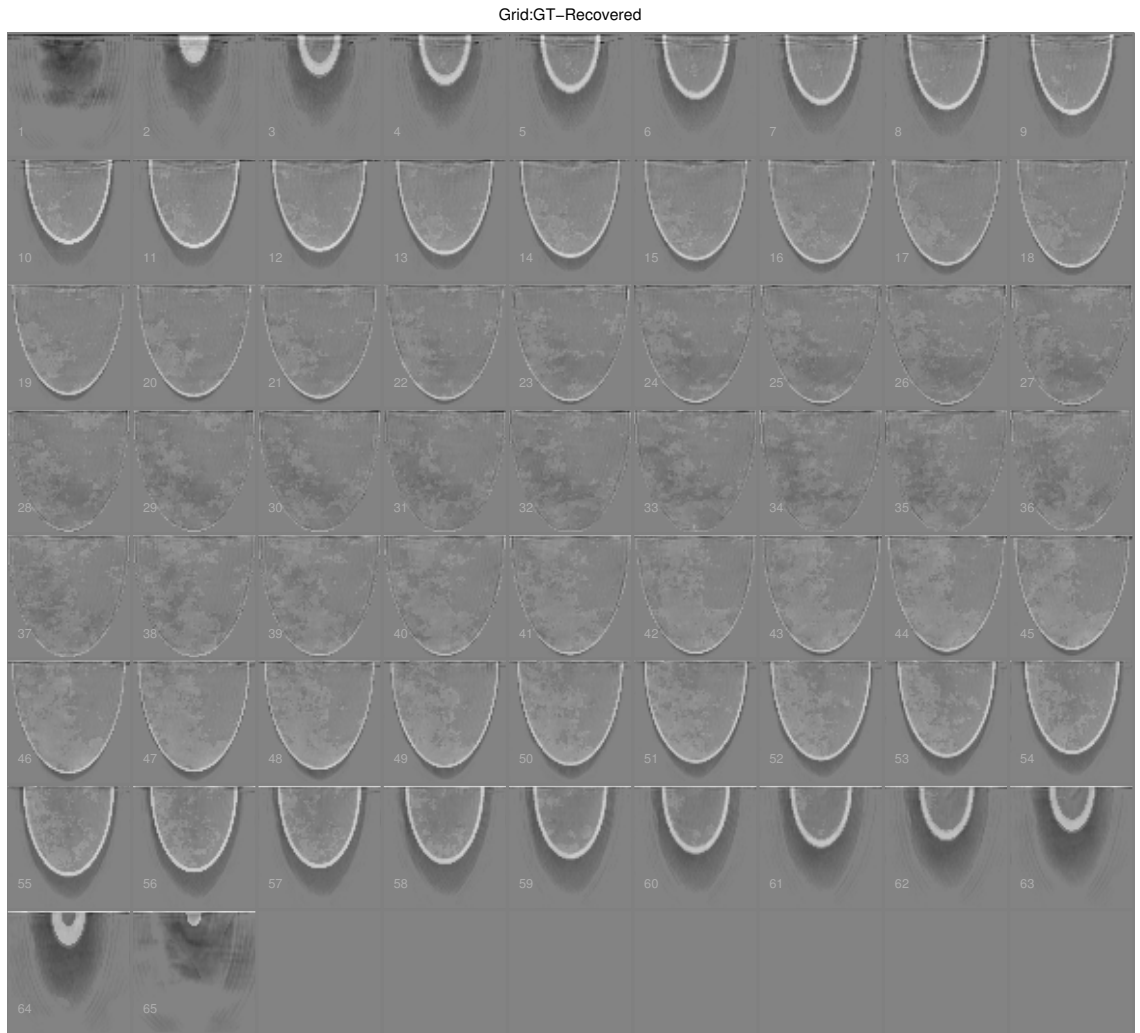


Figure 6.34: A montage view of the difference image between the simultaneous result (Figure 6.33) and the original fixed phantom (Figure 6.31).

6.6.3 Experiment SB3: Test on Different Initial TRE

In order to demonstrate the relationship between initial TRE (initial displacement) and final TRE and SSD error, we present this set of experiment using various initial TRE levels. Similar to Sections 5.5.7 and 6.5.3, we define three levels of initial displacement. However, because we apply the B-spline transformation model here, the displacement level is measured using initial TRE rather than different simulated rotations. Thus, the three levels of initial displacement are defined as low (1mm to 10mm initial TRE with 5 data sets), medium (11mm to 20mm initial TRE with 5 data sets), and high

displacement (21mm to 30mm initial TRE with 5 data sets) levels, and all the experiments in this section consider no noise environment. Results (as seen in Figure 6.35) also confirm that superior reconstruction can be obtained using larger initial displacement, but it has associated with lower registration accuracy. In addition, due to the initial displacement here is not dominated by rotation angles; therefore, the null-space problem has not been mitigated as our affine simulation, and the SSD error has not been reduced significantly.

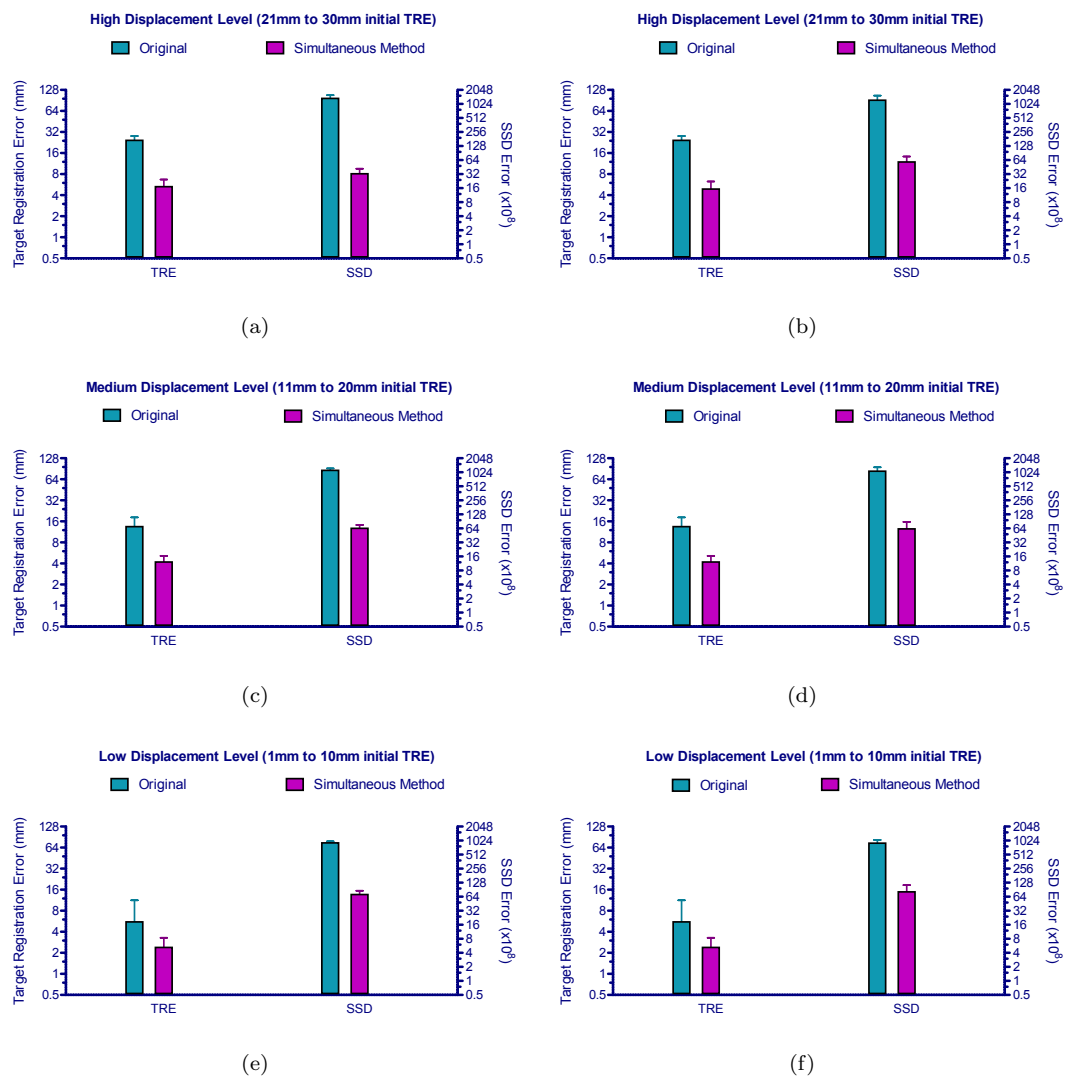


Figure 6.35: Experiment on different initial displacements (TRE levels) with final TRE and SSD error (on log₂ scale). (a), (c), and (e): Test on the toroid phantom image showing initial and final TRE and SSD with respect to the various initial TRE levels; (b), (d), and (f): The same test on the breast MRI images.

6.7 Conclusions and Discussion

As far as we aware this is the first time that the simultaneous reconstruction and registration of DBT data sets using a decoupled optimisation approach has been found to be superior to the conventional sequential method. This approach jointly considers reconstruction and registration components of DBT, and it is capable of recovering both the deformation parameters, and an enhanced, reconstructed image. By integrating the registration directly into the framework of the reconstruction problem, we are able to fully explore the interdependence between the transformation parameters and the 3D volume to be reconstructed.

Significantly, compared to the previous research on combining reconstruction and registration (or motion correction), our combined limited angle DBT problem has a much larger null space and is severely ill-posed, which makes the inverse problem more intriguing and more challenging. From Table 6.1, we can see that for a typical 2D super-resolution problem previous studies used 5 low resolution images to restore a high resolution image recovering only rotations and translations, and 32 low resolution images for the affine registration. In general 3D problems, the authors used at least 60 and up to 799 forward projections covering a full-range of views, *i.e.*, 180° or 360°, to perform the joint estimations. However, for our DBT application, we have two sets of data, which are observed at two time-points. Each of the data is acquired using only 11 forward projections covering just 50° ($\pm 25^\circ$), and the two data sets overlap to a certain degree according to the original unknown deformations.

We analysed our simultaneous method with various data sets using an affine transformation model, and the simultaneous method has made achieved clearly superior results compared to the conventional sequential method. First, the experiment on the 3D toroid image clearly revealed that this approach has an advantage over the conventional method. Second, the results of the breast MR image have further strengthened our confidence in the hypothesis that the reconstruction and registration have a reciprocal relationship. Importantly, plots of the cross-sectional line profiles confirmed that our combined method produced a superior reconstruction than the conventional method. In addition, the recovery of the transformation parameters was consistently accurate for both the 3D toroid and the breast MR data sets. Next, we attempted to reconstruct and register simulated DBT data sets created from real medio-lateral compressions of a breast imaged using MRI. As anticipated, the simultaneous approach still outperformed the conventional sequential method as demonstrated by the image appearance and SSD comparison (Figure 6.14 and Table 6.3). Although the improvements were limited in this experiment, this can be attributed, at least in part, to the fact

that the affine transformation, which is a global parametric model, is insufficient to capture such a non-rigid breast deformation.

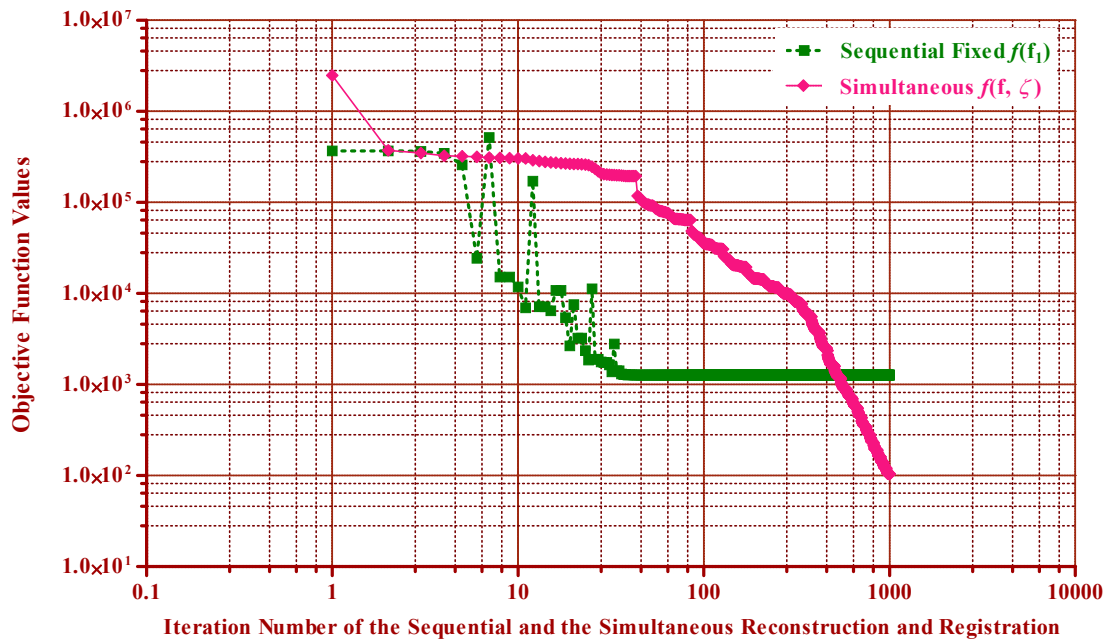


Figure 6.36: The 3D toroid test case 1. Comparison of the objective function of the fixed image reconstruction using the sequential method $f(f_1) = \frac{1}{2} \|Af_1 - p_1\|^2$, and the objective function of the simultaneous method $f(f, \zeta) = \frac{1}{2} (\|Af - p_1\|^2 + \|A\mathcal{T}_\zeta f - p_2\|^2)$.

Figure 6.36 and Figure 6.37 show that the objective function decreases smoothly using our simultaneous method, but the convergence rate is slow. The total number of the reconstruction and registration iterations was set to be 1000 for both the simultaneous and sequential methods. Figure 6.36 shows that our simultaneous method obtained a better convergence than the sequential method, but nevertheless Figure 6.37 shows a lower convergent value using the sequential method. In fact, contrary to the objective function of the simultaneous method, we only displayed the $f(f_1)$ part which is the reconstruction of the fixed image of the sequential method. Additionally, the trend of the objective function was still downwards using the simultaneous method.

A different number of inner iterations of the two decoupled optimisation steps would affect convergence. A common way to compare the convergence rate of optimisation algorithms is to plot the objective function value as a function of the iteration. Since each method in this study optimised a different objective function, direct comparison of the individual objective function values might not

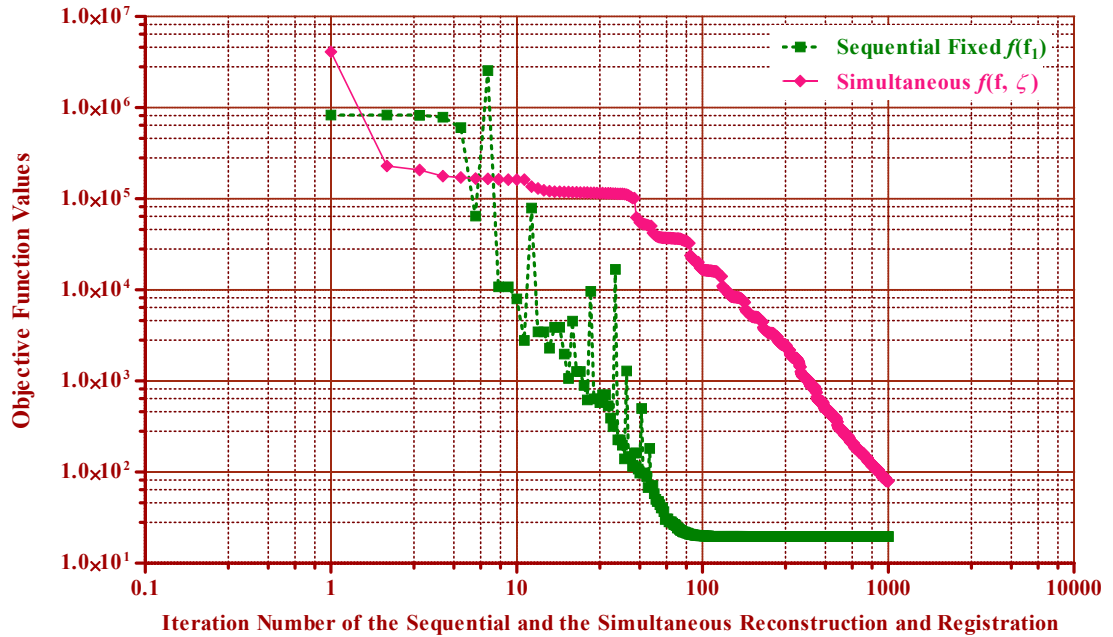


Figure 6.37: The breast MRI test case 8. Comparison of the objective function of the fixed image reconstruction using the sequential method $f(f_1) = \frac{1}{2} \|Af_1 - p_1\|^2$, and the objective function of the simultaneous method $f(f, \zeta) = \frac{1}{2} (\|Af - p_1\|^2 + \|A\mathcal{T}_\zeta f - p_2\|^2)$.

be strictly sensible. Despite this, the plot of the objective function of each method might still reflect the convergence rate and the magnitude of reconstruction and registration accuracy.

As was mentioned, we also calculated the SSD error and the relative error between the reconstruction and registration results and the original fixed image, *i.e.*, ground truth, for the two methods (Table 6.3 and 6.4). These comparison of the SSD and the relative error indicate that our simultaneous method has always produced a better result, and it is in line with our hypothesis that combining the two tasks leads to an improvement in the reconstruction which in turn enables a more accurate registration.

Furthermore, we have also incorporated a non-rigid transformation model into our combined framework. In particular, we employed the B-spline transformation model and tested it with our simultaneous method. Results generated using a 3D Shepp-Logan phantom image offer compelling evidence that our simultaneous method has successfully reconstructed the volume with accurate recovery of the non-rigid deformations. Further experiments on a 3D breast phantom image also show promising results.

Table 6.3: Comparison of the SSD error and the TRE. The SSD error of the sequential method is $\|f_1^* - f_1^g\|^2$ (Difference between the result of the transformed moving image reconstruction and the original fixed image), and the SSD error of the simultaneous method is given by $\|f^* - f_1^g\|^2$.

	Initial	Sequential Method	Simultaneous Method
Toroid Phantom	4.51×10^{11}	2.56×10^9	8.23×10^7
Misregistration TRE (mm)	11.9	8.1	2.6
Uncompressed Breast MRI	1.40×10^{11}	7.18×10^8	3.58×10^8
Misregistration TRE (mm)	24.6	12.1	9.8
In-vivo DBT simulation	1.18×10^{14}	8.14×10^{11}	7.12×10^{11}
Misregistration TRE (mm)	32.7	9.6	8.8

Table 6.4: Comparison of the relative error, which is defined by $\frac{\|f_1^* - f_1^g\|^2}{\|f_1^g\|^2}$ and $\frac{\|f^* - f_1^g\|^2}{\|f_1^g\|^2}$ for the sequential and simultaneous method respectively.

	Initial	Sequential Method	Simultaneous Method
Toroid Phantom	1	0.0057	0.0002
Uncompressed Breast MRI	1	0.0051	0.0026
In-vivo DBT simulation	1	0.0058	0.0051

In conclusion, we have presented a novel simultaneous method to combine reconstruction and registration using limited angle DBT settings. Additionally, we employ a decoupled approach to solve this problem. Our work has led us to conclude that our simultaneous approach improves both the registration accuracy and the quality of the reconstruction when compared to the conventional sequential method using an affine transformation model. Furthermore, our investigation into the B-spline transformation model shows that our combined framework is generic and sufficiently flexible to allow this non-rigid transformation models to be incorporated with success in both reconstruction fidelity and registration accuracy.

Conclusion

A new trend in non-invasive breast cancer radiology is tomographic imaging of soft tissue for tumour detection and diagnosis, therapy planning, and outcome analysis. DBT is a noteworthy option, and there are substantial potential benefits offered by its 3D reconstructions and its comparable X-ray dose to 2D mammography. There are two main techniques available for aiding the human observer to process breast images using DBT, *i.e.*, reconstruction and registration. The reconstructed 3D information addresses the limitation of superimposition of dense fibro-glandular tissue associated with conventional mammography. In addition, the registration of temporal DBT volumes searches for the optimum transformation to align two observed images of the same breast object into a common reference frame. We hypothesise that the registration results will ultimately aid the reading process.

The objective of this thesis is to develop new algorithms to combine reconstruction and registration tasks applied to DBT data and geometry. Conventional studies proposed in the literature separate these steps, solving each task independently. This can be effective if reconstructing using a complete set of data, *e.g.*, in cone beam CT, assuming that only simple deformations exist. However, for the ill-posed problem of limited-angle DBT, estimating the deformations is difficult because of significant artefacts associated with DBT reconstructions, leading to severe inaccuracies in the registration. Rather than separate these two tasks and perform them sequentially, we investigate the techniques of combining them, and test the hypothesis that the performance of the joint estimation will be of benefit to each task.

Firstly, we have presented a method to iteratively reconstruct and register temporal DBT data sets. We have compared this approach with performing the two tasks sequentially. Secondly, we also present an innovative algorithm, which combines reconstruction of a pair of temporal DBT acquisitions with their simultaneous registration. Both affine and B-spline transformation models can be plugged-in and have been tested. We approach this nonlinear inverse problem using a decoupled

optimisation scheme. Interestingly, the *decoupled approach* has been applied in various applications involving fully coupled simultaneous optimisation; however, to our knowledge, this is the first time this approach has been applied to the reconstruction and registration of limited angle DBT.

These methods ultimately aim to address the problem of detecting changes between the two sets of temporal DBT data. Essentially, the embedding of registration provides more information for the reconstruction; however, it does not simply increase the number of forward projections because of the overlapping of the temporal data sets. SSD was employed as the registration metric, to formulate the cost criterion. This metric calculated the differences between the volume estimation f and the original two sets of acquisitions p_1 and p_2 . To evaluate the performance of our two methods, we use 3D software synthetic images, breast MR images, and DBT simulations from MRI with in-vivo breast compressions. Taken together, the evidence from this study intimates that both iterative and simultaneous methods reduce misregistration artefacts and offer superior reconstruction fidelity when compared to the conventional sequential method.

This research has also raised many interesting points to explore in future work. First, we would like to implement GPU acceleration for some components of our framework, *e.g.*, forward and backward projectors. If this method is to be used in a clinical environment manipulating real DBT data, the algorithms need to run as close to real-time as possible. Second, we could also tackle this large-scale optimisation problem using multi-scale and multi-resolution techniques to speed up the application and avoid possible local minima. Constrained optimisation can provide an alternative method to formulate the simultaneous reconstruction and registration problem (See Appendix E). Furthermore, our framework should be straightforward to incorporate other non-rigid transformation models and priors to regularise the solution. Also, registration offers considerable value when used to combine images acquired from different views, *e.g.*, registration of supine and prone CT colonography scans. This method has application for the detection of changes in temporal DBT data sets. It may be applied to the combined reconstruction and registration of two view (CC and MLO views) DBT data sets, to overcome the null-space limitation of the individual views and produce a single reconstructed volume with improved depth resolution. In addition, finding an appropriate balance between the convergent rate and the image fidelity will be an interesting task.

Finally, all the work completed makes vital progress towards addressing the research objective of improving both the reconstruction quality and registration accuracy of combined methods. Therefore, we believe that our combined methods offer great potential benefits for further applications in the field of breast cancer detection and diagnosis, therapy planning, and outcome analysis.

APPENDIX

A

Forward and Inverse Radon Transform

Firstly, we try to derive the forward Radon transform with Dirac delta function, which is a mathematical construct introduced by the British theoretical physicist Paul Dirac (Figure 3.3). Informally, it represents an infinitely sharp peak bounding unit area. In other words, a function $\delta(x)$ that has the value zero everywhere except at $x = 0$ where its value is infinitely large, and its total integral is 1. Thus, we can prove Equation 3.11 as follows.

Proof. I. The Equation 3.7 of \mathcal{L} can be rewritten as

$$\begin{pmatrix} x \\ y \end{pmatrix} = \begin{pmatrix} \cos \theta & -\sin \theta \\ \sin \theta & \cos \theta \end{pmatrix} \cdot \begin{pmatrix} \rho \\ \sigma \end{pmatrix} = \begin{pmatrix} \rho \cos \theta - \sigma \sin \theta \\ \sigma \cos \theta + \rho \sin \theta \end{pmatrix}, \quad (\text{A.1})$$

and its affine transform is

$$\begin{pmatrix} \rho \\ \sigma \end{pmatrix} = \begin{pmatrix} \cos \theta & \sin \theta \\ -\sin \theta & \cos \theta \end{pmatrix} \cdot \begin{pmatrix} x \\ y \end{pmatrix} = \begin{pmatrix} x \cos \theta + y \sin \theta \\ y \cos \theta - x \sin \theta \end{pmatrix}. \quad (\text{A.2})$$

Therefore, Equation 3.11 can be rewritten as

$$\begin{aligned} P(\rho, \theta) &= \int_{-\infty}^{\infty} f((\rho \cos \theta - \sigma \sin \theta), (\rho \sin \theta + \sigma \cos \theta)) d\sigma \\ &= \int_{-\infty}^{\infty} \int_{-\infty}^{\infty} f((\rho \cos \theta - \sigma \sin \theta), (\rho \sin \theta + \sigma \cos \theta)) \delta(\rho - \rho) d\rho d\sigma \\ &= \int_{-\infty}^{\infty} \int_{-\infty}^{\infty} f(\cdot) \delta(\rho - (\rho(\cos^2 \theta + \sin^2 \theta) + \sigma \cos \theta \sin \theta - \sigma \cos \theta \sin \theta)) d\rho d\sigma \\ &= \int_{-\infty}^{\infty} \int_{-\infty}^{\infty} f(\cdot) \delta(\rho - ((\rho \cos \theta - \sigma \sin \theta) \cos \theta + (\rho \sin \theta + \sigma \cos \theta) \sin \theta)) d\rho d\sigma. \end{aligned} \quad (\text{A.3})$$

From Equations 3.7 and A.1 we know that $x = \rho \cos \theta - \sigma \sin \theta$, and $y = \rho \sin \theta + \sigma \cos \theta$. In addition, we can get the *Jacobian determinant* J of the Equation A.2 as follows.

$$\begin{aligned}
d\rho d\sigma &= J \cdot dx dy \\
&= \begin{vmatrix} \frac{\partial \rho}{\partial x} & \frac{\partial \sigma}{\partial x} \\ \frac{\partial \rho}{\partial y} & \frac{\partial \sigma}{\partial y} \end{vmatrix} \cdot dx dy \\
&= \begin{vmatrix} -\sin \theta & -\cos \theta \\ \cos \theta & -\sin \theta \end{vmatrix} \cdot dx dy \\
&= (\sin^2 \theta - (-\cos^2 \theta)) \cdot dx dy \\
&= dx dy.
\end{aligned} \tag{A.4}$$

Thus, we can prove the Equation 3.11 by substituting x , y and $dxdy$ into the Equation A.3

$$P(\rho, \theta) = \int_{-\infty}^{\infty} \int_{-\infty}^{\infty} f(x, y) \delta(\rho - (x \cos \theta + y \sin \theta)) dx dy. \tag{A.5}$$

□

Proof. II. Furthermore, we can also derive the Equation 3.11 as follows.

$$\begin{aligned}
P(\rho, \theta) &= \int_{-\infty}^{\infty} f((\rho \cos \theta - \sigma \sin \theta), (\rho \sin \theta + \sigma \cos \theta)) d\sigma \\
&= \frac{1}{|\sin \theta|} \cdot \int_{-\infty}^{\infty} f(x, y) dx,
\end{aligned} \tag{A.6}$$

and it is obvious that

$$\frac{1}{|\sin \theta|} dx = \frac{1}{|\sin \theta|} d(\rho \cos \theta - \sigma \sin \theta) = \frac{1}{|\sin \theta|} (-\sin \theta) d\sigma. \tag{A.7}$$

When $\sin \theta < 0$ there is

$$\frac{1}{|\sin \theta|} dx = d\sigma. \tag{A.8}$$

From the Equation A.1 we know that

$$\sigma \sin \theta = \rho \cos \theta - x, \quad (\text{A.9})$$

$$\sigma \cos \theta = -\rho \sin \theta + y, \quad (\text{A.10})$$

$$-\rho \sin \theta + y = \rho \cos \theta \cot \theta - x \cot \theta. \quad (\text{A.11})$$

Therefore,

$$\begin{aligned} y &= \rho \cos \theta \cot \theta - x \cot \theta + \rho \sin \theta \\ &= \rho(\cos \theta \cot \theta + \sin \theta) - x \cot \theta \\ &= \rho(\cos \theta \cdot \frac{\cos \theta}{\sin \theta} + \sin \theta) - x \cot \theta \\ &= \rho(\frac{\cos^2 \theta + \sin^2 \theta}{\sin \theta}) - x \cot \theta \\ &= \frac{\rho}{\sin \theta} - x \cot \theta, \end{aligned} \quad (\text{A.12})$$

and we can rewrite the Equation A.6 as

$$\begin{aligned} P(\rho, \theta) &= \frac{1}{|\sin \theta|} \cdot \int_{-\infty}^{\infty} f(x, y) dx \\ &= \frac{1}{|\sin \theta|} \cdot \int_{-\infty}^{\infty} f(x, \frac{\rho}{\sin \theta} - x \cot \theta) dx. \end{aligned} \quad (\text{A.13})$$

By introducing the concept of the Dirac delta function into the Equation A.13, and assuming that $\sin \theta < 0$, we have

$$\begin{aligned} P(\rho, \theta) &= \frac{1}{|\sin \theta|} \cdot \int_{-\infty}^{\infty} \int_{-\infty}^{\infty} f(x, y) \delta(y - \frac{\rho}{\sin \theta} + x \cot \theta) dx dy \\ &= \int_{-\infty}^{\infty} \int_{-\infty}^{\infty} f(x, y) \delta(\rho - x \cos \theta - y \sin \theta) dx dy \\ &= \int_{-\infty}^{\infty} \int_{-\infty}^{\infty} f(x, y) \delta(\rho - (x \cos \theta + y \sin \theta)) dx dy \end{aligned} \quad (\text{A.14})$$

□

Secondly, we can derive the inverse Radon transform, *i.e.*, the formula of the FBP algorithm.

Proof. Firstly, the inverse Fourier Transform is expressed as follows

$$f(x, y) = \int_{-\infty}^{\infty} \int_{-\infty}^{\infty} F(\mu, v) e^{i2\pi(\mu x + vy)} d\mu dv. \quad (\text{A.15})$$

If we change it from the Cartesian coordinates into the polar coordinates using (ω, θ) instead of (μ, v) . In addition, we change the $d\mu dv$ into $\omega \cdot d\omega d\theta$ using the Jacobian determinant. The polar form of the inverse Fourier Transform can be expressed as

$$f(x, y) = \int_0^{2\pi} \int_0^{\infty} F(\omega, \theta) e^{i2\pi\omega(x \cos \theta + y \sin \theta)} \omega d\omega d\theta. \quad (\text{A.16})$$

Thus, in the Equation A.16 there is

$$\begin{aligned} d\mu dv &= J \cdot d\omega d\theta \\ &= \begin{vmatrix} \frac{\partial \mu}{\partial \omega} & \frac{\partial \mu}{\partial v} \\ \frac{\partial \mu}{\partial \theta} & \frac{\partial v}{\partial \theta} \end{vmatrix} \cdot d\omega d\theta \\ &= \begin{vmatrix} \cos \theta & \sin \theta \\ -\sin \theta \cdot \omega & \cos \theta \cdot \omega \end{vmatrix} \cdot d\omega d\theta \\ &= (\cos^2 \theta \cdot \omega - (-\sin^2 \theta \cdot \omega)) \cdot d\omega d\theta \\ &= \omega d\omega d\theta. \end{aligned} \quad (\text{A.17})$$

Furthermore, if θ separates into two parts 0° to 180° and 180° to 360° , and the Equation A.16 can be rewritten as

$$\begin{aligned} f(x, y) &= \int_0^{\pi} \int_0^{\infty} F(\omega, \theta) e^{i2\pi\omega(x \cos \theta + y \sin \theta)} \omega d\omega d\theta \\ &\quad + \int_0^{\pi} \int_0^{\infty} F(\omega, \theta + \pi) e^{i2\pi\omega(x \cos(\theta + \pi) + y \sin(\theta + \pi))} \omega d\omega d\theta. \end{aligned} \quad (\text{A.18})$$

Substitute the property of $F(\omega, \theta + \pi) = F(-\omega, \theta)$, we can rewrite the Equation A.18 as

$$f(x, y) = \int_0^{\pi} \left[\int_0^{\infty} F(\omega, \theta) |\omega| e^{i2\pi\omega\rho} d\omega \right] d\theta \quad (\text{A.19})$$

in which

$$\rho = x \cos \theta + y \sin \theta. \quad (\text{A.20})$$

If we use the Fourier Transform of the projection data at view angle θ , which is $S_\theta(\omega)$ in the Equation 3.17 instead of the 2D Fourier Transform $F(\mu, v)$ that is

$$f(x, y) = \int_0^\pi \left[\int_0^\infty S_\theta(\omega) |\omega| e^{i2\pi\omega\rho} d\omega \right] d\theta, \quad (\text{A.21})$$

and it can be rewritten as

$$f(x, y) = \int_0^\pi Q_\theta(x \cos \theta + y \sin \theta) d\theta \quad (\text{A.22})$$

in which

$$Q_\theta(\rho) = \int_{-\infty}^\infty S_\theta(\omega) |\omega| e^{i2\pi\omega\rho} d\omega \quad (\text{A.23})$$

If we set $S_\theta(\omega)|\omega| = S_\theta(\omega)\omega \cdot sgn(\omega)$, and $Q_\theta(\rho)$ can be expressed using the convolution method as follows

$$\begin{aligned} Q_\theta(\rho) &= F^{-1}[S_\theta(\omega)|\omega|] = F^{-1}[S_\theta(\omega)\omega] \otimes F^{-1}[sgn(\omega)] \\ &= \left[\frac{1}{i2\pi} \cdot \frac{\partial P(\rho, \theta)}{\partial \rho} \right] \otimes \left[\frac{-1}{i\pi\rho} \right] = \frac{1}{2\pi^2} \int_{-\infty}^\infty \left[\frac{\partial P(\sigma, \theta)}{\partial \sigma} \right] \frac{1}{\rho - \sigma} d\sigma. \end{aligned} \quad (\text{A.24})$$

Therefore, we can derive the classical form of the FBP algorithm as Equation 3.25 denoted

$$\begin{aligned} f(x, y) &= \int_0^\pi Q_\theta(\rho) d\theta \\ &= \int_0^\pi \left[\int_0^\infty S_\theta(\omega) |\omega| e^{i2\pi\omega\rho} d\omega \right] d\theta \\ &= \int_0^\pi F^{-1}[S_\theta(\omega)|\omega|] d\theta \\ &= \int_0^\pi F^{-1}[S_\theta(\omega)\omega \cdot sgn(\omega)] d\theta = \int_0^\pi \underbrace{F^{-1}[S_\theta(\omega)\omega] \otimes F^{-1}[sgn(\omega)]}_{\text{Filtering}} d\theta \\ &\quad \underbrace{\phantom{F^{-1}[S_\theta(\omega)\omega] \otimes F^{-1}[sgn(\omega)]} \text{Backprojection}} \\ &= \int_0^\pi \left[\frac{1}{i2\pi} \cdot \frac{\partial P(\rho, \theta)}{\partial \rho} \right] \otimes \left[\frac{-1}{i\pi\rho} \right] d\theta \\ &= \int_0^\pi \frac{1}{2\pi^2} \int_{-\infty}^\infty \left[\frac{\partial P(\sigma, \theta)}{\partial \sigma} \right] \frac{1}{\rho - \sigma} d\sigma d\theta \\ &= \frac{1}{2\pi^2} \int_0^\pi \int_{-\infty}^\infty \left[\frac{\partial P(\sigma, \theta)}{\partial \sigma} \right] \frac{1}{x \cos \theta + y \sin \theta - \sigma} d\sigma d\theta, \end{aligned} \quad (\text{A.25})$$

which includes a filtering and a backprojection procedure, and sgn is the sign function. \square

APPENDIX B

Optimality Conditions

B.1 Taylor's Theorem

We now state an important theorem, which forms the fundamental of optimisation theories.

Theorem B.1.1. (*Taylor's Theorem*)

Suppose that $f : \mathbb{R}^n \mapsto \mathbb{R}$ is n^{th} continuously differentiable which is a single-valued function of $x \in \mathbb{R}^n$ and $a \leq x \leq b$. Then we have that

$$f(x) = f(a) + \frac{(x-a)}{1!} f'(a) + \frac{(x-a)^2}{2!} f''(a) + \cdots + \frac{(x-a)^n}{n!} f^n(a) + \epsilon_n(x), \quad (\text{B.1})$$

where $\epsilon_n(x)$ is the remainder in Lagrange form as follows

$$\epsilon_n(x) = \frac{(x-a)^{n+1}}{(n+1)!} f^{n+1}(\xi). \quad (\text{B.2})$$

or the Cauchy form of the remainder term states that

$$\epsilon_n(x) = \frac{(x-\xi)^n (x-a)}{n!} f^{n+1}(\xi), \quad (\text{B.3})$$

and $a < \xi < x$. An significant alternative form of Equation B.1 may be obtained by changing x to $a+x$. Then

$$f(a+x) = f(a) + \frac{x}{1!} f'(a) + \frac{x^2}{2!} f''(a) + \cdots + \frac{x^n}{n!} f^n(a) + \epsilon_n(x), \quad (\text{B.4})$$

and if we change the notation of a in Equation B.4 into x and define a small neighbourhood Δx of x ; Thus

$$f(x + \Delta x) = f(x) + \frac{\Delta x}{1!} f'(x) + \frac{\Delta x^2}{2!} f''(x) + \cdots + \frac{\Delta x^n}{n!} f^n(x) + \epsilon_n(\Delta x), \quad (\text{B.5})$$

where now, from Equation B.2,

$$\epsilon_n(\Delta x) = \frac{\Delta x^{n+1}}{(n+1)!} f^{n+1}(x + \tau \Delta x), \quad (\text{B.6})$$

and $0 < \tau < 1$.

B.2 Local Minimum

Definition B.2.1. (*Local Minimum*)

Given a scalar $\delta > 0$, and $f : \mathbb{R}^n \mapsto \mathbb{R}$. We have the strict local minimiser x^* of $f(x)$ satisfied by all the neighbourhood Δx that

$$f(x^*) < f(x^* + \Delta x) \quad \text{for } 0 < |\Delta x| \leq \delta. \quad (\text{B.7})$$

B.3 First-Order Necessary Conditions

Theorem B.3.1. (*First-Order Necessary Conditions*)

If x^* is a local minimum and $f : \mathbb{R}^n \mapsto \mathbb{R}$ is continuously differentiable in an open neighbourhood of x^* , then $f'(x^*) = 0$.

Proof. Suppose for contradiction that $f'(x^*) \neq 0$. According to the Taylor's Theorem B.1.1, if the neighbourhood Δx of x^* is small enough to neglect the terms with Δx^2 or the higher orders and the remainder then Equation B.5 is approximated by

$$f(x + \Delta x) = f(x) + \frac{\Delta x}{1!} f'(x). \quad (\text{B.8})$$

By substitute x with x^* we have

$$f(x^* + \Delta x) = f(x^*) + \Delta x f'(x^*) \quad (\text{B.9})$$

and

$$\begin{cases} f(x^*) \leq f(x^* + \Delta x) & \text{iff } \Delta x > 0, \text{ when } f'(x^*) > 0; \\ f(x^*) < f(x^* + \Delta x) & \text{iff } \Delta x < 0, \text{ when } f'(x^*) < 0. \end{cases} \quad (\text{B.10})$$

We have a contradiction with Definition B.2.1. Therefore, $f'(x^*) = 0$ is a necessary condition of finding the local minimum. \square

Here x^* is known as a stationary point of $f(x)$ if $f'(x^*) = 0$ which could be a maximum, a minimum, an inflection or a saddle point.

B.4 Second-Order Necessary Conditions

Theorem B.4.1. (*Second-Order Necessary Conditions*)

If x^* is a local minimum and $f : \mathbb{R}^n \mapsto \mathbb{R}$ is twice continuously differentiable in an open neighbourhood of x^* , then $f'(x^*) = 0$ and $f''(x^*)$ is positive semidefinite.

Proof. According to the Taylor's Theorem B.1.1, if the neighbourhood Δx of x^* is small enough to neglect the terms with Δx^3 or the higher orders and the remainder then Equation B.5 is approximated by

$$f(x + \Delta x) = f(x) + \frac{\Delta x}{1!} f'(x) + \frac{\Delta x^2}{2!} f''(x). \quad (\text{B.11})$$

By substitute x with x^* we have

$$f(x^* + \Delta x) = f(x^*) + \Delta x f'(x^*) + \frac{\Delta x^2}{2!} f''(x^*), \quad (\text{B.12})$$

where $f'(x^*) = 0$ and

$$f(x^* + \Delta x) = f(x^*) + \frac{\Delta x^2}{2!} f''(x^*) \quad (\text{B.13})$$

$$= f(x^*) + \frac{\Delta x^T f''(x^*) \Delta x}{2!} \quad (\text{B.14})$$

Therefore, x^* is the local minimum iff $f''(x^*) \succeq 0$ in which $\succeq 0$ denotes positive semidefinite. \square

B.5 Second-Order Sufficient Conditions

Theorem B.5.1. (*Second-Order Sufficient Conditions*)

If $f : \mathbb{R}^n \mapsto \mathbb{R}$ is twice continuously differentiable in an open neighbourhood of x^* and that $f'(x^*) = 0$ and $f''(x^*)$ is positive definite. x^* is a strict local minimiser of the function $f(x)$.

Proof. Abridged. \square

APPENDIX C

Conditioning of Least Squares Problem

Here we discuss the conditioning of a linear least squares problem. Suppose the data p defined in Section 3.2.3 is

$$p = p_{\text{exact}} + \Delta p, \quad (\text{C.1})$$

where Δp represents the measurement error. Then the minimum norm solution of

$$\arg \min_f f(f) = \frac{1}{2} \|Af - (p_{\text{exact}} + \Delta p)\|_2^2 \quad (\text{C.2})$$

is

$$f^* = A^\dagger p \quad (\text{C.3})$$

$$= \sum_{i=1}^r \frac{u_i^T p}{\varsigma_i} v_i \quad (\text{C.4})$$

$$= \sum_{i=1}^r \left(\frac{u_i^T p_{\text{exact}}}{\varsigma_i} + \frac{u_i^T \Delta p}{\varsigma_i} \right) v_i \quad (\text{C.5})$$

where $A = U\Sigma V^T = \sum_{i=1}^r u_i \varsigma_i v_i^T$ and r is the rank of matrix A , and A^\dagger is the pseudo-inverse of A ; hence a large $\frac{u_i^T \Delta p}{\varsigma_i}$ even if $u_i^T \Delta p$ is small when a singular value ς_i is small. This shows that the error Δp of the data is magnified by small singular values.

Nonlinear Optimisation Algorithms

There are many optimisation algorithms. In this section, we provide a brief overview on some classical and widely used nonlinear optimisation methods, which we have applied for our problem of combining reconstruction and registration. Firstly, we introduce the nonlinear steepest descents and conjugate gradient algorithms. There are two main differences between these two nonlinear algorithms with their linear alternatives: First, a line search step is necessary to determine the step length; Second, we need to define a termination criterion. In general, we consider a nonlinear least squares as an example in this section that is

$$f^* = \arg \min_f \left(f(f) = \frac{1}{2} \|\mathcal{T}f - p\|^2 \right), \quad (\text{D.1})$$

in which \mathcal{T} is a nonlinear operator. In addition, p represents the data and f denotes the unknown. The nonlinear steepest descent algorithm is summarised as follows.

Algorithm 3: Nonlinear Steepest Descent Method

```

Input:  $k$ ,  $f_{\text{initial}}$ .
Output:  $f_{\text{optimised}}$ .
begin
    while stopping criterion unfulfilled do
         $d_k := -g(f_k);$ 
         $\tau_k := \arg \min_{\tau > 0} f(f_k + \tau d_k); \quad \% \text{Line Search}$ 
         $f_{k+1} := f_k + \tau_k d_k; \quad \% \text{Update the } f$ 
         $k := k + 1;$ 
     $f_{\text{optimised}} := f_{k+1};$ 

```

For the non-linear least squares problem in Equation D.1, the descent direction is

$$-g(f_k) = -\mathcal{T}^*(\mathcal{T}f - p), \quad (\text{D.2})$$

in which \mathcal{T}^* is the adjoint operator of \mathcal{T} .

Furthermore, a general form of the non-linear conjugate gradient algorithm is summarised as follows.

Algorithm 4: Nonlinear Conjugate Gradient Method

```

Input:  $k$ ,  $f_{\text{initial}}$ .
Output:  $f_{\text{optimised}}$ .
begin
     $d_{\text{initial}} := -g(f_{\text{initial}})$ ;      % Initial search direction is the negative gradient
     $r_{\text{initial}} := d_{\text{initial}}$ ;      % Initialise  $r_{\text{initial}}$ 
    while stopping criterion unfulfilled do
         $\tau_k := \arg \min_{\tau > 0} f(f_k + \tau d_k)$ ;      % Line Search
         $f_{k+1} := f_k + \tau_k d_k$ ;      % Update the  $f$ 
         $r_{k+1} := -g(f_{k+1})$ ;
         $\beta_k := \frac{\|r_{k+1}\|^2}{\|r_k\|^2}$ ;      % Fletcher-Reeves Method
        Or
         $\beta_k := \frac{\langle r_{k+1} - r_k, r_{k+1} \rangle}{\langle r_{k+1} - r_k, d_k \rangle}$ ;      % Polak-Ribière Method
         $d_{k+1} := r_{k+1} + \beta_k d_k$ ;
         $k := k + 1$ ;
     $f_{\text{optimised}} := f_{k+1}$ ;

```

In both algorithms, there is a line search sub-problem, which contains a one-dimensional optimisation that is

$$f_{k+1} := f_k + \tau_k d_k, \quad (\text{D.3})$$

where d_k is the search direction and we solve the step length τ . The search direction should satisfy

$$\langle g(f_k), d_k \rangle < 0 \quad (\text{D.4})$$

to be a descent direction. Therefore, the negative gradient direction is suitable because

$$\langle g(f_k), g(f_k) \rangle = \|g(f_k)\|^2 < 0. \quad (\text{D.5})$$

More generally, the step length must fulfil the Wolfe conditions, which guarantee the sufficient decrease and satisfy the curvature condition.

In addition, we give a brief description of the nonlinear Newton method as

Algorithm 5: Nonlinear Newton Method

Input: k , f_{initial} .

Output: $f_{\text{optimised}}$.

$H_{\text{initial}} := I$; % Initialise the inverse Hessian matrix as identity matrix

begin

while stopping criterion unfulfilled do

$d_k := -H_k g(f_k)$; % If $H_k \approx J_k^T J_k$ is used, it is called Gauss-Newton Method

$\tau_k := \arg \min_{\tau > 0} f(f_k + \tau d_k)$; % Line Search

$f_{k+1} := f_k + \tau_k d_k$; % Update the f

$k := k + 1$;

$f_{\text{optimised}} := f_{k+1}$;

Similarly, its alternative quasi-Newton method using DFP and BFGS approximations is described as follows.

Algorithm 6: quasi-Newton Method

Input: k , f_{initial} .

Output: $f_{\text{optimised}}$.

$H_{\text{initial}} := I$; % Initialise the inverse Hessian matrix as identity matrix
 $d_{\text{initial}} := -H_{\text{initial}}g(f_{\text{initial}})$; % Initial search direction is the negative gradient

begin

| **while** stopping criterion unfulfilled **do**

| | $\tau_k := \arg \min_{\tau > 0} f(f_k + \tau d_k)$; % Line Search

| | $f_{k+1} := f_k + \tau_k d_k$; % Update the f

| | $s_k := f_{k+1} - f_k$;

| | $z_k := g(f_{k+1}) - g(f_k)$;

$H_{k+1} := H_k - \frac{H_k z_k z_k^T H_k}{z_k^T H_k z_k} + \frac{s_k s_k^T}{z_k^T s_k}$; % DFP

| | **Or**

$H_{k+1} := H_k + \frac{1}{s_k^T z_k} \left[\left(1 + \frac{z_k^T H_k z_k}{s_k^T z_k} \right) s_k s_k^T - H_k z_k s_k^T - s_k z_k^T H_k \right]$; % BFGS

$d_{k+1} := -H_{k+1}g(f_{k+1})$; % Update the search direction

$k := k + 1$;

$f_{\text{optimised}} := f_{k+1}$;

Next, we introduce the Levenberg-Marquardt method as follows.

Algorithm 7: Levenberg-Marquardt Method

Input: k , f_{initial} , λ_{initial} , C_{scale} .

Output: $f_{\text{optimised}}$.

$H_{\text{initial}} := I$; % Initialise the inverse Hessian matrix as identity matrix

$\lambda_{\text{initial}} :=$ A large value

$C_{\text{scale}} :=$ Scaling constant > 1

begin

while stopping criterion unfulfilled do

Here: $d_k := -(H_k^{-1} + \lambda I)^{-1}g(f_k)$;

if $f(f_k + d_k) < f(f_k)$ then

$\lambda = \frac{\lambda}{C_{\text{scale}}}$

else

$\lambda = \lambda \times C_{\text{scale}}$

Goto Here

$f_{k+1} := f_k + d_k$; % Update the f

$k := k + 1$;

$f_{\text{optimised}} := f_{k+1}$;

Lastly, there are several stopping criteria (threshold ϵ). For instance,

(a) Functional reduction is sufficient

$$\frac{f(f_k)}{f(f_{\text{Initial}})} \leq \epsilon; \quad (\text{D.6})$$

(b) Relative change of the functional is less than a threshold

$$\frac{f(f_{k+1}) - f(f_k)}{f(f_{k+1})} \leq \epsilon; \quad (\text{D.7})$$

(c) The gradient of the functional is less than a threshold

$$\|g(f_{k+1})\| \leq \epsilon. \quad (\text{D.8})$$

APPENDIX **E**

Constrained Reconstruction and Registration

Constrained optimisation provides an alternative formulation to tackle the simultaneous reconstruction and registration problem. We propose an algorithm that minimises the total variation (TV) of the deformed image subject to constraints that the estimated projections are within specified tolerances of a pair of temporal DBT acquisitions and that the values of the intensities are non-negative.

The TV regularisation term has been used in iterative image reconstruction algorithms for both cone beam CT and DBT applications, [260] [143]. Generally, the TV term denoises the image with an edge-preserving smoothing. In our DBT application, there is no unique solution for our simultaneous reconstruction and registration objective functional because of the incompleteness of the data. The TV term, which tunes the trade-off between reconstruction fidelity and regularity, is able to select a unique solution for our joint objective functional (lower TV means worse data fidelity). Therefore, we believe a constrained model, in which the TV term forms the objective function with reconstruction fidelity as constraints, is a natural choice to solve our combined problem. In addition, we can maintain the data fidelity while the image TV is lowered, and it is also straightforward to incorporate the non-negativity constraint. Consequently, we form our constrained model using the TV term and three additional constraints as follows

$$(f^*, \zeta^*) = \arg \min_{f, \zeta} \left(f(f, \zeta) = \|\mathcal{T}_\zeta f\|_{TV} \right) \quad (E.1)$$

$$s.t. \quad Af - p_1 = 0 \quad (E.2)$$

$$A\mathcal{T}_\zeta f - p_2 = 0 \quad (E.3)$$

$$f \geq 0 \quad (E.4)$$

Furthermore, the Lagrangian $\mathcal{L}(f, \zeta, \lambda, \chi, \xi)$ is

$$\mathcal{L}(f, \zeta, \lambda, \chi, \xi) = \|\mathcal{T}_\zeta f\|_{TV} + \lambda(Af - p_1)^T + \chi(A\mathcal{T}_\zeta f - p_2)^T - \xi f^T, \quad (\text{E.5})$$

in which f and ζ are primary variables, and λ , χ and ξ are vectors representing dual variables.

For a constrained minimisation problem the necessary conditions for a solution $(f^*, \zeta^*, \lambda^*, \chi^*, \xi^*)$ to be the optimal one are called the Karush-Kuhn-Tucker (KKT) conditions. These are

(a) Non-negativity

$$\xi^* \geq 0 \quad (\text{E.6})$$

(b) Complementarity

$$\lambda^* c_1(f^*, \zeta^*) = 0, \quad \chi^* c_1(f^*, \zeta^*) = 0 \quad (\text{E.7})$$

in which $i = 1, 2, \dots, N + 2$ and N is equal to the number of voxels, and

$$c_1(f^*, \zeta^*) = Af^* - p_1 = 0 \quad (\text{E.8})$$

$$c_2(f^*, \zeta^*) = A\mathcal{T}_\zeta^* f^* - p_2 = 0 \quad (\text{E.9})$$

$$c_i(f^*, \zeta^*) = -f^* \leq 0 \quad i \in [3, N + 2] \quad (\text{E.10})$$

The conditions for optimality of potential solutions are therefore equations E.8, E.9, and E.10 together with

$$\nabla \mathcal{L}(f, \zeta, \lambda, \chi, \xi) = 0 \quad (\text{E.11})$$

The above equation E.11 could be written as

$$\begin{aligned}\nabla_f \mathcal{L} &= \nabla_f \|\mathcal{T}_\zeta f\|_{TV} - \lambda \nabla_f c_1(f, \zeta) - \chi \nabla_f c_2(f, \zeta) + \sum_{i=3}^{N+2} \xi \nabla_f c_i(f, \zeta) \\ &= \nabla_f \|\mathcal{T}_\zeta f\|_{TV} - A^T \lambda - \mathcal{T}_\zeta^* A^T \chi - \xi\end{aligned}\quad (\text{E.12})$$

$$\begin{aligned}\nabla_\zeta \mathcal{L} &= \nabla_\zeta \|\mathcal{T}_\zeta f\|_{TV} - \lambda \nabla_\zeta c_1(f, \zeta) - \chi \nabla_\zeta c_2(f, \zeta) + \sum_{i=3}^{N+2} \xi \nabla_\zeta c_i(f, \zeta) \\ &= f^T \mathcal{T}_\zeta'^* A^T \chi\end{aligned}\quad (\text{E.13})$$

$$\begin{aligned}\nabla_\lambda \mathcal{L} &= \nabla_\lambda \|\mathcal{T}_\zeta f\|_{TV} - \lambda \nabla_\lambda c_1(f, \zeta) - \chi \nabla_\lambda c_2(f, \zeta) + \sum_{i=3}^{N+2} \xi \nabla_\lambda c_i(f, \zeta) \\ &= p_1 - Af\end{aligned}\quad (\text{E.14})$$

$$\begin{aligned}\nabla_\chi \mathcal{L} &= \nabla_\chi \|\mathcal{T}_\zeta f\|_{TV} - \lambda \nabla_\chi c_1(f, \zeta) - \chi \nabla_\chi c_2(f, \zeta) + \sum_{i=3}^{N+2} \xi \nabla_\chi c_i(f, \zeta) \\ &= p_2 - A \mathcal{T}_\zeta f\end{aligned}\quad (\text{E.15})$$

$$\begin{aligned}\nabla_\xi \mathcal{L} &= \nabla_\xi \|\mathcal{T}_\zeta f\|_{TV} - \lambda \nabla_\xi c_1(f, \zeta) - \chi \nabla_\xi c_2(f, \zeta) + \sum_{i=3}^{N+2} \xi \nabla_\xi c_i(f, \zeta) \\ &= -f\end{aligned}\quad (\text{E.16})$$

Therefore,

$$\nabla \mathcal{L}(f, \zeta, \lambda, \chi, \xi) = \begin{pmatrix} \nabla_f \|\mathcal{T}_\zeta f\|_{TV} - A^T \lambda - \mathcal{T}_\zeta^* A^T \chi - \xi \\ f^T \mathcal{T}_\zeta'^* A^T \chi \\ p_1 - Af \\ p_2 - A \mathcal{T}_\zeta f \\ -f \end{pmatrix} = 0 \quad (\text{E.17})$$

Here the cost function and the relevant gradient with respect to f , ζ , λ , χ , and ξ for our constrained optimisation problem are shown in E.5 and E.17 above respectively. We have not implemented and tested this constrained framework; however, we hope this method will be investigated in future work.

Bibliography

- [1] *A guide to mammography and other breast imaging procedures: (report no. 149)*. Tech. rep., National Council on Radiation Protection and Measurements (NCRP) (2004). URL http://knovel.com/web/portal/browse/display?_EXT_KNOVEL_DISPLAY_bookid=1635&VerticalID=0. [Cited on page 58.]
- [2] *All breast cancer report*. Tech. rep., National Health Service (2006). URL <http://www.cancerscreening.nhs.uk/breastscreen/all-breast-cancer-report.pdf>. [Cited on pages 35 and 54.]
- [3] *Breast cancer booklet*. Tech. rep., Cancer Council Victoria (2007). URL http://www.cancervic.org.au/downloads/brochures/cancer_types/Breast_Cancer_booklet07.pdf. [Cited on pages 21 and 37.]
- [4] *Breast screening in the UK: A brief history*. Tech. rep., CRUK (2011). URL <http://info.cancerresearchuk.org/cancerstats/types/breast/screening/history/index.htm>. [Cited on pages 35 and 54.]
- [5] ANDERSEN, A. *Algebraic reconstruction in CT from limited views*. Medical Imaging, IEEE Transactions on, vol. 8(1) (1989), pp. 50–55. [Cited on page 85.]
- [6] ANDERSEN, A. AND KAK, A. *Simultaneous algebraic reconstruction technique (SART): A superior implementation of the ART algorithm*. Ultrasonic Imaging, vol. 6(1) (1984), pp. 81 – 94. URL <http://www.sciencedirect.com/science/article/pii/0161734684900087>. [Cited on page 85.]
- [7] AVRIL, N., ET AL. *Glucose metabolism of breast cancer assessed by 18F-FDG PET: Histologic and immunohistochemical tissue analysis*. Journal of Nuclear Medicine, vol. 42(1) (2001), pp. 9–16. URL <http://jnm.snmjournals.org/content/42/1/9.abstract>. [Cited on page 57.]
- [8] BADEA, C., KOLITSI, Z., AND PALLIKARAKIS, N. *A wavelet-based method for removal of out-of-plane structures in digital tomosynthesis*. Computerized Medical Imaging and Graphics, vol. 22(4) (1998), pp. 309 – 315. URL <http://www.sciencedirect.com/science/article/pii/S0895611198000378>. [Cited on page 78.]
- [9] BADT, S. *Two algorithms for taking advantage of temporal coherence in ray tracing*. The Visual Computer, vol. 4 (1988), pp. 123–132. URL <http://dx.doi.org/10.1007/BF01908895>. 10.1007/BF01908895. [Cited on page 125.]
- [10] BAEZ, E., ET AL. *Minimal invasive complete excision of benign breast tumors using a three-dimensional ultrasound-guided mammotome vacuum device*. Ultrasound in Obstetrics and Gynecology, vol. 21(3) (2003), pp. 267–272. URL <http://dx.doi.org/10.1002/uog.74>. [Cited on page 48.]
- [11] BAILY, N. A., CREPEAU, R. L., AND LASSER, E. C. *Fluoroscopic tomography*. Investigative Radiology, vol. 9(2) (1974), pp. 94–103. URL http://journals.lww.com/investigativeradiology/Fulltext/1974/03000/Fluoroscopic_Tomography.8.aspx. [Cited on page 59.]

- [12] BAILY, N. A. AND KAMPP, T. D. *Digitized longitudinal tomography*. Investigative Radiology, vol. 16(2) (1981), pp. 126–132. URL http://journals.lww.com/investigativeradiology/Fulltext/1981/03000/Digitized_Longitudinal_Tomography.9.aspx. [Cited on page 59.]
- [13] BAILY, N. A., LASSER, E. C., AND CREPEAU, R. L. *Electrofluoroplanigraphy*. Radiology, vol. 107(3) (1973), pp. 669–671. URL <http://radiology.rsna.org/content/107/3/669.abstract>. [Cited on page 59.]
- [14] BAILY, N. A., ET AL. *The capability of fluoroscopic systems for the production of computerized axial tomograms*. Investigative Radiology, vol. 11(5) (1976), pp. 434–439. URL http://journals.lww.com/investigativeradiology/Fulltext/1976/09000/The_Capability_of_Fluoroscopic_Systems_for_the.148.aspx. [Cited on page 59.]
- [15] BAJCSY, R. AND KOVÁČIČ, S. *Multiresolution elastic matching*. Computer Vision, Graphics, and Image Processing, vol. 46(1) (1989), pp. 1–21. URL <http://www.sciencedirect.com/science/article/pii/S0734189X89800143>. [Cited on page 108.]
- [16] BAKIC, P., RICHARD, F., AND MAIDMENT, A. *2d-to-3d x-ray breast image registration*. In PLUIM, J., LIKAR, B., AND GERRITSEN, F. (Editors), *Biomedical Image Registration*, vol. 4057 of *Lecture Notes in Computer Science*. Springer Berlin / Heidelberg (2006), pp. 84–91. URL http://dx.doi.org/10.1007/11784012_11. [Cited on page 116.]
- [17] BALDWIN, P. *Digital breast tomosynthesis*. Radiologic Technology, vol. 81(1) (2009), pp. 57M–74M. URL <http://www.radiologictechnology.org/content/81/1/57M.abstract>. [Cited on page 61.]
- [18] BANKMAN, I. *Handbook of Medical Imaging: Processing and Analysis*. Academic Press, 1st edn. (2000). [Cited on page 99.]
- [19] BAĞCI, U. AND BAI, L. *Multiresolution elastic medical image registration in standard intensity scale*. In *Computer Graphics and Image Processing, 2007. SIBGRAPI 2007. XX Brazilian Symposium on* (2007), pp. 305–312. [Cited on page 99.]
- [20] BERG, W. A., ET AL. *Combined screening with ultrasound and mammography vs mammography alone in women at elevated risk of breast cancer*. JAMA: The Journal of the American Medical Association, vol. 299(18) (2008), pp. 2151–2163. URL <http://jama.ama-assn.org/content/299/18/2151.abstract>. [Cited on page 48.]
- [21] BERTERO, M. AND BOCCACCI, P. *Introduction to Inverse Problems in Imaging*. Taylor & Francis, 1st edn. (1998). [Cited on page 94.]
- [22] BICK, U., ET AL. *Digital Mammography: Current Concepts (Medical Radiology/Diagnostic Imaging)*. Springer, 1st edn. (2009). [Cited on pages 23, 55, and 69.]
- [23] BIJKER, N., ET AL. *Risk factors for recurrence and metastasis after breast-conserving therapy for ductal carcinoma-in-situ: Analysis of european organization for research and treatment of cancer trial 10853*. Journal of Clinical Oncology, vol. 19(8) (2001), pp. 2263–2271. URL <http://jco.ascopubs.org/content/19/8/2263.abstract>. [Cited on page 38.]
- [24] BISSONNETTE, M., ET AL. *Digital breast tomosynthesis using an amorphous selenium flat panel detector*. vol. 5745. SPIE (2005), pp. 529–540. URL <http://link.aip.org/link/?PSI/5745/529/1>. [Cited on pages 60, 65, 75, and 84.]
- [25] BLEUET, P., ET AL. *An adapted fan volume sampling scheme for 3D algebraic reconstruction in linear tomosynthesis*. Nuclear Science, IEEE Transactions on, vol. 49(5) (2002), pp. 2366 – 2372. [Cited on page 88.]

- [26] BOEHLER, T. AND PEITGEN, H.-O. *Reducing motion artifacts in 3D breast ultrasound using non-linear registration*. In METAXAS, D., ET AL. (Editors), *Medical Image Computing and Computer-Assisted Intervention MICCAI 2008*, vol. 5242 of *Lecture Notes in Computer Science*. Springer Berlin / Heidelberg (2008), pp. 998–1005. URL http://dx.doi.org/10.1007/978-3-540-85990-1_120. [Cited on page 48.]
- [27] BOONE, J. M., ET AL. *Dedicated breast CT: Radiation dose and image quality evaluation*. Radiology, vol. 221(3) (2001), pp. 657–667. URL <http://radiology.rsna.org/content/221/3/657.abstract>. [Cited on page 58.]
- [28] ———. *Performance assessment of a pendant-geometry ct scanner for breast cancer detection*. vol. 5745. SPIE (2005), pp. 319–323. URL <http://link.aip.org/link/?PSI/5745/319/1>. [Cited on page 116.]
- [29] BORST, M. J. AND INGOLD, J. A. *Metastatic patterns of invasive lobular versus invasive ductal carcinoma of the breast*. Surgery, vol. 114(4) (1993), pp. 637–642. URL <http://www.ncbi.nlm.nih.gov/pubmed/8211676>. [Cited on page 38.]
- [30] BOYD, S. AND VANDENBERGHE, L. *Convex Optimization*. Cambridge University Press, 1st edn. (2004). [Cited on page 94.]
- [31] BRASCH, R., WEINMANN, H., AND WESBEY, G. *Contrast-enhanced NMR imaging: animal studies using gadolinium-DTPA complex*. American Journal of Roentgenology, vol. 142(3) (1984), pp. 625–630. URL <http://www.ajronline.org/content/142/3/625.abstract>. [Cited on page 44.]
- [32] BRONZINO, J. D. (Editor). *The Biomedical Engineering Handbook: Vol. 1&2*. Springer, 2nd edn. (2000), pp. 1157–1168. [Cited on page 72.]
- [33] BROWN, L. G. *A survey of image registration techniques*. ACM Comput. Surv., vol. 24 (1992), pp. 325–376. URL <http://doi.acm.org/10.1145/146370.146374>. [Cited on pages 99, 106, and 109.]
- [34] BUSHBERG, J. T., ET AL. *The Essential Physics of Medical Imaging*. Lippincott Williams & Wilkins, 2nd edn. (2001). [Cited on pages 23, 49, 51, 62, and 63.]
- [35] BUZUG, T. M. *Computed Tomography: From Photon Statistics to Modern Cone-Beam CT*. Springer, 1st edn. (2008). URL <http://www.springerlink.com/content/978-3-540-39408-2#section=158980&page=1>. [Cited on pages 72 and 145.]
- [36] BYRNE, C. *Block-iterative methods for image reconstruction from projections*. Image Processing, IEEE Transactions on, vol. 5(5) (1996), pp. 792 –794. [Cited on page 85.]
- [37] CHAKRABORTY, D. P., ET AL. *Self-masking subtraction tomosynthesis*. Radiology, vol. 150(1) (1984), pp. 225–229. URL <http://radiology.rsna.org/content/150/1/225.abstract>. [Cited on page 59.]
- [38] CHAN, H.-P. *Computer-aided diagnosis in breast tomosynthesis and chest CT*. Communication of the Imaging Group of the JSRT, vol. 32(1) (2009), pp. 8–18. URL <http://ci.nii.ac.jp/naid/110007161104/en/>. [Cited on page 90.]
- [39] CHAN, H.-P., ET AL. *Computer-aided detection system for breast masses on digital tomosynthesis mammograms: Preliminary experience*. Radiology, vol. 237(3) (2005), pp. 1075–1080. URL <http://radiology.rsna.org/content/237/3/1075.abstract>. [Cited on page 116.]
- [40] CHEN, S. C., ET AL. *Initial clinical experience with contrast-enhanced digital breast tomosynthesis*. Academic Radiology, vol. 14(2) (2007), pp. 229 – 238. URL <http://www.sciencedirect.com/science/article/pii/S1076633206006647>. [Cited on page 64.]

- [41] CHEN, Y. *Digital breast tomosynthesis (DBT)-a novel imaging technology to improve early breast cancer detection: Implementation, comparison and optimization*. Ph.D. thesis, Duke University (2007). [Cited on pages 24 and 84.]
- [42] CHENG, H., ET AL. *Automated breast cancer detection and classification using ultrasound images: A survey*. Pattern Recognition, vol. 43(1) (2010), pp. 299 – 317. URL <http://www.sciencedirect.com/science/article/pii/S0031320309002027>. [Cited on page 48.]
- [43] CHOU, Y.-Y. *Transitive and symmetric nonrigid image registration*. Master's thesis, Georgia Institute of Technology (2004). [Cited on page 152.]
- [44] CHRISTENSEN, G., RABBITT, R., AND MILLER, M. *Deformable templates using large deformation kinematics*. Image Processing, IEEE Transactions on, vol. 5(10) (1996), pp. 1435 –1447. [Cited on page 108.]
- [45] CHUNG, J., HABER, E., AND NAGY, J. *Numerical methods for coupled super-resolution*. Inverse Problems, vol. 22(4) (2006), p. 1261. URL <http://stacks.iop.org/0266-5611/22/i=4/a=009>. [Cited on page 156.]
- [46] CHUNG, J., STERNBERG, P., AND YANG, C. *High-performance three-dimensional image reconstruction for molecular structure determination*. International Journal of High Performance Computing Applications, vol. 24(2) (2010), pp. 117–135. URL <http://hpc.sagepub.com/content/24/2/117.abstract>. [Cited on page 157.]
- [47] CLAUS, B., ET AL. *Generalized filtered back-projection reconstruction in breast tomosynthesis*. In ASTLEY, S., ET AL. (Editors), *Digital Mammography*, vol. 4046 of *Lecture Notes in Computer Science*. Springer Berlin / Heidelberg (2006), pp. 167–174. URL http://dx.doi.org/10.1007/11783237_24. [Cited on page 76.]
- [48] CLEMONS, M. AND GOSS, P. *Estrogen and the risk of breast cancer*. New England Journal of Medicine, vol. 344(4) (2001), pp. 276–285. URL <http://www.nejm.org/doi/full/10.1056/NEJM200101253440407>. [Cited on page 37.]
- [49] COLE-BEUGLET, C., ET AL. *Ultrasound mammography*. Radiologic Clinics of North America, vol. 18(1) (1980), pp. 133–143. [Cited on page 47.]
- [50] COLLIGNON, A., ET AL. *Automated multi-modality image registration based on information theory*. Information Processing in Medical Imaging (1995), pp. 263–274. [Cited on page 110.]
- [51] COUCH, F. J., ET AL. *BRCA1 mutations in women attending clinics that evaluate the risk of breast cancer*. New England Journal of Medicine, vol. 336(20) (1997), pp. 1409–1415. URL <http://www.nejm.org/doi/full/10.1056/NEJM199705153362002>. [Cited on page 37.]
- [52] CRUM, W. R., HARTKENS, T., AND HILL, D. L. G. *Non-rigid image registration: theory and practice*. British Journal of Radiology, vol. 77(suppl 2) (2004), pp. S140–S153. URL http://bjr.birjournals.org/content/77/suppl_2/S140.abstract. [Cited on page 106.]
- [53] CUI, Y., ET AL. *Malignant lesion segmentation in contrast-enhanced breast mr images based on the marker-controlled watershed*. Medical Physics, vol. 36(10) (2009), pp. 4359–4369. URL <http://link.aip.org/link/?MPH/36/4359/1>. [Cited on page 45.]
- [54] DALLESSIO, K. M. *Three-dimensional digital breast tomosynthesis: An introduction*. eRADIMAGING (2011). [Cited on pages 23 and 69.]
- [55] DASH, N., ET AL. *Magnetic resonance imaging in the diagnosis of breast disease*. American Journal of Roentgenology, vol. 146(1) (1986), pp. 119–125. URL <http://www.ajronline.org/content/146/1/119.abstract>. [Cited on page 44.]

- [56] DEFRISE, M. AND CLACK, R. *A cone-beam reconstruction algorithm using shift-variant filtering and cone-beam backprojection*. Medical Imaging, IEEE Transactions on, vol. 13(1) (1994), pp. 186 –195. [Cited on page 83.]
- [57] DEGANI, H., ET AL. *Mapping pathophysiological features of breast tumors by MRI at high spatial resolution*. Nature Medicine, vol. 3(7) (1997), pp. 780–782. [Cited on page 45.]
- [58] DERSHAW, D. D. *Film or digital mammographic screening?* New England Journal of Medicine, vol. 353(17) (2005), pp. 1846–1847. URL <http://www.nejm.org/doi/full/10.1056/NEJMMe058253>. [Cited on page 55.]
- [59] DESAI, M. AND JENKINS, W. *Convolution backprojection image reconstruction for spotlight mode synthetic aperture radar*. Image Processing, IEEE Transactions on, vol. 1(4) (1992), pp. 505–517. [Cited on page 76.]
- [60] DIEKMANN, F. AND BICK, U. *Tomosynthesis and contrast-enhanced digital mammography: recent advances in digital mammography*. European Radiology, vol. 17 (2007), pp. 3086–3092. URL <http://dx.doi.org/10.1007/s00330-007-0715-x>. 10.1007/s00330-007-0715-x. [Cited on page 64.]
- [61] DIEKMANN, F., ET AL. *Thick slices from tomosynthesis data sets: Phantom study for the evaluation of different algorithms*. Journal of Digital Imaging, vol. 22 (2009), pp. 519–526. URL <http://dx.doi.org/10.1007/s10278-007-9075-y>. 10.1007/s10278-007-9075-y. [Cited on page 63.]
- [62] DOBBINS III, J. T. AND GODFREY, D. J. *Digital X-ray tomosynthesis: current state of the art and clinical potential*. Physics in Medicine and Biology, vol. 48(19) (2003), p. R65. URL <http://stacks.iop.org/0031-9155/48/i=19/a=R01>. [Cited on pages 61 and 78.]
- [63] DOYLEY, M. M., ET AL. *A freehand elastographic imaging approach for clinical breast imaging: system development and performance evaluation*. Ultrasound in Medicine & Biology, vol. 27(10) (2001), pp. 1347–1357. URL <http://www.sciencedirect.com/science/article/pii/S030156290100429X>. [Cited on page 48.]
- [64] DREW, P., CAWTHORN, S., AND MICHELL, M. *Interventional Ultrasound of the Breast*. Informa Healthcare (2007). [Cited on page 46.]
- [65] DRUKKER, K., SENNETT, C., AND GIGER, M. *Automated method for improving system performance of computer-aided diagnosis in breast ultrasound*. Medical Imaging, IEEE Transactions on, vol. 28(1) (2009), pp. 122 –128. [Cited on page 48.]
- [66] DURYEA, J., III, J. T. D., AND LYNCH, J. A. *Digital tomosynthesis of hand joints for arthritis assessment*. Medical Physics, vol. 30(3) (2003), pp. 325–333. URL <http://link.aip.org/link/?MPH/30/325/1>. [Cited on page 68.]
- [67] EGGERMONT, P., HERMAN, G., AND LENT, A. *Iterative algorithms for large partitioned linear systems, with applications to image reconstruction*. Linear Algebra and its Applications, vol. 40(0) (1981), pp. 37 – 67. URL <http://www.sciencedirect.com/science/article/pii/0024379581901397>. [Cited on page 85.]
- [68] EL YOUSEF, S. J., ET AL. *Initial experience with nuclear magnetic resonance (NMR) imaging of the human breast*. Journal of Computer Assisted Tomography, vol. 7(2) (1983), pp. 215–218. URL http://journals.lww.com/jcat/Fulltext/1983/04000/Initial_Experience_with_Nuclear_Magnetic_Resonance.1.aspx. [Cited on page 44.]
- [69] ELBAKRI, I., ET AL. *Integrated full-field digital mammography and 3d breast ultrasound system* (2004), p. 100959. [Cited on page 115.]
- [70] ETTINGER, G. J. *Hierarchical three-dimensional medical image registration*. Phd thesis, Massachusetts Institute of Technology, Cambridge, MA, USA (1997). [Cited on page 99.]

- [71] FALKENBERRY, S. S. AND LEGARE, R. D. *Risk factors for breast cancer*. Obstetrics and Gynecology Clinics of North America, vol. 29(1) (2002), pp. 159 – 172. URL <http://www.sciencedirect.com/science/article/pii/S0889854503000597>. Breast Disease: Diagnosis and Contemporary Management. [Cited on page 37.]
- [72] FELDKAMP, L. A., DAVIS, L. C., AND KRESS, J. W. *Practical cone-beam algorithm*. J. Opt. Soc. Am. A, vol. 1(6) (1984), pp. 612–619. URL <http://josaa.osa.org/abstract.cfm?URI=josaa-1-6-612>. [Cited on page 83.]
- [73] FELDMAN, R. P. AND GOODRICH, J. T. *The edwin smith surgical papyrus*. Child's Nervous System, vol. 15 (1999), pp. 281–284. URL <http://dx.doi.org/10.1007/s003810050395>. 10.1007/s003810050395. [Cited on page 42.]
- [74] FENSTER, A., DOWNEY, D. B., AND CARDINAL, H. N. *Three-dimensional ultrasound imaging*. Physics in Medicine and Biology, vol. 46(5) (2001), p. R67. URL <http://stacks.iop.org/0031-9155/46/i=5/a=201>. [Cited on page 48.]
- [75] FESSLER, J. *Optimization transfer approach to joint registration / reconstruction for motion-compensated image reconstruction*. In *Biomedical Imaging: From Nano to Macro, 2010 IEEE International Symposium on* (2010), pp. 596 –599. [Cited on page 157.]
- [76] FISCHER, B. AND MODERSITZKI, J. *Ill-posed medicinean introduction to image registration*. Inverse Problems, vol. 24(3) (2008), p. 034,008. URL <http://stacks.iop.org/0266-5611/24/i=3/a=034008>. [Cited on pages 106, 110, and 112.]
- [77] FITZPATRICK, J. M. AND WEST, J. B. *The distribution of target registration error in rigid-body point-based registration*. Medical Imaging, IEEE Transactions on, vol. 20(9) (2001), pp. 917–927. URL <http://view.ncbi.nlm.nih.gov/pubmed/11585208>. [Cited on page 112.]
- [78] FLETCHER, R. AND REEVES, C. M. *Function minimization by conjugate gradients*. The Computer Journal, vol. 7(2) (1964), pp. 149–154. URL <http://comjnl.oxfordjournals.org/content/7/2/149.abstract>. [Cited on page 95.]
- [79] FORD, D., ET AL. *Genetic heterogeneity and penetrance analysis of the BRCA1 and BRCA2 genes in breast cancer families*. The American Journal of Human Genetics, vol. 62(3) (1998), pp. 676 – 689. URL <http://www.sciencedirect.com/science/article/pii/S0002929707638488>. [Cited on page 36.]
- [80] FUNG, G., IP, H., AND LAW, K. *Ray tracing stereoscopic images*. In CHIN, R., ET AL. (Editors), *Image Analysis Applications and Computer Graphics*, vol. 1024 of *Lecture Notes in Computer Science*. Springer Berlin / Heidelberg (1995), pp. 313–321. URL http://dx.doi.org/10.1007/3-540-60697-1_116. [Cited on page 125.]
- [81] GAL, Y., ET AL. *Denoising of dynamic contrast-enhanced mr images using dynamic nonlocal means*. Medical Imaging, IEEE Transactions on, vol. 29(2) (2010), pp. 302 –310. [Cited on page 46.]
- [82] GARRISON, J. B., ET AL. *Three dimensional roentgenography*. American Journal of Roentgenology, vol. 105(4) (1969), pp. 903–908. URL <http://www.ajronline.org/content/105/4/903.abstract>. [Cited on page 59.]
- [83] GE. *GEs digital flat panel detector*. http://www.e-radiography.net/radtech/f/flat_panel.htm (2012). [Cited on pages 22 and 53.]
- [84] GEFEN, S., ET AL. *ROC analysis of ultrasound tissue characterization classifiers for breast cancer diagnosis*. Medical Imaging, IEEE Transactions on, vol. 22(2) (2003), pp. 170 –177. [Cited on page 48.]

- [85] GILBERT, P. *Iterative methods for the three-dimensional reconstruction of an object from projections*. Journal of Theoretical Biology, vol. 36(1) (1972), pp. 105 – 117. URL <http://www.sciencedirect.com/science/article/pii/0022519372901804>. [Cited on page 85.]
- [86] GLASBEY, C. A. AND MARDIA, K. V. *A review of image-warping methods*. Journal of Applied Statistics, vol. 25(2) (1998), pp. 155–171. URL <http://www.tandfonline.com/doi/abs/10.1080/02664769823151>. [Cited on page 106.]
- [87] GOOD, W. F., ET AL. *Digital breast tomosynthesis: A pilot observer study*. American Journal of Roentgenology, vol. 190(4) (2008), pp. 865–869. URL <http://www.ajronline.org/content/190/4/865.abstract>. [Cited on page 64.]
- [88] GORDON, R., BENDER, R., AND HERMAN, G. T. *Algebraic reconstruction techniques (ART) for three-dimensional electron microscopy and x-ray photography*. Journal of Theoretical Biology, vol. 29(3) (1970), pp. 471 – 481. URL <http://www.sciencedirect.com/science/article/pii/0022519370901098>. [Cited on page 85.]
- [89] GOSHTASBY, A. *2-D and 3-D Image Registration: for Medical, Remote Sensing, and Industrial Applications*. Wiley-Interscience, New York, 1st edn. (2005). [Cited on page 106.]
- [90] GOULD, T. A. *How MRI works*. <http://www.howstuffworks.com/mri.htm/printable> (2010). [Cited on page 44.]
- [91] GRAINGER, R. G., ET AL. *Grainger & Allison's Diagnostic Radiology: A Textbook of Medical Imaging*. Churchill Livingstone, 5th edn. (2007). [Cited on page 44.]
- [92] GRANT, D. G. *Tomosynthesis: A three-dimensional radiographic imaging technique*. Biomedical Engineering, IEEE Transactions on, vol. BME-19(1) (1972), pp. 20 –28. [Cited on pages 59 and 76.]
- [93] GROS, C. M. *Methodologie: Symposium sur le sein*. J Radiol Electrol Med Nucl, vol. 48 (1967), pp. 638–655. [Cited on page 54.]
- [94] GROSSMANN, G. *Lung tomography*. Br J Radiol, vol. 8(96) (1935), pp. 733–751. URL <http://bjr.birjournals.org/cgi/content/abstract/8/96/733>. [Cited on page 59.]
- [95] GUO, Y., SURI, J., AND SIVARAMAKRISHNA, R. *Image registration for breast imaging: A review*. In *Engineering in Medicine and Biology Society, 2005. IEEE-EMBS 2005. 27th Annual International Conference of the* (2005), pp. 3379 –3382. [Cited on page 113.]
- [96] GUR, D. *Tomosynthesis: Potential clinical role in breast imaging*. American Journal of Roentgenology, vol. 189(3) (2007), pp. 614–615. URL <http://www.ajronline.org/content/189/3/614.short>. [Cited on page 63.]
- [97] GUR, D., ET AL. *Digital breast tomosynthesis: Observer performance study*. American Journal of Roentgenology, vol. 193(2) (2009), pp. 586–591. URL <http://www.ajronline.org/content/193/2/586.abstract>. [Cited on page 64.]
- [98] HADJIISKI, L., ET AL. *Automated registration of breast lesions in temporal pairs of mammograms for interval change analysis—local affine transformation for improved localization*. Medical Physics, vol. 28(6) (2001), pp. 1070–1079. URL <http://link.aip.org/link/?MPH/28/1070/1>. [Cited on page 114.]
- [99] HAJNAL, J. V., HILL, D. L. G., AND HAWKES, D. J. *Medical Image Registration (Biomedical Engineering)*. CRC Press, 1st edn. (2001). [Cited on page 112.]

- [100] HAMBLY, N. M., ET AL. *Comparison of digital mammography and screen-film mammography in breast cancer screening: A review in the irish breast screening program.* American Journal of Roentgenology, vol. 193(4) (2009), pp. 1010–1018. URL <http://www.ajronline.org/content/193/4/1010.abstract>. [Cited on page 55.]
- [101] HARRIS, K. M. AND VOGEL, V. G. *Breast cancer screening.* Cancer and Metastasis Reviews, vol. 16 (1997), pp. 231–262. URL <http://dx.doi.org/10.1023/A:1005893126451>. 10.1023/A:1005893126451. [Cited on page 54.]
- [102] HATA, T., ET AL. *Magnetic resonance imaging for preoperative evaluation of breast cancer: a comparative study with mammography and ultrasonography.* Journal of the American College of Surgeons, vol. 198(2) (2004), pp. 190 – 197. URL <http://www.sciencedirect.com/science/article/pii/S1072751503012043>. [Cited on page 45.]
- [103] HAYTON, P. M., ET AL. *A non-rigid registration algorithm for dynamic breast mr images.* Artificial Intelligence, vol. 114(1-2) (1999), pp. 125 – 156. URL <http://www.sciencedirect.com/science/article/pii/S0004370299000739>. [Cited on page 113.]
- [104] HE, Y., ET AL. *A nonlinear least square technique for simultaneous image registration and super-resolution.* Image Processing, IEEE Transactions on, vol. 16(11) (2007), pp. 2830 –2841. [Cited on page 157.]
- [105] HEDDSON, B., ET AL. *Digital versus screen-film mammography: A retrospective comparison in a population-based screening program.* European Journal of Radiology, vol. 64(3) (2007), pp. 419 – 425. URL <http://www.sciencedirect.com/science/article/pii/S0720048X07001076>. Pulmonary Functional Imaging. [Cited on page 63.]
- [106] HENDRICK, R. E. *Breast MRI: Fundamentals and Technical Aspects.* Springer, 1st edn. (2007). [Cited on pages 43 and 44.]
- [107] HERMAN, G. AND MEYER, L. *Algebraic reconstruction techniques can be made computationally efficient positron emission tomography application.* Medical Imaging, IEEE Transactions on, vol. 12(3) (1993), pp. 600 –609. [Cited on page 85.]
- [108] HERMAN, G. T. AND LENT, A. *Iterative reconstruction algorithms.* Computers in Biology and Medicine, vol. 6(4) (1976), pp. 273 – 294. URL <http://www.sciencedirect.com/science/article/pii/0010482576900664>. Advances in Picture Reconstruction: Theory and Applications. [Cited on page 85.]
- [109] HERMAN, G. T., LENT, A., AND ROWLAND, S. W. *ART: Mathematics and applications: A report on the mathematical foundations and on the applicability to real data of the algebraic reconstruction techniques.* Journal of Theoretical Biology, vol. 42(1) (1973), pp. 1 – 32. URL <http://www.sciencedirect.com/science/article/pii/0022519373901458>. [Cited on page 85.]
- [110] HESTENES, M. R. AND STIEFEL, E. *Methods of conjugate gradients for solving linear systems.* Journal of research of the National Bureau of Standards, vol. 49(6) (1952), pp. 409–436. [Cited on page 95.]
- [111] HEYWANG-KÖBRUNNER, S. *Contrast-enhanced magnetic resonance imaging of the breast.* Investigative Radiology, vol. 29(1) (1994), pp. 94–104. URL http://journals.lww.com/investigativeradiology/Fulltext/1994/01000/Contrast_Enhanced_Magnetic_Resonance_Imaging_of.19.aspx. [Cited on page 45.]
- [112] HEYWANG-KÖBRUNNER, S. AND BECK, R. *Contrast Enhanced MRI of the Breast.* Springer Verlag, 2^{ed} edn. (1995). [Cited on page 45.]

- [113] HEYWANG-KÖBRUNNER, S., ET AL. *MR imaging of the breast using Gadolinium-DTPA*. Journal of Computer Assisted Tomography, vol. 10(2) (1986), pp. 199–204. URL http://journals.lww.com/jcat/Fulltext/1986/03000/MR_Imaging_of_the_Breast_Using_Gadolinium_DTPA.5.aspx. [Cited on page 45.]
- [114] ———. *MR imaging of the breast with Gd-DTPA: use and limitations*. Radiology, vol. 171(1) (1989), pp. 95–103. URL <http://radiology.rsna.org/content/171/1/95.abstract>. [Cited on page 45.]
- [115] ———. *Contrast-enhanced MRI of the breast: accuracy, value, controversies, solutions*. European Journal of Radiology, vol. 24(2) (1997), pp. 94 – 108. URL <http://www.sciencedirect.com/science/article/pii/S0720048X96011424>. [Cited on page 45.]
- [116] HILL, D. L. G., ET AL. *Medical image registration*. Physics in Medicine and Biology, vol. 46(3) (2001), p. R1. URL <http://stacks.iop.org/0031-9155/46/i=3/a=201>. [Cited on pages 99 and 106.]
- [117] HIPWELL, J., ET AL. *Intensity-based 2-D-3-D registration of cerebral angiograms*. Medical Imaging, IEEE Transactions on, vol. 22(11) (2003), pp. 1417 –1426. [Cited on page 116.]
- [118] ———. *A new validation method for X-ray mammogram registration algorithms using a projection model of breast X-ray compression*. Medical Imaging, IEEE Transactions on, vol. 26(9) (2007), pp. 1190 –1200. [Cited on pages 115 and 116.]
- [119] HOLDEN, M. *A review of geometric transformations for nonrigid body registration*. Medical Imaging, IEEE Transactions on, vol. 27(1) (2008), pp. 111 –128. [Cited on page 106.]
- [120] HORN, B. K. AND SCHUNCK, B. G. *Determining optical flow*. Artificial Intelligence, vol. 17(1-3) (1981), pp. 185 – 203. URL <http://www.sciencedirect.com/science/article/pii/0004370281900242>. [Cited on pages 108 and 110.]
- [121] HSIEH, J. *Computed Tomography: Principles, Design, Artifacts, and Recent Advances*, vol. PM114 of *Mono-graph*. SPIE Publications, 1st edn. (2003), pp. 37–90. [Cited on pages 79, 81, and 82.]
- [122] HU, Y.-H., ZHAO, B., AND ZHAO, W. *Image artifacts in digital breast tomosynthesis: Investigation of the effects of system geometry and reconstruction parameters using a linear system approach*. Medical Physics, vol. 35(12) (2008), pp. 5242–5252. URL <http://link.aip.org/link/?MPH/35/5242/1>. [Cited on pages 77 and 172.]
- [123] HUDSON, H. AND LARKIN, R. *Accelerated image reconstruction using ordered subsets of projection data*. Medical Imaging, IEEE Transactions on, vol. 13(4) (1994), pp. 601 –609. [Cited on page 85.]
- [124] IKEDO, Y., ET AL. *Development of a fully automatic scheme for detection of masses in whole breast ultrasound images*. Medical Physics, vol. 34(11) (2007), pp. 4378–4388. URL <http://link.aip.org/link/?MPH/34/4378/1>. [Cited on page 48.]
- [125] JACOBSON, M. AND FESSLER, J. *Joint estimation of image and deformation parameters in motion-corrected PET*. In *Nuclear Science Symposium Conference Record, 2003 IEEE*, vol. 5 (2003), pp. 3290 – 3294 Vol.5. [Cited on page 157.]
- [126] JAN, J. *Medical Image Processing, Reconstruction and Restoration: Concepts and Methods*. CRC, 1st edn. (2005). [Cited on page 81.]
- [127] JANNIN, P., ET AL. *Validation of medical image processing in image-guided therapy*. Medical Imaging, IEEE Transactions on, vol. 21(12) (2002), pp. 1445 –1449. [Cited on page 112.]

- [128] JANSSON, T., ET AL. *Positron emission tomography studies in patients with locally advanced and/or metastatic breast cancer: a method for early therapy evaluation?* Journal of Clinical Oncology, vol. 13(6) (1995), pp. 1470–7. URL <http://jco.ascopubs.org/content/13/6/1470.abstract>. [Cited on page 115.]
- [129] JATOI, I., KAUFMANN, M., AND PETIT, J. Y. *Atlas of Breast Surgery*. Springer-Verlag Berlin Heidelberg (2006), pp. 7–17. [Cited on pages 21, 36, and 42.]
- [130] JELLINS, J., ET AL. *Ultrasonic visualisation of the breast*. The Medical Journal of Australia, vol. 1 (1971), pp. 305–307. [Cited on page 47.]
- [131] JIANG, M. AND WANG, G. *Convergence of the simultaneous algebraic reconstruction technique (SART)*. Image Processing, IEEE Transactions on, vol. 12(8) (2003), pp. 957 – 961. [Cited on page 85.]
- [132] JOUVELOT, P. AND GIFFORD, D. *Algebraic reconstruction of types and effects*. In *Proceedings of the 18th ACM SIGPLAN-SIGACT symposium on Principles of programming languages*, POPL '91. ACM, New York, NY, USA (1991), pp. 303–310. URL <http://doi.acm.org/10.1145/99583.99623>. [Cited on page 85.]
- [133] KACHELRIESS, M., KNAUP, M., AND BOCKENBACH, O. *Hyperfast parallel-beam and cone-beam backprojection using the cell general purpose hardware*. Medical Physics, vol. 34(4) (2007), pp. 1474–1486. URL <http://link.aip.org/link/?MPH/34/1474/1>. [Cited on page 84.]
- [134] KACZMARZ, S. *Angenaherte auflösung von systemen linearer gleichungen*. Bull. Acad. Pol. Sci. Lett. A, vol. 6-8A (1937), pp. 355–357. [Cited on pages 85 and 86.]
- [135] KAISER, W. *MRI of the female breast. first clinical results*. Archives Of Physiology And Biochemistry, vol. 93(5) (1985), pp. 67–76. URL <http://informahealthcare.com/doi/abs/10.3109/13813458509080627>. [Cited on page 44.]
- [136] KAISER, W. A. *Signs in MR-Mammography*. Springer, 1st edn. (2007). [Cited on page 43.]
- [137] KAK, A. *Computerized tomography with X-ray, emission, and ultrasound sources*. Proceedings of the IEEE, vol. 67(9) (1979), pp. 1245 – 1272. [Cited on page 85.]
- [138] KAK, A. C. AND SLANEY, M. *Principles of Computerized Tomographic Imaging*. Society for Industrial Mathematics, new edn. (2001), pp. 56–60. [Cited on pages 78, 81, 82, 85, and 87.]
- [139] KAPUR, A., ET AL. *Fusion of digital mammography with breast ultrasound: a phantom study*. vol. 4682. SPIE (2002), pp. 526–537. URL <http://link.aip.org/link/?PSI/4682/526/1>. [Cited on page 116.]
- [140] ——. *Combination of digital mammography with semi-automated 3d breast ultrasound*. Technol Cancer Res Treat, vol. 3(4) (2004), pp. 325–34-. URL <http://ukpmc.ac.uk/abstract/MED/15270583>. [Cited on page 116.]
- [141] KARELLAS, A., LO, J. Y., AND ORTON, C. G. *Cone beam X-ray ct will be superior to digital X-ray tomosynthesis in imaging the breast and delineating cancer*. Medical Physics, vol. 35(2) (2008), pp. 409–411. URL <http://link.aip.org/link/?MPH/35/409/1>. [Cited on page 64.]
- [142] KARSSEMEIJER, N., ET AL. *Breast cancer screening results 5 years after introduction of digital mammography in a population-based screening program*. Radiology, vol. 253(2) (2009), pp. 353–358. URL <http://radiology.rsna.org/content/253/2/353.abstract>. [Cited on page 56.]
- [143] KASTANIS, I., ET AL. *3D digital breast tomosynthesis using total variation regularization*. In KRUPINSKI, E. (Editor), *Digital Mammography*, vol. 5116 of *Lecture Notes in Computer Science*. Springer Berlin / Heidelberg (2008), pp. 621–627. URL http://dx.doi.org/10.1007/978-3-540-70538-3_86. [Cited on pages 97 and 219.]

- [144] KAUL, K. AND DAGUILH, F. M. L. *Early detection of breast cancer: Is mammography enough?* HOSPITAL PHYSICIAN, vol. 38 (2002), pp. 49–54. [Cited on page 65.]
- [145] KELSEY, J. AND BERNSTEIN, L. *Epidemiology and prevention of breast cancer.* Annual Review of Public Health, vol. 17 (1996), pp. 47–67. URL <http://www.annualreviews.org/doi/pdf/10.1146/annurev.pu.17.050196.000403>. [Cited on page 37.]
- [146] KEY, T. J., VERKASALO, P. K., AND BANKS, E. *Epidemiology of breast cancer.* The Lancet Oncology, vol. 2(3) (2001), pp. 133 – 140. URL <http://www.sciencedirect.com/science/article/pii/S1470204500002540>. [Cited on page 37.]
- [147] KHALKHALI, I., ET AL. *^{99m}Tc Sestamibi Breast Imaging for the Examination of Patients with Dense and Fatty Breasts: Multicenter Study.* Radiology, vol. 222(1) (2002), pp. 149–155. URL <http://radiology.rsna.org/content/222/1/149.abstract>. [Cited on page 57.]
- [148] KIM, H. H., ET AL. *Comparison of calcification specificity in digital mammography using soft-copy display versus screen-film mammography.* American Journal of Roentgenology, vol. 187(1) (2006), pp. 47–50. URL <http://www.ajronline.org/content/187/1/47.abstract>. [Cited on page 55.]
- [149] KING, M.-C., ET AL. *Breast and ovarian cancer risks due to inherited mutations in BRCA1 and BRCA2.* Science, vol. 302(5645) (2003), pp. 643–646. URL <http://www.sciencemag.org/content/302/5645/643.abstract>. [Cited on page 36.]
- [150] KO, H. AND KIHM, K. *An extended algebraic reconstruction technique (ART) for density-gradient projections: laser speckle photographic tomography.* Experiments in Fluids, vol. 27 (1999), pp. 542–550. URL <http://dx.doi.org/10.1007/s003480050378>. 10.1007/s003480050378. [Cited on page 85.]
- [151] KOBAYASHI, T. *Diagnostic ultrasound in breast cancer: Analysis of retrotumorous echo patterns correlated with sonic attenuation by cancerous connective tissue.* Journal of Clinical Ultrasound, vol. 7 (1979), pp. 471–479. [Cited on page 47.]
- [152] KOLITSI, Z., PANAYIOTAKIS, G., AND PALLIKARAKIS, N. *A method for selective removal of out-of-plane structures in digital tomosynthesis.* Medical Physics, vol. 20(1) (1993), pp. 47–50. URL <http://link.aip.org/link/?MPH/20/47/1>. [Cited on page 78.]
- [153] KOPANS, D. B. *Double reading.* Radiologic Clinics of North America, vol. 38(4) (2000), pp. 719 – 724. URL <http://www.sciencedirect.com/science/article/pii/S0033838905701962>. [Cited on page 55.]
- [154] ——. *Breast Imaging.* Lippincott Williams and Wilkins, Philadelphia, 3rd edn. (2006). [Cited on pages 68, 76, and 120.]
- [155] KRÜCKER, J. F., ET AL. *3D spatial compounding of ultrasound images using image-based nonrigid registration.* Ultrasound in Medicine & Biology, vol. 26(9) (2000), pp. 1475 – 1488. URL <http://www.sciencedirect.com/science/article/pii/S0301562900002866>. [Cited on page 48.]
- [156] KUDO, H., NOO, F., AND DEFRISE, M. *Cone-beam filtered-backprojection algorithm for truncated helical data.* Physics in Medicine and Biology, vol. 43(10) (1998), p. 2885. URL <http://stacks.iop.org/0031-9155/43/i=10/a=016>. [Cited on page 76.]
- [157] KUHL, C. *The current status of breast MR imaging part I. choice of technique, image interpretation, diagnostic accuracy, and transfer to clinical practice.* Radiology, vol. 244(2) (2007), pp. 356–378. URL <http://radiology.rsna.org/content/244/2/356.abstract>. [Cited on page 45.]

- [158] KUHL, C. K. *Current status of breast MR imaging part II. clinical applications.* Radiology, vol. 244(3) (2007), pp. 672–691. URL <http://radiology.rsna.org/content/244/3/672.abstract>. [Cited on page 45.]
- [159] KUHL, C. K., ET AL. *Dynamic breast MR imaging: Are signal intensity time course data useful for differential diagnosis of enhancing lesions?* Radiology, vol. 211(1) (1999), pp. 101–110. URL <http://radiology.rsna.org/content/211/1/101.abstract>. [Cited on page 45.]
- [160] KUMAR, R., ET AL. *Application of 3d registration for detecting lesions in magnetic resonance breast scans.* vol. 2710. SPIE (1996), pp. 646–656. URL <http://link.aip.org/link/?PSI/2710/646/1>. [Cited on page 113.]
- [161] LAKSHMINARAYANAN, A. AND LENT, A. *Methods of least squares and SIRT in reconstruction.* Journal of Theoretical Biology, vol. 76(3) (1979), pp. 267 – 295. URL <http://www.sciencedirect.com/science/article/pii/0022519379903138>. [Cited on page 85.]
- [162] LASSEUR, E. C., BAILY, N. A., AND CREPEAU, R. L. *Fluoroplanigraphy system for rapid presentation of single plane body sections.* American Journal of Roentgenology, vol. 113(3) (1971), pp. 574–577. URL <http://www.ajronline.org/content/113/3/574.short>. [Cited on page 59.]
- [163] LAURITSCH, G. AND HAERER, W. H. *Theoretical framework for filtered back projection in tomosynthesis.* vol. 3338. SPIE (1998), pp. 1127–1137. URL <http://link.aip.org/link/?PSI/3338/1127/1>. [Cited on page 76.]
- [164] LAUTERBUR, P. C. *Image formation by induced local interactions: Examples employing nuclear magnetic resonance.* Nature, vol. 242(5394) (1973), pp. 190–191. URL <http://dx.doi.org/10.1038/242190a0>. [Cited on page 44.]
- [165] LEACH, M. O., ET AL. *Screening with magnetic resonance imaging and mammography of a uk population at high familial risk of breast cancer: a prospective multicentre cohort study (maribs).* The Lancet, vol. 365(9473) (2005), pp. 1769 – 1778. URL <http://www.sciencedirect.com/science/article/pii/S0140673605664811>. [Cited on page 128.]
- [166] LEBORGNE, R. *Diagnosis of Tumours of Breast by Simple Roentgenography: Calcifications in Carcinoma.* Am. J Roentgenol Radium Ther Nucl Med, vol. 65 (1951), pp. 1–11. [Cited on page 54.]
- [167] LEESER, M., ET AL. *Parallel-beam backprojection: An FPGA implementation optimized for medical imaging.* The Journal of VLSI Signal Processing, vol. 39 (2005), pp. 295–311. URL <http://dx.doi.org/10.1007/s11265-005-4846-5>. 10.1007/s11265-005-4846-5. [Cited on page 83.]
- [168] LEHTIMAKI, M., ET AL. *First results with real-time selenium-based full-field digital mammography three-dimensional imaging system.* vol. 5368. SPIE (2004), pp. 922–929. URL <http://link.aip.org/link/?PSI/5368/922/1>. [Cited on page 60.]
- [169] LESTER, H. AND ARRIDGE, S. R. *A survey of hierarchical non-linear medical image registration.* Pattern Recognition, vol. 32(1) (1999), pp. 129 – 149. URL <http://www.sciencedirect.com/science/article/pii/S0031320398000958>. [Cited on pages 99 and 106.]
- [170] LEVMAN, J., ET AL. *Classification of dynamic contrast-enhanced magnetic resonance breast lesions by support vector machines.* Medical Imaging, IEEE Transactions on, vol. 27(5) (2008), pp. 688 –696. [Cited on page 45.]
- [171] LEWIN, J. M., HENDRICK, R. E., AND D'ORSI, C. J. *Causes of differences between full-field digital mammography and screen-film mammography interpretations in the colorado/massachusetts full-field digital mammography screening trial.* Radiology, vol. 217 (2000), pp. 199–199. [Cited on page 55.]

- [172] LEWIN, J. M. AND NIKLASON, L. *Advanced applications of digital mammography: Tomosynthesis and contrast-enhanced digital mammography*. Seminars in Roentgenology, vol. 42(4) (2007), pp. 243 – 252. URL <http://www.sciencedirect.com/science/article/pii/S0037198X07000405>. Breast Imaging. [Cited on page 64.]
- [173] LEWIN, J. M., ET AL. *Comparison of full-field digital mammography with screen-film mammography for cancer detection: Results of 4,945 paired examinations1*. Radiology, vol. 218(3) (2001), pp. 873–880. URL <http://radiology.rsna.org/content/218/3/873.abstract>. [Cited on page 55.]
- [174] ——. *Clinical comparison of full-field digital mammography and screen-film mammography for detection of breast cancer*. American Journal of Roentgenology, vol. 179(3) (2002), pp. 671–677. URL <http://www.ajronline.org/content/179/3/671.abstract>. [Cited on page 55.]
- [175] LI, C. M., ET AL. *Three-dimensional computer generated breast phantom based on empirical data*. vol. 6913. SPIE (2008), p. 6913:14. URL <http://link.aip.org/link/?PSI/6913/691314/1>. [Cited on page 190.]
- [176] ——. *Methodology for generating a 3D computerized breast phantom from empirical data*. Medical Physics, vol. 36(7) (2009), pp. 3122–3131. URL <http://link.aip.org/link/?MPH/36/3122/1>. [Cited on page 190.]
- [177] LI, X., ET AL. *Validation of an algorithm for the nonrigid registration of longitudinal breast MR images using realistic phantoms*. Medical Physics, vol. 37(6) (2010), pp. 2541–2552. URL <http://link.aip.org/link/?MPH/37/2541/1>. [Cited on page 46.]
- [178] LINDHARDT, F. *White paper of digital breast tomosynthesis: A clinical assessment based on literature*. Tech. rep., Siemens (2010). [Cited on page 39.]
- [179] LIU, B., ET AL. *Automated segmentation of ultrasonic breast lesions using statistical texture classification and active contour based on probability distance*. Ultrasound in Medicine & Biology, vol. 35(8) (2009), pp. 1309 – 1324. URL <http://www.sciencedirect.com/science/article/pii/S0301562908005978>. [Cited on page 48.]
- [180] ——. *Fully automatic and segmentation-robust classification of breast tumors based on local texture analysis of ultrasound images*. Pattern Recognition, vol. 43(1) (2010), pp. 280 – 298. URL <http://www.sciencedirect.com/science/article/pii/S0031320309002210>. [Cited on page 48.]
- [181] ——. *Probability density difference-based active contour for ultrasound image segmentation*. Pattern Recognition, vol. 43(6) (2010), pp. 2028 – 2042. URL <http://www.sciencedirect.com/science/article/pii/S0031320310000324>. [Cited on page 48.]
- [182] LOUIS, A. K. *Filter design in three-dimensional cone beam tomography: circular scanning geometry*. Inverse Problems, vol. 19(6) (2003), p. S31. URL <http://stacks.iop.org/0266-5611/19/i=6/a=052>. [Cited on page 83.]
- [183] MADABUSHI, A. AND METAXAS, D. *Combining low-, high-level and empirical domain knowledge for automated segmentation of ultrasonic breast lesions*. Medical Imaging, IEEE Transactions on, vol. 22(2) (2003), pp. 155 –169. [Cited on page 48.]
- [184] MAIDMENT, A., ET AL. *Evaluation of a photon-counting breast tomosynthesis imaging system*. vol. 5745. SPIE (2005), pp. 572–582. URL <http://link.aip.org/link/?PSI/5745/572/1>. [Cited on page 63.]
- [185] MAINTZ, J. AND VIERGEVER, M. A. *A survey of medical image registration*. Medical Image Analysis, vol. 2(1) (1998), pp. 1 – 36. URL <http://www.sciencedirect.com/science/article/pii/S1361841501800268>. [Cited on pages 99, 104, 106, and 112.]

- [186] MALUR, S., ET AL. *Comparison of written reports of mammography, sonography and magnetic resonance mammography for preoperative evaluation of breast lesions, with special emphasis on magnetic resonance mammography*. Breast Cancer Research, vol. 3 (2000), pp. 1–6. URL <http://dx.doi.org/10.1186/bcr271>. 10.1186/bcr271. [Cited on page 115.]
- [187] MARAVILLA, K., MURRY, R., AND HORNER, S. *Digital tomosynthesis: technique for electronic reconstructive tomography*. American Journal of Roentgenology, vol. 141(3) (1983), pp. 497–502. URL <http://www.ajronline.org/content/141/3/497.abstract>. [Cited on page 59.]
- [188] MARAVILLA, K. R., ET AL. *Digital tomosynthesis: technique modifications and clinical applications for neurovascular anatomy*. Radiology, vol. 152(3) (1984), pp. 719–724. URL <http://radiology.rsna.org/content/152/3/719.abstract>. [Cited on page 59.]
- [189] MARTIN, A.-M. AND WEBER, B. L. *Genetic and hormonal risk factors in breast cancer*. Journal of the National Cancer Institute, vol. 92(14) (2000), pp. 1126–1135. URL <http://jnci.oxfordjournals.org/content/92/14/1126.abstract>. [Cited on page 37.]
- [190] MATSUO, H., ET AL. *Three-dimensional image reconstruction by digital tomo-synthesis using inverse filtering*. Medical Imaging, IEEE Transactions on, vol. 12(2) (1993), pp. 307 –313. [Cited on pages 76 and 84.]
- [191] MCGAUGHEY, K. J. AND YOUNG, R. P. *Comparison of ART, SIRT, Least-Squares, and SVD two-dimensional tomographic inversions of field data*. SEG Technical Program Expanded Abstracts, vol. 9(1) (1990), pp. 74–77. URL <http://link.aip.org/link/?SGA/9/74/1>. [Cited on page 88.]
- [192] MCPHERSON, K., STEEL, C. M., AND DIXON, J. M. *Breast cancer — epidemiology, risk factors, and genetics*. British Medical Journal, vol. 321(7261) (2000), pp. 624–628. URL <http://www.bmjjournals.org/content/321/7261/624.short>. [Cited on pages 35 and 37.]
- [193] MCSWEENEY, M. B. AND MURPHY, C. H. *Whole-breast sonography*. The Radiologic clinics of North America, vol. 23 (1985), pp. 157–167. [Cited on page 47.]
- [194] MCSWEENEY, M. B., ET AL. *Magnetic resonance imaging in the diagnosis of breast disease: use of transverse relaxation times*. Radiology, vol. 153(3) (1984), pp. 741–744. URL <http://radiology.rsna.org/content/153/3/741.abstract>. [Cited on page 44.]
- [195] MEDOFF, B. P., ET AL. *Iterative convolution backprojection algorithms for image reconstruction from limited data*. J. Opt. Soc. Am., vol. 73(11) (1983), pp. 1493–1500. URL <http://www.opticsinfobase.org/abstract.cfm?URI=josa-73-11-1493>. [Cited on page 76.]
- [196] MERTELMEIER, T., ET AL. *Optimizing filtered backprojection reconstruction for a breast tomosynthesis prototype device*. vol. 6142. SPIE (2006), p. 61420F. URL <http://link.aip.org/link/?PSI/6142/61420F/1>. [Cited on pages 83 and 84.]
- [197] MERTZANIDOU, T., ET AL. *An intensity-based approach to x-ray mammography: Mri registration*. vol. 7623. SPIE (2010), p. 76232Z. URL <http://link.aip.org/link/?PSI/7623/76232Z/1>. [Cited on page 116.]
- [198] ——. *X-ray mammography MRI registration using a volume-preserving affine transformation and an EM-MRF for breast tissue classification*. In MART, J., ET AL. (Editors), *Digital Mammography*, vol. 6136 of *Lecture Notes in Computer Science*. Springer Berlin / Heidelberg (2010), pp. 23–30. URL http://dx.doi.org/10.1007/978-3-642-13666-5_4. [Cited on pages 116 and 129.]

- [199] MEYER, C. R., ET AL. *Semiautomatic registration of volumetric ultrasound scans*. Ultrasound in Medicine & Biology, vol. 25(3) (1999), pp. 339 – 347. URL <http://www.sciencedirect.com/science/article/pii/S0301562998001483>. [Cited on page 114.]
- [200] MIGA, M. I. *A new approach to elastography using mutual information and finite elements*. Physics in Medicine and Biology, vol. 48(4) (2003), p. 467. URL <http://stacks.iop.org/0031-9155/48/i=4/a=304>. [Cited on page 115.]
- [201] MIKI, Y., ET AL. *A strong candidate for the breast and ovarian cancer susceptibility gene BRCA1*. Science, vol. 266(5182) (1994), pp. 66–71. URL <http://www.sciencemag.org/content/266/5182/66.abstract>. [Cited on page 36.]
- [202] MILLER, E. R., McCURRY, E. M., AND HRUSKA, B. *An infinite number of laminograms from a finite number of radiographs*. Radiology, vol. 98(2) (1971), pp. 249–255. URL <http://radiology.rsna.org/content/98/2/249.abstract>. [Cited on page 59.]
- [203] MITCHELL, D. P. AND NETRAVALI, A. N. *Reconstruction filters in computer-graphics*. In *Proceedings of the 15th annual conference on Computer graphics and interactive techniques, SIGGRAPH '88*. ACM, New York, NY, USA (1988), pp. 221–228. URL <http://doi.acm.org/10.1145/54852.378514>. [Cited on page 101.]
- [204] MODERSITZKI, J. *Numerical Methods for Image Registration (Numerical Mathematics and Scientific Computation)*. Oxford University Press, New York, 1st edn. (2004). [Cited on pages 106 and 112.]
- [205] MORRIS, E. AND LIBERMAN, L. (Editors). *Breast MRI Diagnosis and Intervention*. Springer New York (2005). [Cited on pages 23, 44, 65, and 67.]
- [206] MOSKALIK, A., ET AL. *Registration of three-dimensional compound ultrasound scans of the breast for refraction and motion correction*. Ultrasound in Medicine & Biology, vol. 21(6) (1995), pp. 769 – 778. URL <http://www.sciencedirect.com/science/article/pii/030156299500018M>. [Cited on pages 48 and 114.]
- [207] MUELLER, K. AND YAGEL, R. *Rapid 3D cone-beam reconstruction with the simultaneous algebraic reconstruction technique (sart) using 2-d texture mapping hardware*. Medical Imaging, IEEE Transactions on, vol. 19(12) (2000), pp. 1227 –1237. [Cited on page 85.]
- [208] MURTHY, K., ET AL. *Positron emission mammographic instrument: Initial results*. Radiology, vol. 215(1) (2000), pp. 280–285. URL <http://radiology.rsna.org/content/215/1/280.abstract>. [Cited on page 115.]
- [209] ———. *Results of preliminary clinical trials of the positron emission mammography system pem-i: A dedicated breast imaging system producing glucose metabolic images using fdg*. Journal of Nuclear Medicine, vol. 41(11) (2000), pp. 1851–1858. URL <http://jnm.snmjournals.org/content/41/11/1851.abstract>. [Cited on page 115.]
- [210] NARAYANASAMY, G., ET AL. *Spatial registration of temporally separated whole breast 3D ultrasound images*. Medical Physics, vol. 36(9) (2009), pp. 4288–4300. URL <http://link.aip.org/link/?MPH/36/4288/1>. [Cited on page 48.]
- [211] NEEMUCHWALA, H., HERO, A., AND CARSON, P. *Image matching using alpha-entropy measures and entropic graphs*. Signal Process., vol. 85 (2005), pp. 277–296. URL <http://dl.acm.org/citation.cfm?id=1066532.1066537>. [Cited on page 114.]
- [212] NELSON, T. R. AND PRETORIUS, D. H. *Three-dimensional ultrasound imaging*. Ultrasound in Medicine & Biology, vol. 24(9) (1998), pp. 1243 – 1270. URL <http://www.sciencedirect.com/science/article/pii/S030156299800043X>. [Cited on page 48.]

- [213] NIE, K., ET AL. *Development of a quantitative method for analysis of breast density based on three-dimensional breast mri.* Medical Physics, vol. 35(12) (2008), pp. 5253–5262. URL <http://link.aip.org/link/?MPH/35/5253/1>. [Cited on page 45.]
- [214] ——. *Quantitative analysis of breast parenchymal patterns using 3D fibroglandular tissues segmented based on MRI.* Medical Physics, vol. 37(1) (2010), pp. 217–226. URL <http://link.aip.org/link/?MPH/37/217/1>. [Cited on page 45.]
- [215] NIKLASON, L. T., ET AL. *Digital tomosynthesis in breast imaging.* Radiology, vol. 205(2) (1997), pp. 399–406. URL <http://radiology.rsna.org/content/205/2/399.abstract>. [Cited on pages 39, 60, and 76.]
- [216] NOBLE, J. AND BOUKERROUI, D. *Ultrasound image segmentation: A survey.* Medical Imaging, IEEE Transactions on, vol. 25(8) (2006), pp. 987–1010. [Cited on page 48.]
- [217] NOCEDAL, J. AND WRIGHT, S. *Numerical Optimization.* Springer, 2nd edn. (2006). [Cited on pages 94 and 95.]
- [218] ODILLE, F., ET AL. *Generalized reconstruction by inversion of coupled systems (GRICS) applied to free-breathing mri.* Magnetic Resonance in Medicine, vol. 60(1) (2008), pp. 146–157. URL <http://dx.doi.org/10.1002/mrm.21623>. [Cited on page 157.]
- [219] OREL, S. G. AND SCHNALL, M. D. *MR imaging of the breast for the detection, diagnosis, and staging of breast cancer.* Radiology, vol. 220(1) (2001), pp. 13–30. URL <http://radiology.rsna.org/content/220/1/13.abstract>. [Cited on page 45.]
- [220] PARK, B. K., ET AL. *Diffractive ultrasound in the evaluation of solid breast masses: Preliminary results.* Investigative Radiology, vol. 40(7) (2005), pp. 486–493. URL http://journals.lww.com/investigativeradiology/Fulltext/2005/07000/Diffractive_Ultrasound_in_the_Evaluation_of_Solid.14.aspx. [Cited on page 65.]
- [221] PARK, J. M., ET AL. *Breast tomosynthesis: Present considerations and future applications.* Radiographics, vol. 27(suppl 1) (2007), pp. S231–S240. URL http://radiographics.rsna.org/content/27/suppl_1/S231.abstract. [Cited on page 63.]
- [222] PAULSEN, K. D., MEANEY, P. M., AND GILMAN, L. *Alternative Breast Imaging: Four Model-Based Approaches.* Springer, 1st edn. (2004). [Cited on page 36.]
- [223] PERIASWAMY, S. *General purpose medical image registration.* Phd thesis, Dartmouth College, Hanover, NH, USA (2003). [Cited on page 99.]
- [224] PHILPOTTS, L. E. AND SMITH, R. A. *Screening for breast cancer.* Seminars in Roentgenology, vol. 38(1) (2003), pp. 19 – 33. URL <http://www.sciencedirect.com/science/article/pii/S0037198X0300004X>. Radio-logic Screening. [Cited on page 38.]
- [225] PICARD, J. D. *History of Mammography.* Bull Acad Natl Med, vol. 182 (1998), pp. 1613–1620. [Cited on page 54.]
- [226] PICCOLI, C. *Contrast-enhanced breast MRI: Factors affecting sensitivity and specificity.* European Radiology, vol. 7(5) (1997), pp. S281–S288. [Cited on page 44.]
- [227] PIO, B., ET AL. *Usefulness of 3-[F-18]fluoro-3-deoxythymidine with positron emission tomography in predicting breast cancer response to therapy.* Molecular Imaging and Biology, vol. 8 (2006), pp. 36–42. URL <http://dx.doi.org/10.1007/s11307-005-0029-9>. 10.1007/s11307-005-0029-9. [Cited on page 65.]

- [228] PIRON, C., ET AL. *A hybrid breast biopsy system combining ultrasound and MRI*. Medical Imaging, IEEE Transactions on, vol. 22(9) (2003), pp. 1100 –1110. [Cited on pages 48 and 115.]
- [229] PISANO, E. D., YAFFE, M. J., AND KUZMIAK, C. M. *Digital Mammography*. Lippincott Williams and Wilkins, Philadelphia, 1st edn. (2003). [Cited on page 50.]
- [230] PISANO, E. D., ET AL. *Diagnostic performance of digital versus film mammography for breast-cancer screening*. New England Journal of Medicine, vol. 353(17) (2005), pp. 1773–1783. URL <http://www.nejm.org/doi/full/10.1056/NEJMoa052911>. [Cited on page 55.]
- [231] POPLACK, S. P., ET AL. *Digital breast tomosynthesis: Initial experience in 98 women with abnormal digital screening mammography*. American Journal of Roentgenology, vol. 189(3) (2007), pp. 616–623. URL <http://www.ajronline.org/content/189/3/616.abstract>. [Cited on page 63.]
- [232] RADON, J. *Über die bestimmung von funktionen durch ihre integralwerte längs gewisser mannigfaltigkeiten (Determination of functions from their integrals along certain manifolds)*. Berichte über die Verhandlungen der Sächsischen Akademie der Wissenschaften (Reports on the proceedings of the Royal Saxonian Society of Physical and Mathematical Sciences), vol. 69 (1917), pp. 262–277. [Cited on page 58.]
- [233] ——. *On the determination of functions from their integral values along certain manifolds*. Medical Imaging, IEEE Transactions on, vol. 5(4) (1986), pp. 170 –176. [Cited on page 58.]
- [234] REISER, I., ET AL. *Computerized mass detection for digital breast tomosynthesis directly from the projection images*. Medical Physics, vol. 33(2) (2006), pp. 482–491. URL <http://link.aip.org/link/?MPH/33/482/1>. [Cited on page 116.]
- [235] REN, B., ET AL. *Design and performance of the prototype full field breast tomosynthesis system with selenium based flat panel detector*. vol. 5745. SPIE (2005), pp. 550–561. URL <http://link.aip.org/link/?PSI/5745/550/1>. [Cited on page 75.]
- [236] REN, L., ET AL. *Automatic registration between reference and on-board digital tomosynthesis images for positioning verification*. Medical Physics, vol. 35(2) (2008), pp. 664–672. URL <http://link.aip.org/link/?MPH/35/664/1>. [Cited on page 116.]
- [237] RICHARD, F. J. AND COHEN, L. D. *A new image registration technique with free boundary constraints: application to mammography*. Computer Vision and Image Understanding, vol. 89(2-3) (2003), pp. 166 – 196. URL <http://www.sciencedirect.com/science/article/pii/S1077314203000067>. Nonrigid Image Registration. [Cited on page 115.]
- [238] ROGELJ, P. AND KOVACIĆ, S. *Symmetric image registration*. Medical Image Analysis, vol. 10(3) (2006), pp. 484–493. URL <http://www.sciencedirect.com/science/article/pii/S1361841505000472>. Special Issue on The Second International Workshop on Biomedical Image Registration (WBIR03). [Cited on page 152.]
- [239] ROHLFING, T., ET AL. *Volume-preserving nonrigid registration of mr breast images using free-form deformation with an incompressibility constraint*. Medical Imaging, IEEE Transactions on, vol. 22(6) (2003), pp. 730 –741. [Cited on page 114.]
- [240] ROHLING, R. N., GEE, A., AND BERMAN, L. *Automatic registration of 3D ultrasound images*. Ultrasound in Medicine & Biology, vol. 24(6) (1998), pp. 841 – 854. URL <http://www.sciencedirect.com/science/article/pii/S030156299700210X>. [Cited on page 48.]

- [241] ROSS, R. J., ET AL. *Nuclear magnetic resonance imaging and evaluation of human breast tissue: preliminary clinical trials*. Radiology, vol. 143(1) (1982), pp. 195–205. URL <http://radiology.rsna.org/content/143/1/195.abstract>. [Cited on page 44.]
- [242] ROTTEN, D., LEVAILLANT, J. M., AND ZERAT, L. *Analysis of normal breast tissue and of solid breast masses using three-dimensional ultrasound mammography*. Ultrasound in Obstetrics and Gynecology, vol. 14(2) (1999), pp. 114–124. URL <http://dx.doi.org/10.1046/j.1469-0705.1999.14020114.x>. [Cited on page 48.]
- [243] RUECKERT, D. AND SCHNABEL, J. *Biomedical Image Processing*, chap. 5. Springer, 1st edn. (2011), pp. 131–154. [Cited on page 108.]
- [244] RUECKERT, D., ET AL. *Comparison and evaluation of rigid and nonrigid registration of breast mr images*. vol. 3661. SPIE (1999), pp. 78–88. URL <http://link.aip.org/link/?PSI/3661/78/1>. [Cited on pages 109 and 110.]
- [245] ———. *Nonrigid registration using free-form deformations: application to breast mr images*. Medical Imaging, IEEE Transactions on, vol. 18(8) (1999), pp. 712 –721. [Cited on pages 45, 105, and 113.]
- [246] RUITER, N. V., ET AL. *Registration of X-ray mammograms and MR-volumes of the female breast based on simulated mammographic deformation*. In *IWDM'04: Proceedings of the 7th International Workshop on Digital Mammography*. Lecture Notes in Computer Science, Springer-Verlag Berlin Heidelberg (2004), pp. 498–503. [Cited on page 115.]
- [247] SABIN, M. *Tutorials on Multiresolution in Geometric Modelling*. Mathematics and Visualization Summer School Lecture Notes. Springer (2002), pp. 4–6. [Cited on page 102.]
- [248] SALLAM, M. Y. AND BOWYER, K. W. *Registration and difference analysis of corresponding mammogram images*. Medical Image Analysis, vol. 3(2) (1999), pp. 103 – 118. URL <http://www.sciencedirect.com/science/article/pii/S1361841599800012>. [Cited on page 114.]
- [249] SALOMON, A. *Beitrage zur pathologie und klinik der mamma carcinoma*. Arch Kein Chir, vol. 110 (1913), pp. 573–568. [Cited on page 54.]
- [250] SAMANI, A., ET AL. *Biomechanical 3-D finite element modeling of the human breast using mri data*. Medical Imaging, IEEE Transactions on, vol. 20(4) (2001), pp. 271 –279. [Cited on page 45.]
- [251] SANJAY-GOPAL, S., ET AL. *A regional registration technique for automated interval change analysis of breast lesions on mammograms*. Medical Physics, vol. 26(12) (1999), pp. 2669–2679. URL <http://link.aip.org/link/?MPH/26/2669/1>. [Cited on page 114.]
- [252] SASLOW, D., ET AL. *American cancer society guidelines for breast screening with MRI as an adjunct to mammography*. CA: A Cancer Journal for Clinicians, vol. 57(2) (2007), pp. 75–89. URL <http://dx.doi.org/10.3322/canjclin.57.2.75>. [Cited on page 45.]
- [253] SCHNABEL, J., ET AL. *Validation of nonrigid image registration using finite-element methods: application to breast mr images*. Medical Imaging, IEEE Transactions on, vol. 22(2) (2003), pp. 238 –247. [Cited on page 46.]
- [254] SCHUMACHER, H., MODERSITZKI, J., AND FISCHER, B. *Combined reconstruction and motion correction in SPECT imaging*. Nuclear Science, IEEE Transactions on, vol. 56(1) (2009), pp. 73 –80. [Cited on page 157.]
- [255] SHANKS, S. C., KERLEY, P., AND TWINING, E. W. *A Textbook of X-Ray Diagnosis*. Lewis, London (1938). [Cited on page 59.]

- [256] SHARP, P. F., GEMMELL, H. G., AND MURRAY, A. D. *Practical Nuclear Medicine*. Springer-Verlag London Limited, 3rd edn. (2005), pp. 28–30. [Cited on page 94.]
- [257] SHATTUCK-EIDENS, D., ET AL. *BRCA1 sequence analysis in women at high risk for susceptibility mutations*. JAMA: The Journal of the American Medical Association, vol. 278(15) (1997), pp. 1242–1250. URL <http://jama.ama-assn.org/content/278/15/1242.abstract>. [Cited on page 37.]
- [258] SHI, J., ET AL. *Treatment response assessment of breast masses on dynamic contrast-enhanced magnetic resonance scans using fuzzy c-means clustering and level set segmentation*. Medical Physics, vol. 36(11) (2009), pp. 5052–5063. URL <http://link.aip.org/link/?MPH/36/5052/1>. [Cited on page 45.]
- [259] SICKLES, E. A., ET AL. *Performance benchmarks for diagnostic mammography*. Radiology, vol. 235(3) (2005), pp. 775–790. URL <http://radiology.rsna.org/content/235/3/775.abstract>. [Cited on page 117.]
- [260] SIDKY, E. Y. AND PAN, X. *Image reconstruction in circular cone-beam computed tomography by constrained, total-variation minimization*. Physics in Medicine and Biology, vol. 53(17) (2008), p. 4777. URL <http://stacks.iop.org/0031-9155/53/i=17/a=021>. [Cited on pages 97 and 219.]
- [261] SIDKY, E. Y., ET AL. *Enhanced imaging of microcalcifications in digital breast tomosynthesis through improved image-reconstruction algorithms*. Medical Physics, vol. 36(11) (2009), pp. 4920–4932. URL <http://link.aip.org/link/?MPH/36/4920/1>. [Cited on pages 90 and 97.]
- [262] SINHA, S. P., ET AL. *Image registration for detection and quantification of change on digital tomosynthesis mammographic volumes*. American Journal of Roentgenology, vol. 192(2) (2009), pp. 384–387. URL <http://www.ajronline.org/content/192/2/384.full.pdf+html>. [Cited on page 116.]
- [263] SIVARAMAKRISHNA, R. *3D breast image registration - a review*. Technology in Cancer Research & Treatment, vol. 4(1) (2005), pp. 39–48. Workshop on Alternatives to Mammography. [Cited on page 113.]
- [264] SKAANE, P., HOFVIND, S., AND SKJENNALD, A. *Randomized trial of screen-film versus full-field digital mammography with soft-copy reading in population-based screening program: Follow-up and final results of Oslo II study*. Radiology, vol. 244(3) (2007), pp. 708–717. URL <http://radiology.rsna.org/content/244/3/708.abstract>. [Cited on page 55.]
- [265] SKAANE, P. AND SKJENNALD, A. *Screen-film mammography versus full-field digital mammography with soft-copy reading: Randomized trial in a population-based screening program-the Oslo II study*. Radiology, vol. 232(1) (2004), pp. 197–204. URL <http://radiology.rsna.org/content/232/1/197.abstract>. [Cited on page 55.]
- [266] SKAANE, P., YOUNG, K., AND SKJENNALD, A. *Population-based mammography screening: Comparison of screen-film and full-field digital mammography with soft-copy reading-Oslo I study*. Radiology, vol. 229(3) (2003), pp. 877–884. URL <http://radiology.rsna.org/content/229/3/877.abstract>. [Cited on page 55.]
- [267] SKAANE, P., ET AL. *Breast lesion detection and classification: Comparison of screen-film mammography and full-field digital mammography with soft-copy readingobserver performance study*. Radiology, vol. 237(1) (2005), pp. 37–44. URL <http://radiology.rsna.org/content/237/1/37.abstract>. [Cited on page 55.]
- [268] SMITH, S. W. *The Scientist and Engineers Guide to Digital Signal Processing*. California Technical, 1st edn. (1997), pp. 423–450. URL <http://www.dspsguide.com/CH25.PDF>. [Cited on pages 24, 78, 82, and 83.]
- [269] SONE, S., ET AL. *Development of a high-resolution digital tomosynthesis system and its clinical application*. Radiographics, vol. 11(5) (1991), pp. 807–822. URL <http://radiographics.rsna.org/content/11/5/807.abstract>. [Cited on page 59.]

- [270] ——. *Chest imaging with dual-energy subtraction digital tomosynthesis*. Acta Radiologica, vol. 34(4) (1993), pp. 346–350. URL <http://informahealthcare.com/doi/abs/10.1080/02841859309173255>. [Cited on page 59.]
- [271] ——. *Image processing in the digital tomosynthesis for pulmonary imaging*. European Radiology, vol. 5 (1995), pp. 96–101. URL <http://dx.doi.org/10.1007/BF00178089>. 10.1007/BF00178089. [Cited on pages 59 and 68.]
- [272] SPRAWLS, P. *Mammography physics and technology for effective clinical imaging*. <http://www.sprawls.org/resources/MAMMO/module.htm#11> (2011). [Cited on pages 23 and 62.]
- [273] STACK, J. P., ET AL. *Breast disease: tissue characterization with Gd-DTPA enhancement profiles*. Radiology, vol. 174(2) (1990), pp. 491–494. URL <http://radiology.rsna.org/content/174/2/491.abstract>. [Cited on page 45.]
- [274] STAVROS, A. T., ET AL. *Solid breast nodules: use of sonography to distinguish between benign and malignant lesions*. Radiology, vol. 196(1) (1995), pp. 123–134. URL <http://radiology.rsna.org/content/196/1/123.abstract>. [Cited on page 47.]
- [275] STERNBERG, S. S. *Histology for Pathologists*. Lippincott Williams and Wilkins, 2^{ed} edn. (1997). [Cited on page 36.]
- [276] STEVENS, G. M., FAHRIG, R., AND PELC, N. J. *Filtered backprojection for modifying the impulse response of circular tomosynthesis*. Medical Physics, vol. 28(3) (2001), pp. 372–380. URL <http://link.aip.org/link/?MPH/28/372/1>. [Cited on page 76.]
- [277] STUDHOLME, C. *Measures of 3d medical image alignment*. Phd thesis, University of London, London, UK (1997). [Cited on pages 99 and 110.]
- [278] STUDHOLME, C., HILL, D., AND HAWKES, D. *An overlap invariant entropy measure of 3d medical image alignment*. Pattern Recognition, vol. 32(1) (1999), pp. 71 – 86. URL <http://www.sciencedirect.com/science/article/pii/S0031320398000910>. [Cited on page 110.]
- [279] SU, B., ET AL. *The use of simultaneous iterative reconstruction technique for electrical capacitance tomography*. Chemical Engineering Journal, vol. 77(1-2) (2000), pp. 37 – 41. URL <http://www.sciencedirect.com/science/article/pii/S1385894799001345>. [Cited on page 85.]
- [280] SUETENS, P. *Fundamentals of Medical Imaging*. Cambridge University Press, 2nd edn. (2009). [Cited on pages 49 and 50.]
- [281] SURI, J. S., WILSON, D., AND LAXMINARAYAN, S. *Handbook of Biomedical Image Analysis- Volume 3: Registration Models*. Springer, 1st edn. (2005). [Cited on pages 99 and 106.]
- [282] SURI, J. S., ET AL. (Editors). *Advances in Diagnostic and Therapeutic Ultrasound Imaging*. Artech House Publishers, 1st edn. (2008). [Cited on page 47.]
- [283] SURYANARAYANAN, S., ET AL. *Evaluation of linear and nonlinear tomosynthetic reconstruction methods in digital mammography*. Academic Radiology, vol. 8(3) (2001), pp. 219 – 224. URL <http://www.sciencedirect.com/science/article/pii/S1076633203805305>. [Cited on page 61.]
- [284] SVAHN, T., ET AL. *The diagnostic accuracy of dual-view digital mammography, single-view breast tomosynthesis and a dual-view combination of breast tomosynthesis and digital mammography in a free-response observer*

- performance study.* Radiation Protection Dosimetry, vol. 139(1-3) (2010), pp. 113–117. URL <http://rpd.oxfordjournals.org/content/139/1-3/113.abstract>. [Cited on page 64.]
- [285] TABAR, L., AKERLUND, E., AND GAD, A. *Five-year experience with single-view mammography randomized controlled screening in sweden recent results.* Cancer Research, vol. 90 (1984), pp. 105–113. [Cited on page 54.]
- [286] TAILLEFER, R., ET AL. *Technetium-99m-Sestamibi prone scintimammography to detect primary breast cancer and axillary lymph node involvement.* Journal of Nuclear Medicine, vol. 36(10) (1995), pp. 1758–1765. URL <http://jnm.snmjournals.org/content/36/10/1758.short>. [Cited on page 57.]
- [287] TANG, A., ET AL. *Simultaneous ultrasound and MRI system for breast biopsy: Compatibility assessment and demonstration in a dual modality phantom.* Medical Imaging, IEEE Transactions on, vol. 27(2) (2008), pp. 247–254. [Cited on page 48.]
- [288] TANNER, C., ET AL. *Volume and shape preservation of enhancing lesions when applying non-rigid registration to a time series of contrast enhancing MR breast images.* In DELP, S., DiGOIA, A., AND JARAMAZ, B. (Editors), *Medical Image Computing and Computer-Assisted Intervention MICCAI 2000*, vol. 1935 of *Lecture Notes in Computer Science*. Springer Berlin / Heidelberg (2000), pp. CH371–CH371. URL http://dx.doi.org/10.1007/978-3-540-40899-4_33. [Cited on page 113.]
- [289] ——. *A method for the comparison of biomechanical breast models.* In *Mathematical Methods in Biomedical Image Analysis, 2001. MMBIA 2001. IEEE Workshop on* (2001), pp. 11–18. [Cited on page 113.]
- [290] ——. *Large breast compressions: Observations and evaluation of simulations.* Medical Physics, vol. 38(2) (2011), pp. 682–690. URL <http://link.aip.org/link/?MPH/38/682/1>. [Cited on page 46.]
- [291] THEVENAZ, P., BLU, T., AND UNSER, M. *Interpolation revisited [medical images application].* Medical Imaging, IEEE Transactions on, vol. 19(7) (2000), pp. 739–758. [Cited on page 100.]
- [292] TIMONER, S. J. *Compact representations for fast nonrigid registration of medical images.* Phd thesis, Massachusetts Institute of Technology, Cambridge, MA, USA (2003). [Cited on page 99.]
- [293] TURBELL, H. *Cone-beam reconstruction using filtered backprojection.* Ph.D. thesis, Linköping University, Sweden, SE-581 83 Linköping, Sweden (2001). Dissertation No. 672, ISBN 91-7219-919-9. [Cited on page 126.]
- [294] TWINING, E. W. *Tomography, by means of a simple attachment to the potter-bucky couch.* Br J Radiol, vol. 10(112) (1937), pp. 332–347. URL <http://bjr.birjournals.org/cgi/content/abstract/10/112/332>. [Cited on page 59.]
- [295] VAN DE SOMPEL, D. AND BRADY, M. *Systematic performance analysis of SART as applied to digital breast tomosynthesis.* In KRUPINSKI, E. (Editor), *Digital Mammography*, vol. 5116 of *Lecture Notes in Computer Science*. Springer Berlin / Heidelberg (2008), pp. 561–569. URL http://dx.doi.org/10.1007/978-3-540-70538-3_78. [Cited on page 90.]
- [296] VAN ENGELAND, S., ET AL. *A comparison of methods for mammogram registration.* Medical Imaging, IEEE Transactions on, vol. 22(11) (2003), pp. 1436–1444. [Cited on page 114.]
- [297] VAN ONGEVAL, C., BOSMANS, H., AND VAN STEEN, A. *Current status of digital mammography for screening and diagnosis of breast cancer.* Current Opinion in Oncology, vol. 18(6) (2006), pp. 547–554. URL http://journals.lww.com/co-oncology/Fulltext/2006/11000/Current_status_of_digital_mammography_for.2.aspx. [Cited on page 55.]

- [298] VEDANTHAM, S., ET AL. *Full breast digital mammography with an amorphous silicon-based flat panel detector: Physical characteristics of a clinical prototype.* Medical Physics, vol. 27(3) (2000), pp. 558–567. URL <http://link.aip.org/link/?MPH/27/558/1>. [Cited on page 60.]
- [299] VERHOEVEN, D. *Limited-data computed tomography algorithms for the physical sciences.* Appl. Opt., vol. 32(20) (1993), pp. 3736–3754. URL <http://ao.osa.org/abstract.cfm?URI=ao-32-20-3736>. [Cited on page 85.]
- [300] VERHOEVEN, D. D. *MART-type CT algorithms for the reconstruction of multidirectional interferometric data.* vol. 1553. SPIE (1992), pp. 376–387. URL <http://link.aip.org/link/?PSI/1553/376/1>. [Cited on page 85.]
- [301] VINNICOMBE, S., ET AL. *Full-field digital versus screen-film mammography: Comparison within the uk breast screening program and systematic review of published data.* Radiology, vol. 251(2) (2009), pp. 347–358. URL <http://radiology.rsna.org/content/251/2/347.abstract>. [Cited on page 55.]
- [302] VIOLA, P. AND WELLS III, W. M. *Alignment by maximization of mutual information.* International Journal of Computer Vision, vol. 24 (1997), pp. 137–154. URL <http://dx.doi.org/10.1023/A:1007958904918>. [Cited on page 110.]
- [303] VIOLA, P. A. *Alignment by maximization of mutual information.* Phd thesis, Massachusetts Institute of Technology (1995). [Cited on page 110.]
- [304] VOGEL, C. R. *Computational Methods for Inverse Problems.* SIAM (2002), pp. 9, 33–44, 74–75, 129–149. [Cited on pages 94 and 95.]
- [305] VUJOVIC, N. AND BRZAKOVIC, D. *Establishing the correspondence between control points in pairs of mammographic images.* Image Processing, IEEE Transactions on, vol. 6(10) (1997), pp. 1388 –1399. [Cited on page 114.]
- [306] WAHL, R. L., ET AL. *Primary and metastatic breast carcinoma: initial clinical evaluation with pet with the radiolabeled glucose analogue 2-[f -18]-fluoro-2-deoxy-d-glucose.* Radiology, vol. 179(3) (1991), pp. 765–770. URL <http://radiology.rsna.org/content/179/3/765.abstract>. [Cited on page 57.]
- [307] ——. *Prospective multicenter study of axillary nodal staging by positron emission tomography in breast cancer: A report of the staging breast cancer with pet study group.* Journal of Clinical Oncology, vol. 22(2) (2004), pp. 277–285. URL <http://jco.ascopubs.org/content/22/2/277.abstract>. [Cited on page 57.]
- [308] WALSH, T., ET AL. *Spectrum of mutations in BRCA1, BRCA2, CHEK2, and TP53 in families at high risk of breast cancer.* JAMA: The Journal of the American Medical Association, vol. 295(12) (2006), pp. 1379–1388. URL <http://jama.ama-assn.org/content/295/12/1379.abstract>. [Cited on pages 36 and 37.]
- [309] WANG, B., BARNER, K., AND LEE, D. *Algebraic tomosynthesis reconstruction.* vol. 5370. SPIE (2004), pp. 711–718. URL <http://link.aip.org/link/?PSI/5370/711/1>. [Cited on page 88.]
- [310] WARNER, E., ET AL. *Comparison of breast magnetic resonance imaging, mammography, and ultrasound for surveillance of women at high risk for hereditary breast cancer.* Journal of Clinical Oncology, vol. 19(15) (2001), pp. 3524–3531. URL <http://jco.ascopubs.org/content/19/15/3524.abstract>. [Cited on page 45.]
- [311] WEESE, J., ET AL. *Fast voxel-based 2D/3D registration algorithm using a volume rendering method based on the shear-warp factorization.* vol. 3661. SPIE (1999), pp. 802–810. URL <http://link.aip.org/link/?PSI/3661/802/1>. [Cited on page 99.]

- [312] WEINMANN, H., ET AL. *Characteristics of Gadolinium-DTPA complex: a potential NMR contrast agent*. American Journal of Roentgenology, vol. 142(3) (1984), pp. 619–624. URL <http://www.ajronline.org/content/142/3/619.abstract>. [Cited on page 44.]
- [313] WEISMANN, C. F., ET AL. *Three-dimensional targeting: a new three-dimensional ultrasound technique to evaluate needle position during breast biopsy*. Ultrasound in Obstetrics and Gynecology, vol. 16(4) (2000), pp. 359–364. URL <http://dx.doi.org/10.1046/j.1469-0705.2000.00182.x>. [Cited on page 48.]
- [314] WESTBROOK, C., ROTH, C. K., AND TALBOT, J. *MRI in Practice*. Wiley-Blackwell, 3rd edn. (2005). [No cited.]
- [315] WIENER, J. I., ET AL. *Breast and axillary tissue mr imaging: correlation of signal intensities and relaxation times with pathologic findings*. Radiology, vol. 160(2) (1986), pp. 299–305. URL <http://radiology.rsna.org/content/160/2/299.abstract>. [Cited on page 44.]
- [316] WIKIPEDIA. *Torus*. <http://en.wikipedia.org/wiki/Torus>. [Cited on page 127.]
- [317] ——. *Scintillator*. <http://en.wikipedia.org/wiki/Scintillator> (2011). [Cited on page 53.]
- [318] ——. *Ultrasound*. http://en.wikipedia.org/wiki/Ultrasound#cite_note-3 (2011). [Cited on page 46.]
- [319] WILD, J. J. AND REID, J. M. *Further pilot echographic studies on the histologic structure of tumors of the living intact human breast*. The American Journal of Pathology, vol. 28(5) (1952), pp. 839–861. [Cited on page 47.]
- [320] WIRTH, M. A., NARHAN, J., AND GRAY, D. W. S. *Nonrigid mammogram registration using mutual information*. vol. 4684. SPIE (2002), pp. 562–573. URL <http://link.aip.org/link/?PSI/4684/562/1>. [Cited on page 114.]
- [321] WU, T., ET AL. *Tomographic mammography using a limited number of low-dose cone-beam projection images*. Medical Physics, vol. 30(3) (2003), pp. 365–380. URL <http://link.aip.org/link/?MPH/30/365/1>. [Cited on page 75.]
- [322] ——. *A comparison of reconstruction algorithms for breast tomosynthesis*. Medical Physics, vol. 31(9) (2004), pp. 2636–2647. URL <http://link.aip.org/link/?MPH/31/2636/1>. [Cited on pages 61, 63, and 77.]
- [323] ——. *Digital tomosynthesis mammography using a parallel maximum-likelihood reconstruction method*. vol. 5368. SPIE (2004), pp. 1–11. URL <http://link.aip.org/link/?PSI/5368/1/1>. [Cited on page 85.]
- [324] ——. *Tomosynthesis imaging system and method* (2008). URL <http://www.google.com/patents/US7356113>. [Cited on page 124.]
- [325] XIAO, G., ET AL. *Nonrigid registration of 3D free-hand ultrasound images of the breast*. Medical Imaging, IEEE Transactions on, vol. 21(4) (2002), pp. 405 –412. [Cited on pages 48 and 114.]
- [326] XU, F. AND MUELLER, K. *Accelerating popular tomographic reconstruction algorithms on commodity PC graphics hardware*. Nuclear Science, IEEE Transactions on, vol. 52(3) (2005), pp. 654 – 663. [Cited on page 83.]
- [327] ——. *Real-time 3d computed tomographic reconstruction using commodity graphics hardware*. Physics in Medicine and Biology, vol. 52(12) (2007), p. 3405. URL <http://stacks.iop.org/0031-9155/52/i=12/a=006>. [Cited on page 83.]

- [328] YAFFE, M. J. AND ROWLANDS, J. A. *X-ray detectors for digital radiography*. Physics in Medicine and Biology, vol. 42(1) (1997), p. 1. URL <http://stacks.iop.org/0031-9155/42/i=1/a=001>. [Cited on page 60.]
- [329] YAN, H., ET AL. *Accelerating reconstruction of reference digital tomosynthesis using graphics hardware*. Medical Physics, vol. 34(10) (2007), pp. 3768–3776. URL <http://link.aip.org/link/?MPH/34/3768/1>. [Cited on page 84.]
- [330] YANG, C., NG, E. G., AND PENCZEK, P. A. *Unified 3-d structure and projection orientation refinement using quasi-newton algorithm*. Journal of Structural Biology, vol. 149(1) (2005), pp. 53 – 64. URL <http://www.sciencedirect.com/science/article/pii/S1047847704001716>. [Cited on page 157.]
- [331] YANG, G. AND ZHOU, O. *Stationary digital breast tomosynthesis for breast cancer detection*. Tech. rep. (2008). URL <http://spie.org/documents/Newsroom/Imported/1042/1042-2008-01-29.pdf>. [Cited on page 75.]
- [332] YANG, G., ET AL. *Combined reconstruction and registration of digital breast tomosynthesis*. In MART, J., ET AL. (Editors), *Digital Mammography*, vol. 6136 of *Lecture Notes in Computer Science*. Springer Berlin / Heidelberg (2010), pp. 760–768. URL http://dx.doi.org/10.1007/978-3-642-13666-5_102. [Cited on pages 40, 120, and 161.]
- [333] ——. *Combined reconstruction and registration of digital breast tomosynthesis: Sequential method versus iterative method*. In RAJPOOT, N. (Editor), *Medical Image Understanding and Analysis*. University of Warwick, Coventry. (2010). URL http://www2.warwick.ac.uk/fac/sci/dcs/events/past/miua2010/proceedings/paper_27.pdf. [Cited on pages 40, 120, and 161.]
- [334] ——. *Unconstrained simultaneous scheme to fully couple reconstruction and registration for digital breast tomosynthesis: A feasible study*. In TANNER, C., ET AL. (Editors), *Workshop on Breast Image Analysis*. In conjunction with MICCAI 2011 (2011), pp. 25–32. URL <http://www.diku.dk/BIA2011proceedings.pdf>. [Cited on pages 40 and 154.]
- [335] ——. *Joint registration and limited-angle reconstruction of digital breast tomosynthesis*. In *Digital Mammography, IWDM'12*, Lecture Notes in Computer Science. Springer Berlin / Heidelberg (2012). Submitted. [Cited on pages 40 and 154.]
- [336] ——. *A nonlinear least squares method for solving the joint reconstruction and registration problem in digital breast tomosynthesis*. In *Workshop on Biomedical Image Registration, WBIR'12*, Lecture Notes in Computer Science. Springer Berlin / Heidelberg (2012). Submitted. [Cited on pages 40 and 154.]
- [337] ——. *Numerical methods for coupled reconstruction and registration in digital breast tomosynthesis*. Medical Image Analysis (2012). Submitting. [Cited on pages 40 and 154.]
- [338] YANG, K. *Development and evaluation of a dedicated breast ct scanner*. Ph.D. thesis, University of California, Davis (2007). [Cited on page 65.]
- [339] YANG, W. T., ET AL. *Comparison of full-field digital mammography and screen-film mammography for detection and characterization of simulated small masses*. American Journal of Roentgenology, vol. 187(6) (2006), pp. W576–W581. URL <http://www.ajronline.org/content/187/6/W576.abstract>. [Cited on page 55.]
- [340] YAP, K.-H., ET AL. *A nonlinear L1-norm approach for joint image registration and super-resolution*. Signal Processing Letters, IEEE, vol. 16(11) (2009), pp. 981 –984. [Cited on page 157.]
- [341] YIN, F.-F., ET AL. *Computerized detection of masses in digital mammograms: Automated alignment of breast images and its effect on bilateral-subtraction technique*. Medical Physics, vol. 21(3) (1994), pp. 445–452. URL <http://link.aip.org/link/?MPH/21/445/1>. [Cited on page 114.]

- [342] YOO, T. S. *Insight into Images: Principles and Practice for Segmentation, Registration, and Image Analysis*. AK Peters, 1st edn. (2004). [Cited on page 104.]
- [343] YORKER, J. G., ET AL. *Characterization of a full-field digital mammography detector based on direct x-ray conversion in selenium*. vol. 4682. SPIE (2002), pp. 21–29. URL <http://link.aip.org/link/?PSI/4682/21/1>. [Cited on page 60.]
- [344] ZHANG, Y., ET AL. *A comparative study of limited-angle cone-beam reconstruction methods for breast tomosynthesis*. Medical Physics, vol. 33(10) (2006), pp. 3781–3795. URL <http://link.aip.org/link/?MPH/33/3781/1>. [Cited on pages 61, 78, and 89.]
- [345] ———. *Tomosynthesis reconstruction using the simultaneous algebraic reconstruction technique (SART) on breast phantom data*. vol. 6142. SPIE (2006), p. 614249. URL <http://link.aip.org/link/?PSI/6142/614249/1>. [Cited on pages 78 and 89.]
- [346] ZHENG, Y., ET AL. *STEP: Spatiotemporal enhancement pattern for MR-based breast tumor diagnosis*. Medical Physics, vol. 36(7) (2009), pp. 3192–3204. URL <http://link.aip.org/link/?MPH/36/3192/1>. [Cited on page 45.]
- [347] ZIEDSES DES PLANTES, B. G. *New method of differentiation in radiography (Planigraphy). (eine neue methode zur differenzierung in der röentgenographie (planigraphie))*. Acta Radiologica (Old Series), vol. 13 (1932), pp. 182–191. [Cited on page 59.]
- [348] ZITOVÁ, B. AND FLUSSER, J. *Image registration methods: a survey*. Image and Vision Computing, vol. 21(11) (2003), pp. 977–1000. URL <http://www.sciencedirect.com/science/article/pii/S0262885603001379>. [Cited on pages 99 and 106.]
- [349] ZUO, C. S., ET AL. *Automatic motion correction for breast MR imaging*. Radiology, vol. 198(3) (1996), pp. 903–906. URL <http://radiology.rsna.org/content/198/3/903.abstract>. [Cited on page 113.]

[This page intentionally left blank]

[This page intentionally left blank]